

Nanostructured Metal Oxides for Highly- Selective VOC and Gas Sensing

Ph.D. Thesis

By
BISWAJIT MANDAL



**DEPARTMENT OF ELECTRICAL ENGINEERING
INDIAN INSTITUTE OF TECHNOLOGY INDORE**

JULY 2020

Nanostructured Metal Oxides for Highly- Selective VOC and Gas Sensing

A THESIS

*Submitted in partial fulfillment of the
requirements for the award of the degree*

of

DOCTOR OF PHILOSOPHY

By

BISWAJIT MANDAL



**DEPARTMENT OF ELECTRICAL ENGINEERING
INDIAN INSTITUTE OF TECHNOLOGY INDORE**

JULY 2020

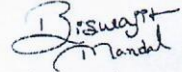


INDIAN INSTITUTE OF TECHNOLOGY INDORE

CANDIDATE'S DECLARATION

I hereby certify that the work which is being presented in the thesis entitled **Nanostructured Metal Oxides for Highly-Selective VOC and Gas Sensing**, in the partial fulfillment of the requirements for the award of the degree of **Doctor of Philosophy** and submitted in the **Department of Electrical Engineering, Indian Institute of Technology Indore**, is an authentic record of my own work carried out during the time period from **November 2015 to July 2020** under the supervisions of **Dr. Shaibal Mukherjee**, Associate Professor, Electrical Engineering, IIT Indore.

The matter presented in this thesis has not been submitted by me for the award of any other degree of this or any other institute.

 03/08/2020

Signature of the student with date

BISWAJIT MANDAL

This is to certify that the above statement made by the candidate is correct to the best of our knowledge.

 3/8/2020

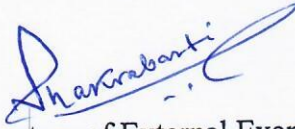
Dr. SHAIBAL MUKHERJEE

Signature of Thesis Supervisor with date

BISWAJIT MANDAL has successfully given his Ph.D. Oral Examination held on December 17, 2020.



Signature of Chairman OEB
Date: 17.12.2020



Signature of External Examiner
Date: 17.12.2020



Signature of Thesis Supervisor
Date: 17/12/2020



Signature of PSPC Member #1
Date: 17/12/2020



Signature of PSPC Member #2
Date: 17/12/2020



Signature of Convener, DPGC
Date: 17/12/2020



Signature of Head of Department
Date: 17/12/2020

ACKNOWLEDGEMENTS

*kārpanya-doṣopahata-svabhāvaḥ
prcchāmi tvāṁ dharmā-sammūḍha-cetāḥ
yac chreyah syān niścitaṁ brūhi tan me
śiṣyas te 'haṁ śādhi mām tvāṁ prapannam*

First, I would like to thank Almighty God श्रीकृष्ण for guiding me throughout this period and hoping he will guide me for the rest of my life.

I would like to express my deep sense of gratitude to my supervisor **Dr. Shaibal Mukherjee** for his outstanding mentorship and support provided throughout these years. Under his guidance and encouragement, I successfully surpassed many difficulties and learned a lot.

I am profoundly grateful to **Dr. Apurba K Das** for his insightful ideas on hybrid materials research and support throughout this entire period.

I am extremely grateful to my doctoral committee members **Dr. Mukesh Kumar** and **Dr. Tushar Kanti Mukherjee** for giving me valuable advice on my research and kindly going through my dissertation.

My sincere appreciation to **Dr. Ajay Agarwal**, Sr. Principal Scientist and Head of Nano Biosensors Group at CSIR-CEERI, Pilani, India, for providing valuable suggestions on CO sensing work. I am grateful to **Dr. Myo Than Htay**, Hashimoto-Myo Laboratory, Department of Electrical and Computer Engineering, Shinshu University, Japan, for his support with TEM imaging and valuable feedbacks with the manuscripts. I would like to express my gratitude to **Dr. Sharath Sriram** and **Dr. Madhu Bhaskaran**, leaders of the Functional Materials and Microsystems Research Group, RMIT University, Australia, for their help with XPS measurements and brilliant suggestions with the

manuscripts. I am very grateful for their untiring support during the work on flexible sensor.

I would like to thank **Dr. Neelesh Kumar Jain**, Director (officiating), IIT Indore, for providing the essential experimental facilities and financial support in attending international conferences. I want to acknowledge the support provided by sophisticated instrumentation center (SIC) at IIT Indore, for performing SEM, EDX, TGA, BET and XRD measurements.

I would like to thank, Ministry of Electronics and Information Technology (MeitY), Government of India, for providing fellowship under Visvesvaraya Ph.D. Scheme for Electronics and Information Technology. This work was supported by the research and development work undertaken in the project under the Visvesvaraya Ph.D. Scheme of Ministry of Electronics and Information Technology (MeitY), Government of India, being implemented by Digital India Corporation (formerly Media Lab Asia).

I would like to thank my colleagues including **Dr. Vishnu Awasthi, Dr. Pankaj Sharma, Dr. Aaryashree, Dr. Vivek Garg, Dr. Brajendra Singh Sengar, Dr. Amitesh Kumar, Md Arif Khan, Ritesh Bhardwaj, Mangal Das, Gaurav Siddharth, Pawan Kumar, Sanjay Kumar, Ruchi Singh, Chandrabhan Patel, Mayank Dubey, Jyoti Kumari, and Sumit Chaudhary** for their moral support, best wishes, and unforgettable days we spent together. I am grateful for all of you for providing a stimulating and fun environment.

I owe very special thanks to **Sayan Maiti** and **Ankan Biswas**, for their brilliant collaboration during this thesis work.

I am thankful to **Vasudev Chaudhari, Nivedita Jaiswal, and Uday Kumar Singh** for their moral support.

I am very thankful to **Nimai Sundar Das** for his spiritual guidance during difficult times.

I am very grateful to my wife **Ananya** for her immense support and selfless services in the last two and half years of my PhD.

Last, but far from least, I must thank to my parents and brother, who have supported me throughout this life. I owe a lot to them.

Biswajit Mandal

© Copyright by BISWAJIT MANDAL 2020

All Rights Reserved

Dedicated to my Father

LIST OF PUBLICATIONS

A: Publications from PhD Thesis Work

A1. In Peer-reviewed Journals

1. **Biswajit Mandal**, Sayan Maiti, Aaryashree, Gaurav Siddharth, Mangal Das, Ajay Agarwal, Apurba K. Das, Shaibal Mukherjee, “*Organo-Di-Benzoic Acidified ZnO Nanohybrids for Highly Selective Detection of CO Gas at Low Temperature*”, **Journal of Physical Chemistry C**, vol. 124, no. 13, pp. 7303-7316, March 2020. (Impact Factor: 4.3)
2. **Biswajit Mandal**, Aaryashree, Mangal Das, Myo Than Htay, Shaibal Mukherjee, “*Architecture Tailoring of MoO₃ Nanostructures for Superior Ethanol Sensing Performance*”, **Materials Research Bulletin**, vol. 109, pp. 281–290, January 2019. (Impact Factor: 3.35)
3. **Biswajit Mandal**, Ankan Biswas, Aaryashree, Daya S. Sharma, Ritesh Bhardwaj, Mangal Das, Md Aatur Rahman, Sruthi Kuriakose, Madhu Bhaskaran, Sharath Sriram, Myo Than Htay, Apurba K. Das, Shaibal Mukherjee, “ *π -Conjugated Amine-ZnO Nanohybrids for the Selective Detection Of CO₂ Gas at Room Temperature*”, **ACS Applied Nano Materials**, vol. 1, no. 12, pp. 6912–6921, November 2018. (New Journal)
4. **Biswajit Mandal**, Aaryashree, Rohit Singh, Shaibal Mukherjee, “*Highly Selective and Sensitive Methanol Sensor Using Rose-Like ZnO Microcube and MoO₃ Micrograss Based Composite*”, **IEEE Sensors Journal**, vol. 18, no.7, pp. 2659–2666, April 2018. (Impact Factor: 3.07)

A2. In Proceedings of International Conferences

1. **Biswajit Mandal**, Ankan Biswas, Aaryashree, Apurba K. Das, Shaibal Mukherjee, “*Layer-By-Layer Assembly of π -Conjugated Amine and ZnO Nanohybrids for Room Temperature CO₂ Detection*”, **18th International Meeting on Chemical Sensors (IMCS 2020)**, Montreal, Canada, May 10-14, 2020.
2. **Biswajit Mandal**, Ankan Biswas, Aaryashree, Apurba K. Das, Shaibal Mukherjee, “*Organic Amine Functionalized ZnO for CO₂ Sensing Application*”, **6th Nano Today Conference**, Lisbon, Portugal, June 17-20, 2019.
3. **Biswajit Mandal**, Ankan Biswas, Aaryashree, Daya S. Sharma, Mangal Das, Madhu Bhaskaran, Sarath Sriram, Apurba K. Das, Shaibal Mukherjee, “*Nanohybrid Thin-Film on Flexible Substrate for Room Temperature CO₂ Detection*”, **4th International Conference of Emerging Electronics (IEEE-ICEE, 2018)**, Royal Orchid Resort & Convention Centre, Bangalore, December 16-19, 2018.
4. **Biswajit Mandal**, Daya S. Sharma, Gaurav Siddharth, Ritesh Bhardwaj, Mangal Das, Amitesh Kumar, Shaibal Mukherjee, “*Growth of Ultra-High Oriented Vertically Aligned ZnO Nanorod Arrays on a DIBS Grown Seed Layer Towards Minimum Interspace Area*”, **CMNA 2018**, Indore, India, November 01-03, 2018.
5. **Biswajit Mandal**, Aaryashree, Ritesh Bhardwaj, Mangal Das, Daya S. Sharma, Shaibal Mukherjee, “*Enhancement in Methanol Selectivity Using MoO₃ Micrograss Encapsulated ZnO Microcube*”, **IEEE SENSOR 2018**, New Delhi, India, October 28-31, 2018.
6. **Biswajit Mandal**, Aaryashree, Ritesh Bhardwaj, Mangal Das, Daya S. Sharma, Myo Than Htay, Shaibal Mukherjee, “*Defect Control in MoO₃ Nanostructures as Ethanol Sensor*”, **IEEE SENSOR 2018**, New Delhi, India, October 28-31, 2018.

7. **Biswajit Mandal**, Aaryashree, Mangal Das, Shaibal Mukherjee, “*Synthesis of Micrograss Like α - MoO_3 and Their Enhance Ethanol Sensing Performance*”, **International Symposium on Integrated functionalities (ISIF 2017)**, Shangri-La’s Eros Hotel, New Delhi, India, December 10-13, 2017.
8. **Biswajit Mandal**, Aaryashree, Mangal Das, Shaibal Mukherjee, “*Synthesis of High Crystalline Nanobelt-Like α - MoO_3 and Their Alcohol Sensing Performance*”, **19th International Workshop on The Physics of Semiconductor Devices (IWPSD 2017)**, IIT Delhi, India, December 11-15, 2017.

A3. Patent

1. *Organo-Acidified Zinc Oxide Carbon Monoxide Gas Sensor*

Inventors: Shaibal Mukherjee, Apurba K. Das, Ajay Agarwal, **Biswajit Mandal**, Aaryashree, Sayan Miati

Patent no. 201921026594, Jul 3, 2019 (**Status: Published**)

B: Other Publications during PhD

B1. In Peer-reviewed Journals

1. Sayan Maiti, **Biswajit Mandal**, Meenu Sharma, Shaibal Mukherjee, Apurba K. Das, “*Covalent Organic Polymer as an Efficient Chemosensor for Highly Selective H_2S detection Through Proton Conduction*”, **ChemComm**, vol. 56, no. 65, pp. 9348–9351, July 2020. (**Impact Factor: 6.16**)
2. Aaryashree, **Biswajit Mandal**, Ankan Biswas, Ritesh Bhardwaj, Ajay Agarwal, Apurba K Das, and Shaibal Mukherjee, “*Mesoporous Tyrosine Functionalized BTC-ZnO Composite for Highly Selective Capacitive CO Sensor*”, **IEEE Sensors Journal**, Accepted, September 2020. (**Impact Factor: 3.07**)

3. Mangal Das, Amitesh Kumar, Sanjay Kumar, **Biswajit Mandal**, Gaurav Siddharth, Pawan Kumar, Myo Than Htay, and Shaibal Mukherjee, “*Impact of interfacial SiO₂ on dual ion beam sputtered Y₂O₃-based memristive system*”, **IEEE Transactions on Nanotechnology**, vol. 19, no. 1, pp. 332–337, April 2020. **(Impact Factor: 2.85)**
4. Aaryashree, **Biswajit Mandal**, Ritesh Bhardwaj, Sayan Maiti, Daya S. Sharma, Apurba K. Das, Shaibal Mukherjee, “*Functionalized Oligo(p-Phenylenevinylene) and ZnO Based Nanohybrid for Selective Ammonia Sensing at Room Temperature*”, **IEEE Sensors Journal**, vol. 19, no. 8, pp. 2847–2854, December 2018. **(Impact Factor: 3.07)**
5. Mangal Das, Amitesh Kumar, Sanjay Kumar, **Biswajit Mandal**, Md Arif Khan, Shaibal Mukherjee, “*Effect of Surface Variations on the Performance of Ytria Based Memristive System*”, **IEEE Electron Device Letters**, vol. 39, no. 12, pp. 1852–1855, October 2018. **(Impact Factor: 3.75)**
6. Mangal Das, Amitesh Kumar, **Biswajit Mandal**, Myo Than Htay, Shaibal Mukherjee, “*Impact of Schottky Junctions in the Transformation of Switching Modes in Amorphous Y₂O₃-Based Memristive System*”, **Journal of Physics D: Applied Physics**, vol. 51, no. 31, p. 315102, July 2018. **(Impact Factor: 2.82)**
7. Aaryashree, Pankaj Sharma, **Biswajit Mandal**, Anakn Biswas, Manoj K. Manna, Sayan Maiti, Apurba K. Das, Shaibal Mukherjee, “*Synergetic Accrual of Lamellar Nanohybrids for Band-Selective Photodetection*”, **Journal of Physical Chemistry C**, vol. 121, no. 26, pp. 14037–14044, June 2016. **(Impact Factor: 4.30)**
8. Gaurav Siddharth, Ruchi Singh, Vivek Garg, Brajendra S. Sengar, Mangal Das, **Biswajit Mandal**, Myo Than Htay, Mukul Gupta, and Shaibal Mukherjee, “*Investigation of DIBS-deposited CdZnO/ZnO-based multiple quantum well for large-area photovoltaic application*”, **IEEE Transactions on Electron**

Devices, vol. 67, no. 12, pp. 5587–5592, November 2020.
(Impact Factor: 2.62)

B2. In Proceedings of International Conferences

1. Mangal Das, Amitesh Kumar, Sanjay Kumar, **Biswajit Mandal**, Pawan Kumar, Shaibal Mukherjee, “*Impact of Schottky Junction on the Resistive Switching of Yttrium Oxide*”, **9th International Conference on Key Engineering Materials (ICKEM)**, Oxford, United Kingdom, March 29-April 01, 2019.
2. Mangal Das, Amitesh Kumar, Sanjay Kumar, **Biswajit Mandal**, Shaibal Mukherjee, “*Effect of Schottky Junction in Y_2O_3 Based Memristive Devices*”, **4th International Conference of Emerging Electronics (IEEE-ICEE, 2018)**, Royal Orchid Resort & Convention Centre, Bangalore, December 16-19, 2018.
3. Ritesh Bhardwaj, **Biswajit Mandal**, Md Arif Khan, Aaryashree, Amitesh Kumar, Shaibal Mukherjee, “*Spectral Photoresponse Tunability of MgZnO Based UV Photodetectors*”, **18th IEEE International Conference on Nanotechnology (IEEE NANO 2018)**, Cork, Ireland, July 23-26 2018.
4. Amitesh Kumar, Mangal Das, **Biswajit Mandal**, Ritesh Bhardwaj, Aaryashree, Abhinav Kranti, Shaibal Mukherjee, “*Nano-Scaled ZnO Based Resistive Memory Device Fabricated by Dual Ion Beam Sputtering*”, **18th IEEE International Conference on Nanotechnology (IEEE NANO 2018)**, Cork, Ireland, July 23-26 2018.
5. Aaryashree, **Biswajit Mandal**, Ritesh Bhardwaj, Sayan Maiti, Apurba K. Das, Shaibal Mukherjee, “*Self-Assembled Zn-OPV Composite for Ammonia Sensing*”, **17th International Meeting on Chemical Sensors (IMCS 2018)**, University of Vienna, Vienna, Austria, July 15-19, 2018.
6. Mangal Das, Amitesh Kumar, **Biswajit Mandal**, Brajendra S. Sengar, Shaibal Mukherjee, “*Synaptic Learning and Memory Functions in Amorphous Yttria-Based Memristive Systems*”,

- Materials Research Society (MRS) Spring Meeting**, Phoenix, Arizona, USA, April 2-6, 2018.
7. Amitesh Kumar, Mangal Das, Brajendra S. Sengar, **Biswajit Mandal**, Rohit Singh, Abhinav Kranti, Shaibal Mukherjee, “*Novel Forming-Free Resistive Memory Based on Dual Ion Beam Sputtering Engineered Oxygen Vacancies/Interstitial Defects in ZnO*”, **Materials Research Society (MRS) Spring Meeting**, Phoenix, Arizona, USA, April 2-6, 2018.
 8. Aaryashree, **Biswajit Mandal**, Rohit G. Jadhav, Mangal Das, Apurba K. Das, Shaibal Mukherjee, “*Study of ZnO-Oligophenylenevinylene Nanohybrid for Optoelectronic Applications*”, **6th International Symposium on Integrated Functionalities (ISIF 2017)**, Shangri-La’s Eros Hotel, Delhi, India, December 10-13, 2017.
 9. Mangal Das, Amitesh Kumar, **Biswajit Mandal**, Shaibal Mukherjee, “*Influence of Deposition Temperature on Memristance in n-Si/Y₂O₃/Al Structure*”, **6th International Symposium on Integrated Functionalities (ISIF 2017)**, New Delhi, India, December 10-13, 2017.
 10. Amitesh Kumar, Mangal Das, Rohit Singh, Md Arif Khan, **Biswajit Mandal**, Abhinav Kranti, Shaibal Mukherjee, “*ZnO Based Resistive Switching Memory Fabricated by Dual Ion Beam Sputtering with Excellent Endurance*”, **6th International Symposium on Integrated Functionalities (ISIF 2017)**, New Delhi, India, December 10-13, 2017.
 11. Aaryashree, **Biswajit Mandal**, Rohit G. Jadhav, Apurba K. Das, Shaibal Mukherjee, “*Molar Concentration Variation in Hydrothermal Growth for Highly Porous Zn-BTC Metal Organic Framework*”, **19th International Workshop on The Physics of Semiconductor Devices (IWPSD 2017)**, IIT Delhi, India, December 11-15, 2017.
 12. Mangal Das, Amitesh Kumar, **Biswajit Mandal**, Shaibal Mukherjee, “*Influence of Crystallinity on Memristance in n-*

Si/Y₂O₃/Al Structure”, **19th International Workshop on The Physics of Semiconductor Devices (IWPSD 2017)**, IIT Delhi, India, December 11-15, 2017.

B3. Patent

1. *Hybrid Mesoporous Composites Gas Sensors*

Inventors: Shaibal Mukherjee, Apurba K. Das, Ajay Agarwal, Aaryashree, **Biswajit Mandal**, Ankan Biswas

Patent no. 201921026576, Jul 3, 2019 (**Status: Published**)

2. *Ultrasensitive NO₂ Sensor Based on S and N Doped Carbon Dot Functionalized Tungsten Oxide*

Inventors: Shaibal Mukherjee, Apurba K. Das, Chandrabhan Patel, **Biswajit Mandal**, Rohit G. Jadhav

Patent no. 202021041967, Sep 28, 2020 (**Status: Published**)

TABLE OF CONTENTS

TITLE PAGE.....	i
DECLARATION PAGE.....	ii
ACKNOWLEDGEMENTS.....	iii
DEDICATION PAGE.....	v
LIST OF PUBLICATIONS.....	vii
TABLE OF CONTENTS.....	xiv
LIST OF FIGURES.....	xx
LIST OF TABLES.....	xxvi
ACRONYMS.....	xxvii
NOMENCLATURE.....	xxix
ABSTRACT.....	xxx

Chapter 1 Introduction-Gas Sensor

1.1 Introduction	1
1.2 History of Gas Sensor Development	2
1.3 Gas/VOC Sensor Types	3
1.4 Gas/VOC Sensing Terminology	7
1.5 Semiconducting Metal Oxide (MOX) Gas/VOC Sensors	8
1.5.1 General Sensing Mechanism	9
1.5.2 Factors affects sensing performance	13
1.5.2.1 Grain Size Effect	13
1.5.2.2 Effect of crystallographic plane	15
1.5.2.3 Geometrical aspect	15
1.5.2.4 Effect of noble metals additive	15
1.5.2.5 Others factors	16

1.6	Material Selection	17
1.6.1	Ideal characteristics of a gas sensing material	17
1.6.2	Why metal oxide? And why ZnO or MoO ₃ ?	18
1.7	Aim and Objectives	24
1.8	Organization of Thesis	25
1.9	References	26

Chapter 2 Synthesis and Characterization Techniques

2.1	Introduction	35
2.2	Substrate Selection and Its Cleaning Procedure	36
2.2.1	'Si' Substrate Cleaning Procedure	36
2.2.2	Glass Substrate Cleaning Procedure	37
2.2.3	PDMS Substrate Cleaning Procedure	37
2.3	Synthesis/Deposition Techniques	38
2.3.1	Hydrothermal Synthesis Method	38
	Hydrothermal Synthesis for the Growth of	
2.3.1.1	Single Crystalline Inorganics and Organic-	39
	Inorganic Hybrids	
2.3.1.2	Hydrothermal Chamber: Autoclave	41
2.3.1.3	Hydrothermal Procedure	42
2.3.2	Reactive DC Magnetron Sputtering	43
2.3.3	E-Beam Evaporation	45
2.4	Material Characterization Techniques	48
2.4.1	X-Ray Diffraction	48
	Field Emission Scanning Electron	
2.4.2	Microscopy/Energy	50
	Dispersive X-ray Spectroscopic	
2.4.3	Transmission Electron Microscopy	53
2.4.4	X-Ray Photoelectron Spectroscopy	56
2.4.5	Thermogravimetric Analysis	58
2.4.6	Brunauer-Emmett-Teller Surface Area Analysis	60
2.5	Gas/VOC Sensing Measurement system	62
2.5.1	VOC sensing measurement system	62
2.5.2	Gas sensing measurement system	64
2.6	References	65

Chapter 3 Synthesis of NBA-ZnO Nanohybrids for CO₂ Gas Detection

3.1	Introduction	67
3.2	Experimental	69
3.2.1	Substrate Preparation	69
3.2.2	Synthesis of naphthalene based amine (NBA)	70
3.2.3	In-Situ growth of NBA-ZnO Nanohybrids and ZnO Nanorods on Prepared Flexible Substrate	73
3.3	Results and Discussion	73
3.3.1	Structural and morphological study	73
3.3.1.1	Field Emission Scanning Electron Microscopy	73
3.3.1.2	Transmission Electron Microscopy	75
3.3.1.3	X-Ray Diffraction	76
3.3.1.4	Energy Dispersive X-ray Spectroscopy	77
3.3.1.5	Density Functional Theory Study of NBA NPs	77
3.3.2	Growth Mechanism	78
3.3.3	CO ₂ sensing properties of the NBA-ZnO nanohybrids	79
3.3.4	CO ₂ Sensing Mechanism	83
3.4	Conclusion	86
3.5	References	87

Chapter 4 Synthesis of ODBA-ZnO Nanohybrids for CO gas Detection

4.1	Introduction	95
4.2	Experimental	97
4.2.1	Synthesis of Organo-Di-Benzoic Acid (ODBA)	97
4.2.2	Single-Pot Hydrothermal Synthesis of Organo-Di-Benzoic Acidified ZnO	100
4.2.3	Sensor Fabrication	101
4.3	Results and Discussion	102

4.3.1	Morphology and Composition	102
4.3.1.1	Field Emission Scanning Electron Microscopy	102
4.3.1.2	Energy Dispersive X-Ray Spectroscopy	103
4.3.1.3	X-Ray Diffraction	103
4.3.1.4	Thermogravimetric Analysis	104
4.3.1.5	BET Surface Area Analysis	105
4.3.2	Growth Mechanism	106
4.3.3	Gas Sensing Properties	106
4.3.4	CO Sensing Mechanism	112
4.4	Conclusion	113
4.5	References	114

Chapter 5 Synthesis of ZnO/MoO₃ Composite for Methanol Sensing Application

5.1	Introduction	125
5.2	Experimental	126
5.2.1	Synthesis of ZnO Microcubes	126
5.2.2	Synthesis of MoO ₃ Micrograss	126
5.2.3	Synthesis of Rose-Like ZnO/MoO ₃ Composite	126
5.2.4	Sensor Fabrication	127
5.3	Results and Discussion	127
5.3.1	Morphology and Crystalline Structure	127
5.3.1.1	Field Emission Scanning Electron Microscopy	127
5.3.1.2	X-Ray Diffraction	128
5.3.1.3	X-Ray Photoluminescence Spectroscopy	129
5.3.1.4	Brunauer–Emmett–Teller Surface Area Analysis	130
5.3.1.5	Formation Mechanism	131
5.3.2	VOCs Sensing Performance of Composite Material	132
5.3.3	VOCs Sensing Mechanism	137
5.4	Conclusion	139

5.5	References	140
-----	------------	-----

Chapter 6 Synthesis of MoO₃ Nanostructures for Ethanol Sensing Application

6.1	Introduction	143
6.2	Experimental Section	144
6.2.1	Synthesis of MoO ₃ Nanocrystals	144
6.2.2	Sensor Fabrication	145
6.3	Results and Discussions	145
6.3.1	Structural and Morphological Characteristics	145
6.3.1.1	X-Ray Diffraction	145
6.3.1.2	Field Emission Scanning Electron Microscopy	148
6.3.1.3	Transmission Electron Microscopy	149
6.3.1.4	Brunauer–Emmett–Teller Surface Area Analysis	150
6.3.1.5	Growth Mechanism	151
6.3.2	Ethanol Sensing Properties	154
6.3.3	Ethanol Sensing Mechanism	160
6.4	Conclusion	161
6.5	References	162

Chapter 7 Simulation and Realization of Readout Circuits Towards the Development of Lab-Based Portable Gas/VOC Sensors

7.1	Introduction	167
7.2	Sensor Circuits	169
7.2.1	Resistance Readout Circuits	169
7.2.2	Temperature Control Circuits	171
7.3	Simulation of the Circuits	173
7.4	Practical Realization	181
7.5	Drawbacks	182
7.6	PCB Layout Design	182

7.7 Conclusion	183
7.8 References	184

Chapter 8 Conclusion and Future Scope

8.1 Conclusions	185
8.2 Future Scopes	188

LIST OF FIGURES

Figure No.	Figure Caption	Page No.
Figure 1.1	<i>Various types of gas/VOC sensors based on the principles of detection.</i>	5
Figure 1.2	<i>Adsorbed oxygen species at SnO₂ surface at different temperatures through Fourier transform infrared analysis (FTIR), temperature programmed desorption (TDP), and electron paramagnetic resonance (EPR) technique.</i>	9
Figure 1.3	<i>Schematic of the energy band diagram, the relationship between the adsorbed oxygen species and the depletion layer, and the potential barrier for charge carriers under (a) vacuum, (b) open air, (c) reducing gas, and (d) oxidizing gas ambient atmosphere, taking n-type MOX as an example.</i>	11
Figure 1.4	<i>Schematic of the grain contact model and electronic band of (a) grain boundary contact (b) neck contact.</i>	13
Figure 1.5	<i>Schematic models for grain size effect.</i>	14
Figure 1.6	<i>(a) Chemical and (b) electronic sensitization of noble metal added SnO₂ sensor.</i>	16
Figure 1.7	<i>ZnO crystal structure (wurtzite).</i>	20
Figure 1.8	<i>Orthorhombic α-MoO₃ crystal structure.</i>	22
Figure 2.1	<i>Phase diagram of the water.</i>	39
Figure 2.2	<i>(a) Density and (b) dielectric constant of the water as a function of temperature and pressure.</i>	40
Figure 2.3	<i>Pressure against temperature under different degree of vessel filling.</i>	41
Figure 2.4	<i>Stainless steel Teflon lined autoclave.</i>	42
Figure 2.5	<i>Schematic of the flow process of the hydrothermal method.</i>	43
Figure 2.6	<i>Schematic representation of reactive DC magnetron sputtering.</i>	45
Figure 2.7	<i>Schematic of the E-beam evaporation technique.</i>	46

Figure 2.8	<i>The system used to grow seed layer and metal electrodes in this work.</i>	47
Figure 2.9	<i>Schematic representation of diffraction of X-rays by a set of crystal planes relying on Bragg's law.</i>	49
Figure 2.10	<i>Image of the Rigaku SmartLab Automated Multipurpose X-ray Diffractometer.</i>	50
Figure 2.11	<i>Schematic of electron solid interaction.</i>	51
Figure 2.12	<i>Schematic of the FESEM/EDX working principle.</i>	52
Figure 2.13	<i>Image of the FESEM/EDX system, ZEISS Supra55.</i>	53
Figure 2.14	<i>Schematic of the TEM working principle.</i>	54
Figure 2.15	<i>Image of the HRTEM system used in this thesis work.</i>	55
Figure 2.16	<i>Schematic of photoelectric effect.</i>	56
Figure 2.17	<i>Schematic of working principle of XPS.</i>	57
Figure 2.18	<i>Image of the XPS system used in the present thesis work.</i>	58
Figure 2.19	<i>Different type of TGA plot.</i>	59
Figure 2.20	<i>Image of the Mettler Toledo Thermal Analyzer used in this thesis work.</i>	60
Figure 2.21	<i>Various type of adsorption isotherms as classified by IUPAC.</i>	61
Figure 2.22	<i>Image of the Autosorb iQ2, used in the present thesis work for BET surface area analysis.</i>	62
Figure 2.23	<i>Schematic of the VOC sensing setup.</i>	63
Figure 2.24	<i>Schematic of the gas sensing setup.</i>	64
Figure 2.25	<i>Image of the gas/VOC sensing setup developed in this thesis work.</i>	65
Figure 3.1	<i>(a) Device schematic of the flexible sensor. (b) Flexibility of as-fabricated sensor. (c) Scanning electron micrograph of interdigitated electrodes (IDEs) showing inter-electrode dimensions.</i>	69
Figure 3.2	<i>Synthesis scheme of NBA (compound 1).</i>	72
Figure 3.3	<i>FESEM image of NBA nanoparticles.</i>	73
Figure 3.4	<i>FESEM images of NBA-ZnO nanohybrids after (a) 1 h, (b) 2 h, and (c) 3 h reaction time. (d) Higher magnification micrograph of 3 h reaction time nanohybrids.</i>	74
Figure 3.5	<i>FESEM image of ZnO nanorods grown on IDEs patterned seed layer coated flexible substrate (reaction time 3 h). Inset shows ZnO nanorods at higher magnification.</i>	74

Figure 3.6	<i>(a) Low magnification TEM image, (b) High magnification TEM image, (c) HRTEM image, and (d) SAED pattern of NBA-ZnO nanohybrid.</i>	75
Figure 3.7	<i>XRD pattern of ZnO nanorods, NBA nanoparticle, and NBA-ZnO nanohybrids sample.</i>	76
Figure 3.8	<i>EDX pattern of NBA-ZnO nanohybrid.</i>	77
Figure 3.9	<i>DFT study of NBA NPs.</i>	77
Figure 3.10	<i>Growth schematic of NBA-ZnO nanohybrids.</i>	78
Figure 3.11	<i>Current-voltage characteristics of NBA-ZnO nanohybrids under different bending diameter at room temperature. Inset shows current in log scale vs. voltage.</i>	79
Figure 3.12	<i>(a) Dynamic response of the three types of sensor to 2000 ppm CO₂. (b) Time-dependent response/recovery characteristics and (c) the dynamic response/recovery characteristics of the NBA-ZnO nanohybrids sensor tested under various concentrations of CO₂ gas. (d) Response of the NBA-ZnO nanohybrid sensor as a function of CO₂ gas concentration.</i>	81
Figure 3.13	<i>(a) Single cycle response of the NBA-ZnO nanohybrid sensor to 5000 ppm CO₂ gas. (b) Repeatability test under different bending diameters at 5000 ppm CO₂ gas. (c) Effect of humidity on the CO₂ sensing properties of the NBA-ZnO nanohybrids. Inset shows change in sensor resistance under different humidity condition. (d) Selectivity study against other gases.</i>	83
Figure 3.14	<i>(a) CO₂ reaction mechanism with the primary amine of the nanohybrid. (b) Band formation between p-type NBA and n-type ZnO.</i>	84
Figure 4.1	<i>Synthesis schematic of the compound 1 (ODBA).</i>	100
Figure 4.2	<i>Schematic of the synthesis steps of organo-dibenzoic acidified ZnO nanostructures.</i>	101
Figure 4.3	<i>(a) Device schematic, (b) FESEM image of the interdigitated electrodes on the glass substrate, (c) FESEM image of the sensing layer deposited on interdigitated electrodes patterned glass substrate, (d) magnified FESEM of the sensing layer.</i>	102

Figure 4.4	<i>FESEM images of ODBA-ZnO hybrid material at (a) lower magnification, (b) higher magnification. Inset of Figure 6.4(a) shows higher magnification of the ODBA-ZnO hierarchal structures.</i>	102
Figure 4.5	<i>FESEM image of ZnO NPs sample.</i>	103
Figure 4.6	<i>EDX pattern of the ODBA-ZnO nanohybrid.</i>	103
Figure 4.7	<i>XRD pattern of ZnO nanoparticles (red), ODBA-ZnO hybrid (green), and amorphous ODBA (blue).</i>	104
Figure 4.8	<i>TGA analysis of the ODBA-ZnO hybrids.</i>	105
Figure 4.9	<i>BET surface area analysis of ODBA-ZnO hybrid material. Inset shows pore size distribution of the ODBA-ZnO hybrid material.</i>	105
Figure 4.10	<i>Growth mechanism of ODBA-ZnO hybrid architecture.</i>	106
Figure 4.11	<i>Effect of ODBA weight variation on the CO sensing performance by the ODBA-ZnO nanohybrid sensors.</i>	107
Figure 4.12	<i>(a) Temperature-dependent response for ZnO NPs, OZ10, OZ50, and OZ100 sensor, (b) dynamic response-recovery characteristics to CO concentration varying from 5 to 500 ppm, (c) response vs. concentration of CO, and (d) single transient response of OZ50 sensor.</i>	109
Figure 4.13	<i>(a) Dynamic response properties to step-wise increase in CO concentration, (b) repeatability study to 100 ppm CO, (c) effect of humidity on the response, and (d) selectivity study against different gases of OZ50 sensor.</i>	110
Figure 5.1	<i>FESEM images of (a) ZnO microcubes, (a) MoO₃ micrograsses, (c) ZnO/MoO₃ composite before calcination, (d) ZnO/MoO₃ composite after calcination, respectively. Insets in (a) (c) and (d), represent magnified images of ZnO microcube and rose like composites, respectively.</i>	128
Figure 5.2	<i>XRD pattern of (a) MoO₃ micrograss, (b) ZnO microcubes, (c) ZnO/MoO₃(1:1), (d) ZnO/MoO₃(1:2), and (e) ZnO/MoO₃(2:1) composites.</i>	129
Figure 5.3	<i>XPS spectra of ZnO/MoO₃(1:1) composite (a) O 1s core level region, (b) Zn 2p core level region, and (c) Mo 3d core level region.</i>	130

Figure 5.4	<i>Nitrogen adsorption-desorption isotherm of (a) ZnO microcubes, (b) MoO₃ micrograss and (c) rose-like ZnO/MoO₃(1:1) composite.</i>	131
Figure 5.5	<i>Formation mechanism of rose-like ZnO/MoO₃ composite.</i>	132
Figure 5.6	<i>Response of 5 different devices for different temperatures at 100 ppm methanol.</i>	132
Figure 5.7	<i>Real-time dynamic response and recovery characteristics for sensors based on (a) α-MoO₃ micrograss, (b) ZnO microcubes, (c) ZnO/MoO₃(1:1), (d) ZnO/MoO₃(1:2), and (e) ZnO/MoO₃(2:1) composites, respectively, towards varied methanol concentrations (5-500 ppm) at their optimum operating temperature. (f) Response of 5 different type sensors as a function of methanol vapor concentration at their optimum operating temperature. Inset of Figure 5.7(f) shows response (%) vs. concentration at low concentration range of 5-50 ppm methanol.</i>	134
Figure 5.8	<i>(a) Single transient response, (b) selectivity against other interference, (c) repeatability, (d) long-term stability, of the ZnO/MoO₃(1:1) composite sensor at 500 ppm methanol at the optimized operating temperature 200 °C.</i>	135
Figure 5.9	<i>(a) Schematic diagram of the proposed reaction mechanism of the as-prepared composite in vacuum, air and methanol, respectively. (b) schematic illustration of the sensing mechanism of ZnO/MoO₃ heterostructure composite.</i>	137
Figure 6.1	<i>Schematic of growth plan for all the samples (M₁-M₈).</i>	144
Figure 6.2	<i>XRD pattern of M₁-M₈ samples. Inset shows comparison of diffraction peak intensity of M₈ and M₄ samples.</i>	146
Figure 6.3	<i>FESEM images of samples M₄ (a-b), M₃ (c-d), M₂ (e-f), and M₁ (g-h) which are grown at constant temperature for different reaction time.</i>	147
Figure 6.4	<i>FESEM images of samples M₈ (a-b), M₇ (c-d), M₆ (e-f), and M₅ (g-h) which are grown at constant time (48 h) with different frequency of pulsed temperature.</i>	148
Figure 6.5	<i>(a) STEM image of MoO₃ nanofibers on the TEM grid, (b) TEM image of MoO₃ nanofibers, showing width in 200-300 nm range (c) and (d)</i>	150

	<i>are HRTEM and SAED pattern of the nanofibers, respectively.</i>	
Figure 6.6	<i>BET surface analysis of (a) MoO₃ nanobelts (M₄) and (b) MoO₃ nanofibers (M₈) samples.</i>	151
Figure 6.7	<i>Schematic of growth mechanism of (a) MoO₃ nanobelts and (b) nanofibers.</i>	152
Figure 6.8	<i>Reduction mechanism of different Mo valance state.</i>	153
Figure 6.9	<i>Response of M₁-M₈ devices in exposure to 100 ppm ethanol at different measurement temperatures.</i>	155
Figure 6.10	<i>Real-time dynamic response and recovery characteristics of (a) M₁-M₄, (c) M₅-M₈ devices and corresponding response vs. concentration plot of (b) M₁-M₄, (d) M₅-M₈ devices.</i>	156
Figure 6.11	<i>(a) and (c) shows repeatability study of M₈ and M₄ device, (b) and (d) shows single-cycle response and recovery characteristics of M₈ and M₄ device.</i>	157
Figure 6.12	<i>Selectivity study of M₈ and M₄ sample at their optimum operating temperature in exposure to 200 ppm of different VOCs.</i>	158
Figure 7.1	<i>(a) classical/indirect interface (b) direct interface.</i>	168
Figure 7.2	<i>(a) RC circuit (b) resistance readout circuit.</i>	170
Figure 7.3	<i>Temperature control circuit: (a) load independent VCCS and (b) differential amplifier</i>	172
Figure 7.4	<i>Simulation of the circuits under phase 1.</i>	174
Figure 7.5	<i>Simulation of the circuits under phase 2.</i>	175
Figure 7.6	<i>Resistance readout circuit: captured response in oscilloscope.</i>	175
Figure 7.7	<i>Practical realized resistance readout circuit in breadboard platform.</i>	181
Figure 7.8	<i>Monitoring the resistance of the MoO₃ nanofibers sensor with the resistance readout circuit at 50 ppm ethanol exposure at 275 °C.</i>	182
Figure 7.9	<i>Rearranging the components for PCB layout design.</i>	183
Figure 7.10	<i>3-D view of the PCB layout design.</i>	183

LIST OF TABLES

Table No.	Table Title	Page No.
Table 1.1	<i>Resistance change of metal oxide in presence of different ambient gases.</i>	12
Table 1.2	<i>Basic properties of wurtzite ZnO crystal.</i>	20
Table 1.3	<i>ZnO based reported gas/VOC sensors.</i>	21
Table 1.4	<i>Basic properties of α-MoO₃ crystal.</i>	23
Table 1.5	<i>MoO₃ based reported gas sensors.</i>	23
Table 3.1	<i>Performance comparison of room temperature CO₂ sensing.</i>	86
Table 4.1	<i>Comparative performance analysis of various CO sensors.</i>	111
Table 5.1	<i>Comparison of methanol sensing performance of MOX based sensors.</i>	136
Table 6.1	<i>Comparison of ethanol sensing properties of various MoO₃ nanostructures.</i>	159

ACRONYMS

MOX	<i>Metal Oxide</i>
VOCs	<i>Volatile Organic Compounds</i>
IDEs	<i>Interdigitated Electrodes</i>
TEA	<i>Triethylamine</i>
TCE	<i>Trichloroethylene</i>
HMTA	<i>Hexamethylenetetramine</i>
HF	<i>Hydrofluoric Acid</i>
DI	<i>De-Ionized</i>
LPG	<i>Liquid Petroleum Gas</i>
RT	<i>Room Temperature</i>
I-V	<i>Current-Voltage</i>
FESEM	<i>Field Emission Scanning Electron Microscopy</i>
XRD	<i>X-Ray Diffraction</i>
FWHM	<i>Full Width at Half Maximum</i>
CTEM	<i>Conventional Transmission Electron Microscopy</i>
HRTEM	<i>High Resolution Transmission Electron Microscopy</i>
SAED	<i>Selected Area Electron Diffraction</i>
EDX	<i>Energy Dispersive X-ray Spectroscopic</i>
XPS	<i>X-Ray Photoelectron Spectroscopy</i>
TGA	<i>Thermogravimetric Analysis</i>
BET	<i>Brunauer–Emmett–Teller</i>

LOD	<i>Limit of Detection</i>
DC	<i>Direct Current</i>
RF	<i>Radio Frequency</i>
eV	<i>Electron Volt</i>
NRs	<i>Nanorods</i>
NPs	<i>Nanoparticles</i>
NBs	<i>Nanobelts</i>
NWs	<i>Nanowires</i>
DFT	<i>Density Functional Theory</i>
HOMO	<i>Highest Occupied Molecular Orbital</i>
LUMO	<i>Lowest Unoccupied Molecular Orbital</i>
Si	<i>Silicon</i>
SiO ₂	<i>Silicon Dioxide</i>
PDMS	<i>Polydimethylsiloxane</i>
ZnO	<i>Zinc Oxide</i>
MoO ₃	<i>Molybdenum Oxide</i>
MCU	<i>Microcontroller Unit</i>
ADC	<i>Analog to Digital Converter</i>
VCCS	<i>Voltage Controlled Current Source</i>
FET	<i>Field Effect Transistor</i>
PWM	<i>Pulse Width Modulation</i>
LCD	<i>Liquid Crystal Display</i>
PCB	<i>Printed Circuit Board</i>

NOMENCLATURE

ϵ	<i>Dielectric Constant</i>
E_a	<i>Activation Energy</i>
m_o	<i>Electron Mass</i>
λ	<i>Wavelength</i>
$h\nu$	<i>Photon Energy</i>
a,b,c	<i>Lattice Constant</i>
Φ_B	<i>Potential Barrier</i>
E_{vac}	<i>Vacuum level Energy</i>
E_c	<i>Conduction Band Energy</i>
E_v	<i>Valance Band Energy</i>
E_g	<i>Energy Band gap</i>
E_F	<i>Fermi Level Energy</i>
R_a	<i>Resistance in Air</i>
R_g	<i>Resistance in Test Gas</i>
R	<i>Response/Sensitivity</i>
S	<i>Selectivity</i>
τ_{Res}	<i>Response Time</i>
τ_{Rec}	<i>Recovery Time</i>
T	<i>Operating Temperature</i>
M	<i>Material</i>
S/D	<i>Synthesis/Deposition Method</i>

ABSTRACT

Nanostructured Metal Oxides for Highly-Selective VOC and Gas Sensing

by

Biswajit Mandal

Hybrid Nanodevice Research Group,
Department of Electrical Engineering,
Indian Institute of Technology Indore

Supervisor: Dr. Shaibal Mukherjee

Gas and volatile organic compounds (VOCs) sensors are essential part of many intelligent systems for safety purpose. Their varied applications are prevalent in automotive industry (e.g., detection of vehicle emission gases), indoor air quality (e.g., detection of CO) monitoring, greenhouse gas (e.g., CO₂ and methane) monitoring, medical application (e.g., detection of volatile organic compounds from exhaled human breath), and coal mine application (e.g., methane detection). Depending upon the detection mechanism, there are different types of gas and VOC sensors available in the market such as resistive, capacitive, calorimetric, colorimetric, and optical based sensors. However, among these semiconducting metal oxide (MOX) based conductometric/resistive type sensors are one of the most promising candidate due to their low-cost manufacturing, easy fabrication methodologies, user-friendly nature in terms of deployability, and capability of integration of detection nodes for multiple gases/VOCs on a single device/cheap. Primary drawbacks of MOX-based sensors are their lack of selectivity towards a particular test gas/VOC and require high temperature for their

sensing operation. Sensors with high sensitivity to multiple gases/VOCs or low selectivity to particular gas/VOC are not suitable for practical application, due to the fact that they can produce false alarm or can disrupt the function of the safety system. Thereby, it is necessary to have a gas/VOC sensor with high selectivity as well as high sensitivity. In the past few decades, research work has been carried out worldwide to improve the selectivity and sensitivity of such sensors working at low or room temperature. In principle, the improvement is carried out by four methods: (1) architecture tailoring of MOX nanostructures, (2) surface modification by noble metals such as Pd, Pt, and Au etc., (3) usage of MOX composites, and (4) organic-inorganic hybrids. However, the highest level of selectivity achieved so far by these methods are still inadequate for the realization of practical gas/VOC sensors. Thus, research work has been pursued in search for superior material, which can exhibit ideal gas/VOC sensing characteristics with high values of sensitivity as well as selectivity. Among many MOXs, ZnO is widely studied as a sensing material, due to its wide energy band gap ($E_g \sim 3.37$ eV), intrinsic *n*-type conductivity, wide range of conductance variability, high thermal and chemical stability, and large surface area. In addition, ZnO's precursor can easily be combined with other MOX precursors or organic component, i.e., making ZnO based hybrids is an easy task. Therefore, ZnO is an ideal candidate for producing new kind of hybrid materials. Also, recently, MoO₃ has attracted the attention as a gas/VOC sensing material due to its wide band gap ($E_g \sim 2.4-3.8$ eV), *n*-type conductivity, good thermal and chemical stability. The presence of structural anisotropy and variable oxidation states, by which it can form various nanostructures such as nanobelts, nanorods, nanoflakes and nanoflowers etc., which are useful for gas/VOC sensing application due to their high surface area and morphology dependent unique sensing properties. However, the use of α -MoO₃ as a gas/VOC sensing material is not well explored. Exploration of α -MoO₃ is necessary to yield new morphology dependent unique gas/VOC sensing properties.

In this thesis research work, aforementioned two *n*-type wide bandgap based MOX material, i.e., ZnO and MoO₃ has been used in its bare, composite, or hybrid system to increase the selectivity and sensitivity towards CO, CO₂ gas and alcohol.

A π -conjugated amine and ZnO based organic-inorganic hybrid material was synthesized for the detection of CO₂ gas. Naphthalene based π -conjugated amine (NBA) was synthesized *via* conventional chemical synthesis method. Next, NBA-ZnO nanohybrid was synthesized *via in-situ* hydrothermal process on an interdigitated electrodes (IDEs) coated PDMS substrate. Material characterization techniques assured the growth of NBA-ZnO nanohybrids. A comprehensive room temperature CO₂ sensing study revealed that nanohybrid sensor had a good sensitivity of ~ 9% to 500 ppm CO₂ and almost negligible response to other gases viz. CO, NH₃, and H₂S, implying excellent selectivity (~ 91%) to CO₂ by the nanohybrid sensor. Good mechanical stability under bending conditions, excellent repeatability, and low humidity effect on CO₂ sensing properties of the nanohybrid sensor suggest that the nanohybrid sensor has great potential for developing room temperature wearable CO₂ sensor.

An organo-di-benzoic acidified ZnO hybrid material was developed for the detection of CO gas. Initially, an organo-di-benzoic acid (ODBA) was synthesized through conventional chemical synthesis method, later it was used in a single-pot hydrothermal method for the synthesis of ODBA-ZnO nanohybrids. Material characterization results revealed that as synthesized ODBA-ZnO nanohybrids were highly porous and comprised of net-like hierarchical structures. Optimum operating temperature of the nanohybrid sensor was 125 °C, which was supported by thermogravimetric analysis data. At 125 °C nanohybrid sensor exhibits highest response of 35% to 100 ppm CO with selectivity around 88%. Unprecedented selectivity to CO, low humidity effect, and low operating temperature of the ODBA-ZnO nanohybrid sensor suggest that ODBA-ZnO nanohybrids is a good candidate for developing low cost CO sensors.

A rose-like composite consisting of ZnO microcubes and MoO₃ micrograss-like structures was hydrothermally synthesized for methanol detection. Experimental characterization results revealed that pistil-like ZnO microcube was surrounded by petal-like MoO₃ micrograss in the composite. The surface area dramatically increased in the composite as compared to bare ZnO microcubes and MoO₃ micrograss material. VOCs sensing results revealed that composite sensor had excellent selectivity to methanol as compared ZnO microcubes-based and MoO₃ micrograss-based sensor. Nearly 60% selectivity was achieved by the composite sensor to 500 ppm methanol at 200 °C. Thirty days stability study of the composite sensor exhibited nearly stable response (56% to 500 ppm methanol) throughout the entire period. Presence of *n-n* heterojunction, increased surface area, and unique rose-like structure were possible reasons for getting enhance methanol selectivity and sensitivity by rose-like ZnO/MoO₃ composite sensor.

A novel temperature modulation technique was adopted to alter architecture of MoO₃ nanostructures from nanobelts to ultra-long nanofibers. Two sets of experiments were carried out to synthesize MoO₃ nanostructures. In 1st set, hydrothermal reactions were carried out at 120 °C for different hours to optimize the growth time for the growth of uniform nanostructures. In 2nd set, hydrothermal reactions were carried out at different frequency dependent pulsed temperature at 120 °C for the optimized time (48 h). Experimental characterization results revealed that MoO₃ nanofibers grown by pulsed temperature method at low frequency (1/24 h⁻¹) for 48 hours has higher surface defects and higher surface area as compared to MoO₃ nanobelts grown by constant temperature method for 48 hours. Detailed VOCs sensing study of the fabricated sensors revealed that MoO₃ nanofibers-based sensor has highest sensitivity of 53 (R_a/R_g) to 200 ppm ethanol at an optimum temperature of 275 °C. MoO₃ nanofibers-based sensor also exhibited good selectivity (~ 67%) to ethanol with an excellent repeatability.

Finally, with the aim of developing lab-based low-cost portable gas/VOC sensors, an interface circuit, including a low cost resistance

readout circuit for monitoring sensor resistance and a temperature control circuit for controlling the temperature of the microheater was simulated through Proteus 8 software. Next, the resistance read out circuit was practically realized and the response of the MoO₃ nanofibers sensor was monitored for 50 ppm ethanol with good accuracy. At last the printed circuit board (PCB) layout design of the resistance read out circuit and temperature control circuit was realized towards one step forward for achieving the aim of developing lab-based portable gas/VOC sensors.

Chapter 1

Introduction-Gas/VOC Sensor

1.1. Introduction

The primary goal of modern technology is to provide a simpler and safer life in every possible aspect. Sensor technology is the seeds in all aspects of life, including safety, security, surveillance, and monitoring. The modern and busy life of human society forces us to work in an unfriendly environment containing different types of combustible, flammable, and toxic gases, and volatile organic compounds (VOCs). These gases and VOCs are hazardous to humans or any other living beings. The human nose has very little ability to distinguish these gases, or, by inhaling the first time, can have an adverse effect on health. Gas/VOC sensor technology is the only solution to the aforementioned problem. A gas/VOC sensor is a tool for the detection of a gas or VOC in an environment, in particular gases/VOCs that are dangerous for humans or animals. A gas/VOC sensor is an alternative to expensive and bulky gas/VOC analyzers such as gas chromatography, optical spectroscopy, or mass spectroscopy, which detects gases/VOCs by direct examination of the target gas/VOC molecular mass or vibratory spectrum. Nowadays, gas/VOC sensors are used not only in environment safety applications but also in the fuel industry, automobile industry, chemical industry, food industry, and many other domestic applications. Recent advancement in technology has imposed more stringent requirements on the performance of gas/VOC sensors such as low cost, wearable sensor device, portable, room temperature operation, etc. Furthermore, the application in environmental protection includes highly sensitive and selective gas/VOC sensors. All of this has led to tremendous work to develop high performance gas/VOC sensors. This thesis research work presents the development of gas/VOC sensors with

improved performance, especially selectivity to detect CO, CO₂, and alcohols.

1.2. History of Gas/VOC Sensor Development

Many of the first attempts were made in coal mines to identify flammable conditions. Coal mines are the source of both flammable and poisonous gases, and low oxygen levels. To avoid the fatalities and injuries of the worker, initially, people have used an open flame lamp as a combustible gas detection system. A combustion-gas rich atmosphere would lead to a lighter fire, while a low oxygen atmosphere would lead to a slow-burning or disappearance of the flames. However, this detection method was not safe in the presence of excessive combustible gas, which can result in a heavy explosion. The use of small caged birds to identify hazardous conditions was another safe detection technique. The idea was to demonstrate the impact of the toxic atmosphere on those birds before they could hurt humans. This method was problematic because these birds could not detect all the harmful gases present in the atmosphere.

In the 1920s, significant advancement was taken place in the field of gas sensor. In 1927, Dr. Oliver Johnson introduces a method for the detection of flammable gases using a catalyst of platinum, which is now considered as a first commercial gas sensor [1].

In the 1960s, a massive demand for better gas/VOC sensors came into play in Japan due to the liquid petroleum (LP) gas bottle explosion accident. In 1962, Seiyama *et al.* [2] reported on a new type of gas/VOC sensor based on semiconducting metal oxide (zinc oxide), which works on semiconductor catalysis mechanism, i.e., the resistance of the zinc oxide changes upon adsorption of test gas/VOC. This new finding led the research and development of metal oxide semiconductor gas/VOC sensors by various groups. After that, Taguchi invented a gas/VOC sensor by using a novel metal-doped tin oxide and commercialized it in 1969. These inventions led to reduce the gas/VOC leak related accidents and triggered the investigation on the gas/VOC sensor as safety devices.

After that, oxygen sensor is introduced by Robert Bosch GmbH under the supervision of Dr. Günter Bauman, which was based on the zirconia ceramic and platinum electrode in thimble shape. Later it was entered in the market in the planner form with fast response characteristics.

Next, Matsusita Electric Industry Company introduced a humidity sensor made of metal oxides composites, which measured the change in humidity at elevated temperature. Later it was integrated with an electronic oven for automated cooking.

After the 1980s, gas/VOC sensors formed a mature market focused on various types of flammable, toxic, and oxygen gas sensors and VOCs sensors. Since then, research and development has continued to replace old sensors with new and competitive ones.

1.3. Gas/VOC Sensor Types

The main principle of the gas/VOC sensor is that the receptor (interactions between gas species and the surface of the sensor material) and transducer (conversion of chemical energy to an electrical signal) functions transform the chemical energy into an electrical signal. Depending upon the reception and transducer principle, electrical signal variability can be tracked in several ways such as resistance change, capacitance change, or optical properties changes. Based on the type of electrical signal, the gas / VOC sensors are classified as below.

Resistive Gas/VOC Sensor:

Generally, made of semiconductive material, mostly metal oxides such as ZnO, WO₃, SnO₂, TiO₂, MoO₃, etc., and can detect gases such as CO₂, CO, NO_x, H₂S, NH₃, and VOCs. The sensing mechanism involves changes in resistance of these materials to test gas/VOC exposure. Usually, the test gas/VOC responds to the oxygen adsorbed by metal oxides on the surface. Depending on the type of metal oxide (i.e., *n*- or *p*-type) and test gas/VOC type (i.e., reducing or oxidizing), resistance of the metal oxides can either decrease or increase. This type of sensor is fabricated by placing the sensing material on an insulating substrate and

on or between two metal (such as Au, Pt) electrodes for electrical resistance monitoring.

Capacitive Gas/VOC Sensor:

A capacitive gas/VOC sensor changes its dielectric properties (i.e., dielectric constant ϵ) of the sensing material, which indirectly changes the capacitance of the sensor in response to the test gas/VOC. Capacitive humidity sensors are generally made of hydrophilic inorganic oxides such as Ta_2O_5 , Al_2O_3 , and SiO_2 , which can measure humidity over a range of temperatures and pressure with high accuracy, low hysteresis, and excellent stability.

Potentiometric Gas/VOC Sensor:

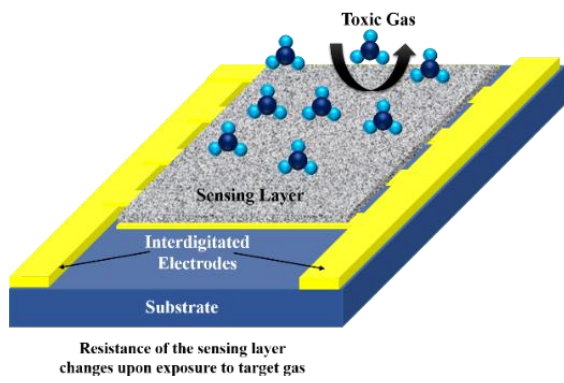
Potentiometric gas/VOC sensors are an electrochemical cell consisting of a reference electrode, a working electrode, and a solid electrolyte between them. Working electrode potential varies according to test gas/VOC concentration, and the potential difference between the reference electrode and working electrode is measured as a response signal. Solid electrolytes have high ionic conductivity while remaining as insulator electronically. The most developed solid electrolyte is stabilized zirconia, and due to its high oxygen ion conductivity, it is used as an excellent oxygen gas sensor.

Calorimetric Gas/VOC Sensor:

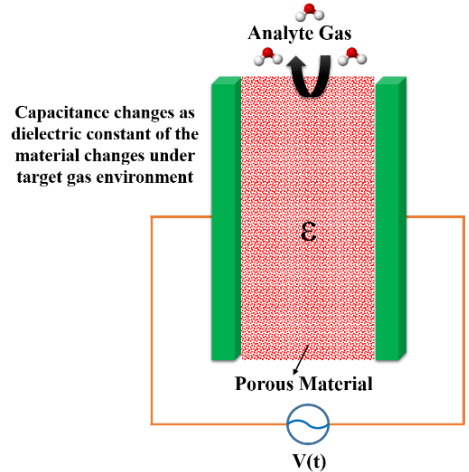
Calorimetric gas/VOC sensors are generally used to detect flammable gas/VOC like Methane, LPG, Hydrogen, and carbon monoxide. The detection mechanism relies on the calorimetric principle, i.e., the temperature of the catalytic element or sensing element rises, resulting from an oxidation process with the flammable gas/VOC, operating at a certain temperature.

Colorimetric Gas/VOC Sensor:

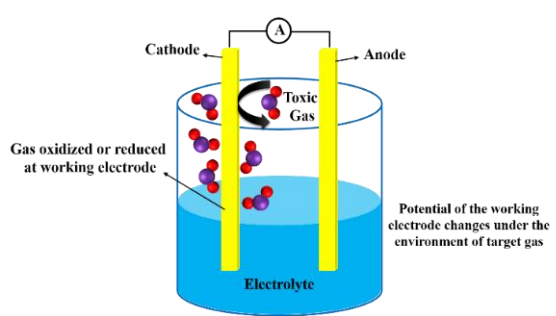
The colorimetric gas/VOC sensor's detection principle relies on the color change of the sensing reagent/element upon exposure to test gas/



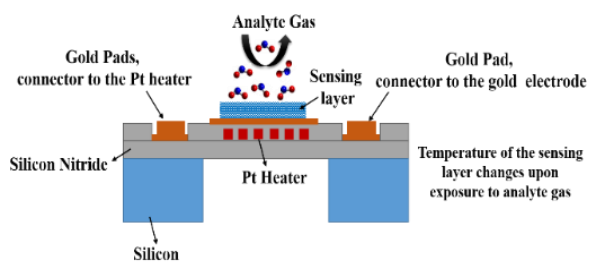
Resistive Gas Sensor



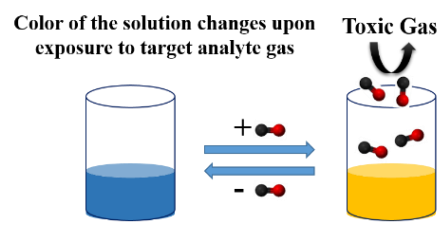
Capacitive Gas Sensor



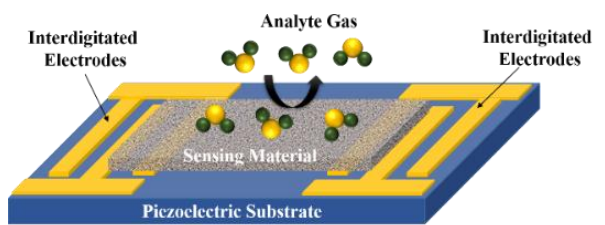
Potentiometric Gas Sensor



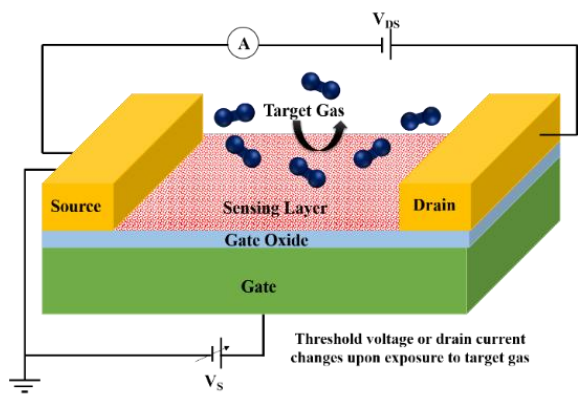
Calorimetric Gas Sensor



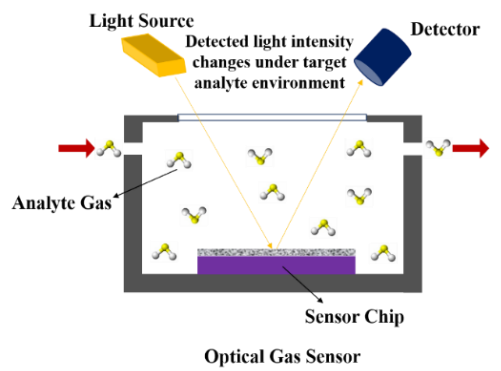
Colorimetric Gas sensor



SAW-Based Gas Sensor



FET-Based Gas Sensor



Optical Gas Sensor

Figure 1.1. Various types of gas/VOC sensors based on the principles of detection.

VOC to be detected. Recently, colorimetric sensor tube is used to detect different gas/VOC. The air or gas/VOC stream is drawn through a reagent-containing tube that changes its color after gas/VOC and reagent interaction. The concentration of gas/VOC is then measured by reading the length of the color stain in the reagent. The advantage of a colorimetric gas detection method is its simplicity of use, low cost, rapid response, and very low maintenance cost.

Surface-Acoustic-Wave (SAW) Gas/VOC Sensor:

Surface acoustic wave gas/VOC sensor consist of a sensing membrane and two sets of interdigitated piezoelectric transducer at both sides of the membrane. On the input transducer, a high-frequency signal is used, which spreads through the sensor membrane to the output transducer. The phase velocity of the propagated SAW changes when the test gas/VOC is entered in the sensing membrane, and the concentration of the test gas/VOC can be estimated by measuring the phase difference between the output and input signal. For a stable SAW propagation over a long period of time, a suitable material is required for the sensing membrane, which must have good adhesion to the substrate. Generally, thin film grown by sputtering of metal oxides or thermal evaporation of metals and solid electrolytes is used as a sensing membrane.

Field-Effect Transistor (FET) Gas/VOC Sensor:

Generally, a metal-oxide-semiconductor field-effect transistor (MOSFET) device structure is used as a gas/VOC sensor. Channel is coated with a sensing material, when test gas/VOC interacts with the channel, the threshold voltage or drain to source current of the MOSFET changes.

Optical Gas/VOC Sensor:

The optical gas/OC sensor is an optical fiber-based waveguide sensor, where, cladding of the optical fiber is replaced by a sensing material. In the presence of a test gas/VOC, optical properties of the cladding changes, which alters the optical properties of the light passing through the core. By measuring the change in optical parameters like phase,

polarity, wavelength etc., one can measure the particular gas/VOC and their concentration.

1.4. Gas/VOC Sensing Terminology

The parameters for the gas/VOC sensor must be established before entering the details of the semiconductor gas/VOC sensors. The fundamental parameters behind all gas/VOC sensors are as follows:

Response/Sensitivity (R):

The response/sensitivity of a sensor is defined as the ratio of change in physical/chemical or electrical properties to baseline physical/chemical or electrical properties, when the sensor is exposed from an open-air to a test gas/VOC under fixed operating conditions.

$$\text{Response}_{X(f)} = \left| \frac{X_{\text{baseline}} - X_{\text{gas/VOC}}}{X_{\text{baseline}}} \right| \times 100 \text{ or } \frac{X_{\text{gas/VOC}}}{X_{\text{baseline}}} \text{ or } \frac{X_{\text{baseline}}}{X_{\text{gas/VOC}}} \quad (1.1)$$

Where, X_{baseline} and $X_{\text{gas/VOC}}$ is the measurable physical/chemical or electrical parameter of the sensor in open air and under test gas/VOC environment, respectively, and f is the fixed operating conditions.

Selectivity (S):

Selectivity is the ability of a sensor to distinguish one particular gas/VOC from a mixture of gases/VOCs. By comparing the measured parameters for each test gas/VOC, selectivity can be determined. The selectivity of a sensor to gas/VOC 'a' with gas/VOC 'b' can be written as below.

$$\text{Selectivity}_{Y(f) \text{ gas/VOC(a)}} = \left| \frac{Y_{\text{gas/VOC(a)}} - Y_{\text{gas/VOC(b)}}}{Y_{\text{gas/VOC(a)}}} \right| \times 100 \quad (1.2)$$

Where, $Y_{\text{gas/VOC(a)}}$ and $Y_{\text{gas/VOC(b)}}$ is the measurable parameters of 'a' and 'b', respectively. And f is the fixed operating conditions under which the Y parameter for both the gas/VOC is measured.

Reversibility:

It is the sensor's capability to return its original state after withdrawing the test gas/VOC from its surroundings.

Response Time (τ_{Res}):

When the sensor is subjected to a test gas/VOC, the transition time to reach from 0% to 90% of the saturated response is defined as the response time.

Recovery Time (τ_{Rec}):

After withdrawing the test gas/VOC from the sensor surroundings, the transition time to reach from saturated response to 10% of the saturated response is defined as the recovery time.

Operating Temperature (T):

The temperature, at which point, the response/sensitivity of the sensor is maximum, is known as the optimum operating temperature of the sensor.

Repeatability:

It is the capability of a sensor to produce a constant response/sensitivity every time, when, it is cycled many times through test gas/VOC exposure and test gas/VOC withdrawing process.

Long-term Stability:

It is the sensor's ability to maintain a constant response or other sensing characteristics throughout a long period of time.

1.5. Semiconducting Metal Oxide (MOX) Gas/VOC Sensors

Generally, MOX based gas/VOC sensors are conductometric or resistive type sensors, i.e., the detection principle relies on changes in electrical resistance as the test gas/VOC molecules are adsorbed. For the first time in 1962, Seiyama *et al.* [2] observed the improvement of ZnO's conductivity with reactive gases in the air. Several kinds of metal oxides, mainly, SnO₂, ZnO, WO₃, In₂O₃, CuO, TiO₂, NiO, MoO₃, Fe₂O₃, and MnO₂, have since been used for the detection of gases and VOCs and, as mentioned in section 1.3, there are various techniques for their detection. Nonetheless, MOX based resistive type gas/VOC sensors is one of the most promising method for developing an integrated gas/VOC detection system. Due to their high sensitivity to test gas/VOC,

high stability in adverse conditions, low cost and low power consumption, and compatibility with silicon technology [3]–[5].

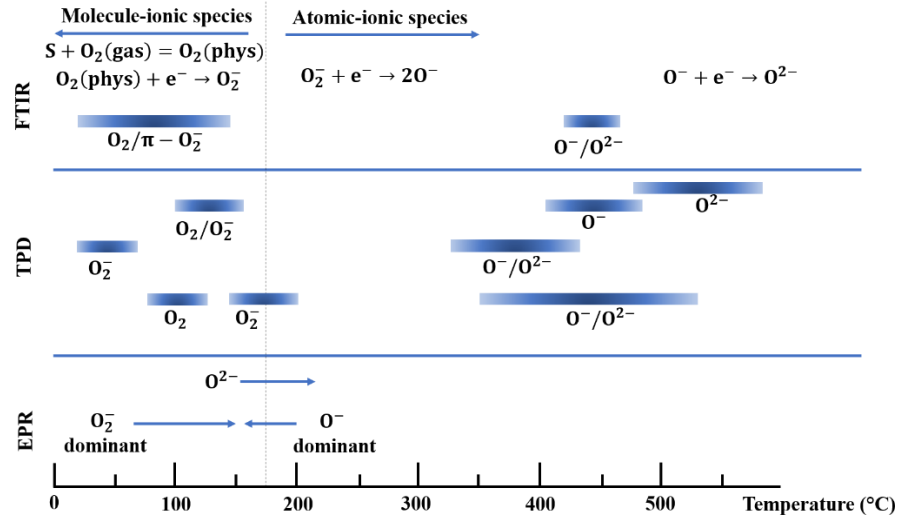
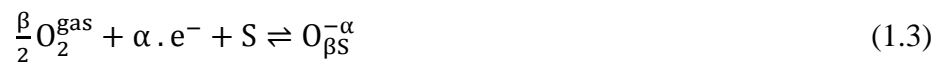


Figure 1.2. Adsorbed oxygen species at SnO_2 surface at different temperatures through Fourier transform infrared analysis (FTIR), temperature programmed desorption (TDP), and electron paramagnetic resonance (EPR) technique [6].

1.5.1. General Sensing Mechanism

On most of the MOX surfaces, oxygen vacancies are active electrically and chemically; on the other hand, the most active component in the air is oxygen, and it is occupied approximately 20.9% by volume. So naturally, oxygen molecules can easily bind to these vacancy sites and trap electrons from the MOX surface, when the MOX surface is exposed to air. Figure 1.2 displays the experimental findings of SnO_2 surface-adsorbed oxygen species from room temperature to above 500 °C. It is found that below 150 °C the interaction of atmospheric oxygen with the SnO_2 surface leads to major ionosorption in molecular form (O_2^- , O_2^{2-}) and above this temperature, major ionosorption take place in the atomic form (O^- , O^{2-}). In general, for n -type MOX, these adsorbed oxygen species forms surface states that trap electrons and consequently create a charge depletion layer near the surface. Assuming the ionosorption dominated by one species, the oxygen chemisorption can be written as:



where, O_2^{gas} is the atmospheric oxygen molecule, e^- is an electron that can overcome the potential barrier of the depletion region, $O_{\beta S}^{-\alpha}$ is a chemisorbed oxygen species, S is an unoccupied site for oxygen, generally, surface oxygen vacancies and other surface defects, α indicates whether chemisorbed oxygen species is single ionized ($\alpha = 1$) or double ionized ($\alpha = 2$) and β indicates whether chemisorbed oxygen species in the atomic form ($\beta = 1$) or in molecular form ($\beta = 2$). The adsorption and desorption reaction kinetics of oxygen species can be deduced from Equation 1.3 using the mass action law as follows:

$$k_{ads} \cdot [S] \cdot n_S^\alpha \cdot p_{O_2}^{\beta/2} = k_{des} \cdot [O_{\beta S}^{-\alpha}] \quad (1.4)$$

where k_{ads} and k_{des} are the adsorption and desorption reaction constants, respectively, and $n_S = [e^-]$.

If $[S_t]$ is the total concentration of the surface sites for oxygen adsorption, we can write as follows:

$$[S] + [O_{\beta S}^{-\alpha}] = [S_t] \quad (1.5)$$

by defining a surface coverage factor

$$\theta = \frac{[O_{\beta S}^{-\alpha}]}{[S_t]} \quad (1.6)$$

Equation 1.4 can be rewritten as

$$(1 - \theta) \cdot k_{ads} \cdot n_S^\alpha \cdot p_{O_2}^{\beta/2} = k_{des} \cdot \theta \quad (1.7)$$

Equation 1.7 describes the relation between surface coverage ionosorbed oxygen and surface-accessible electron concentration.

The above discussion clarifies how oxygen species are adsorbed to the MOX surface, resulting in an electron depleted layer close to the surface of an n -type MOX. Figure 1.3 further explains how the thickness of this depletion layer varies and affects the resistance of the MOXs under different ambient conditions, taking n -type MOX as an example.

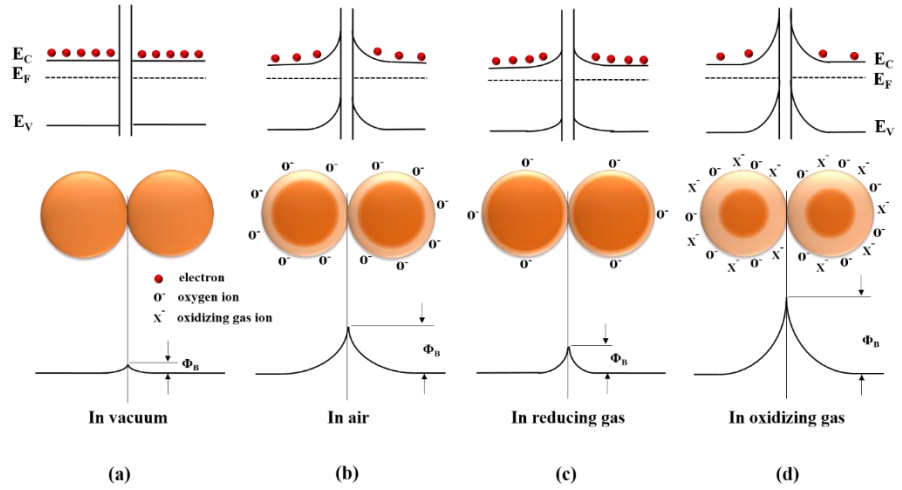
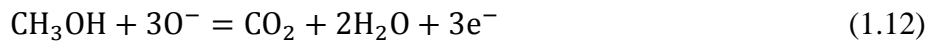
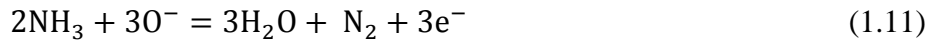


Figure 1.3. Schematic of the energy band diagram, the relationship between the adsorbed oxygen species and the depletion layer, and the potential barrier for charge carriers under (a) vacuum, (b) open air, (c) reducing gas, and (d) oxidizing gas ambient atmosphere, taking n-type MOX as an example [7].

In vacuum, where no gas species are present in the ambient, there is no adsorbed oxygen on the MOX surface, this contributes to no charge depletion below the MOX surface. Here, the bands are almost flat close to the surface of the MOX particle. Nonetheless, a very small contact barrier or potential barrier that provides most of the device resistance is present between nearby particles due to the presence of surface defects (Figure 1.3(a)). Device resistance is minimum under the vacuum condition. In air, oxygen species binds to the MOX surface and traps the electrons from the bulk, creating a charge depletion layer below the surface. The width of the charge depletion region (L) depends on the Debye length and the strength of the oxygen chemisorption. Negatively charged oxygen species and positively charged bulk produce an electric field near the surface, which is responsible for the formation of band bending on MOX particles close to surface (Figure 1.3(b)). Band bending formation creates a potential barrier (Φ_B) for an electron trying to participate in the particle-to-particle conduction process. In other words, these build up charge depletion layers increases the overall resistance of the device. If the device is exposed to reducing gas/VOC such as H_2 , CO , NH_3 , H_2S , and CH_3OH etc., the adsorbed oxygen

species reacts with the reducing gas and releases captured electron to the bulk as shown in below equations.



This decreases the amount of oxygen adsorbed on the MOX surface and consequently reduces the width of the depletion layer and the height of the potential barrier (Figure 1.3(c)). Which reduces the total resistance of the device as compared to the device resistance in the air. If the device is exposed to oxidizing gas such as O₃, NO₂, and SO₂ etc., these oxidizing gases plays a similar role to that of oxygen in the air, i.e., they trap more and more electrons at the surface as shown in below equations.



Consequently, depletion layer width and potential barrier height increases, which in turn increases device resistance as compared to the device resistance in the air (Figure 1.3(d)). Device resistance is maximum under oxidizing gas ambient.

Table 1.1. Resistance change of metal oxide in presence of different ambient gases.

Semiconductor type	Reducing gas	Oxidizing gas
<i>n</i> -type	Resistance decreases	Resistance increases
<i>p</i> -type	Resistance increases	Resistance decreases

For *p*-type MOXs such as CuO and NiO, exactly opposite phenomena occur, i.e., in case of reducing gas ambient resistance increases and for

oxidizing gas ambient resistance decreases. Table 1.1 summarizes the resistance change of MOXs in presence of different type ambient gases.

1.5.2. Factors Affect Sensing Performance

Several factors are known to influence the properties of the MOX based gas/VOC sensors [8], [9]. Factors such as grain size, crystallographic plane, geometry, etc. that affect the gas/VOC sensing efficiency must be considered in order to further improve the performance of MOX based gas/VOC sensors.

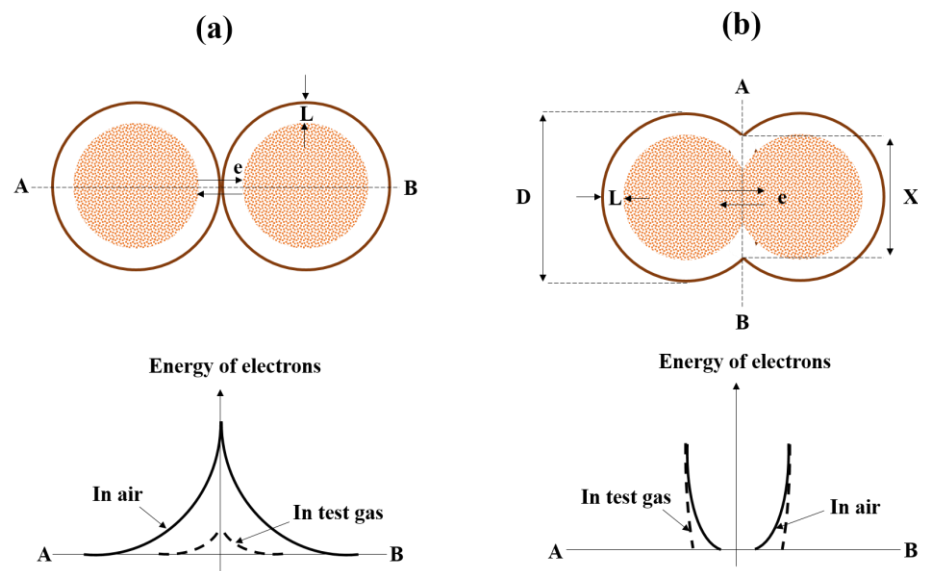


Figure 1.4. Schematic of the grain contact model and electronic band of (a) grain boundary contact and (b) neck contact.

1.5.2.1. Grain Size Effect

MOX particles are generally connected to their neighbors either by grain or neck contacts. In the first example, i.e., for grain contacts, conduction electrons at each grain border pass through a potential barrier (Figure 1.4(a)). Here, resistance depends on the potential barrier height, which depends directly on the ambient atmosphere [10]. Therefore, in this case, gas/VOC sensitivity is independent of the metal oxide particles' grain size. In the second example, i.e., for neck contacts, conduction electrons move through a conduction channel penetrating each neck (Figure 1.4(b)), necks aperture depends on the surface space charge [11]. Here, major resistance is contributed by the neck resistance. Assuming, the

sensor is comprised of a three dimensional array of uniform grains of diameter D and they are connected to their neighbors through a uniform neck diameter of X. If R_a and R_g are the neck resistance in air and in test gas/VOC, respectively, then in this case the sensitivity can be written as:

$$S = \frac{R_a}{R_g} = \left\{ (1-x)^2 + \frac{n_L}{n_0} (1 - (1-x)^2) \right\}^{-1} \quad (1.16)$$

where, $x = \frac{2L}{X}$, L is the depletion layer width, n_0 and n_L are the concentration of conduction electron at the core and space charge region, respectively.

The diameter of the neck X is proportional with grain size D, i.e., $X = kD$ with a proportionality factor $k = 0.8 \pm 0.1$. Figure 1.5 explains three possible situations in the case of neck control electron conduction.

First, for $D \gg 2L$: When D is very large than 2L, electron conduction affected by the grain contacts. Here, the electrical resistance and sensitivity of the chain is governed by grain boundary contacts.

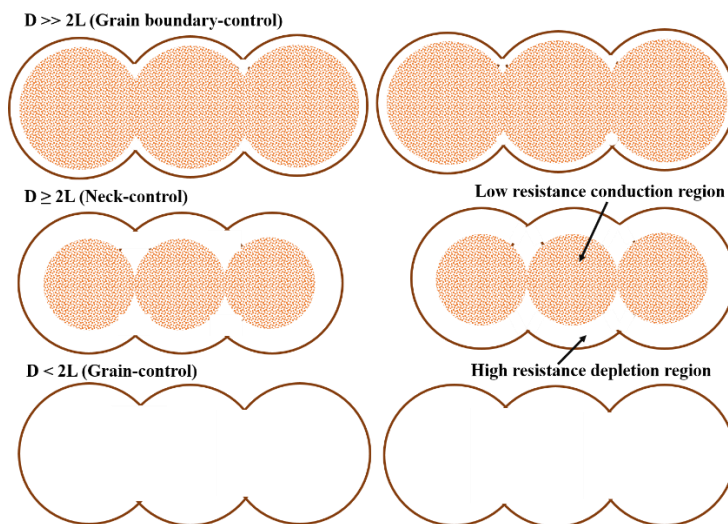


Figure 1.5. Schematic models for grain size effect.

Second, for $D \geq 2L$: When D is large and comparable to 2L, electron conduction affected by a neck. In this case, sensitivity increases with decreasing grain diameter.

Third, for $D < 2L$: When D is smaller than $2L$, the entire grain is depleted of charge carriers and electron conduction effected by the whole grain. Gas/VOC sensing process in this case has not yet been well understood.

1.5.2.2. Effect of Crystallographic Plane

The crystallographic plane has a significant impact on gas/VOC sensing when its type of grain is dominated by $D \gg 2L$ category. During the growth of MOX nanoparticle, depending on the growth direction, different crystallographic planes may appear. In most of the metal oxides, different crystallographic planes have different density of metal atoms. For instance, the distance between two adjacent Sn atoms in different planes is as $d_{(110)} < d_{(100)} < d_{(101)} < d_{(001)}$ for SnO₂ nanocrystals developed by spray pyrolysis method on Si substrate [12]. The different atomic distance means different oxygen chemisorption and dissociation energy requirements. Thus, the crystallographic plane can alter the sensing properties of the MOXs. Growth conditions can tune the surface facets of the particulate MOX, and usually smaller particles have higher facet indexing or higher gas/VOC sensing efficiency.

1.5.2.3. Geometrical Aspect

Another critical factor that can affect the gas/VOC sensing efficiency is the geometry of MOX particles. When the gas/VOC interacts with the outer sites of the particles, if the reaction rates is higher than the diffusion rate, the gas molecules are unable to reach the inner sites of the particles. As a consequence, gas/VOC is detected by only the outer sites of the particles and the inner sites remains unused. The geometry of the particles and the distance from the outer to the inner site must also be taken into account.

1.5.2.4. Effect of Noble Metals Additive

The introduction of small amounts of noble metals such as Pd, Pt, and Ag into metal oxide materials can not only improve the sensitivity and response time but also reduces the optimum operating temperature of the sensor [8]. Noble metal particles can promote the performance of the

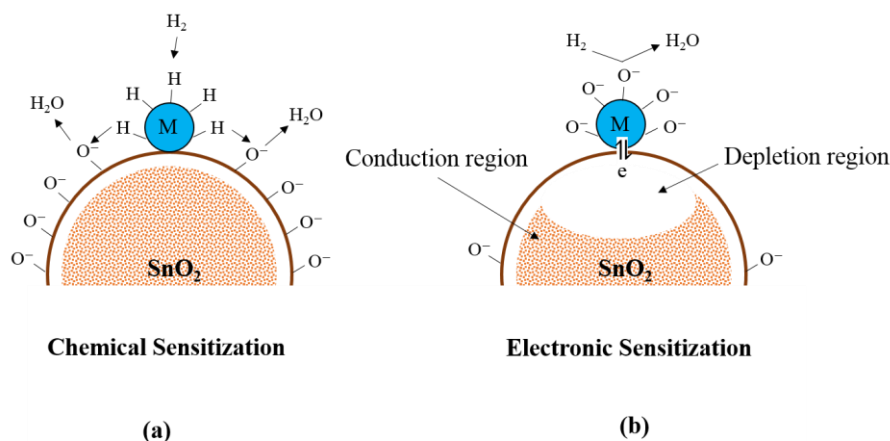


Figure 1.6. (a) Chemical and (b) electronic sensitization of noble metal added SnO₂ sensor.

MOXs by chemical sensitization or by electronic sensitization process. In case of chemical sensitization process, noble metal (e.g., Pt) activates the test gas/VOC and spill-over it on the metal oxide (e.g., SnO₂) surface for catalytic oxidation process (Figure 1.6(a)). The rate of chemical reaction is then increases between the adsorbed oxygen ion and the test gas/VOC, explaining the increased sensitivity to the test gas/VOC. In case of electronic sensitization process, noble metal (e.g., Pd and Ag) can easily form stable oxides (e.g., PdO and Ag₂O) in air, while they can be easily reduced to metal in exposure to any reducing gas (e.g., H₂). It is due to the fact that, generally, noble metal (Pd) have higher work function as compare to MOX (SnO₂), leading to migration of charge carriers from MOX to noble metal. Further, oxide formation of noble metal can trap more electron from the MOX and consequently create a charge depletion region inside the MOX (Figure 1.6(b)).

1.5.2.5. Others Factors

Additional factors, such as sensor configuration and porosity of the material, may affect the sensing performance of the sensors.

Material Porosity: Porosity of the material enables fast migration of gas/VOC molecules through or out of MOX. The porosity also increases the overall surface area of the material, which increases the sites for gas/VOC adsorption. High porosity material may therefore not only

have short response and recovery time, but also high sensitivity as well [13].

Sensor Configuration: Mainly the position of metal electrodes and its configuration may cause the sensor response to either decrease or increase. If the metal electrode is on the surface of the MOX film, the change in surface resistance is measured; however, the change in bulk resistance remains unmeasured. If the metal electrode is below the MOX film, the surface as well as the bulk resistance change are measured in this case. So the overall resistance change in the second case is greater or the response/sensitivity is greater. Generally, the configuration of the metal electrodes is patterned either in the form of two contact pad or in the form of interdigitated electrodes (IDEs). IDEs are usually preferred for gas/VOC sensing because they provide additional surface area for gas/VOC adsorption. Nevertheless, the thickness of the electrode, the distance between two electrodes, and the deposition method of the electrodes can have an effect on the sensing performance.

1.6. Material Selection

In developing a gas/VOC sensor, choice of appropriate sensing material is the utmost important factor. Though any material subject to certain changes in parameters on exposure to gas/VOC can be used as the sensing material, usually, MOXs, solid electrolytes, covalent semiconductors, polymers, and organic semiconductors are used as a sensing material. However, appropriate material must be chosen for the detection of a particular type of gas/VOC.

1.6.1. Ideal Characteristics of a Gas/VOC Sensing Material

An ideal gas/VOC sensing material should have the following characteristics [14]:

1. High sensitivity to test gas/VOC.
2. Low cross sensitivity to other gas/VOC.
3. Stable performance with change in ambient humidity.
4. Good long-term stability.

5. Low drift in baseline resistance other than gas/VOC composition and temperature effect.
6. High adsorption rate.
7. Short response and recovery time.
8. High reproducibility of the sensing material.
9. High Si-technology compatibility for easy integration in systems.

1.6.2. Why Metal Oxide? And Why ZnO or MoO₃?

The primary requirement of a general gas/VOC sensor is the reversible interaction of its sensing material with the test gas/VOC. For instance, if the sensing material shows a change in electrical resistance during test gas/VOC exposure, the changes must be reversed when the test gas/VOC is removed from the sensing material's surroundings. This material characteristic allow us to use the sensing material repetitively, thereby reduces the operational cost of the sensor. Use of single crystalline metals or semiconductors as gas/VOC sensor material is risky, as these metals or semiconductors can easily form an oxide layer during high temperature (>300°C) operation of the sensor, which can completely change the sensing operation or degrade the operation of the sensor. The simplest way to overcome the problem of oxide layer growth is to use an oxide material as a sensing material. As the probability of an oxide material getting further oxidized is negligible. This leads to the second requirement, that the sensing material should be highly stable even at higher temperatures for a long period of time. If the mechanism for gas/VOC sensing is based on resistivity or conductivity shifts, then changes in sensing material conductivity after target gas/VOC exposure can be expressed as follows [15].

$$\sigma = A \cdot e^{-E_a/kT} \cdot P_{O_2}^{1/N} \quad (1.17)$$

Where A is a constant, k is the Boltzmann constant, E_a is activation energy required for conduction, T is the temperature, P_{O_2} is the partial pressure of oxygen, and N is a constant, and depends on the nature of point defects that are caused by removal of a lattice oxygen. Above

equation explains that the shift in sensing material's conductivity depends on the material's activation energy. Equations 1.17 also indicate that the conductivity changes are higher if activation energy is lower, in other words, the material's sensitivity is higher. However, the activation energy of chemisorption is inversely proportional to the activation energy of desorption. So, low activation energy will reduce the response time but it will increase the recovery time of the sensing material. Thus, the sensing material should be chosen whose activation energy should be neither too low nor too high.

There are different types of semiconducting MOXs, i.e., pre-transition, transition, and post-transition metal oxides, which can satisfy the above mentioned criteria. However, in contrast to transition or post-transition metal oxides, pre-transition MOXs are very inert, as the oxidation and reduction of these pre-transition MOXs are not an easy phenomena. Also, MOXs with extremely high resistance are often not effective for the application of resistive type gas/VOC sensing due to conductivity measurement problems. Since 1960, ZnO, SnO₂, TiO₂, WO₃, MoO₃, In₂O₃, CuO, and NiO etc. are the most widely used MOXs in the gas sensing industry.

Among many MOXs, ZnO is widely studied as a gas/VOC sensing material, because of its wide band gap ($E_g \sim 3.37$ eV), intrinsic *n*-type conductivity, high thermal and chemical stability, large surface area, and a wide range of conductance variability [16]. Precursor of ZnO can easily integrate with other MOX precursors or organic component, in other words, making hybrid material with ZnO is an easy task. Therefore, ZnO is an ideal candidate for producing new kinds of hybrid materials. ZnO can have three types of crystal structures, namely Zinc blende, wurtzite, and rocksalt. Among these, wurtzite crystal structure is thermodynamically stable under ambient conditions. The wurtzite ZnO has a hexagonal closed-packed unit cell in which 44% is occupied by ions and leaves relatively large free volume. Figure 1.7 shows a wurtzite ZnO crystal structure.

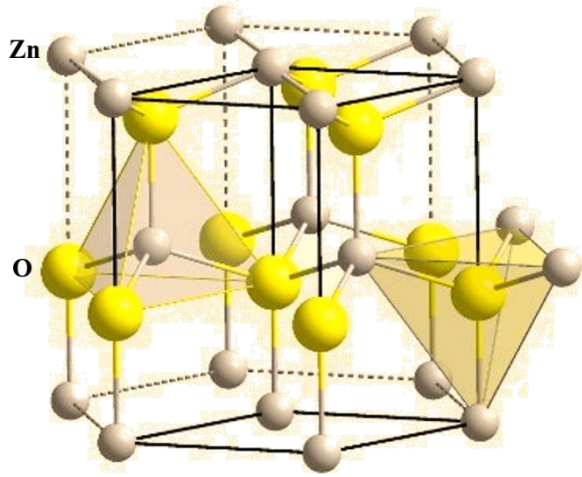


Figure 1.7. ZnO crystal structure (wurtzite) [17].

Table 1.2. Basic properties of wurtzite ZnO crystal [18].

Stable crystal structure	Wurtzite
Molecular weight	81.38 g/mol
Lattice parameters	$a = b = 3.25 \text{ \AA}$, $c = 5.21 \text{ \AA}$
Density	5.606 gm/cm^3
Melting point	$1975 \text{ }^\circ\text{C}$
Dielectric constant	8.66
Bandgap at room temperature	3.37 eV
Exciton binding energy	60 meV
Electron effective mass	$0.24 m_0$
Hole effective mass	$0.59 m_0$
Electron mobility	$100\text{-}200 \text{ cm}^2/\text{V-s}$
Hole mobility	$5\text{-}50 \text{ cm}^2/\text{V-s}$

Oxygen vacancies are major defects in ZnO crystals under the ambient conditions, which makes it naturally an *n*-type material. Table 1.2 shows some basic properties of wurtzite ZnO.

Due to non-toxicity, amenability to doping, high chemical and thermal stability, and low cost of ZnO, since its first discovery in 1962 as gas sensitive material, it has been widely used to detect gases and VOCs. Table 1.3 lists some literature reported resistive type gas/VOC sensors based on ZnO as a sensing material.

Table 1.3. ZnO based reported gas/VOC sensors.

M	S/D	Gas/ VOC	C (ppm)	T (°C)	R	Ref.
ZnO NPs	Hydro thermal	Ethanol	3000	370	20	[19]
ZnO NRs	Hydro thermal	Ethanol	1000	332	50	[20]
ZnO NRs	Hydro thermal	NO ₂ CO	1 50	350	1.8 1	[21]
ZnO NWs	CVD	NO ₂	100	250	6	[22]
ZnO NBs	Oxidation	TMA	5	400	41.0 4	[23]
Au/ZnO	Sol-gel	Ethanol	100	380	33.6	[24]
La/ZnO	Hydro thermal	CO ₂	5000	400	65%	[25]
Al-ZnO	Hydro thermal	CO	50	300	80%	[26]
Pd-ZnO	Hydro thermal	NH ₃	50	210	45.7	[27]
Co-ZnO	Electro chemical deposition	CO	50	350	16%	[28]
SnO ₂ -ZnO	Sol-gel	NO ₂	4	200	105	[29]
NiO-ZnO	Hydro thermal	Acetone	100	330	13	[30]
ZnO-CNT	Thermal oxidation	NH ₃	100	RT	330	[31]
Poly(3- hexylthiop hene)/ZnO	Sol-gel	NO ₂	4	RT	60%	[32]

M: Material, S/D: Synthesis/deposition method, C: Gas/VOC concentration, T: Operating temperature, R: Response/sensitivity

Initially, ZnO has been used in its bare form to detect ethanol [19], [20], NO₂ [21], [22], and TMA [23]. Later, it was found that either metal-doped or metal surface-functionalized ZnO can be used to enhance the sensitivity of ethanol [24], CO₂ [25], CO [26], [28], and NH₃ [27]. Recently, researchers are using ZnO and other MOXs based composites and hybrids for achieving high selectivity, high sensitivity, and low optimal temperature of operation [29]-[32].

MoO₃ is a wide band gap ($E_g \sim 2.4\text{-}3.8$ eV) *n*-type material having good thermal and chemical stability. Recently, MoO₃ has also been employed as a gas/VOC sensing material owing to its variable oxidation states and structural anisotropy, through which it can form various nanostructures, e.g. nanostars [33], nanobelts [34], [35], nanoribbons [36], nanorods [37]–[40], nanoplatelets [41], nanosheets [42], nanowires [43], [44], nanowhiskers [45], nanoflakes [46], nanotubes [47], [48], nanoflowers [49], nanospheres [50] and nanoslabs [51] etc. Distinctive morphologies are useful for gas/VOC sensing due to their high surface area and the shape and geometry dependent unique sensing properties. However, the use of MoO₃ as a gas/VOC sensing material is not well explored. To develop new morphological dependent specific gas/VOC sensing characteristics, MoO₃ exploration is important.

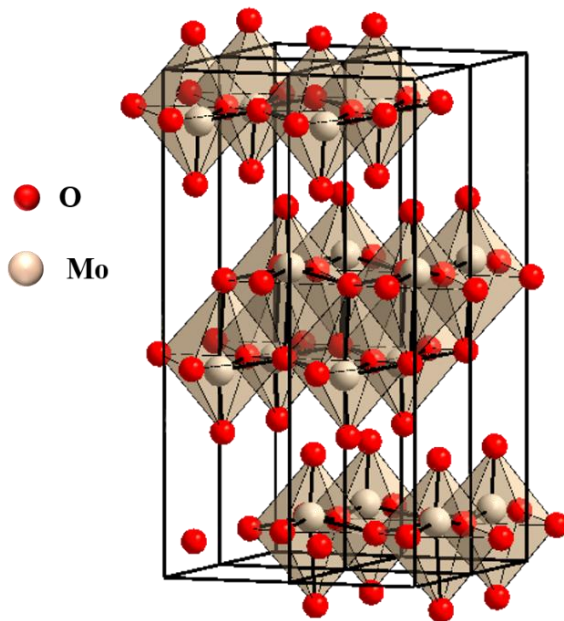


Figure 1.8. Orthorhombic α -MoO₃ crystal structure [52].

Like ZnO, MoO₃ has three different types of crystal structures: orthorhombic (α -MoO₃), hexagonal (h-MoO₃), and monoclinic (β -MoO₃). Among these, the thermodynamic stable phase is orthorhombic α -MoO₃, in ambient condition. Figure 1.8 shows the crystal structure of orthorhombic α -MoO₃. Orthorhombic α -MoO₃ is a highly anisotropic layered structure and it is formed by stacking of bilayer MoO₆ octahedra sheets with van der Waals forces, in which each molybdenum atom is coordinated by six oxygen atoms. It is also an *n*-type metal oxide in atmospheric conditions due to the excess oxygen vacancy in MoO₃. Table 1.4 shows some basic properties of α -MoO₃.

Table 1.4. Basic properties of α -MoO₃ crystal [53].

Stable crystal phase	Orthorhombic α -MoO ₃
Molecular weight	143.94 g/mol
Lattice parameters	a = 3.96 Å, b = 13.85 Å, c = 3.69 Å
Density	4.70 g/cm ³
Melting point	795 °C
Refractive index	2.30
Dielectric constant	5.7
Band gap	2.39-2.9 eV

To date, α -MoO₃ has been used for H₂S, ethanol, and TEA sensing. Table 1.5 displays several α -MoO₃ based gas and VOC sensors reported in the literature.

Table 1.5. MoO₃ based reported gas sensors.

M	S/D	Gas/ VOC	C (ppm)	T (°C)	R	Ref.
α -MoO ₃ NPs	Solvo thermal	Ethanol	800	300	58	[54]
α -MoO ₃ NBs	E-beam evaporation	H ₂ S	100	175	225	[55]

3D α -MoO ₃ nanoflower	Solvo thermal	TEA	100	250	416	[56]
Net-like α -MoO ₃	Hydro thermal	Ethanol	400	350	23	[57]
2D α -MoO ₃ nanoflake	Solvent-assisted grinding	H ₂	10000	200	50%	[58]
Fe-MoO ₃	Hydro thermal	H ₂ S	100	270	184	[59]
PANI/ α -MoO ₃	Hydro thermal	TEA	10	RT	5.8	[60]
CuO/ α -MoO ₃	Hydro thermal	H ₂ S	10	270	272	[61]
RGO/ α -MoO ₃	<i>In-situ</i> microwave	H ₂ S	40	110	59	[62]
M: Material, S/D: Synthesis/deposition method, C: Gas/VOC concentration, T: Operating temperature, R: Response/sensitivity						

1.7. Main Aim and Objectives

The main aim of this thesis research work is to develop ZnO and MoO₃ based tailored, composite, and hybrid materials towards the improvement of the selectivity and sensitivity to CO, CO₂, and alcohols.

To accomplish the aforementioned aim, the work of this thesis includes the following objectives:

- To develop a sensing set-up for testing gas/VOC sensing performance of the fabricated sensors. A set-up consist of sensing chamber, heater assembly, PID temperature controller, gas flow controller unit, VOC container, dilution chamber, test gas and carrier gas cylinders, humidity generator, and a multimeter interfaced with a computer.
- To prepare active/sensing layer of the sensor, active layer comprises of ZnO and MoO₃ based tailored, composite, and

hybrid materials, which are to be synthesized *via* hydrothermal method. Subsequently, device/sensor fabrication using the active layer.

- To investigate various morphological and structural properties of the grown material/active layer using different material characterization techniques such as FESEM, EDX, XPS, XRD, TEM, HRTEM, BET, TGA etc.
- To study the gas/VOC sensing characteristics of the sensors using the indigenously developed sensing set-up. Sensing study includes the repeatability, selectivity and long term stability study of the sensors. It also includes the effect of temperature, test gas/VOC concentration, and humidity on the sensing properties of the sensors.
- To realize a low-cost interface circuit for controlling the temperature of the microheater and measuring the real-time resistance of the sensors. The utilization of the developed circuits for practical application.

1.8. Organization of Thesis

The thesis consists of 8 chapters and they are organized as follow:

Chapter 1 describes the basics of gas/VOC sensors, including introduction, type of gas/VOC sensors, sensing parameters, MOX as gas/VOC sensing material, different techniques to improve the sensing properties like sensitivity and stability. It also describes the use ZnO and MoO₃ as a sensing material and some information on ZnO and MoO₃ based previously reported gas sensors.

Chapter 2 provides the description of different types of substrates and their cleaning procedure, basics of hydrothermal synthesis method and other physical vapor deposition methods, principle of operation of various material characterization instruments utilized in this thesis work, e.g., field-emission scanning electron microscope (FESEM),

transmission electron microscopy (TEM), X-ray diffraction (XRD), X-ray photoelectron spectroscopy (XPS), energy dispersive X-ray spectroscopic (EDX), thermogravimetric analysis (TGA), Brunauer–Emmett–Teller surface area analysis (BET) etc. This chapter also provides the detailed description of the gas and VOC sensing set-up used in this thesis work.

Chapter 3 discusses the synthesis of a new type of organic-inorganic hybrid material based on naphthalene based π -conjugated amine and ZnO. The details of *in-situ* fabrication of hybrid material on flexible substrate and room temperature CO₂ sensing properties of the fabricated sensor are described here.

Chapter 4 discusses the synthesis of an organo-di-benzoic acidified ZnO nanohybrids as a highly selective CO sensing material. From synthesis, device fabrication, and comparative CO sensing properties of the organo-di-benzoic acidified ZnO nanohybrids sensor are described in detail in this chapter.

Chapter 5 demonstrates the synthesis of rose-like composites using ZnO microcube and MoO₃ micrograss material and their highly selective methanol sensing characteristics.

Chapter 6 discusses the synthesis of MoO₃ nanofibers by a novel temperature modulation technique during the hydrothermal process as a superior ethanol sensing material.

Chapter 7 discusses the simulation and implementation of the resistance readout and temperature control circuits.

Chapter 8 concludes this thesis work and the framework for further study is suggested.

1.9. References

- [1] W. Weppner, “Solid-state electrochemical gas sensors,” *Sensors and Actuators*, vol. 12, no. 2, pp. 107–119, Aug. 1987.
- [2] T. Seiyama, A. Kato, K. Fujiishi, and M. Nagatani, “A New

- Detector for Gaseous Components Using Semiconductive Thin Films.,” *Anal. Chem.*, vol. 34, no. 11, pp. 1502–1503, Oct. 1962.
- [3] C. Soldano, E. Comini, C. Baratto, M. Ferroni, G. Faglia, and G. Sberveglieri, “Metal oxides mono-dimensional nanostructures for gas sensing and light emission,” *J. Am. Ceram. Soc.*, vol. 95, no. 3, pp. 831–850, Jan. 2012.
- [4] N. Van Quy, V. A. Minh, N. Van Luan, V. N. Hung, and N. Van Hieu, “Gas sensing properties at room temperature of a quartz crystal microbalance coated with ZnO nanorods,” *Sensors Actuators B Chem.*, vol. 153, no. 1, pp. 188–193, Mar. 2011.
- [5] M. J. S. Spencer, “Gas sensing applications of 1D-nanostructured zinc oxide: Insights from density functional theory calculations,” *Prog. Mater. Sci.*, vol. 57, no. 3, pp. 437–486, Apr. 2012.
- [6] N. Barsan and U. Weimar, “Conduction Model of Metal Oxide Gas Sensors,” *J. Electroceramics*, vol. 7, no. 3, pp. 143–167, 2001.
- [7] H. Ji, W. Zeng, and Y. Li, “Gas sensing mechanisms of metal oxide semiconductors: a focus review,” *Nanoscale*, vol. 11, no. 47, pp. 22664–22684, Dec. 2019.
- [8] N. Yamazoe, Y. Kurokawa, and T. Seiyama, “Effects of additives on semiconductor gas sensors,” *Sensors and Actuators*, vol. 4, pp. 283–289, Jan. 1983.
- [9] G. Heiland, “Homogeneous semiconducting gas sensors,” *Sensors and Actuators*, vol. 2, no. C, pp. 343–361, Jan. 1982.
- [10] H. Ihokura, “SnO₂-based inflammable gas sensors,” 1983.
- [11] H. Mitsudo, “Ceramics for gas and humidity sensors (part I)—gas sensor,” *Ceramics*, vol. 15, pp. 339–345, 1980.
- [12] V. Brinzari, G. Korotcenkov, V. Golovanov, J. Schwank, V. Lantto, and S. Saukko, “Morphological rank of nano-scale tin dioxide films deposited by spray pyrolysis from SnCl₄·5H₂O

- water solution,” *Thin Solid Films*, vol. 408, no. 1–2, pp. 51–58, Apr. 2002.
- [13] R. W. J. Scott, S. M. Yang, G. Chabanis, N. Coombs, D. E. Williams, and G. A. Ozin, “Tin Dioxide Opals and Inverted Opals: Near-Ideal Microstructures for Gas Sensors,” *Adv. Mater.*, vol. 13, no. 19, pp. 1468–1472, Sep. 2001.
- [14] G. Korotcenkov, “Metal oxides for solid-state gas sensors: What determines our choice?,” *Mater. Sci. Eng. B*, vol. 139, no. 1, pp. 1–23, Apr. 2007.
- [15] P. T. Moseley, “Solid state gas sensors,” *Meas. Sci. Technol.*, vol. 8, no. 3, pp. 223–237, Mar. 1997.
- [16] L. E. Greene, B. D. Yuhas, M. Law, D. Zitoun, and P. Yang, “Solution-Grown Zinc Oxide Nanowires,” *Inorg. Chem.*, vol. 45, no. 19, pp. 7535–7543, Sep. 2006.
- [17] M. A. Borysiewicz, “ZnO as a functional material, a review,” *Crystals*, vol. 9, no. 10, p. 505, Oct. 2019.
- [18] F. C. Van De Pol, “Thin film ZnO-properties and applications,” *Am. Ceram. Soc. Bull.*, vol. 0, no. 69, pp. 1959–1965, 1990, Accessed: Aug. 02, 2019.
- [19] H. Xu, X. Liu, D. Cui, M. Li, and M. Jiang, “A novel method for improving the performance of ZnO gas sensors,” *Sensors Actuators B Chem.*, vol. 114, no. 1, pp. 301–307, Mar. 2006.
- [20] X. Jiaqiang, C. Yuping, C. Daoyong, and S. Jianian, “Hydrothermal synthesis and gas sensing characters of ZnO nanorods,” *Sensors Actuators B Chem.*, vol. 113, no. 1, pp. 526–531, Jan. 2006.
- [21] P.-S. Cho, K.-W. Kim, and J.-H. Lee, “NO₂ sensing characteristics of ZnO nanorods prepared by hydrothermal method,” *J. Electroceramics*, vol. 17, no. 2–4, pp. 975–978, Dec. 2006.

- [22] S. Roso, F. Güell, P. R. Martínez-Alanis, A. Urakawa, and E. Llobet, "Synthesis of ZnO nanowires and impacts of their orientation and defects on their gas sensing properties," *Sensors Actuators B Chem.*, vol. 230, pp. 109–114, Jul. 2016.
- [23] C. W. Na, S.-Y. Park, and J.-H. Lee, "Punched ZnO nanobelt networks for highly sensitive gas sensors," *Sensors Actuators B Chem.*, vol. 174, pp. 495–499, Nov. 2012.
- [24] J. Guo, J. Zhang, M. Zhu, D. Ju, H. Xu, and B. Cao, "High-performance gas sensor based on ZnO nanowires functionalized by Au nanoparticles," *Sensors Actuators B Chem.*, vol. 199, pp. 339–345, Aug. 2014.
- [25] Y.-J. Jeong, C. Balamurugan, and D.-W. Lee, "Enhanced CO₂ gas-sensing performance of ZnO nanopowder by La loaded during simple hydrothermal method," *Sensors Actuators B Chem.*, vol. 229, pp. 288–296, Jun. 2016.
- [26] M. Hjiri, L. El Mir, S. G. Leonardi, A. Pistone, L. Mavilia, and G. Neri, "Al-doped ZnO for highly sensitive CO gas sensors," *Sensors Actuators B Chem.*, vol. 196, pp. 413–420, Jun. 2014.
- [27] Y. Zeng *et al.*, "Enhanced ammonia sensing performances of Pd-sensitized flowerlike ZnO nanostructure," *Sensors Actuators B Chem.*, vol. 156, no. 1, pp. 395–400, Aug. 2011.
- [28] Y.-J. Li, K.-M. Li, C.-Y. Wang, C.-I. Kuo, and L.-J. Chen, "Low-temperature electrodeposited Co-doped ZnO nanorods with enhanced ethanol and CO sensing properties," *Sensors Actuators B Chem.*, vol. 161, no. 1, pp. 734–739, Jan. 2012.
- [29] J.-A. Park, J. Moon, S.-J. Lee, S. H. Kim, H. Y. Chu, and T. Zyung, "SnO₂-ZnO hybrid nanofibers-based highly sensitive nitrogen dioxides sensor," *Sensors Actuators B Chem.*, vol. 145, no. 1, pp. 592–595, Mar. 2010.
- [30] Y. Liu, G. Li, R. Mi, C. Deng, and P. Gao, "An environment-

- benign method for the synthesis of *p*-NiO/*n*-ZnO heterostructure with excellent performance for gas sensing and photocatalysis,” *Sensors Actuators B Chem.*, vol. 191, pp. 537–544, Feb. 2014.
- [31] F. Schütt, V. Postica, R. Adelung, and O. Lupan, “Single and Networked ZnO-CNT Hybrid Tetrapods for Selective Room-Temperature High-Performance Ammonia Sensors,” *ACS Appl. Mater. Interfaces*, vol. 9, no. 27, pp. 23107–23118, 2017.
- [32] J. Wang *et al.*, “Hierarchical ZnO Nanosheet-Nanorod Architectures for Fabrication of Poly(3-hexylthiophene)/ZnO Hybrid NO₂ Sensor,” *ACS Appl. Mater. Interfaces*, vol. 8, no. 13, pp. 8600–8607, 2016.
- [33] A. Khademi, R. Azimirad, A. A. Zavarian, and A. Z. Moshfegh, “Growth and Field Emission Study of Molybdenum Oxide Nanostars,” *J. Phys. Chem. C*, vol. 113, no. 44, pp. 19298–19304, Nov. 2009.
- [34] J. Jiang *et al.*, “Facile synthesis of α -MoO₃ nanobelts and their pseudocapacitive behavior in an aqueous Li₂SO₄ solution,” *J. Mater. Chem. A*, vol. 1, no. 7, p. 2588, Jan. 2013.
- [35] X.-L. Li, J.-F. Liu, and Y.-D. Li, “Low-temperature synthesis of large-scale single-crystal molybdenum trioxide (MoO₃) nanobelts,” *Appl. Phys. Lett.*, vol. 81, no. 25, pp. 4832–4834, Dec. 2002.
- [36] L. Cheng, M. Shao, X. Wang, and H. Hu, “Single-Crystalline Molybdenum Trioxide Nanoribbons: Photocatalytic, Photoconductive, and Electrochemical Properties,” *Chem. - A Eur. J.*, vol. 15, no. 10, pp. 2310–2316, Feb. 2009.
- [37] I. Navas *et al.*, “Growth and characterization of molybdenum oxide nanorods by RF magnetron sputtering and subsequent annealing,” *J. Phys. D. Appl. Phys.*, vol. 42, no. 17, p. 175305, Sep. 2009.

- [38] C. V. Subba Reddy, E. H. Walker, S. a. Wicker, Q. L. Williams, and R. R. Kalluru, "Characterization of MoO₃ nanorods for lithium battery using PVP as a surfactant," *J. Solid State Electrochem.*, vol. 13, no. 12, pp. 1945–1949, Dec. 2009.
- [39] V. V. Atuchin, T. A. Gavrilova, V. G. Kostrovsky, L. D. Pokrovsky, and I. B. Troitskaia, "Morphology and structure of hexagonal MoO₃ nanorods," *Inorg. Mater.*, vol. 44, no. 6, pp. 622–627, Jun. 2008.
- [40] A. M. Taurino, A. Forleo, L. Francioso, P. Siciliano, M. Stalder, and R. Nesper, "Synthesis, electrical characterization, and gas sensing properties of molybdenum oxide nanorods," *Appl. Phys. Lett.*, vol. 88, no. 15, p. 152111, Apr. 2006.
- [41] X. M. Wei and H. C. Zeng, "Large-scale organizations of MoO₃ nanoplatelets with single-crystalline MoO₃(4,4'-bipyridyl)_{0.5}," *J. Phys. Chem. B*, vol. 107, no. 12, pp. 2619–2622, Mar. 2003.
- [42] F. Ji *et al.*, "2D-MoO₃ nanosheets for superior gas sensors," *Nanoscale*, vol. 8, no. 16, pp. 8696–8703, Apr. 2016.
- [43] A. Phuruangrat, D. J. Ham, S. Thongtem, and J. S. Lee, "Electrochemical hydrogen evolution over MoO₃ nanowires produced by microwave-assisted hydrothermal reaction," *Electrochem. commun.*, vol. 11, no. 9, pp. 1740–1743, Sep. 2009.
- [44] M. H. Kim *et al.*, "Growth of Metal Oxide Nanowires from Supercooled Liquid Nanodroplets," *Nano Lett.*, vol. 9, no. 12, pp. 4138–4146, Dec. 2009.
- [45] C. V. Krishnan, J. Chen, C. Burger, and B. Chu, "Polymer-Assisted Growth of Molybdenum Oxide Whiskers via a Sonochemical Process," *J. Phys. Chem. B*, vol. 110, no. 41, pp. 20182–20188, Oct. 2006.
- [46] B. Yan *et al.*, "Orientation Controllable Growth of MoO₃ Nanoflakes: Micro-Raman, Field Emission, and Birefringence

- Properties,” *J. Phys. Chem. C*, vol. 113, no. 47, pp. 20259–20263, Nov. 2009.
- [47] S. Hu, X. Ling, T. Lan, and X. Wang, “Cluster-based self-assembly route toward MoO₃ single-walled nanotubes,” *Chem. - A Eur. J.*, vol. 16, no. 6, pp. 1889–1896, Feb. 2010.
- [48] S. Hu and X. Wang, “Single-walled MoO₃ nanotubes,” *J. Am. Chem. Soc.*, vol. 130, no. 26, pp. 8126–8127, Jul. 2008.
- [49] G. Li, L. Jiang, S. Pang, H. Peng, and Z. Zhang, “Molybdenum Trioxide Nanostructures: The Evolution from Helical Nanosheets to Crosslike Nanoflowers to Nanobelts,” *J. Phys. Chem. B*, vol. 110, no. 48, pp. 24472–24475, Dec. 2006.
- [50] T. Liu, Y. Xie, and B. Chu, “Use of block copolymer micelles on formation of hollow MoO₃ nanospheres,” *Langmuir*, vol. 16, no. 23, pp. 9015–9022, Nov. 2000.
- [51] K. P. Chang, U. S. Chen, and H. C. Shih, “Size-controlled MoO₃ nanoslabs synthesized by microwave plasma-enhanced chemical vapor deposition,” *Electrochem. Solid-State Lett.*, vol. 10, no. 3, p. H111, Mar. 2007.
- [52] H. M. M. Munasinghe Arachchige, D. Zappa, N. Poli, N. Gunawardhana, and E. Comini, “Gold functionalized MoO₃ nano flakes for gas sensing applications,” *Sensors Actuators B Chem.*, vol. 269, pp. 331–339, Sep. 2018.
- [53] A.-F. I. Saad, “Dielectric properties of molybdenum oxide thin films-INOE 2000.,” *J. Optoelectron. Adv. Mater.*, vol. 7, no. 5, pp. 2743–2752, 2005, Accessed: Aug. 04, 2019.
- [54] D. Chen *et al.*, “Single-crystalline MoO₃ nanoplates: topochemical synthesis and enhanced ethanol-sensing performance,” *J. Mater. Chem.*, vol. 21, no. 25, p. 9332, Jun. 2011.
- [55] L. Zhang *et al.*, “Self-assembly gridding α -MoO₃ nanobelts for

- highly toxic H₂S gas sensors,” *Sensors Actuators B Chem.*, vol. 237, pp. 350–357, Dec. 2016.
- [56] L. Sui *et al.*, “Construction of three-dimensional flower-like α -MoO₃ with hierarchical structure for highly selective triethylamine sensor,” *Sensors Actuators B Chem.*, vol. 208, pp. 406–414, Mar. 2015.
- [57] W. Zeng, H. Zhang, Y. Li, and W. Chen, “Net-like MoO₃ porous architectures: synthesis and their sensing properties,” *J. Mater. Sci. Mater. Electron.*, vol. 25, no. 1, pp. 338–342, Jan. 2014.
- [58] M. M. Y. A. Alsaif *et al.*, “Two dimensional α -MoO₃ nanoflakes obtained using solvent-assisted grinding and sonication method: Application for H₂ gas sensing,” *Sensors Actuators B Chem.*, vol. 192, pp. 196–204, Mar. 2014.
- [59] Q.-Y. Ouyang *et al.*, “Facile synthesis and enhanced H₂S sensing performances of Fe-doped α -MoO₃ micro-structures,” *Sensors Actuators B Chem.*, vol. 169, pp. 17–25, Jul. 2012.
- [60] S. Bai *et al.*, “Preparation of conducting films based on α -MoO₃/PANI hybrids and their sensing properties to triethylamine at room temperature,” *Sensors Actuators B Chem.*, vol. 239, pp. 131–138, Feb. 2017.
- [61] T.-S. Wang *et al.*, “Synthesis and enhanced H₂S gas sensing properties of α -MoO₃/CuO *p-n* junction nanocomposite,” *Sensors Actuators B Chem.*, vol. 171–172, pp. 256–262, Aug. 2012.
- [62] S. Bai, C. Chen, R. Luo, A. Chen, and D. Li, “Synthesis of MoO₃/reduced graphene oxide hybrids and mechanism of enhancing H₂S sensing performances,” *Sensors Actuators B Chem.*, vol. 216, pp. 113–120, Sep. 2015.

Chapter 2

Synthesis and Characterization Techniques

2.1. Introduction

Over the past four decades, production of thin films for device application plays a vital role in the advancement of modern technology [1]. Recently, nanostructured thin films also plays an important role, given their unique functional properties that are morphology-driven and can be used to build new technologies for potential applications. Nanostructured thin film technology relies mainly on three fundamental principles: fabrication, characterization and application. The physical or chemical deposition process can be used to deposit nanostructured thin film. Both the methods has their own advantages and disadvantages. However, chemical method is economically cheap and simple as compared to physical deposition method. In this thesis work, nanostructured materials are prepared *via* chemical methods (mainly hydrothermal method) and physical deposition method (e.g., sputtering technique) is employed for making metal electrodes for the electrical characterizations of the sensors. Characterizations of the as-prepared materials are done by field emission scanning electron microscopy (FESEM), X-ray diffraction (XRD), transmission electron microscopy (TEM), and high resolution transmission electron microscopy (HRTEM) for the deep analysis of the structures. Elemental analysis of the materials were done by either energy dispersive X-ray (EDX) or X-ray photoluminescence spectroscopy (XPS) technique. Materials are also characterized by Thermogravimetric analysis (TGA) and Brunauer–Emmett–Teller (BET) surface area analysis technique, subject to requirement of the analysis. All the grown material are either *in-situ*

deposited or drop casted on top of an appropriate substrate (glass, or SiO₂/Si, or PDMS). Whereas, electrodes are either made on top of sensing film or on top of insulating substrate for the complete device fabrication. Finally, sensing properties of the devices are measured for different gases/VOCs in different concentrations. The detailed description regarding the substrate selection and its cleaning procedure, deposition methods, material characterization techniques, and gas sensor measurement system are discussed in the following section.

2.2. Substrates Selection and Their Cleaning Procedures

Although the quality of the grown thin film depends on the deposition technique used to grow the thin film, yet, the nature and surface condition of the substrate plays vital role for high quality thin film growth. Some desired properties of the substrate are a) low surface roughness, (b) low chemical reactivity, and (c) good mechanical strength. The choice of substrate selection depends on the application type, cost, process, and packaging of the device. Silicon (100), corning glass, and PDMS are the substrate used in this thesis work for the deposition of sensing film. Silicon and corning glass substrate are used for the application of high temperature sensing, and PDMS substrate is used for the application of room temperature sensing. Contamination present at the substrate surface affects the film purity and their adhesion to the substrates, therefore, it is necessary to clean the substrate properly before the deposition of the sensing film. Depending on the type of substrate and type of contaminants present on the substrate, an appropriate cleaning procedure are followed to clean the substrates.

2.2.1. 'Si' Substrate Cleaning Procedure

In this thesis work, the following steps are employed to clean the Si substrates.

- Remove dust using pipette like blower before cleaning the substrates.
- Ultrasonic cleaning in diluted HF solution to remove native silicon dioxide from wafers.

- Rinse with de-ionized (DI) water to remove any HF remaining.
- Ultrasonic cleaning in diluted TCE solution to remove any fingerprints on the wafer or any other heavy residue on the wafer.
- Rinse with DI water to remove any TCE remaining.
- Ultrasonic cleaning in acetone to remove the organic remnants/contaminants from the wafers.
- Rinse with DI water to remove any acetone remaining.
- Ultrasonic cleaning in diluted isopropanol solution for dissolving non-polar contaminants which are left on the wafers.
- Rinse with DI water to remove any isopropanol remaining.
- Purge with nitrogen to remove any water remaining.

2.2.2. Glass Substrate Cleaning Procedure

In this thesis work, the following steps were employed to clean the glass substrates.

- Ultrasonic cleaning with soap water to remove any fingerprints, or oil contamination.
- Rinse with DI water to remove any soap remaining.
- Ultrasonic cleaning in acetone to remove tiny dust particles on the surface through agitation.
- Isopropanol to remove further contaminants.
- Rinse with DI water and blow off the water-droplets.
- Remove any other dust using nitrogen purging.

2.2.3. PDMS Substrate Cleaning Procedure

Polydimethylsiloxane (PDMS) is an organic polymer and used as a flexible substrate for the development of wearable sensors. Organic solvents such as ether, chloroform, acetone, and propanol can swell PDMS to an extent. Due to this fact, PDMS substrate is cleaned by oxygen plasma cleaning technique. Plasma cleaning is the common technique used to extract organic impurities and contaminants from a substrate's surface. This method involves putting the substrate in a vacuum containing ionized gas (plasma) species for oxygen plasma cleaning, ionized gas species are O^- , O^+ , O_2^+ , O_2^- , and O_3^- . The organic

contaminants react with these ionized oxygen species to create CO₂, CO, H₂O, and hydrocarbons of low molecular weight. Such products have high vapor pressure and quickly evacuate from the chamber, contributing to ultra-clean surface conditions.

2.3. Synthesis/Deposition Techniques

Both the chemical and physical deposition methods are used in the present thesis work. Chemical method mainly hydrothermal synthesis method is employed for the growth of nanostructured materials, which are the active layer or sensing layer of the sensor. Seed layer is grown by reactive magnetron sputtering technique. E-beam evaporation technique is employed for the growth of metal electrodes. All the three systems mentioned above are explained concisely in the following section.

2.3.1. Hydrothermal Synthesis Method

In early 19th century British Geologist Sir Roderick Murchison introduced the term 'Hydrothermal' in describing the formation of rock and minerals on the earth's crust due to high temperature and high pressure water medium. Next, in 1892, Karl Josef Bayer successfully applied hydrothermal synthesis method for the extraction of mineral. Then, in 1946, a large single crystal of quartz was synthesized by Nacken through hydrothermal synthesis method. In 1948, Barrer synthesized single crystalline Zeolite using hydrothermal synthesis method. Since then, hydrothermal synthesis is findings many applications in the field of material science and solid state chemistry for the growth of new materials with new functional properties.

Hydrothermal synthesis is, in essence, a chemical reaction to crystallize materials in the water medium in high temperature and a high pressure in the closed system. This method is one of the most promising method for the growth of single crystalline nanomaterials. Few applications of hydrothermal method is as follows:

- Growth of single crystals

- Growth of nanostructured material with well-defined morphology
- Stabilization or synthesis of new compounds
- Modification, decomposition, etching, corrosion

Some advantages of hydrothermal method over other chemical or physical deposition methods are as follows:

- The process is simple and cost effective
- Nanomaterials are formed directly from the solution
- The size of the particles can be regulated by temperature and time of reaction
- Particles shape can be controlled by controlling on starting material
- Chemical composition or stoichiometry can be controlled ideal for metastable material synthesis

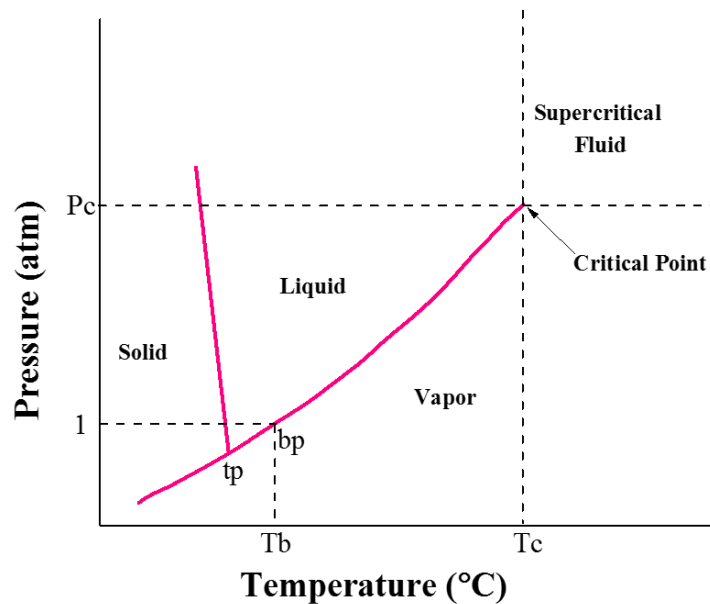


Figure 2.1. Phase diagram of the water [2].

2.3.1.1. Hydrothermal Synthesis for the Growth of Single Crystalline Inorganics and Organic-Inorganic Hybrids

At room temperature, the dielectric constant of water is 78, and the majority of the inorganic salt can be soluble in water at this time. As temperature increases the dielectric constant of the water decreases, when the temperature reaches 374 °C and pressure 22.1 MPa, water is in

its supercritical condition (Figure 2.1). Here, the dielectric constant of the water is below 10 and solubility is much lower than the under normal condition (room temperature). The dielectric constant and density of the water under different pressures and temperatures are shown in Figure 2.2. Under the high temperature and high pressure conditions of the water, the reaction rate is remarkable and a favorable reaction field is created for the formation of the particle according to the theory of electrostatic and nucleation. Under this condition, i.e., at low dielectric constant, inorganic has low solubility whereas organics has high solubility, making the ideal environment for hybrid particle synthesis [3].

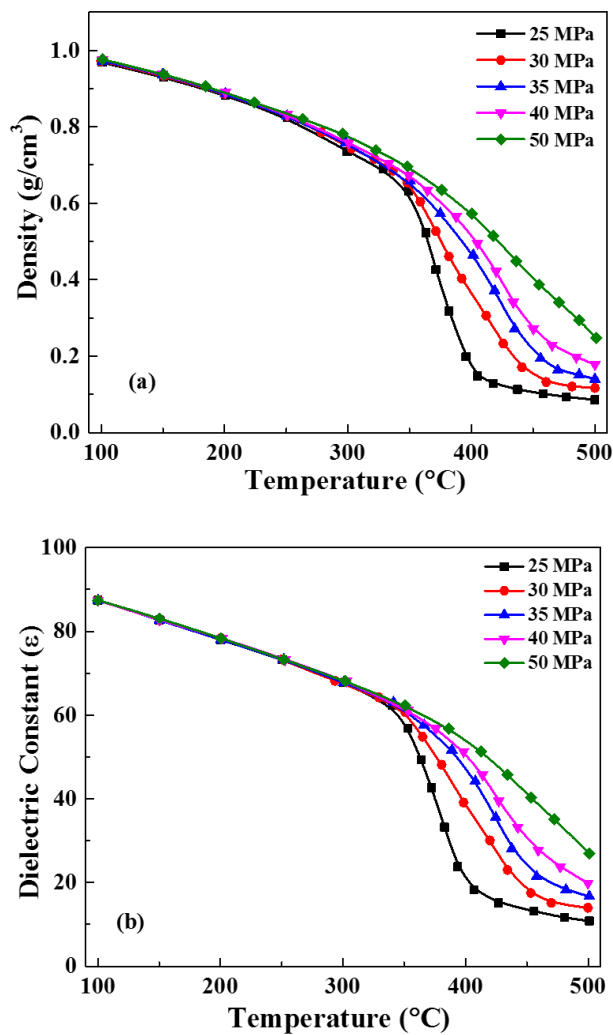


Figure 2.2. (a) Density and (b) dielectric constant of the water as a function of temperature and pressure [3].

At high temperatures and high pressure, the viscosity of the water decreases and the process of agility and diffusion increases. The low viscosity and high agility of water make it a suitable medium for developing metastable phases and high-quality crystals [5].

2.3.1.2. Hydrothermal Chamber: Autoclave

Hydrothermal synthesis occurs in a closed vessel, the pressure of the vessel depends on the temperature provided to it and the degree of filling of the vessel. The crystal growth happens only if the vessel is filled above 32% and more effectively above 65% of the total volume. Figure 2.3 shows the pressure generated at different temperatures and different degrees of filling. The vessel should be such that it can handle extremely corrosive solvents at high pressure and high temperature. The ideal hydrothermal chamber is known as an autoclave [6].

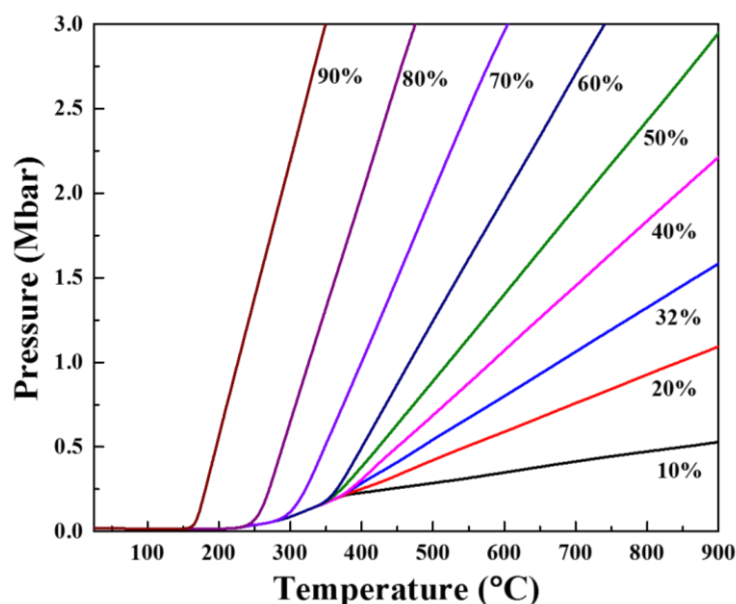


Figure 2.3. Pressure against temperature under different degree of vessel filling [4].

In the 19th century, the first autoclave is made in Europe and later used throughout the world in the 20th century.

An ideal autoclave should include the following features

- Nonreactive to bases, acids, and oxidizing agents
- Easy to use

- Proper shape and size for uniform temperature gradient
- High mechanical strength and leak-proof to tolerate high temperature and high pressure

So far, the most used material for autoclave is stainless steel due to its high mechanical strength and corrosion-resistant properties. The solvents and reagents of the hydrothermal reaction are often corrosive and can attack the vessel at high temperature and high pressure. Therefore, it requires an inner wall inside the autoclave which must be noncorrosive to the solvents and reagents. Here, Teflon beaker is an ideal candidate, which can be placed inside the stainless steel autoclave without leaving any space or minimum space, however, the temperature limit for Teflon beaker is 300 °C. The Teflon lined stainless steel autoclave used in this thesis work is shown in Figure 2.4.



Figure 2.4. *Stainless steel Teflon lined autoclave used in this thesis work.*

2.3.1.3. Hydrothermal Procedure

The aforementioned stainless steel Teflon lined autoclave has been used for hydrothermal reactions. Initially, solutions are prepared in a glass beaker; generally, a certain amount of water is taken in the glass beaker and kept it on the hot plate under constant stirring at room temperature. Then the required inorganic salts are added in the water and stirred until it dissolves in the water. Next, acid or base is added in the solution as

per the requirement of the process and stirred for a minimum 15 min. Finally, if required, an organic component is added and stirred until uniform solution is formed. After that, the solution is transferred from the glass beaker to a Teflon beaker and sealed tightly in an autoclave. During the transferred process, Teflon beaker is filled with the solution above 50% for creating enough pressure in the Teflon beaker during the hydrothermal process. After that, the autoclave is placed in a thermal oven, where the temperature is kept near or above 100 °C for different hours or days as per the requirement. Then, the autoclave is taken out from the oven and naturally cooled to room temperature at the end of the reaction time period. The products are subsequently filtered and washed with ethanol and DI water several times to eliminate remaining impurities from the material. Finally, the products are collected dried and calcined at desired temperatures. The flow chart of the hydrothermal process is shown in Figure 2.5.

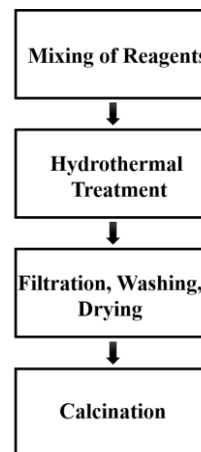


Figure 2.5. Schematic of the flow process of the hydrothermal method.

2.3.2. Reactive DC Magnetron Sputtering

Sputtering is a technique used to deposit physical vapors for thin-film production. The main principle relies on the removal of particles from a target surface by the highly energetic bombarding particles (e.g., ions, electrons, neutrons, neutral atoms, photons). Depending on the working principle and application type there are mainly four types of sputtering techniques are present. These are (1) DC/RF sputtering, (2) magnetron

sputtering, (3) reactive sputtering, and (4) ion-beam sputtering. However, currently most complex version of sputtering is the reactive DC magnetron sputtering technique and it is used to grow oxide/nitride thin films from a conducting target.

Reactive DC magnetron sputtering system consist of the following components:

- Main stainless steel chamber
- Load lock chamber
- Robotic arm
- DC power supply
- Substrate holder (anode)
- Heater assembly
- Temperature reader
- Target (magnetron cathode)
- Gas inlets (source of O₂ and Ar)
- Vacuum pump
- Pressure gauge
- Ion gauge
- Water chiller and other parameter controlling unit

A schematic of the reactive DC magnetic sputtering is shown in Figure 2.6. The system is equipped with a load lock to ensure that the high vacuum is not disturbed during sample loading into the chamber. The chamber is equipped with halogen heat lamps to heat the substrates from RT to 800 °C. A two-inch diameter, 99.99% Zinc target from Lesker is used inside the shuttered DC magnetron sputtering gun. Argon is flown to the source while oxygen gas is flown near the substrate. Mass flow controllers are used to control the flow rates. The base pressure is monitored by ion gauge and pressure during deposition is monitored by the capacitive nanometer. Initially, a cleaned substrate is placed into an Inconel substrate holder or in the robotic arm. Then, the substrate holder is placed face down into the load lock onto the robotic arm. The load lock is pumped down and the substrate holder is transferred to the column connected to the heater assembly. Robotic arm is withdrawn and

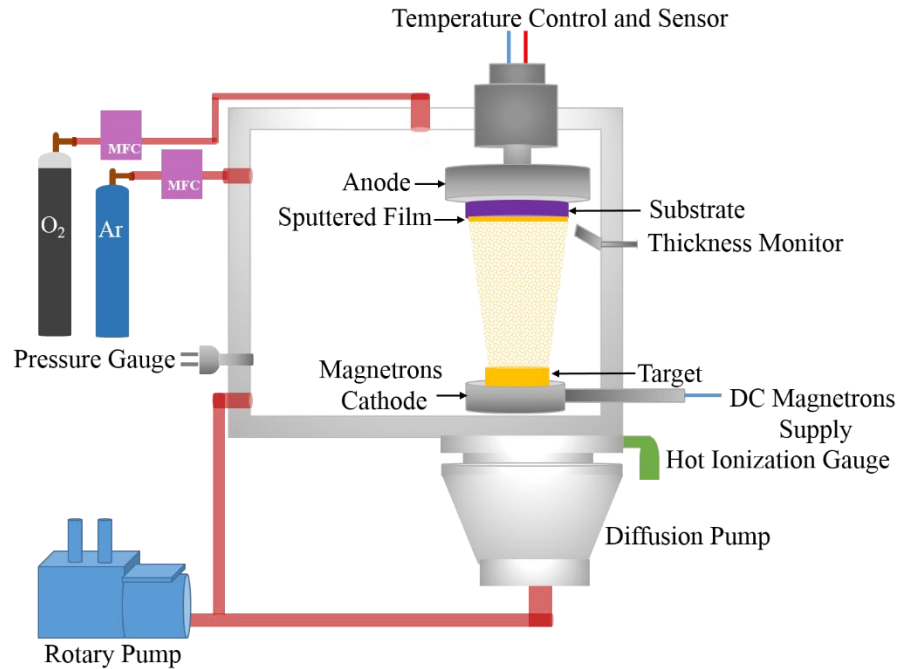


Figure 2.6. Schematic representation of the reactive DC magnetron sputtering.

the gate valve is closed. After that chamber is filled with Ar-O₂ gas up to a desired pressure (30 mtorr). A high negative potential is applied across the electrodes to accelerate the electrons. The energetic electrons will ionize the Ar-O₂ gas atoms, which will lead to plasma generation. The Ar⁺ ions will be accelerated towards the cathode and bombard the target which in turn will eject the target atoms. As the atoms to be deposited, are ejected or sputtered from the target material by bombarding their surfaces with energetic Ar⁺ ions, the sputtered atom chemically react with oxygen ions to form oxide film at the substrate.

2.3.3. E-Beam Evaporation

Another method of vapor deposition used to make thin films is the electron beam (E-beam) evaporation. It uses an electron beam to evaporate the source material (metal pellets) and then evaporated material condenses on the cooled substrate as a thin film. E-beam evaporation technique is an advanced version of the thermal evaporation technique. In thermal evaporation technique source material is heated resistively, whereas, in E-beam evaporation technique source material is

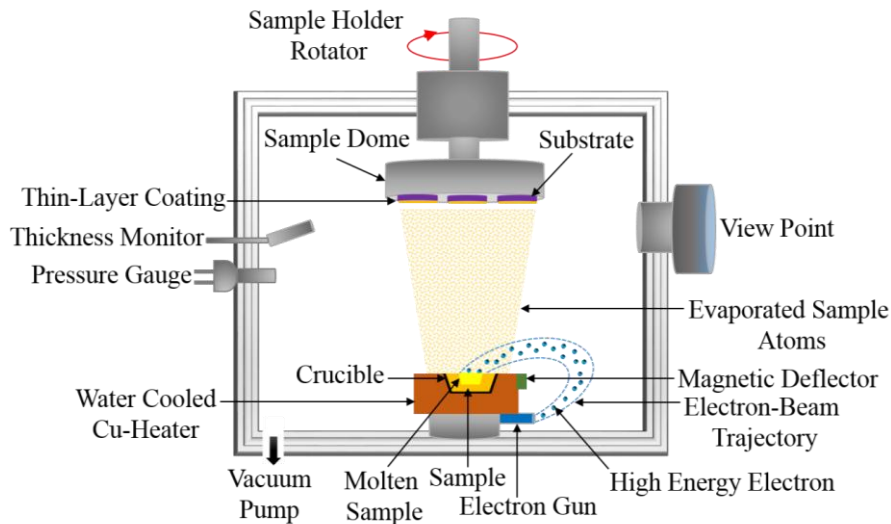


Figure 2.7. Schematic of the E-beam evaporation technique.

heated by an electron beam. The main component of an E-beam evaporation system are as follows:

- Stainless steel chamber (deposition chamber)
- Substrate holder
- Electron beam evaporation unit
 - Crucibles (pellet holder)
 - E-beam source
 - Filament
 - Magnetic beam deflector
- Substrate and E-beam unit cooler system
- Pressure gauge
- Thickness monitor unit
- Vacuum pump
- Chiller and other parameter controlling units

The following are key steps in the process of E-beam evaporation:

- The source material is loaded in the crucible (generally graphite)
- The substrate is loaded facing down above the source material (sample)
- Chamber vacuumed below 10^{-6} Torr
- The source material is heated at evaporate point
 - Filament underneath the crucible is heated by a large current (~ 100 A)

- Hot electrons are emitted from the filament led to a few ~ mA emission current
 - The emitted electrons are accelerated by a high electric field
 - An electromagnetic coil is used to control the dimension and shape of the emitted electron beam to bombard the source material for its evaporation.
- Vaporized atoms are condensed on the cooled substrate and as well as on the chamber wall.

The E-beam evaporation technique scheme is illustrated in Figure 2.7.



Figure 2.8. The system used to grow seed layer and metal electrodes in this work.

https://www.lesker.com/newweb/vacuum_systems/jpg/Photo/Photo-SY-K-ProLinePVD75-OpenFrameStandard-001.jpg

In this thesis work, ZnO seed layer and metal electrodes are grown by Kurt J. Lesker PVD75 Pro-line. Figure 2.8 shows the Kurt J. Lesker PVD75 Pro-line image used in this work.

2.4. Material Characterization Techniques

To describe any morphology dependent gas/VOC sensing properties of the nanomaterial, grown material must characterize through different material characterization techniques to examine the surface/crystal morphology, phase, and elemental composition of the material. The techniques used in this thesis work for the material characterizations are discussed as follows.

2.4.1. X-Ray Diffraction (XRD)

X-ray diffraction is an effective technique for determining the material's crystal-related properties, e.g., lattice constant, crystallography, phase, strain, crystal orientation, and crystallite sizes etc. This technique requires an X-ray source, a sample (thin film, powder, or any solid piece) that needs to be examined under incident X-rays and a detector that detects diffracted X-rays from the sample.

X-rays are produced when high energy particles (e.g., electron) collide with the matter (e.g., copper). During the collision, these high energy particles lost their energy, lost energy then dissipates as electromagnetic radiation (X-ray). X-rays are basically radiation of electromagnetic waves with a wavelength between 0.01 and 100 Å [7]. Generally, the X-ray diffraction technique uses monochromatic X-rays whose wavelength is in the vicinity of 1 Å, which is close to the interatomic space of crystals.

When an X-ray (monochromatic) beam incident on a sample, besides adsorption and other phenomena, it produces a reflected or scattered X-rays of equal wavelength as it in incident X-ray. The intensities and the spatial distribution of the scattered X-rays form a particular diffraction pattern that depends on the type of atomic structure in the sample.

Bragg's law can explain the diffraction of X-rays by a crystal. When the X-rays hits the crystal plane at an angle θ and diffracts from it at the same angle, only under Bragg's condition the diffraction peak can be observed:

$$n\lambda = 2d_{hkl}\sin\theta \quad (2.1)$$

where θ is the scattering angle, λ is the wave length, d_{hkl} is the distance between the neighboring lattice plane, and n is an integer number known as reflection order. For monochromatic X-ray diffraction $n = 1$. The schematic representation of Bragg's Law is shown in Figure 2.9(a).

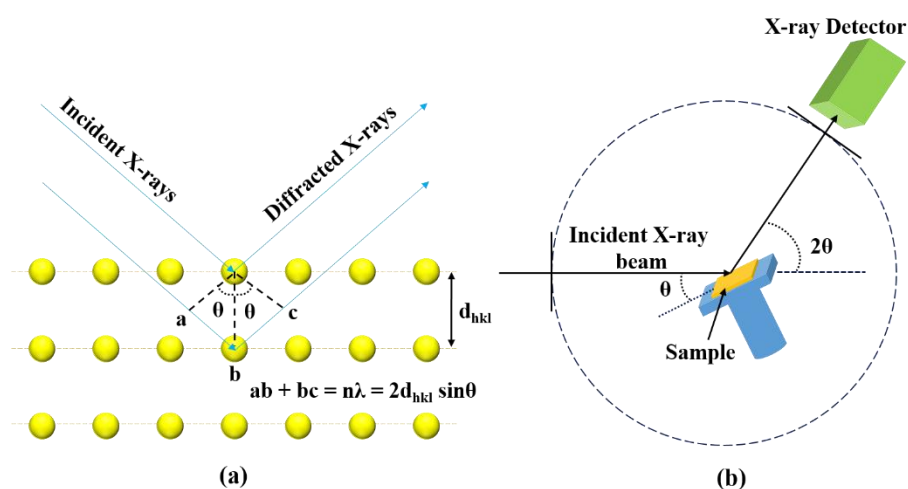


Figure 2.9. Schematic representation of (a) diffraction of X-rays by a set of crystal planes relying on Bragg's law and (b) XRD measurement system.

In a diffractometer, the incident angle between the substrate plane and the incident X-rays is the same as the reflected angle between the substrate plane and the diffracted X-rays. So the crystallographic planes that can be detected are only parallel to the substrate plane. Thereby, varying the incident angle θ results in a spectrum containing of all the crystallographic planes parallel to the substrate plane, mainly known as $\theta/2\theta$ plane (Figure 2.9(b)). All the parameter like crystallographic plane, lattice constant, crystallite size, and strain can be calculated for this diffraction spectrum.

In this thesis work, Rigaku SmartLab Automated Multipurpose X-ray Diffractometer (Cu-K α radiation, $\lambda = 1.54178 \text{ \AA}$) is used to perform the X-ray diffraction analysis of developed materials. Figure 2.10 shows the actual image of the Rigaku X-ray Diffractometer used in this thesis work.



Figure 2.10. Image of the Rigaku SmartLab Automated Multipurpose X-ray Diffractometer.

2.4.2. Field Emission Scanning Electron Microscopy (FESEM)/Energy Dispersive X-ray (EDX) Spectroscopy

The field emission scanning electron microscope is an image obtaining technique of a sample (solid) surface by raster scanning the surface with high energy electron beams. The basic components of a FESEM system are field emission electron gun, lens system, electron detector, and cathode-ray tubes (CRTs). In FESEM, a field emission gun is used to generate electrons which are then focused and accelerated by several electromagnet lenses toward the sample surface in a high vacuum closed chamber. These highly energized electrons (0.5-30 keV) interact with the solid surface and decelerated, resulting in various electronic excitations including backscattered electrons, secondary electrons, X-rays or photons, auger electrons, cathodoluminescence or visible light, elastically scattered electron, inelastically scattered electron, unscattered electron and heat. Figure 2.11 shows the schematic of the electron and solid surface interaction. Among these, the secondary electrons and the back scattered electrons are mainly responsible for producing the FESEM image.

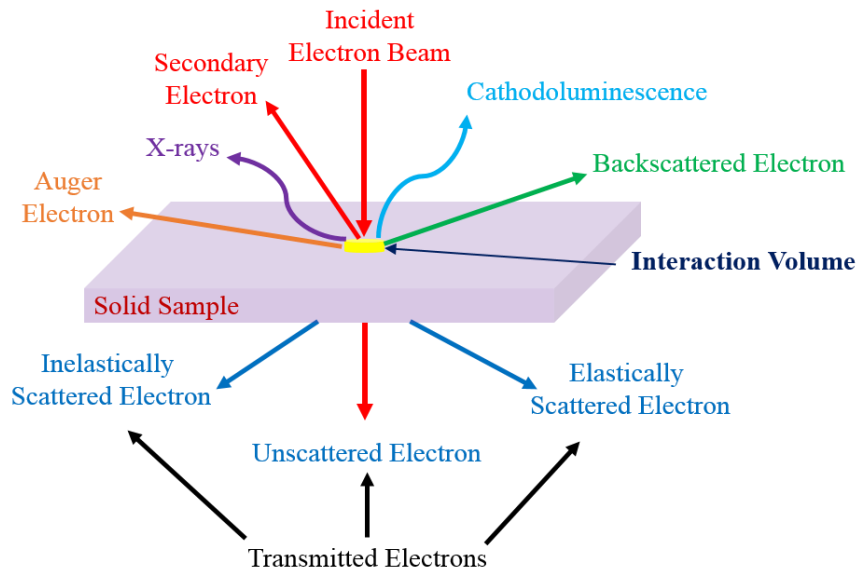


Figure 2.11. Schematic of electron solid interaction.

Secondary electrons are sample electrons generated from the near-surface region (0-10 nm) of the sample. These electrons are outer shell electrons of the sample having low binding energy with the nucleus, they escape from the surface due to sufficient energy provided by the incident high energy electrons. The energy of the secondary electrons is nearly in the range of 0-50 eV and a majority in between 3-5 eV. These secondary electrons produce an image of the surface area of the sample and provide surface morphology detail.

Backscattered electrons are the scattered electrons having energy nearly $\frac{3}{4}$ of incident electron beam energy. At the point of the incident beam, the material's atomic number is responsible for the number of backscattered electrons that is to be produced, the greater the atomic number greater the backscattered electrons. Backscattered electrons provide the information of atomic number contrast and depth within the image. When the high energy incident electron beam takes out an electron from the core shell of the sample surface, instantly, a high energy electron from the outer shell moves in to occupy the empty shell, during this process a characteristic energy (electromagnetic radiation) is emitted in the form of X-rays. The X-rays energy is a characteristic of the atom from which it is generated.

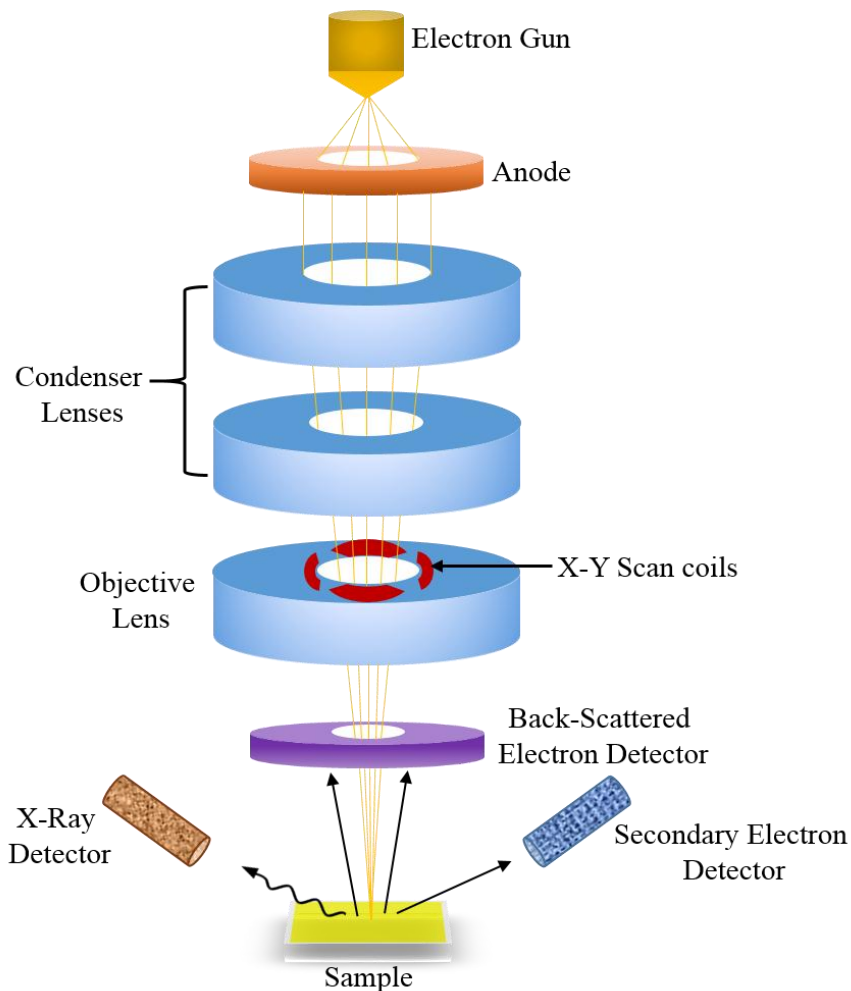


Figure 2.12. Schematic of the FESEM/EDX working principle.

Every element has its distinctive atomic arrangement, hence emitted X-rays are the atomic structure characteristic. The information of the elements present in the sample can be obtained by detecting and analyzing these emitted X-rays. The technique that analyzes the energy of the emitted X-rays known as the energy dispersive X-rays (EDX) spectroscopic technique. An EDX system consists of an electron beam source, X-ray detector, pulse processor, and analyzer. Here, the detector detects the X-rays and converts it to voltage signals. Then this signal is sent to the pulse processor for calculating voltage signals. Finally, the measured voltage signals are passes to the analyzer to show the compositional data analysis [8]. The FESEM / EDX working principle scheme is shown in Figure 2.12. To reduce the overall cost of the system, usually, the EDX system is equipped with the SEM or FESEM system.



Figure 2.13. Image of the FESEM/EDX system, ZEISS Supra⁵⁵.

In this thesis work, ZEISS Supra⁵⁵ system is used for the characterization of FESEM and EDX of the grown material. The image of the ZEISS Supra⁵⁵ is shown in Figure 2.13.

2.4.3. Transmission Electron Microscopy (TEM)

Transmission electron microscopy is a crystal imaging technique of an ultra-thin (~100 nm) specimen/sample. The basic components of a TEM are electron gun, electromagnetic lens system, and imaging system. In TEM, either a thermal emission (CTEM) or field emission (HRTEM) electron gun is used to generate high energy (80-300 keV) electrons which are then accelerated (at a speed of light) and focused by several electromagnet lenses towards an ultra-thin specimen in an ultra-high vacuum column chamber. When these highly energized electrons strike with the specimen, part of these electrons (elastically scattered electron, inelastically scattered electron, and unscattered electron) are transmitted through the specimen depending on the specimen thickness and density.

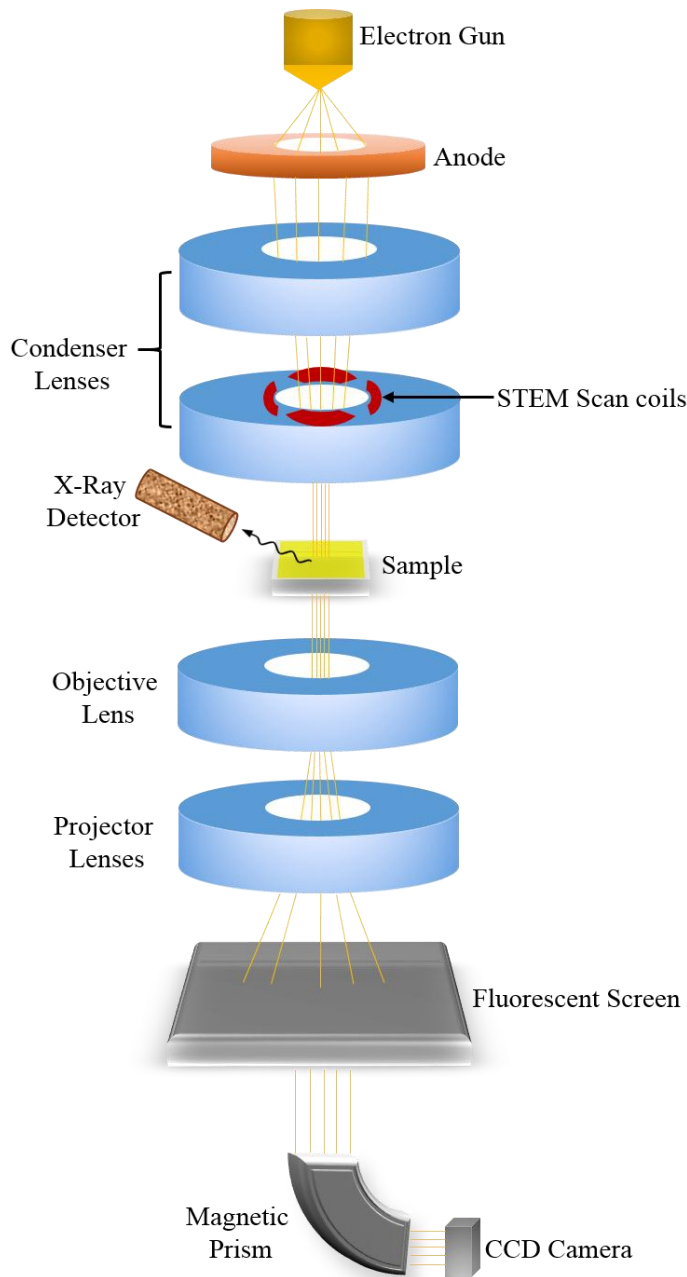


Figure 2.14. Schematic of the TEM working principle.

Then, the transmitted unscattered electrons are focused by the objective lens onto a phosphor screen or CCD camera to produce the image of the internal structure of the crystal. Figure 2.14 illustrates the schematic of the working principle of the TEM operation.

Among the transmitted electrons, there are number of elastically scattered electrons; these are electrons scattered elastically by atoms in the specimen, which means their transmission energy is the same as the incident energy. Elastic electrons scattered at a specific angle may be

collected to create a spot pattern. Every spot corresponds to an explicit atomic spacing. In this way, the diffraction patterns generated by elastically scattered electrons follow Bragg's principle of scattering for a crystalline specimen. The selected area of electron diffraction (SAED) pattern is obtained by illuminating (electron beam) a particular specimen region. From which one can determine the information of atomic arrangement, crystal orientation, and crystal phases present in that specific area.



Figure 2.15. Image of the HRTEM system used in this thesis work.

Finally, there are also electrons that scattered in inelastic fashion by the specimen atoms, which means these electrons lost some energy during the scattering. The lost energy is a characteristic of the specimen element. By extracting these energy information, one can get the compositional information of the specimen.

In this thesis work, Hitachi-HD2300A is used to perform TEM analysis, and JEOL, JEM-2010 was used to perform HRTEM and SAED pattern analysis (Figure 2.15).

2.4.4. X-Ray Photoelectron Spectroscopy (XPS)

X-ray photoelectron spectroscopy is a spectroscopic method used to determine the elemental composition of the surface (1–10 nm) of the sample studied as well as their electronic and chemical state. The basic principle of XPS relies on the photoelectric effect, when a solid material is exposed by photons (in XPS it is monochromatic X-rays) with sufficient energy under high vacuum condition, the surface of the material emits electrons (in XPS these are core electron of atom) having a certain amount of kinetic energy (Figure 2.16), which can be relate to their binding energy with the following equation:

$$K.E. = E - (B.E. + \Phi) \quad (2.2)$$

where K.E. is the measured kinetic energy of the emitted electron/photoelectron, Φ is the work function of the spectrometer, E is the incident photon energy, and B.E. is the binding energy of the electron before ionization.

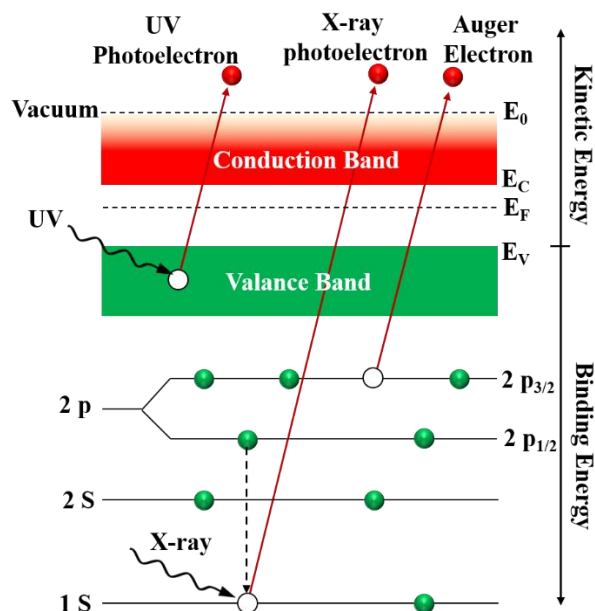


Figure 2.16. Schematic of photoelectric effect.

From the above equation, one can determine the binding energy (B.E.), since other values are known. On the other hand, every element has a specific binding energy group. Thus, by analyzing these binding

energies, one can get the information of each element present on the surface.

A monochromatic X-ray source, an electron analyzer, and a high vacuum chamber are the main components of the XPS technology.

Figure 2.17 shows the schematic of the principal operation of the XPS.

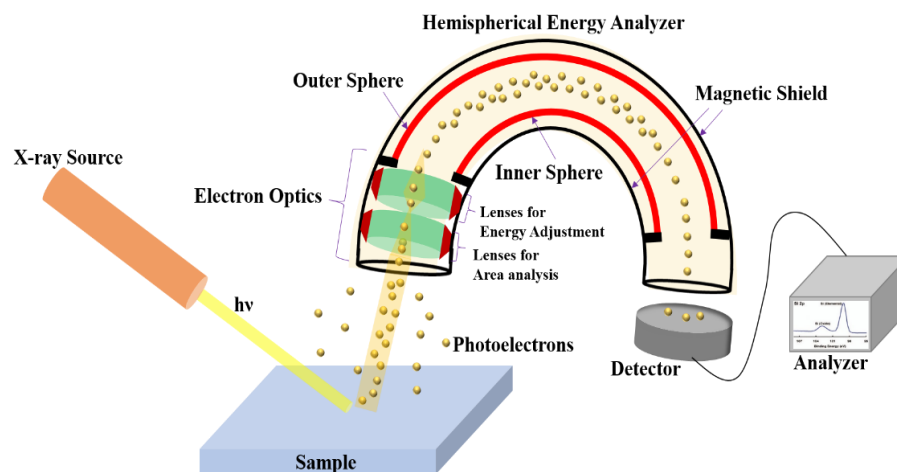


Figure 2.17. Schematic of working principle of XPS.

Some major steps of operation of the XPS technique are described below:

1. X-rays are produced when with high energy electrons collide with the metal, next, these X-rays are monochromated through optic to produce photons with the same wavelength or uniform energy. Generally, Mg $K\alpha$: $h\nu = 1253.6$ eV or Al $K\alpha$: $h\nu = 1486.6$ eV is used in XPS as a monochromatic X-ray source.
2. When exposed to monochromatic X-rays, the core electrons are released from a sample surface. Only those core electrons will emit whose binding energy is less than the incident photon energy.
3. The hemispherical energy analyzer has the outer sphere having positive bias and inner sphere having negative bias they are also guided by two magnetic shields. It passes only photoelectrons having certain energy.
4. The photoelectrons enter the hemispherical energy analyzer with the help of lenses. These lenses also use a voltage to control the

velocity of the photoelectrons. So it can be transported to the detector via a hemispheric energy analyzer.

5. The detector detects the number of electrons that crossed the hemispherical energy analyzer and their corresponding energies to produce a spectrum.

In this thesis work, the Thermo Scientific K-Alpha instrument is used to carry out the XPS study of the samples. Figure 2.18 shows the image of the Thermo Scientific K-Alpha instrument.



Figure 2.18. Image of the XPS system used in the present thesis work.

<https://www.thermofisher.com/order/catalog/product/IQLAADGAAFFACVMAHV#/IQLAADGAAFFACVMAHV>

2.4.5. Thermogravimetric Analysis (TGA)

Thermogravimetric analysis is a method used to calculate a material's weight change due to temperature variations as the material is heated under a controlled temperature system. Basic components of a thermogravimetric analyzer are high precision mass balance and high-temperature furnace. In TGA, the material is put in a crucible in a small quantity (10-50 mg) and the crucible is mounted in the high-precision mass balancing furnace. A desired gas (generally, air/O₂) is then flown through the furnace and balance at a constant flow rate.

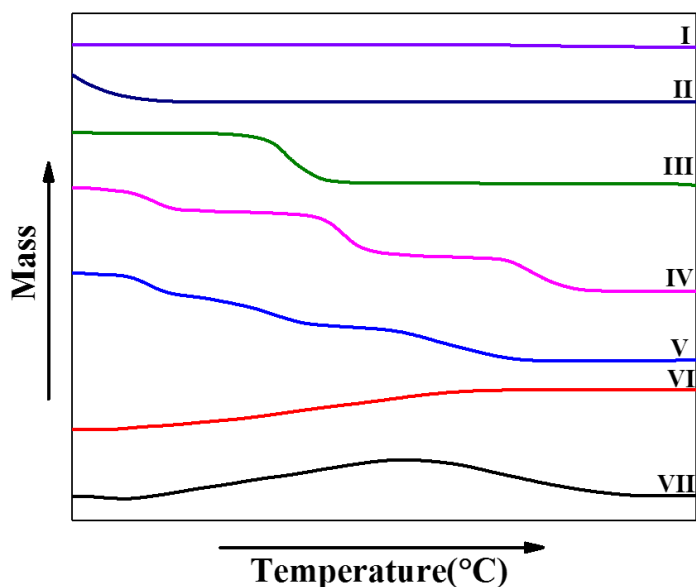


Figure 2.19. Different types of TGA plot.

Next, the furnace is heated to a certain temperature (up to 800-1000 °C) at a fixed rate under a controlled program. During this process, the system produces a quantitative plot of substance mass changes versus temperature. This plot provides the information of (a) thermal stability, (b) oxidative stability, (c) composition of the multi component system, (d) decomposition kinetics, and (e) moisture and volatile content of the substance. In this plot, one may observe the substance weight loss or gain or combination of both as the temperature increases. Weight loss is due to decomposition, evaporation, reduction, and desorption of the substance. Weight gain is due to oxidation and adsorption or absorption. Depending on the weight loss or gain one may observe seven types of plots as shown in Figure 2.19. In Figure 2.19, Type I plot represents no decomposition of the sample throughout the entire range of temperature. Type II represents mass loss is due to drying or desorption. Type III is for single stage decomposition. Type IV is a characteristic of multistage decomposition. Type V is similar to Type IV but due to a fast heating rate or no mediators. Type VI occurs when the mass of the sample increases when sample undergoes atmospheric reactions like oxidation. Type VII is similar to Type VI, but the sample starts decomposing at high temperatures.

Mettler Toledo Thermal Analyzer is used in this thesis work to test the TGA of the hybrid materials. The image of the Mettler Toledo Thermal Analyzer instrument used in this thesis work is shown in Figure 2.20.



Figure 2.20. Image of the Mettler Toledo Thermal Analyzer used in this thesis work.

2.4.6. Brunauer-Emmett-Teller (BET) Surface Area Analysis

Surface area analysis by Brunauer-Emmett-Teller (BET) is a method for evaluating the surface area of solid materials. The physical adsorption of inert gas to the surface of the solid is used here to measure the precise surface area of the material. The amount of gas adsorbed depends on the surface area, temperature, gas pressure, and type of gas-solid interaction. A relative pressure P/P_0 measures the amount of Gas adsorbed by the solid surface, where, P_0 is the vapor pressure of the pure solid material that adsorbs gas at the same temperature and P is the partial pressure of the vapor/adsorbed gas. When the $P/P_0 < 0.01$, it is considered that physical adsorption is negligible, when $P/P_0 \sim 0.1$, it corresponds to monolayer adsorption, as physical adsorption increases relative pressure increases and reaches the maximum when $P/P_0 = 1$, beyond this point no adsorption take place. Typically 200-300 mg sample powder is required to carry out the BET analysis. In BET analysis, nitrogen gas is used due to its inert nature and abundance availability with high purity.

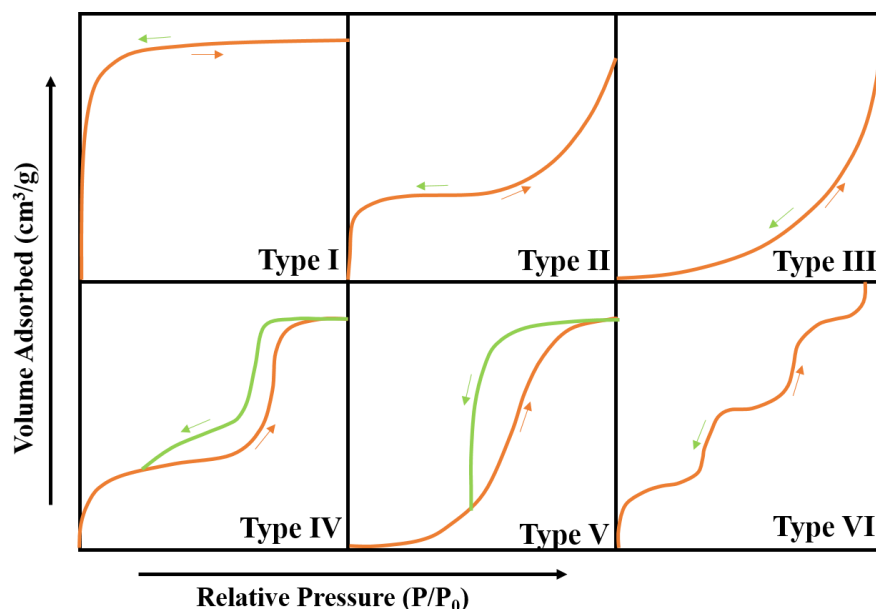


Figure 2.21. Various type of adsorption isotherms as classified by IUPAC [9].

The interaction of N₂ gas with a solid surface is very weak at room or high temperatures. The solid surface is normally cooled with liquid N₂ to calculate the amount of adsorption. A partial vacuum is created to achieve relative pressure less than the atmospheric pressure. Some N₂ gas is then gradually released into the sample cell, and pressure variation due to the adsorption is tracked by a high accuracy pressure gauge. When adsorption layers are formed, no more adsorption occurs, and then sample from the N₂ atmosphere is taken out and heated to extract the adsorbed N₂ and measured. Measured data is then plotted as BET isotherm that displays the adsorbed gas quantity as a function of P/P₀. Figure 2.21 displays existing various types of isotherms, depending upon the type of adsorbent (solid surface). Type I isotherm is a characteristic of microporous (diameter ≤ 2) solids. The type II and type III isotherm are for macroporous solids (diameter ≥ 50), with strong and poor gas-solid interactions, respectively. Type IV isotherm for mesoporous (diameter ≤ 50 nm) solids having a hysteresis behavior. Type V isotherm is of a porous solid having weak gas-solid interactions. Type VI isotherm represents step-wise multilayer adsorption of a non-porous solids.

In this thesis work, Autosorb iQ2 system is used to measure the BET surface area of the grown materials. The actual image of the Autosorb iQ2 system used in this thesis work is shown in Figure 2.22.



Figure 2.22. Image of the Autosorb iQ2, used in the present thesis work for BET surface area analysis.

2.5. Gas/VOC Sensing Measurement system

In this regard, we have approached the development of a dynamic flow-through gas/VOC sensing measurement system. The dynamic flow-through measurement method is superior over the static measurement method in terms of achieving low gas concentration (even ppb level) and flexibility of use. Also, in dynamic flow-through method, there is no need for expensive vacuum pump to clean the chamber, one can flow the synthetic air through the chamber to clean the chamber instantly.

2.5.1. VOC sensing measurement system

The schematic of the VOC sensing measurement system is shown in Figure 2.23, which consists of a custom made stainless steel based cylindrical sensing chamber (volume = 500 cm³ and 5 cm in diameter) with a substrate holder affixed to a heater assembly. The temperature of the heater is precisely controlled by a PID temperature controller (with an accuracy of ± 1 °C). To achieve the desired amount of concentrations of vapor during sensor study, synthetic air is used as a carrier gas. A controlled amount of synthetic air is flown through a bubbler containing

VOC in liquid form. The flow rate is controlled by a mass flow controller, MFC (model: Alicat®, MC 1slpm, USA) and the saturated vapor is carried to a mixing chamber where the desired amount of diluents (synthetic air) is also carried through another MFC and mixed with saturated VOC vapors to achieve desired concentration (in ppm) level of VOC. This mixture of VOC and diluent are then carried to the sensing chamber. The sensor resistance is measured using Keithley-2612A sourcemeter at certain (1-3 V) direct-current (DC) voltage, which is interfaced with a computer. The desired concentration (ppm) of the test VOC vapor is calculated using the following formula [10]:

$$C \text{ (ppm)} = \frac{\alpha\phi_c}{\phi_d + (1+\alpha)\phi_c} \times 10^6 \quad (2.3)$$

where, C is the vapor concentration of VOC diluted in synthetic air, ϕ_c is the carrier gas flow rate and ϕ_d is the dilution gas flow rate, α is the ratio of saturated vapor pressure at a particular temperature and input pressure (atmospheric pressure) in the VOC container. Before each sensing test, the sensor is heated to a set temperature and kept there for 4-5 min in 100 sccm synthetic air flow, to remove previously tested gas/VOC present in the device and in the chamber as well, after which a stable R_a is measured. The test gas/VOC is then carried out into the chamber to measure R_g until a saturated R_g is observed. The chamber is then exposed to synthetic air again until its resistance regain its initial value as seen in the air.

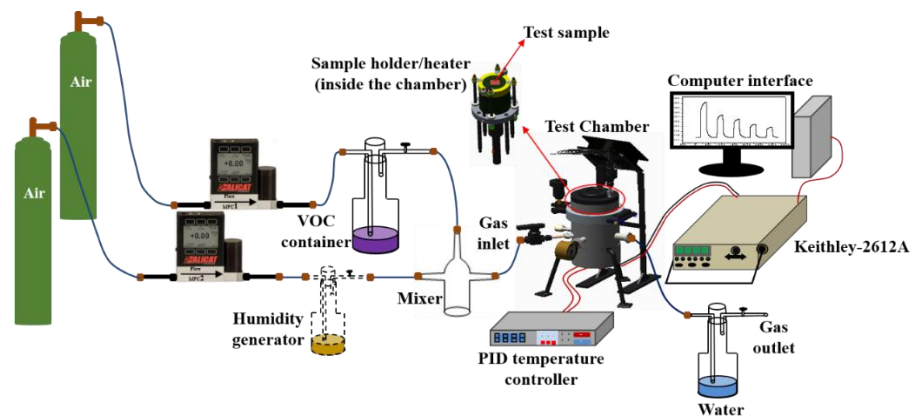


Figure 2.23. Schematic of the VOC sensing setup.

To achieve the desired relative humidity in the sensing chamber, one bubbler is placed in series with the air flow MFC, which contain an appropriate saturated aqueous solution of different salts: $\text{CH}_3\text{CO}_2\text{K}$, K_2CO_3 , KI , and KCl to yield approximate 23%, 42%, 65%, and 85% relative humidity (RH) [11].

2.5.2 Gas sensing measurement system

The gas sensing system is identical to that of the VOC sensing system, except that a different test gas cylinder with a specific concentration of the test gas is used for sensing. The schematic of the gas sensing setup is shown in Figure 2.24. The desired concentration of the test gas delivered to the chamber is calculated using the following formula [12]:

$$C \text{ (ppm)} = \frac{\phi_c}{\phi_c + \phi_d} \times \text{test gas concentration in cylinder (ppm)} \quad (2.4)$$

Where, ϕ_c is the carrier gas/test gas flow rate, ϕ_d is the dilution gas/air flow rate.

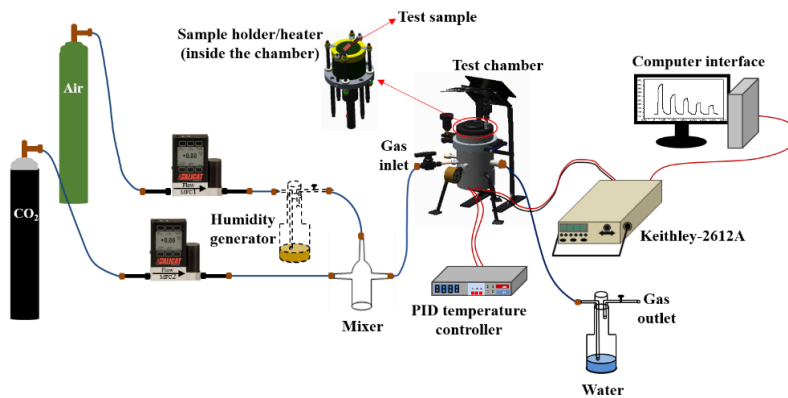


Figure 2.24. Schematic of the gas sensing setup.

The image of the gas/VOC detection system developed in this thesis work is shown in Figure 2.25.

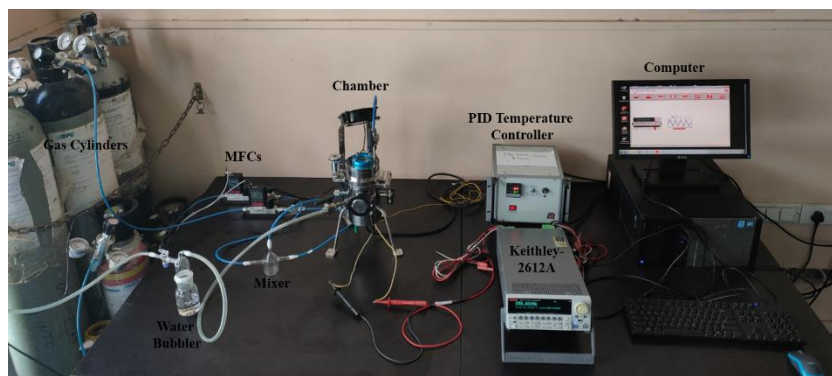


Figure 2.25. Image of the gas/VOC sensing setup developed in this thesis work.

2.6. References

- [1] J. M. Marshall, N. Kirov, A. Vavrek, and J. M. Maud, “Future Directions in Thin Film Science and Technology,” in *Proceedings of the Ninth International School on Condensed Matter Physics*, 1996, p. 616.
- [2] L. Eral, “Hydrothermal synthesis and characterization of transition metal (Mn and V) oxides containing phosphates,” İzmir Institute of Technology, 2006.
- [3] H. Hayashi and Y. Hakuta, “Hydrothermal Synthesis of metal oxide nanoparticles in supercritical water,” *Materials (Basel)*, vol. 3, no. 7, pp. 3794–3817, Jun. 2010.
- [4] R. Xu and Y. Xu, *Modern inorganic synthetic chemistry*, Second. Changchun: Elsevier, 2017.
- [5] K. Byrappa and M. Yoshimura, *Handbook of Hydrothermal Technology*, Second. Waltham, MA: William Andrew, 2013.
- [6] S. Ulrich and N. Hüsing, *Synthesis of Inorganic Materials*, Fourth. Weinheim, Germany: Wiley-VCH, 2019.
- [7] B. B. He, *Two-dimensional X-ray Diffraction*, Second Edi. New Jersey: John Wiley & Sons, Ltd, 2009.

- [8] J. I. Goldstein, D. E. Newbury, P. Echlin, D. C. Joy, C. Fiori, and E. Lifshin, *Scanning Electron Microscopy and X-Ray Microanalysis*. Boston, MA: Springer US, 1981.
- [9] S. Brunauer, P. H. Emmett, and E. Teller, “Adsorption of Gases in Multimolecular Layers,” *J. Am. Chem. Soc.*, vol. 60, no. 2, pp. 309–319, Feb. 1938.
- [10] C. Sapsanis *et al.*, “Insights on Capacitive Interdigitated Electrodes Coated with MOF Thin Films: Humidity and VOCs Sensing as a Case Study,” *Sensors*, vol. 15, no. 8, pp. 18153–18166, Jul. 2015.
- [11] L. Greenspan, “Humidity Fixed Points of Binary Saturated Aqueous Solutions,” *J. Res. Natl. Bur. Stand. A. Phys. Chem.*, vol. 81A, no. 1, pp. 89–96, Dec. 1977.
- [12] Y.-C. Chen, Y.-R. Shen, and C.-L. Hsiao, “A carbon monoxide interdigitated-capacitor gas sensor based upon a n-type Zn_2SnO_4 thin film,” *J. Mater. Sci. Mater. Electron.*, vol. 29, no. 2, pp. 1658–1663, Jan. 2018.

Chapter 3

Synthesis of NBA-ZnO Nanohybrids for CO₂ Gas Detection

3.1. Introduction

Carbon dioxide (CO₂), is the primary greenhouse gas responsible for global warming and climate change. Hence, for the last few decades, researchers from across the world are involved in developing CO₂ sensors and absorbers. Among various type of CO₂ sensors, the resistive types based on single, doped or composite MOX (e.g., SnO₂ [1], BaCeO₃ [2], Ba-SmCoO₃ [3], La-ZnO [4], Ca/Al-ZnO [5], SnO₂-La₂O₃ [6], [7], CuO-SnO₂ [8], CuO-BaTiO₃ [9], [10], and Zeolite-Metglas [11]) have significant advantages, such as small size, low cost, reliability and the potential to integrate in sensor arrays. However, all these MOX based CO₂ sensors have two inherent drawbacks: (1) lack of selectivity and (2) requirement of high operating temperature for sensing operation [12]. Nevertheless, organic-inorganic hybrid type sensing materials have recently been reported to have potential to overcome such demerits by offering advantages of their individual constituents. Inorganic part, i.e., metal oxides are highly stable both chemically and thermally, and easy to fabricate, which allows them to operate under diverse operating conditions [13], [14]. On the other hand, organic materials promise a better chemical specificity, as they can be characterized by a synthetic versatility and reactivity to modulate the molecular structure for enhancing the selectivity towards a particular gas/VOC. Moreover, the properties of the hybrid material not only just result from the addition of the individual contributions of their components but also from the strong synergy created by the presence of a large number of hybrid interfaces

[15]–[17]. The nature of the organic-inorganic interface (i.e., interaction type, linkability) plays a significant role in modulating a number of functional properties (electrical, optical, catalysis, mechanical) of the nanomaterial [18], [19]. Also, organic sensing material such as PANI, polypyrrole, CNTs and graphene etc. can show room temperature or low-temperature sensing [20]–[24], which is a desirable prospect for low power consumption point of view. Further, recent trends for developing smart wearable, handheld and portable sensors require a lighter weight, flexible and stretchable substrates. Interestingly, the last decade has seen a tremendous increase in research towards developing gas/VOC sensors based on organic-inorganic hybrid material on flexible substrates. For example, Yaqoob *et al.* [25] have reported WO₃ nanoparticles decorated with MWCNTs and RGO hybrids on polyimide/polyester (PI/PET) substrates which show high performance towards NO₂ gas. Yi *et al.* [26] have reported graphene-ZnO nanorod hybrid on the flexible substrate for low ppm ethanol sensor. Li *et al.* [27] have studied the room temperature ammonia sensing properties of the PANI@flower-like WO₃ nanocomposite on PET flexible substrate.

Organic monomeric amines such as tetraethylenepentamine, N,N'-bis(2-hydroxyethyl)ethylenediamine [28], tetrakis(hydroxyethyl)ethylenediamine [29] and polymeric imines such as poly(propylenimine) [30], polyethylenimine [31]–[33], polystyrene-bound ethylene diamine [34], aminoalkyl poly(dimethylsiloxane) [30], [34], and alkylamine functionalized polysiloxanes [35]–[37] etc. containing primary, secondary or tertiary amines groups are known to be somewhat sensitive to CO₂ gas [38]. The hard acid CO₂ can efficiently bind with hard base amino groups to form carbamates or bicarbonates (in the presence of humidity) [39], as a consequence of which, the response in terms of resistance or impedance increases. Interestingly, this increase in resistance or impedance is reversible. Ko *et al.* [38] have shown that among the aforementioned types of amine group, the primary amine groups are highly efficient in adsorbing the CO₂ gas. However, there are no reports on organic amine-MOX nanohybrids for CO₂ sensing application. Primary amine based organic amine-MOX nanohybrids

might show enhanced CO₂ sensing properties due to the presence of superior carrier transport path and layer by layer assembly in the structure of nanohybrids.

This chapter describes of a novel naphthalene based π -conjugated amine (NBA)-zinc oxide (ZnO) nanohybrids, synthesized *via in-situ* hydrothermal process on a polydimethylsiloxane (PDMS) flexible substrate, which exhibited excellent selectivity as well as good sensitivity to CO₂ gas at room temperature.

3.2. Experimental

3.2.1. Substrate Preparation

The NBA-ZnO nanohybrids are grown *via in-situ* hydrothermal process on top of IDEs patterned ZnO seed layer coated flexible substrate. The schematic of the device is shown in Figure 3.1. Transparent PDMS as a mixture of two part hardener (Sylgard 184B (curer)) and pre-polymer (Sylgard 184A (base)) in the ratio of 1:10, is spin coated on to an Al coated 3" Si wafer to obtain 250 μm thick elastomer.

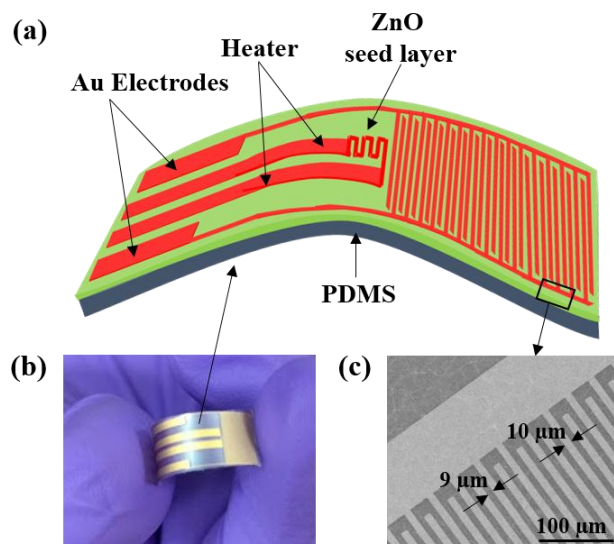


Figure 3.1. (a) Device schematic of the flexible sensor. (b) Flexibility of as-fabricated sensor. (c) Scanning electron micrograph of interdigitated electrodes (IDEs) showing inter-electrode dimensions.

Next, the deposition of 325 nm ZnO thin film is done on top of plasma cleaned elastomer by the reactive magnetron sputtering technique (Kurt J. Lesker PVD75 Pro-line) at 250 $^{\circ}\text{C}$, 100 W, and 40% oxygen in argon

for 30 min. This 325 nm ZnO thin film layer provides a better adhesion as well as a seed layer for the growth of NBA-ZnO nanohybrids. The photolithography process is done on top of seed layer by standard photolithographic steps using 5214 E image reversal photoresist to pattern the 10 μm width and 9 μm spacing IDEs along with the heating elements as shown in Figure 3.1(a)-(c). Lift-off is performed to realize the Cr/Au (20/200 nm) IDEs. Cr/Au (20/200 nm) electrode are deposited by electron beam evaporation technique (1.5×10^{-7} Torr) at a deposition rate of 0.3 $\text{\AA}/\text{s}$ at room temperature. Finally, IDEs/ZnO/PDMS is peeled off from the Al/Si and sectioned for the hydrothermal growth and further characterization.

3.2.2. Synthesis of Naphthalene Based Amine (NBA)

Desire naphthalene based amine (NBA, compound 1) is synthesized by several intermediate steps. In first step, 2-(6-bromo-1,3-dioxo-1H,3H-benzo[de]isoquinolin-2-yl)-succinic acid dimethyl ester (compound 2) is synthesized by nucleophilic substitution reaction with 4-bromo-1,8-naphthalic anhydride and dimethyl ester of L-aspartic acid. The intermediates, 4-trimethylsilanylethynyl-phenylamine (compound 3) and 4-ethynyl-phenylamine (compound 4) are synthesized according to literature reported procedures [40]. 2-[6-(4-amino-phenylethynyl)-1,3-dioxo-1H,3H-benzo[de]isoquinolin-2-yl]-succinic acid dimethyl ester (compound 5) is synthesized by Sonogashira coupling reaction between compound 4 and compound 2. Finally, desired product 2-[6-(4-amino-phenylethynyl)-1,3-dioxo-1H,3H-benzo[de]isoquinolin-2-yl]-succinic acid (compound 1) is obtained by base catalysed hydrolysis of compound 5.

The reaction scheme (Figure 3.2) and detailed synthetic process of the intermediates are as follows.

Synthesis of 2-(6-bromo-1,3-dioxo-1H,3H-benzo[de]isoquinolin-2-yl)-succinic acid dimethyl ester (compound 2):

To a 250 mL round bottom flask (1.118 g, 4.035 mmol) of 4-bromo-1,8-naphthalic anhydride is added and dissolved with 30 mL of ethanol. After that, (0.780 g, 4.845 mmol) of dimethyl ester of L-aspartic acid is

added into the reaction mixture and stirred with a magnetic stirrer. The flask is fitted with a condenser and refluxed at 80 °C for overnight. The reaction is monitored by TLC. After completion of reaction; the reaction mixture is extracted by ethyl acetate and washed with 1 M HCl (30 mL x 3). The organic layer is collected; dried over dry Na₂SO₄ and collected as white solid. Yield = 1.45 g, (3.46 mmol, 86%). ¹H NMR (400 MHz, CDCl₃): δ = 8.68 (d, 1H, *J* = 7.28 Hz), 8.62 (d, 1H, *J* = 8.52 Hz), 8.44 (d, 1H, *J* = 7.76 Hz), 8.07 (d, 1H, *J* = 7.80 Hz), 7.87 (t, 1H, *J* = 7.60 Hz), 6.24 (t, 1H, *J* = 6.76 Hz), 3.73 (s, 3H), 3.67 (s, 3H), 3.56-3.50 (m, 1H), 2.99-2.95 (m, 1H) ppm. ESI-MS *m/z* calculated for C₁₈H₁₄BrNO₆: 441.9902 (M+Na)⁺; Found: 441.9870 (M+Na)⁺.

Synthesis of 2-[6-(4-amino-phenylethynyl)-1,3-dioxo-1H,3H-benzo[de]isoquinolin-2-yl]-succinic acid dimethyl ester (compound 5):

251.4 mg (0.60 mmol) of compound **2** is dissolved in 5 mL THF and 5 mL of Et₃N in a 100 mL, round bottom flask. The flask is capped by septum and argon gas is purged into the solution for 10 min by syringe. After that, CuI (5 mol% of compound **4**) and Pd(PPh₃)₂Cl₂ (5 mol% of compound **4**) are added followed by addition of 77.25 mg (0.66 mmol) of compound **4**. The reaction mixture is refluxed for overnight under argon atmosphere at 70 °C. The reaction is monitored by TLC and after completion; reaction mixture is extracted with ethyl acetate and washed with brine, dried over dry Na₂SO₄. Ethyl acetate is evaporated to get solid crude, which is purified by column chromatography (100 mesh silica gel, 30% ethyl acetate in hexane as eluent) to yield compound **5**. Yield = 213.5 mg (0.46 mmol, 78%). ¹H NMR (400 MHz, CDCl₃): δ = 8.78 (d, 1H, *J* = 8.28 Hz), 8.64 (d, 1H, *J* = 7.28 Hz), 8.55 (d, 1H, *J* = 7.52 Hz), 7.90 (d, 1H, *J* = 8.0 Hz), 7.83 (t, 1H), 7.48 (d, 2H, *J* = 7.28 Hz), 6.70 (d, 2H, *J* = 7.28), 6.27 (t, 1H, *J* = 6.52), 4.01 (s, 2H), 3.74 (s, 3H), 3.68 (s, 3H), 3.56 (dd, 1H, *J* = 6.56 Hz, 6.76 Hz), 2.96 (dd, 1H, *J* = 6.52 Hz, 6.56 Hz). HRMS (ESI) *m/z* calculated for C₂₆H₂₀N₂O₆: 479.1214 (M+Na)⁺, Found: 479.1215 (M+Na)⁺.

Synthesis of 2-[6-(4-amino-phenylethynyl)-1,3-dioxo-1H,3H-benzo[de]isoquinolin-2-yl]-succinic acid (compound 1, NBA):

200 mg (0.44 mmol) of compound **5** is dissolved in 1:1 methanol-THF. After that, 2 mL of 1 (N) aqueous NaOH solution is added into the reaction mixture. The reaction mixture is stirred for overnight. After completion of reaction, reaction mixture is dissolved in 50 mL water and washed with ether (1 x 50 mL). Aqueous part is collected and neutralized by 1 (N) HCl. After getting slightly acidic pH, the desired product is extracted by ethyl acetate (3 x 50 mL) from red turbid aqueous part. Ethyl acetate is dried over dry Na₂SO₄ and evaporated to get desired product as red solid. Yield = 179.3 mg (0.42 mmol, 95%). ¹H NMR (400 MHz, (CD₃)₂SO): δ = 8.80 (d, 1H, *J* = 9.92 Hz), 8.58 (d, 1H, *J* = 7.04 Hz), 8.45 (d, 1H, *J* = 7.04 Hz) 8.00-7.95 (m, 2H), 7.47 (d, 2H, *J* = 7.52 Hz), 6.64 (d, 2H, *J* = 7.56 Hz), 5.96 (m, 1H), 5.88 (s, 2H), 2.77-2.71 (m, 1H), 1.22-1.15 (m, 1H) ppm. HRMS (ESI) *m/z* calculated for C₂₄H₁₆N₂O₆: 451.0901 (M+Na)⁺, Found: 451.0902 (M+Na)⁺.

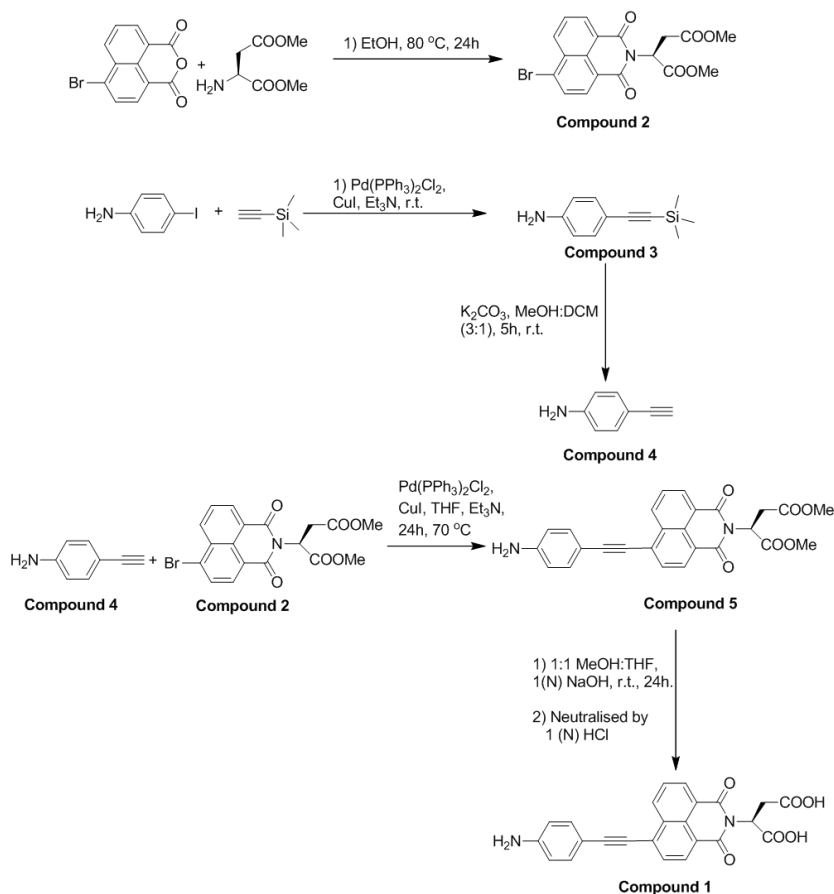


Figure 3.2. Synthesis scheme of NBA (compound 1).

3.2.3. *In-Situ* growth of NBA-ZnO Nanohybrids and ZnO Nanorods on Prepared Flexible Substrate

In a typical experimental procedure, equimolar (25 mM) $\text{Zn}(\text{NO}_3)_2 \cdot 6\text{H}_2\text{O}$ and hexamethylenetetramine (HMTA) are added in a 20 mL of deionized water under constant stirring for 15 min at 65 °C, then 10 mg NBA (1.2 mM) is added slowly in the solution under vigorous stirring until the solution becomes uniform reddish color. After that, the solution is transferred into a Teflon lined autoclave where the flexible substrate is placed vertically in the solution and kept at 95 °C for 1 h, 2 h, and 3 h reaction time. After the hydrothermal reaction, substrate is removed and rinsed with deionized water and ethanol several times, and then dried at 70 °C overnight. Finally, the substrate is annealed at 120 °C for 6 h.

ZnO nanorods (NRs) are grown in similar process to that of NBA-ZnO nanohybrids only NBA is not added in the solution for hydrothermal reaction process.

3.3. Results and Discussion

3.3.1. Structural and Morphological Study

3.3.1.1. Field Emission Scanning Electron Microscopy

The FESEM image of as-synthesized NBA nanoparticles (NPs) is shown in Figure 3.3. They are seen to have an average diameter of 25-100 nm.

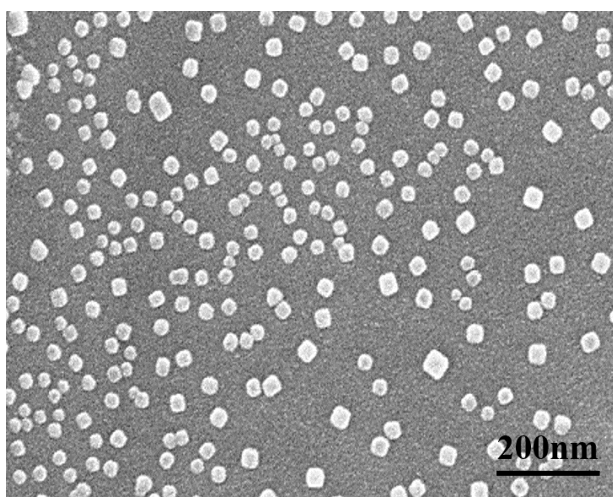


Figure 3.3. FESEM image of NBA nanoparticles.

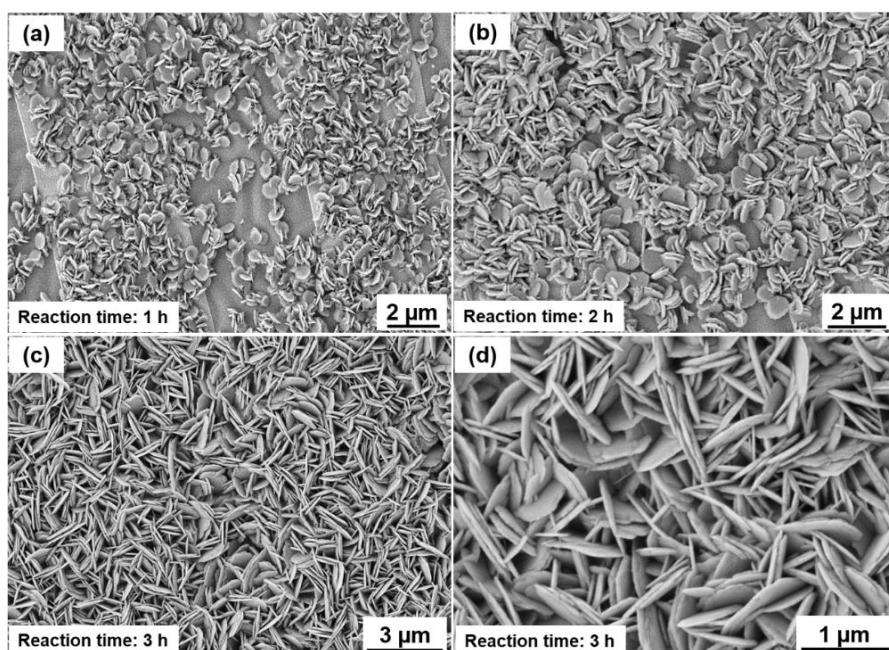


Figure 3.4. FESEM images of NBA-ZnO nanohybrids after (a) 1 h, (b) 2 h, and (c) 3 h reaction time. (d) Higher magnification micrograph of 3 h reaction time nanohybrids.

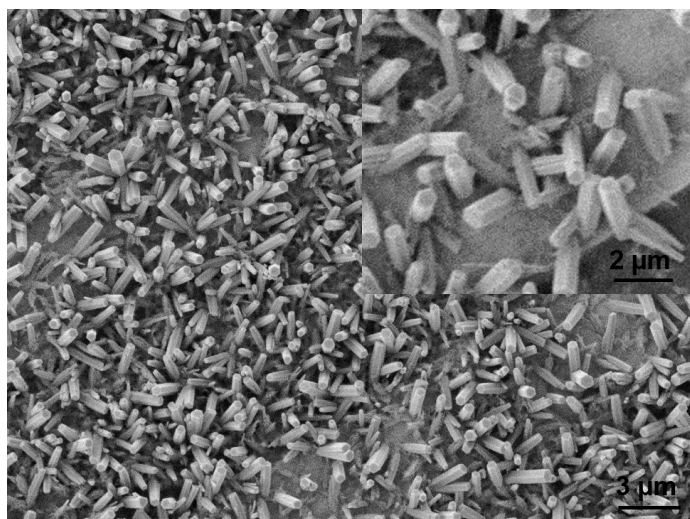


Figure 3.5. FESEM image of ZnO nanorods grown on IDEs patterned seed layer coated flexible substrate (reaction time 3 h). Inset shows ZnO nanorods at higher magnification.

Figure 3.4(a), (b), and (c) shows FESEM images of NBA-ZnO nanohybrids on top of flexible substrate with the reaction time of 1 h, 2 h, and 3 h, respectively. At the first hour of reaction time, the growth of

non-uniform distribution of hexagonal nanoplates are observed, the typical diameter of the nanoplates are 400-500 nm. Increasing reaction time to 2 h, nanoplates tend to aggregate together to form vertically aligned connected nanoplates. The typical diameter of these nanoplates are 700-800 nm. Increasing reaction time to 3 h leads to the formation of a highly dense, uniform distribution, vertically aligned, connected nanoplates. Here, the typical diameter of the nanoplates are 1-1.2 μm . Figure 3.5 shows the FESEM image of ZnO nanorods grown for 3 h reaction time on the flexible substrate. The typical length of the nanorods is 2-3 μm and nanorods are randomly distributed over the substrate.

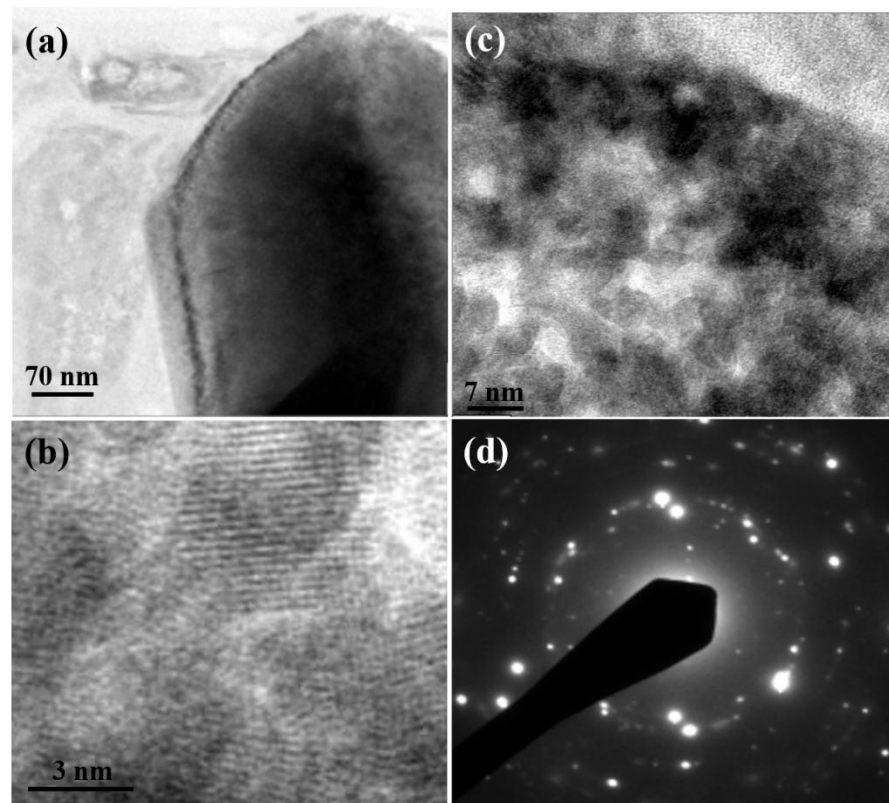


Figure 3.6. (a) Low magnification TEM image, (b) High magnification TEM image, (c) HRTEM image, and (d) SAED pattern of NBA-ZnO nanohybrid.

3.3.1.2. Transmission Electron Microscopy (TEM)

Figure 3.6(a) shows low magnification TEM image of the edge of a single nanostructure, confirming the hexagonal shape of the nanostructures. Figure 3.6(b) shows higher magnification TEM image

of the NBA-ZnO nanohybrid particles, confirming the formation of hybrid architecture. Figure 3.6(c) shows HRTEM image of the NBA-ZnO nanohybrid which confirms the presence of layer-by-layer assembly of naphthalene based π conjugated amine and ZnO in the nanohybrid architecture. Figure 3.6(d) shows SEAD pattern of the NBA-ZnO nanohybrid which confirms the polycrystalline nature of the hybrid.

3.3.1.3. X-Ray Diffraction

XRD is carried out to analyze the crystalline structures of NBA-ZnO nanohybrids, bare NBA nanoparticles (NPs), and bare ZnO nanorods (NRs). Figure 3.7 shows the XRD pattern of ZnO NRs [41], where, the diffraction peaks appearing at $2\theta = 31.69^\circ$, 34.49° , 36.31° , and 47.58° corresponds to a hexagonal ZnO (100), (002), (101), and (102) planes, respectively (JCPDS No.36-1451). A broad diffraction peak corresponding at around $2\theta = 15-37^\circ$ for pure NBA is observed, indicating the amorphous behavior of NBA prepared by chemical synthesis method.

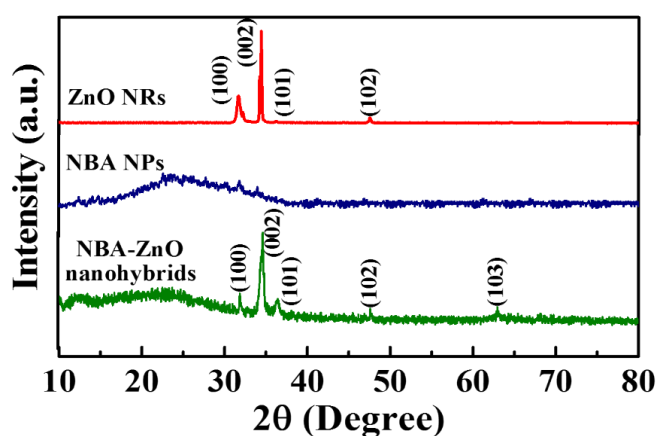


Figure 3.7. XRD pattern of ZnO nanorods, NBA nanoparticle, and NBA-ZnO nanohybrids sample.

It should be noted that a similar broad peak is observed in case of pure polypyrrole [42], however broadening range is more in case of pure NBA. It can be observed that the peak related to NBA ($15-37^\circ$) is not evident in the XRD pattern of NBA-ZnO nanohybrids, probably due to the presence of the high-intensity peak of the ZnO.

3.3.1.4. Energy Dispersive X-ray Spectroscopy

Figure 3.8 shows the EDX spectra of the NBA-ZnO nanohybrids, where strong signal corresponding to elemental zinc and oxygen represents the presence of inorganic ZnO, and strong signal corresponding to elemental nitrogen, carbon, and oxygen represents the presence of organic NBA in the NBA-ZnO nanohybrid.

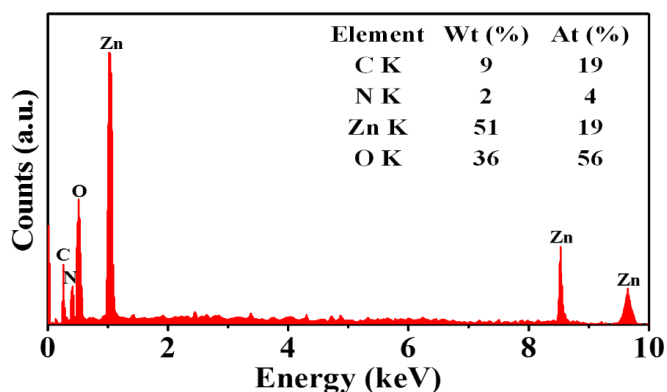


Figure 3.8. EDX pattern of NBA-ZnO nanohybrid.

3.3.1.5. Density Functional Theory Study of NBA NPs

DFT calculation is performed to determine the energy minimized geometry of NBA in the ground state. Theoretical calculation of the highest occupied molecular orbital (HOMO) and the lowest unoccupied

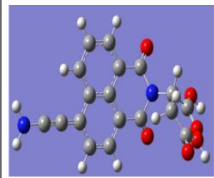
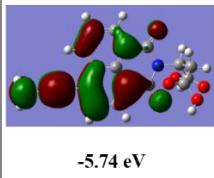
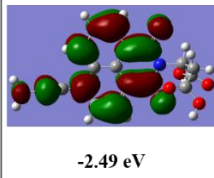
NBA	HOMO	LUMO	Calculated Energy band Gap (eV)
	 -5.74 eV	 -2.49 eV	-3.25 eV

Figure 3.9. DFT study of NBA NPs.

molecular orbital (LUMO) of synthesized NBA is calculated using the B3LYP/6-31G* basis set of Gaussian 09 program. The highest occupied molecular orbital (HOMO) and lowest unoccupied molecular orbital (LUMO) levels of NBA molecule are -5.74 eV and -2.49 eV, respectively. The calculated energy band gap of NBA is 3.25 eV (Figure 3.9).

3.3.2. Growth Mechanism

The advanced functional properties of the nanomaterial are dependent on their growth process and reaction parameter. During hydrothermal synthesis of NBA-ZnO nanohybrids, in the beginning, hexagonal zinc hydroxide nuclei forms from the reaction of reagents ($\text{Zn}(\text{NO}_3)_2 \cdot 6\text{H}_2\text{O}$ and HMTA) in the solution with the help of temperature treatment at 65 °C and constant stirring. After adding NBA in the solution, the carboxylic groups of NBA creates covalent bonds with zinc hydroxide to give structural stability to the nanohybrid architecture [43]–[45]. At the same time, the hexagonal zinc hydroxide nuclei get transformed into a nuclei of inorganic-hydroxide phases in the lamellar NBA-ZnO hybrid. Here, aromatic faces of NBA favour intermolecular π - π stacking interactions to construct supramolecular organic galleries [44], [46]–

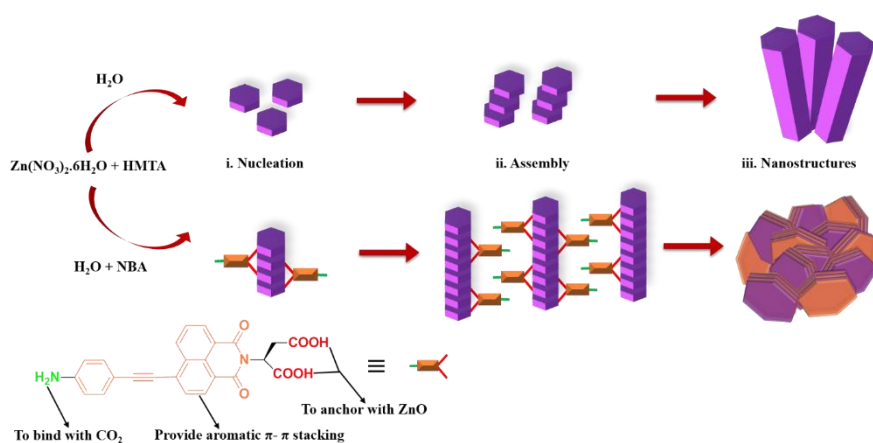


Figure 3.10. Growth schematic of NBA-ZnO nanohybrids.

[48]. After this, these hybrid nuclei connects through assembly process to form vertically aligned connected nanoplates. Finally, the inorganic-hydroxide phases in lamellar NBA-ZnO hybrid are converted into oxide phases upon annealing at 120 °C for 6 h. In the case of ZnO nanorods growth, only hexagonal zinc hydroxide nuclei connects through assembly process to form hexagonal zinc hydroxide nanorods, after which at the time of calcination, zinc hydroxides nanorods are transformed into zinc oxide nanorods. The schematic of the possible growth mechanism of ZnO nanorods and NBA-ZnO nanohybrids is shown in Figure 3.10.

3.3.3. CO₂ Sensing Properties of the NBA-ZnO Nanohybrids

To start with, flexible NBA-ZnO nanohybrids sensor is placed in the sensing chamber, and its sensing behavior towards different gases is investigated. Before each sensing test, the sensor is kept for 5-6 min in 200 sccm synthetic air flow, to remove previously tested gas present in the device and in the chamber as well, after which a stable R_a is measured. Sensor response is defined as $\text{response (\%)} = |R_g - R_a|/R_a \times 100$, where, R_g is the resistance of the hybrid sensor at a given time during exposure to target gas and R_a is the resistance value of the hybrid sensor in the air ambient. Mechanical flexibility and corresponding stable electrical properties of the *in-situ* deposited NBA-ZnO nanohybrids thin film on top of flexible substrates is very important for the determination of its response towards a given concentration of analyte gas. From Figure 3.11 it can be seen that the current-voltage characteristics of the NBA-ZnO nanohybrids sensor under flat (black) and bending condition with diameter of curvature of 20 mm (red) and 10 mm (blue) were nearly ohmic, in the voltage range of -10 V to +10 V. Clearly, the bending of the sensor has no significant change in the current-voltage characteristics.

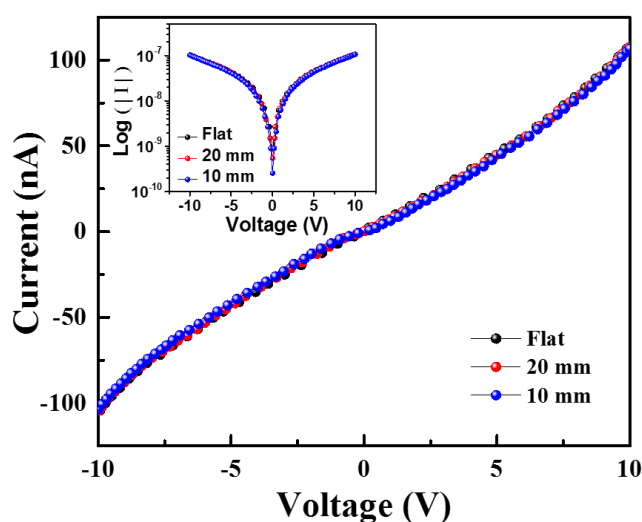


Figure 3.11. Current-voltage characteristics of NBA-ZnO nanohybrids under different bending diameter at room temperature. Inset shows current in log scale vs. voltage.

Thus, NBA-ZnO nanohybrids sensors are successfully fabricated on IDEs patterned seed layer coated flexible substrate with excellent mechanical reliability.

To verify, whether the prepared NBA-ZnO nanohybrids have any enhanced CO₂ sensing properties than the bare NBA NPs and the bare ZnO NRs, because of either synergetic or complementary effect between inorganic ZnO and organic NBA, the sensing properties of the NBA-ZnO nanohybrids, bare NBA NPs, and bare ZnO NRs for 2000 ppm CO₂ gas is tested. Figure 3.12(a) represents the responses of these three materials to 2000 ppm of CO₂ at room temperature. It is found that NBA NPs based sensor showed resistance increasing response to CO₂ but the response is low and sluggish. Whereas, ZnO NRs based sensor exhibited resistance decreasing response to CO₂ gas and the response is negligible. However, sensor based on NBA-ZnO nanohybrids shows resistance increasing, enhanced, fast, and stable response to CO₂ gas at room temperature. It should be noteworthy to mention that similar kind of resistance increasing response is observed in the case of polyethylenimine (PEI) based chemiresistor CO₂ sensor by Doan *et al.* [49], and polypyrrole@WO₃ hybrids for TEA sensor by Sun *et al.* [42], and organically hybridized SnO₂ for CO sensor by Matsubara *et al.* [50]. For further investigation, NBA-ZnO nanohybrids based flexible sensor is then exposed to various concentration of CO₂ gas (viz. 500 ppm, 1000 ppm, 2000 ppm, 5000 ppm, and 10000 ppm) and the corresponding response of the sensor is recorded. Figure 3.12(b) shows the time-dependent resistance increasing and decreasing characteristics of the NBA-ZnO nanohybrid sensor when the sensor is exposed to 500 to 10000 ppm CO₂ gas and air, respectively. The sensor response values to 500, 1000, 2000, 5000, and 10000 ppm CO₂ are 9.1, 14.2, 21.4, 30.3, and 36.6, respectively. Figure 3.12(c) shows the dynamic response/recovery characteristics of the NBA-ZnO nanohybrids-based sensor to different concentration (500-10000 ppm) of CO₂ at room temperature. Clearly, a proportional change in the gas response is observed which is nearly saturated at higher concentration of CO₂ gas,

as can be seen in Figure 3.12(d). The gas response is nearly exponential with CO₂ gas concentration which is exponentially fitted as $y = 4.48 + 32.39(1 - \exp(-0.00034x))$, where y is a gas response in percentage and x is carbon dioxide gas concentration in ppm.

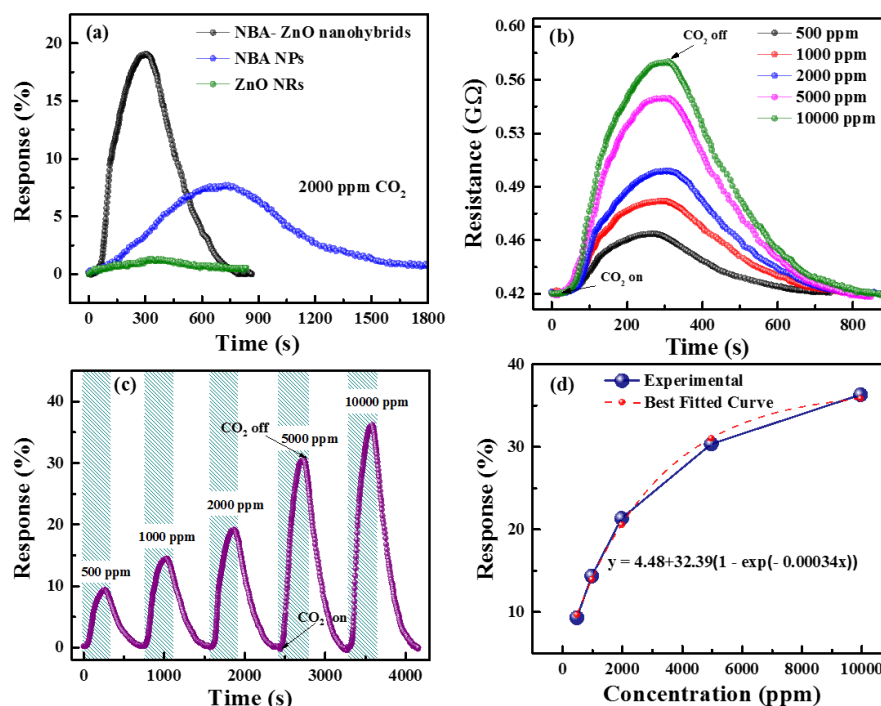


Figure 3.12. (a) Dynamic response of the three types of sensor to 2000 ppm CO₂. (b) Time-dependent response/recovery characteristics and (c) the dynamic response/recovery characteristics of the NBA-ZnO nanohybrids sensor tested under various concentrations of CO₂ gas. (d) Response of the NBA-ZnO nanohybrid sensor as a function of CO₂ gas concentration.

Figure 3.13(a) shows response and recovery characteristics of a single-cycle of the NBA-ZnO nanohybrid sensor to 5000 ppm of CO₂ gas. It is found that average response time and average recovery time of the sensor is ~206 s and ~354 s, respectively. The values of the response and recovery time of the NBA-ZnO nanohybrid sensor are better as compared to those reported in the published literature on CO₂ sensor (Table 3.1). The values of response and recovery time could be further improved by the incorporation of more amine functional group in a single monomer organic amine. To use the NBA-ZnO nanohybrids based

sensor as a flexible gas sensor, its gas sensing properties under two different bending conditions for continuous three cycles at 5000 ppm CO₂ are also studied. In this case, two different cylindrical rods with a diameter of 20 mm and 10 mm are used to attach the sensor for bending. After that, gas sensing measurements are carried out in the same way as aforementioned. It is found that under diameter 20 mm bending condition there is no significant change in the sensor response (0.8%). However, under diameter 10 mm bending condition there is a small change in the sensor response and it is about 3.53% decrease as compared to the value under normal/flat condition (Figure 3.13(b)). It has been observed that the response and recovery time does not get much affected by this bending process. To see the retention properties of the sensor, after it is reverted back to the normal/flat condition after bending, the sensor is then exposed again to 5000 ppm CO₂ in flat condition and the corresponding response is measured to be around 29.7%, nearly preserving the retention properties of the sensor. Durability is an important parameter for flexible sensor, to check this, the sensor is bent many times over 10 mm diameter, then the sensor is exposed to CO₂ gas to measure the gas response, and it is found that repetitive bending did not cause any significant decrease in gas response or any significant damage to the sensor. Humidity is an important parameter to consider especially when the gas sensing is performed at room temperature. The effect of humidity on the CO₂ sensing performance of the NBA-ZnO nanohybrid sensor is investigated systematically. The relative humidity of the open air is observed to be around 24% at room temperature. To measure the sensor response under different humid condition, it is kept in the different constant relative humidity conditions of 43%, 62%, and 85% RH within the chambers ambiance. Under these humidity conditions, the sensor is exposed to 5000 ppm of CO₂ gas at room temperature and the corresponding sensor response is measured. The sensor response to 23%, 43%, 62%, and 85% RH is 29.9%, 29.2%, 29.4%, and 29.2%, respectively (Figure 3.13(c)). The response changes are negligible with the increase in the relative humidity, which can be attributed to the hydrophobic nature of NBA (due to the presence of

hydrophobic phenyl and naphthalene rings). However, the response and recovery time of the sensor slightly increased as the relative humidity increased. To measure the selectivity among different other toxic gasses, the NBA-ZnO nanohybrids sensor is exposed to various test gases at room temperature. Figure 3.13(d) represents selectivity histogram of the NBA-ZnO nanohybrid sensor towards 5000 ppm test gases, including hydrogen sulfide, carbon monoxide, and ammonia. Expectedly, the sensor shows excellent selectivity ($\sim 91\%$) to CO_2 gas.

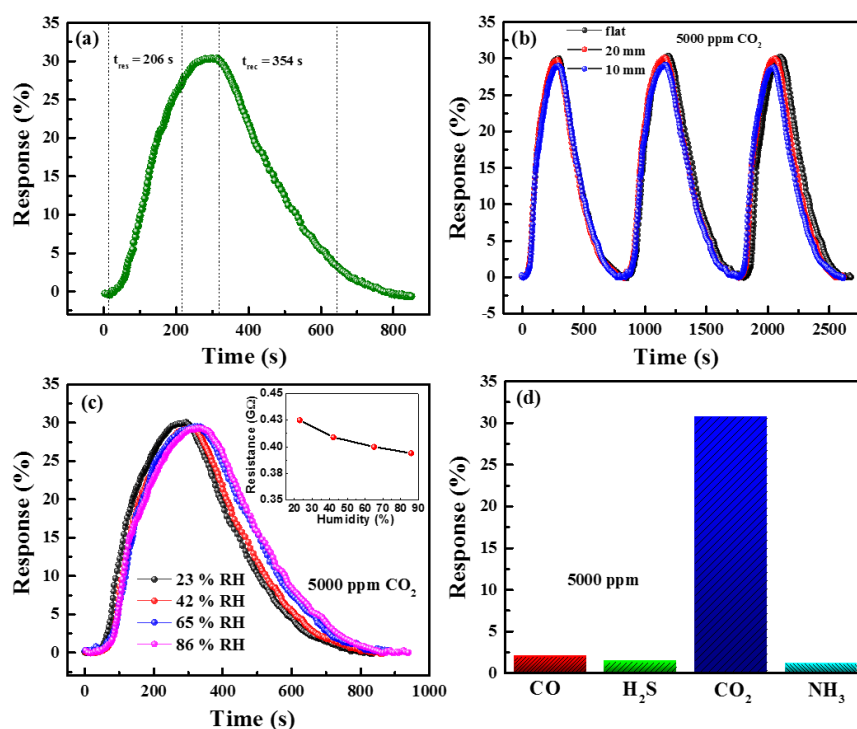


Figure 3.13. (a) Single cycle response of the NBA-ZnO nanohybrid sensor to 5000 ppm CO_2 gas. (b) Repeatability test under different bending diameters at 5000 ppm CO_2 gas. (c) Effect of humidity on the CO_2 sensing properties of the NBA-ZnO nanohybrids. Inset shows change in sensor resistance under different humidity condition. (d) Selectivity study against other gases.

3.3.4. CO_2 Sensing Mechanism

The excellent selectivity of the as-fabricated NBA-ZnO nanohybrid sensor to CO_2 gas can be explained by the following mechanism. The interaction between CO_2 and amine groups can happen by several different mechanisms. Among the three types of amine, primary amine

can directly react with the CO₂ to produce carbamates through an intermediate formation of zwitterionic. First time in 1968, Caplow explained the zwitterionic mechanism for the formation of carbamate from the interaction between the primary amine and CO₂ [51] and later it is summarized by several researchers. The reaction mechanism of CO₂ with primary amine for the formation of carbamates is depicted in Figure 3.14(a) [52]. Theoretically, two primary amines are required to capture

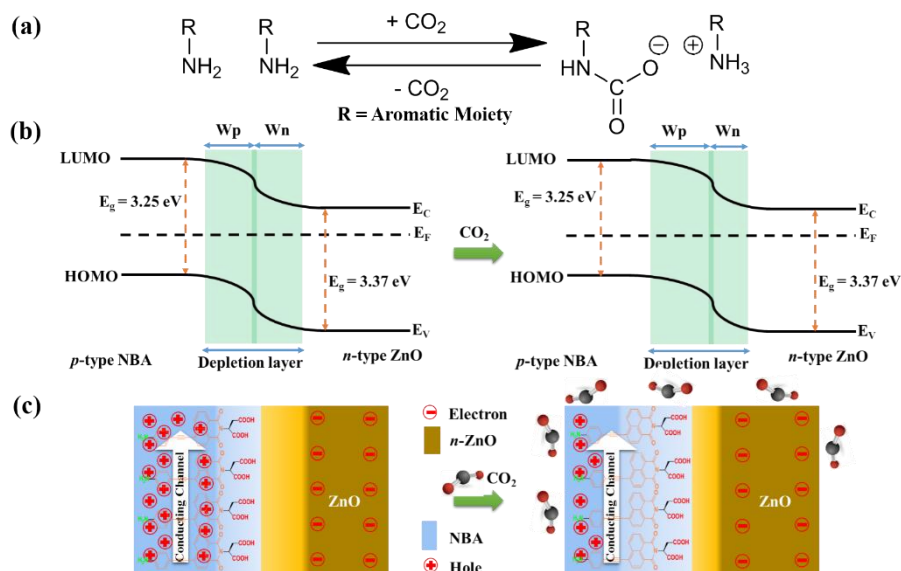


Figure 3.14. (a) CO₂ reaction mechanism with the primary amine of the nanohybrid. (b) Band formation between p-type NBA and n-type ZnO. (c) Schematic illustration of sensing mechanism of NBA-ZnO nanohybrid.

CO₂. At first, lone pair on the amine attaches on carbon from CO₂ to form the zwitterionic then another free amine deprotonates zwitterionic to form the carbamate. In this process, the number of free amines reduces and consequently proton hopping process is hampered along the organic layer, which surely reduces the mobility of the proton or increases the resistance along the organic layer [49], [53]. Additionally, the presence of layer-by-layer assembly of p-type NBA and n-type ZnO in NBA-ZnO nanohybrid might have a p-n heterojunction at the interface in between them, which may be the reason for obtaining a superior response in NBA-ZnO nanohybrids as compared to bare NBA. Due to a mismatch in Fermi level of n-type ZnO and p-type NBA, holes

will flow from NBA to ZnO and electron will flow from ZnO to NBA, until their Fermi energy levels are aligned. As a consequence, there will be a generation of the depletion layer at the interface [42], [54]. Previously calculated energy band gap for *p*-type NBA ~ 3.25 eV and considering the energy band gap for *n*-type ZnO ~ 3.37 eV [55], the band alignment between *p*-type NBA and *n*-type ZnO are depicted in Figure 3.14(b). When CO₂ gas is in the surroundings of the NBA-ZnO nanohybrid sensor, the gas molecules are adsorbed by the surface of the nanohybrid. As a result, the electrons are released in the nanohybrid, particularly at the junction region, into the NBA [56]. Due to these electrons, the majority carriers (holes) in the NBA could be compensated, which may result in the increasing of depletion layer thickness (Figure 3.14(c)). This phenomenon, then, increases the resistance of the NBA-ZnO nanohybrid sensor further, in the presence of CO₂. Moreover, NBA-ZnO nanohybrid sensor exhibits fast response and recovery time to CO₂ as compared to other reported CO₂ sensors. This could be due to the presence of alternating layer-by-layer assemblies of *n*-type ZnO and *p*-type NBA, which provides a superior carrier transport path in NBA-ZnO nanohybrid Sensor [57].

Table 3.1 represents a comparative room temperature CO₂ sensing performance between our NBA-ZnO nanohybrids sensor and literature reported sensor. Waghuley *et al.* [58] reported CO₂ sensing properties of polypyrrole synthesized *via* chemically oxidative polymerization technique. Their sensor, fabricated by the screen-printed technique with Py/FeCl₃ weight ratio of 4.290, shows a response of 0.59 to 700 ppm CO₂. Yagüe and Borrós reported improved CO₂ sensing properties of iodine-doped polypyrrole conducting thin-film prepared by plasma enhanced chemical vapor deposition (PECVD), and their sensor response is 2.4 and 4.6 for the 380 nm and 570 nm thick films, respectively [59]. Chaing *et al.* [60] investigated, polyethylenimine (BPEI)-poly(3,4-ethylenedioxythiophene)(PEDOT) composite sensor for CO₂ detection. They showed that the use of BPEI layer on top of

PEDOT layer enhances the response to CO₂ gas. Their sensor response to 1000 ppm CO₂ is 3.25, however, the sensor in this study shows long

Table 3.1. Performance comparison of room temperature CO₂ sensing.

M	S/D	C (ppm)	R (%)	τ_{Res}	τ_{Rec}	Ref.
NBA-ZnO nanohybrids	<i>In-situ</i> hydrothermal	500	9.16	206 s	354 s	Our Work
Polymerized polypyrrole	Polymerization	700	0.59	210 s	>1100 s	[58]
Iodine-doped polypyrrole	PECVD	-	4.6	>7 min	>14 min	[59]
PEDOT-BPEI	<i>In-situ</i> polymerization	1000	3.2	>13 min	>30 min	[60]
CNT thin film	Transfer method	800	2.23	>20 s	>75 s	[61]
M: Material, S/D: Synthesis/deposition method, C: Gas/VOC concentration, T: Operating temperature, R: Response						

recovery time nearly 1 h, at room temperature. Lin *et al.* [61] reported the direct transfer of high-density carbon nanotubes (CNTs) from a SiO₂/ Si substrate to a flexible substrate with a strong adhesion of CNTs to the flexible substrate. Successively, they investigated CO₂ sensing properties of the sensor, and the sensor response to 800 ppm CO₂ is 2.23 at room temperature. It can be easily seen that our NBA-ZnO nanohybrid sensor exhibited the best performance towards room temperature CO₂ sensing. Superior CO₂ sensing properties of NBA-ZnO nanohybrids is attributed to the presence of primary amine functional group, *p-n* heterojunction between *p*-type NBA and *n*-type ZnO, and layer-by-layer assemblies of *p*-type NBA and *n*-type ZnO.

3.4. Conclusion

In summary, *in-situ* fabrication of NBA-ZnO nanohybrids thin film on IDEs patterned ZnO seed layer coated flexible (PDMS) substrate has

been achieved with excellent mechanical flexibility. The fabricated flexible sensor exhibited a high response to CO₂ at room temperature, with 30% response observed for 5000 ppm CO₂ at room temperature. Bending has shown to have no significant effect on CO₂ sensing properties of the NBA-ZnO nanohybrids sensor. Low humidity impact, excellent mechanical flexibility, high response and high selectivity to carbon dioxide demonstrates that our NBA-ZnO nanohybrid based flexible sensor is a suitable candidate for room temperature CO₂ detection.

3.5. References

- [1] D. Wang *et al.*, “CO₂-sensing properties and mechanism of nano-SnO₂ thick-film sensor,” *Sensors Actuators B Chem.*, vol. 227, pp. 73–84, May 2016.
- [2] T. Hibino and H. Iwahara, “CO₂ sensors using BaCeO₃-based ceramics,” *Sensors Actuators B. Chem.*, vol. 13, no. 1–3, pp. 483–485, May 1993.
- [3] E. Delgado and C. R. Michel, “CO₂ and O₂ sensing behavior of nanostructured barium-doped SmCoO₃,” *Mater. Lett.*, vol. 60, no. 13–14, pp. 1613–1616, Jun. 2006.
- [4] Y.-J. Jeong, C. Balamurugan, and D.-W. Lee, “Enhanced CO₂ gas-sensing performance of ZnO nanopowder by La loaded during simple hydrothermal method,” *Sensors Actuators B Chem.*, vol. 229, pp. 288–296, Jun. 2016.
- [5] R. Dhahri *et al.*, “Enhanced performance of novel calcium/aluminum co-doped zinc oxide for CO₂ sensors,” *Sensors Actuators B Chem.*, vol. 239, pp. 36–44, 2017.
- [6] N. Mizuno, T. Yoshioka, K. Kato, and M. Iwamoto, “CO₂-sensing characteristics of SnO₂ element modified by La₂O₃,” *Sensors Actuators B Chem.*, vol. 13, no. 1–3, pp. 473–475, May 1993.
- [7] D. H. Kim, J. Y. Yoon, H. C. Park, and K. H. Kim, “CO₂-sensing

- characteristics of SnO₂ thick film by coating lanthanum oxide,” *Sensors Actuators B Chem.*, vol. 62, no. 1, pp. 61–66, Jan. 2000.
- [8] J. C. Xu, G. W. Hunter, D. Lukco, C.-C. Liu, and B. J. Ward, “Novel Carbon Dioxide Microsensor Based on Tin Oxide Nanomaterial Doped With Copper Oxide,” *IEEE Sens. J.*, vol. 9, no. 3, pp. 235–236, Mar. 2009.
- [9] T. Ishihara, K. Kometani, Y. Mizuhara, and Y. Takita, “Mixed Oxide Capacitor of CuO-BaTiO₃ as a New Type CO₂ Gas Sensor,” *J. Am. Ceram. Soc.*, vol. 75, no. 3, pp. 613–618, Mar. 1992.
- [10] A. Haeusler and J.-U. Meyer, “A novel thick film conductive type CO₂ sensor,” *Sensors Actuators B Chem.*, vol. 34, no. 1–3, pp. 388–395, Aug. 1996.
- [11] I. G. Giannakopoulos, D. Kouzoudis, C. A. Grimes, and V. Nikolakis, “Synthesis and Characterization of a Composite Zeolite-Metglas Carbon Dioxide Sensor,” *Adv. Funct. Mater.*, vol. 15, no. 7, pp. 1165–1170, Jul. 2005.
- [12] A. Kaushik, R. Kumar, S. K. Arya, M. Nair, B. D. Malhotra, and S. Bhansali, “Organic–Inorganic Hybrid Nanocomposite-Based Gas Sensors for Environmental Monitoring,” *Chem. Rev.*, vol. 115, no. 11, pp. 4571–4606, Jun. 2015.
- [13] Y. K. Mishra and R. Adelung, “ZnO tetrapod materials for functional applications,” *Mater. Today*, vol. 21, no. 6, pp. 631–651, Jul. 2018.
- [14] S. Wang, Y. Kang, L. Wang, H. Zhang, Y. Wang, and Y. Wang, “Organic/inorganic hybrid sensors: A review,” *Sensors Actuators B Chem.*, vol. 182, pp. 467–481, Jun. 2013.
- [15] P. Judeinstein and C. Sanchez, “Hybrid organic–inorganic materials: a land of multidisciplinary,” *J. Mater. Chem.*, vol. 6, no. 4, pp. 511–525, Jan. 1996.

- [16] F. Schütt, V. Postica, R. Adelung, and O. Lupan, "Single and Networked ZnO-CNT Hybrid Tetrapods for Selective Room-Temperature High-Performance Ammonia Sensors," *ACS Appl. Mater. Interfaces*, vol. 9, no. 27, pp. 23107–23118, 2017.
- [17] J. Wang *et al.*, "Hierarchical ZnO Nanosheet-Nanorod Architectures for Fabrication of Poly(3-hexylthiophene)/ZnO Hybrid NO₂ Sensor," *ACS Appl. Mater. Interfaces*, vol. 8, no. 13, pp. 8600–8607, 2016.
- [18] M. Faustini, L. Nicole, E. Ruiz-Hitzky, and C. Sanchez, "History of Organic-Inorganic Hybrid Materials: Prehistory, Art, Science, and Advanced Applications," *Adv. Funct. Mater.*, p. 1704158, Apr. 2018.
- [19] V. K. Tomer, S. Duhan, R. Malik, S. P. Nehra, and S. Devi, "A Novel Highly Sensitive Humidity Sensor Based on ZnO/SBA-15 Hybrid Nanocomposite," *J. Am. Ceram. Soc.*, vol. 98, no. 12, pp. 3719–3725, Dec. 2015.
- [20] D. T. McQuade, A. E. Pullen, and T. M. Swager, "Conjugated Polymer-Based Chemical Sensors," *Chem. Rev.*, vol. 100, no. 7, pp. 2537–2574, Jul. 2000.
- [21] V. . Chabukswar, S. Pethkar, and A. A. Athawale, "Acrylic acid doped polyaniline as an ammonia sensor," *Sensors Actuators B Chem.*, vol. 77, no. 3, pp. 657–663, Jul. 2001.
- [22] J. Huang and R. B. Kaner, "A General Chemical Route to Polyaniline Nanofibers," *J. Am. Chem. Soc.*, vol. 126, no. 3, pp. 851–855, Jan. 2004.
- [23] B. Li and D. N. Lambeth, "Chemical Sensing Using Nanostructured Polythiophene Transistors," *Nano Lett.*, vol. 8, no. 11, pp. 3563–3567, Nov. 2008.
- [24] R. Malik, V. K. Tomer, L. Kienle, V. Chaudhary, S. Nehra, and S. Duhan, "Ordered Mesoporous Ag-ZnO@g-CN Nanohybrid as

- Highly Efficient Bifunctional Sensing Material,” *Adv. Mater. Interfaces*, vol. 5, no. 8, p. 1701357, Apr. 2018.
- [25] U. Yaqoob, A. S. M. I. Uddin, and G.-S. Chung, “A high-performance flexible NO₂ sensor based on WO₃ NPs decorated on MWCNTs and RGO hybrids on PI/PET substrates,” *Sensors Actuators B Chem.*, vol. 224, pp. 738–746, Mar. 2016.
- [26] J. Yi, J. M. Lee, and W. Il Park, “Vertically aligned ZnO nanorods and graphene hybrid architectures for high-sensitive flexible gas sensors,” *Sensors Actuators B Chem.*, vol. 155, no. 1, pp. 264–269, Jul. 2011.
- [27] S. Li *et al.*, “The room temperature gas sensor based on Polyaniline@flower-like WO₃ nanocomposites and flexible PET substrate for NH₃ detection,” *Sensors Actuators B Chem.*, vol. 259, pp. 505–513, Apr. 2018.
- [28] R. Lucklum, B. Henning, P. Hauptmann, K. D. Schierbaum, S. Vaihinger, and W. Göpel, “Quartz microbalance sensors for gas detection,” *Sensors Actuators A. Phys.*, vol. 27, no. 1–3, pp. 705–710, May 1991.
- [29] O. Fatibello-Filho, J. F. De Andrade, A. A. Suleiman, and G. G. Guilbault, “Piezoelectric crystal monitor for carbon dioxide in fermentation processes,” *Anal. Chem.*, vol. 61, no. 7, pp. 746–748, Apr. 1989.
- [30] R. Zhou, D. Schmeisser, and W. Göpel, “Mass sensitive detection of carbon dioxide by amino group-functionalized polymers,” *Sensors Actuators B Chem.*, vol. 33, no. 1–3, pp. 188–193, Jul. 1996.
- [31] M. S. Nieuwenhuizen and A. J. Nederlof, “A SAW gas sensor for carbon dioxide and water. Preliminary experiments,” *Sensors Actuators B Chem.*, vol. 2, no. 2, pp. 97–101, May 1990.
- [32] B. Sun, G. Xie, Y. Jiang, and X. Li, “Comparative CO₂-Sensing

- Characteristic Studies of PEI and PEI/Starch Thin Film Sensors,” *Energy Procedia*, vol. 12, pp. 726–732, Jan. 2011.
- [33] A. Star, T.-R. Han, V. Joshi, J.-C. P. Gabriel, and G. Grüner, “Nanoelectronic Carbon Dioxide Sensors,” *Adv. Mater.*, vol. 16, no. 22, pp. 2049–2052, Nov. 2004.
- [34] R. Zhou, S. Vaihinger, K. E. Geckeler, and W. Göpel, “Reliable CO₂ sensors with silicon-based polymers on quartz microbalance transducers,” *Sensors Actuators B Chem.*, vol. 19, no. 1–3, pp. 415–420, Apr. 1994.
- [35] S. Stegmeier, M. Fleischer, A. Tawil, and P. Hauptmann, “Stepwise improvement of (hetero-) polysiloxane sensing layers for CO₂ detection operated at room temperature by modification of the polymeric network,” *Sensors Actuators B Chem.*, vol. 148, no. 2, pp. 450–458, Jul. 2010.
- [36] S. V. Patel, S. T. Hobson, S. Cemalovic, and T. E. Mlsna, “Materials for capacitive carbon dioxide microsensors capable of operating at ambient temperatures,” *J. Sol-Gel Sci. Technol.*, vol. 53, no. 3, pp. 673–679, Mar. 2010.
- [37] S. Stegmeier, M. Fleischer, A. Tawil, P. Hauptmann, and H.-E. Endres, “Sensing of CO₂ at room temperature using work function readout of (hetero-)polysiloxanes sensing layers,” *Sensors Actuators B Chem.*, vol. 154, no. 2, pp. 206–212, Jun. 2011.
- [38] Y. G. Ko, S. S. Shin, and U. S. Choi, “Primary, secondary, and tertiary amines for CO₂ capture: Designing for mesoporous CO₂ adsorbents,” *J. Colloid Interface Sci.*, vol. 361, no. 2, pp. 594–602, Sep. 2011.
- [39] S. A. Chen and G. W. Hwang, “Structures and properties of the water-soluble self-acid-doped conducting polymer blends: Sulfonic acid ring-substituted polyaniline/poly(vinyl alcohol) and poly(aniline-co-N-propanesulfonic acid aniline)/poly(vinyl

- alcohol),” *Polymer (Guildf.)*, vol. 38, no. 13, pp. 3333–3346, Jan. 1997.
- [40] D. V. Kosynkin and J. M. Tour, “Phenylene Ethynylene Diazonium Salts as Potential Self-Assembling Molecular Devices,” *Org. Lett.*, vol. 3, no. 7, pp. 993–995, Apr. 2001.
- [41] M. E. Fragalà, A. Di Mauro, G. Litrico, F. Grassia, G. Malandrino, and G. Foti, “Controlled large-scale fabrication of sea sponge-like ZnO nanoarchitectures on textured silicon,” *CrystEngComm*, vol. 11, no. 12, p. 2770, Nov. 2009.
- [42] J. Sun *et al.*, “Preparation of polypyrrole@WO₃ hybrids with p-n heterojunction and sensing performance to triethylamine at room temperature,” *Sensors Actuators B Chem.*, vol. 238, pp. 510–517, Jan. 2017.
- [43] S. Verma, M. K. Manna, S. K. Pandey, A. K. Das, and S. Mukherjee, “Benzo[ghi]perylene monoimide based photosensitive lamellar Cd-doped ZnO nanohybrids,” *RSC Adv.*, vol. 4, no. 107, pp. 62603–62614, Nov. 2014.
- [44] M. K. Manna, Aaryashree, S. Verma, S. Mukherjee, and A. K. Das, “Lamellar Peptide-Cadmium-Doped Zinc Oxide Nanohybrids That Emit White Light,” *Chempluschem*, vol. 81, no. 3, pp. 329–337, Mar. 2016.
- [45] Aaryashree *et al.*, “Synergetic Accrual of Lamellar Nanohybrids for Band-Selective Photodetection,” *J. Phys. Chem. C*, vol. 121, no. 26, pp. 14037–14044, Jul. 2017.
- [46] K. Liu *et al.*, “Peptide-Induced Hierarchical Long-Range Order and Photocatalytic Activity of Porphyrin Assemblies,” *Angew. Chemie*, vol. 127, no. 2, pp. 510–515, Jan. 2015.
- [47] W. Jeong, S. Choi, J. S. Choi, and Y. Lim, “Chameleon-like Self-Assembling Peptides for Adaptable Biorecognition Nanohybrids,” *ACS Nano*, vol. 7, no. 8, pp. 6850–6857, Aug.

2013.

- [48] E. R. Draper *et al.*, “Air-stable photoconductive films formed from perylene bisimide gelators,” *J. Mater. Chem. C*, vol. 2, no. 28, pp. 5570–5575, Jun. 2014.
- [49] T. C. D. Doan, J. Baggerman, R. Ramaneti, H. D. Tong, A. T. M. Marcelis, and C. J. M. van Rijn, “Carbon dioxide detection with polyethylenimine blended with polyelectrolytes,” *Sensors Actuators B Chem.*, vol. 201, pp. 452–459, Oct. 2014.
- [50] I. Matsubara, K. Hosono, N. Murayama, W. Shin, and N. Izu, “Organically hybridized SnO₂ gas sensors,” *Sensors Actuators B Chem.*, vol. 108, no. 1–2, pp. 143–147, Jul. 2005.
- [51] M. Caplow, “Kinetics of carbamate formation and breakdown,” *J. Am. Chem. Soc.*, vol. 90, no. 24, pp. 6795–6803, Nov. 1968.
- [52] S. Choi, J. H. Drese, and C. W. Jones, “Adsorbent Materials for Carbon Dioxide Capture from Large Anthropogenic Point Sources,” *ChemSusChem*, vol. 2, no. 9, pp. 796–854, Sep. 2009.
- [53] R. Tanaka, H. Yamamoto, A. Shono, K. Kubo, and M. Sakurai, “Proton conducting behavior in non-crosslinked and crosslinked polyethylenimine with excess phosphoric acid,” *Electrochim. Acta*, vol. 45, no. 8–9, pp. 1385–1389, Jan. 2000.
- [54] H. Tai, Y. Jiang, G. Xie, J. Yu, and X. Chen, “Fabrication and gas sensitivity of polyaniline–titanium dioxide nanocomposite thin film,” *Sensors Actuators B Chem.*, vol. 125, no. 2, pp. 644–650, Aug. 2007.
- [55] S. K. Pandey *et al.*, “Effect of growth temperature on structural, electrical and optical properties of dual ion beam sputtered ZnO thin films,” *J. Mater. Sci. Mater. Electron.*, vol. 24, no. 7, pp. 2541–2547, Jul. 2013.
- [56] J. Sun *et al.*, “Preparation of polypyrrole@WO₃ hybrids with p-n heterojunction and sensing performance to triethylamine at room

- temperature,” *Sensors Actuators B Chem.*, vol. 238, pp. 510–517, Jan. 2017.
- [57] M. Gerard, A. Chaubey, and B. D. Malhotra, “Application of conducting polymers to biosensors,” *Biosens. Bioelectron.*, vol. 17, no. 5, pp. 345–359, May 2002.
- [58] S. A. Waghuley, S. M. Yenorkar, S. S. Yawale, and S. P. Yawale, “Application of chemically synthesized conducting polymer-polypyrrole as a carbon dioxide gas sensor,” *Sensors Actuators B Chem.*, vol. 128, no. 2, pp. 366–373, Jan. 2008.
- [59] J. L. Yagüe and S. Borrós, “Conducting Plasma Polymerized Polypyrrole Thin Films as Carbon Dioxide Gas Sensors,” *Plasma Process. Polym.*, vol. 9, no. 5, pp. 485–490, May 2012.
- [60] C.-J. Chiang *et al.*, “In situ fabrication of conducting polymer composite film as a chemical resistive CO₂ gas sensor,” *Microelectron. Eng.*, vol. 111, pp. 409–415, Nov. 2013.
- [61] Z.-D. Lin, S.-J. Young, and S.-J. Chang, “CO₂ Gas Sensors Based on Carbon Nanotube Thin Films Using a Simple Transfer Method on Flexible Substrate,” *IEEE Sens. J.*, vol. 15, no. 12, pp. 7017–7020, Dec. 2015.

Chapter 4

Synthesis of ODBA-ZnO Nanohybrids for CO gas Detection

4.1. Introduction

Carbon monoxide (CO), an odorless, colorless, and tasteless gas, is generated primarily through the incomplete or partial oxidation of carbon-containing compounds such as carbon based fuels, gas fires, and domestic appliances [1]. The excess concentration (≥ 200 ppm) of CO is considerably toxic to humans and living beings due to its strong ability to bind with oxygen-carrying hemoglobin resulting in the generation of carboxyhemoglobin that stops oxygen transport mechanism in the bodily tissues [2]. Exposure of CO gas, at low concentration can cause dizziness and headaches, whereas at higher concentration it can cause respiratory arrest, coma, and even death [3]. Several methods are available for CO detection, such as electrochemical assays [4], [5], colorimetric [6]–[8], gas chromatography [9], and laser infrared absorption [10]. However, these methods are highly expensive and cannot be used for domestic applications. Alternatively, the MOX based CO sensors are very desirable, especially if the aim is to monitor CO in the environment [11]. Due to their excellent response and light-weight, they are ideal for environmental monitoring, emission monitoring, and automotive applications [12]–[15]. There are several reports on CO sensor based on bare MOX materials such as SnO₂ [16], ZnO [17], TiO₂ [18], CeO₂ [19], β -Ga₂O₃ [20], PdO [21], Zn₂SnO₄ [22], LaCoO₃ [23], metal doped MOX materials such as Pt-SnO₂ [24], Al-ZnO [25], Fe-

WO₃ [26], Cu-TiO₂ [11], Zn-In₂O₃ [27], Pd-SnO₂ [28], Au-CeO₂ [29], Cr/Pt-SnO₂ [30], Cu@CuO [31] and composite MOX materials such as PdO-SnO₂ [32], PdO-NiO [33], ZnO-CuO [34], ZrO₂-MoO₃ [35], CuO/SnO₂-In₂O₃ [36], WO₃@CuWO₄ [37]. In addition to high sensitivity, realizing a CO sensor with high selectivity for various applications such as indoor alarm [1], multi-arrayed sensor etc is crucial [38], [39]. So far, most of the MOX-based CO sensors are either extremely cross sensitive or require high temperatures for operation and that prevent their practical use [40]. Thus, more work is still needed to develop low-cost, highly selective CO sensors that function at a relatively low optimal temperature. Poor stability and low electrical conductivity of organic materials, and low selectivity and high-temperature operation of inorganic materials, prevent their individual usage in the manufacture of functional gas/VOC sensors [40]. On the other hand, the use of organic-inorganic hybrid material may help to eliminate their individual drawbacks, due to the presence of advantages of their constituents, i.e., high stability and easy fabrication of inorganic material, and better chemical specificity to a particular gas/VOC of organic material, contributing to improved sensing properties [41]. Nevertheless, the unique functional properties of the hybrid material are a result of either the synergy or complementary effect generated by the hybrid interfaces [42]–[44]. Interestingly, recent research has focused on the development of CO sensors based on organic-inorganic hybrid material. For instance, a recent report by Chiniforoshan *et al.* [45] describes the sonochemical synthesis of gold containing 4,4'-dicyanamidobiphenyl polymers for low ppm CO sensitivity at room temperature. The palladium-loaded tin dioxide/partially reduced graphene oxide (Pd-SnO₂/PRGO) nanocomposites synthesized *via* facial hydrothermal method were reported by Shojaee *et al.* [46] for room temperature CO sensing. Ha *et al.* [47] have reported ZnO nanoparticles loaded 3 Dimensional reduced graphene oxide (ZnO/3D-RGO) for highly sensitive, fast response and recovery CO sensor. Dang *et al.* [48] have reported cobalt oxide nanoparticles dispersed on polyethylenimine functionalized multiwalled carbon nanotubes

(Co₃O₄/PEI-CNTs), and their sensor shows excellent sensitive to CO gas at room temperature. Kim *et al.* [49] have reported ppm-level CO detection using Au functionalization in reduced graphene oxide-loaded SnO₂ nanofibers (Au/RGO-SnO₂). In a study by Liu *et al.* [50] a chemiresistive sensor based on diiodo(η^5 : η^1 -1-[2-(N,N-dimethylamino)-ethyl]-2,3,4,5-tetramethylcyclopentadienyl)cobalt (III)([Cp[^]CoI₂]) functionalized carbon nanotubes (CNTs), have been reported and their sensor shows excellent selectivity and low limit of detection for CO. Though these sensors work at low or room temperature, yet the selectivity achieved by these sensors is still not sufficient for practical application [41].

Organic monomer containing benzoic acid as a functional group is used with the precursor of MOXs to make organic-inorganic hybrids for various applications [51], [52], due to their easy interaction with the inorganic salts. Recently, organic monomer containing dihydroxybenzoic acid as functional group is used to make hybrids with SnO₂, and the same is used to detect CO with high selectivity, however, the sensor exhibits incomplete recovery process [53].

This chapter describes of an organo-di-benzoic acidified ZnO (ODBA-ZnO) nanohybrid material, prepared *via* single-pot hydrothermal method, which exhibits unprecedented selectivity to CO with moderate sensitivity.

4.2. Experimental

4.2.1. Synthesis of Organo-Di-Benzoic Acid (ODBA)

Desired organo-di-benzoic acid (ODBA, compound **1**) is synthesized *via* several intermediate steps [54], [55]. In the first step, benzo[2,1,3]selenadiazole (compound **5**) is obtained by the condensation reaction between *o*-phenylenediamine and selenium dioxide at 65 °C in ethanol solvent. Next, 4,7-dibromobenzo [2,1,3]selenadiazole (compound **4**) is synthesized from benzo[2,1,3]selenadiazole (compound **5**) in Ag₂SO₄/H₂SO₄ solution in the presence of liquid bromine. Methyl 4-vinylbenzoate (compound **3**) is synthesized by protecting the acid group of 4-vinylbenzoic acid in the presence of

$\text{SOCl}_2/\text{MeOH}$. Heck reaction is performed to synthesize dimethyl 4,4'-((1E,1'E)-benzo[2,1,3]selenadiazole-4,7-diylbis(ethene-2,1-diyl))dibenzoate (compound **2**) from 4,7-dibromobenzo[2,1,3]selenadiazole (compound **4**) and methyl 4-vinylbenzoate (compound **3**). The reaction is performed at 110 °C in DMF, where $\text{Pd}(\text{OAc})_2$ is used as a coupling catalyst, and tetrabutylammonium bromide is used as a phase transfer catalyst. Finally 4,4'-((1E,1'E)-benzo[2,1,3]selenadiazole-4,7-diylbis(ethene-2,1-diyl))dibenzoic acid (ODBA, compound **1**) is synthesized after saponification of dimethyl 4,4'-((1E,1'E)-benzo[2,1,3]selenadiazole-4,7-diylbis(ethene-2,1-diyl))dibenzoate (compound **2**) in MeOH/THF solution.

The reaction scheme (Figure 4.1) and detailed synthetic process of the intermediates are as follows.

Synthesis of benzo[2,1,3]selenadiazole (compound 5): *ortho*-phenylenediamine (2 g, 18.4 mmol) in 50 mL ethanol is taken into a 100 mL round bottom flask and selenium dioxide (2.24 g, 20 mmol) is added into reaction mixture. After that the whole reaction mixture is allowed to reflux at 65 °C for 1 h, solvent is evaporated under reduce pressure to obtain as a faint pink colored solid product (3.2 g, 94% yield).

Synthesis of 4,7-dibromobenzo[2,1,3]selenadiazole (compound 4): Compound **5** (1 g, 5.46 mmol) and silver sulfate (1.68 g, 5.46 mmol) are dissolved in 20 mL concentrated H_2SO_4 at 0 °C. Liquid bromine (588 μL , 11.4 mmol) is added dropwise for 20 minutes into the reaction mixture. After stirring for 24 h, the whole reaction mixture is poured into the cold water and extracted by ethyl acetate and washed with brine (3×100 mL) solution. Finally the organic part is concentrated under vacuum. Residue is purified by column chromatography (silica gel as stationary phase and 1:1 hexane: dichloromethane as eluent) and yellow powder is obtained (0.8 g, 43%).

Synthesis of Methyl 4-vinylbenzoate (compound 3): 10 mL methanol is taken into a 100 mL round bottom flask at 0 °C. After 5 minutes, 538 μL (7.37 mmol) thionyl chloride is added drop wise inside the cooled

methanol. Finally 4-vinylbenzoic acid (1 g, 6.7 mmol) is added into reaction mixture. After stirring for the overnight, thionyl chloride is evaporated under vacuum and washed with ether to afford the desire product as white solid (1.08 g, yield 99%).

Synthesis of the dimethyl 4,4'-((1E,1'E)-benzo[2,1,3]selenadiazole-4,7-diylbis(ethene-2,1-diyl))dibenzoate (compound 2): In a 100 mL two neck round-bottom flask, compound 4 (0.8 g, 2.3 mmol) and compound 3 (0.7 g, 4.7 mmol) are dissolved in dry DMF (25 mL). Potassium carbonate (0.8 g, 4.7 mmol) and tetrabutyl ammonium bromide (1.5 g, 4.7 mmol) is dissolved in reaction mixture. The reaction mixture is purged with nitrogen gas for 30 min. Pd(OAc)₂ (40 mg, 0.14 mmol) is added to the reaction mixture. The reaction mixture is stirred at 110 °C for 48 h. The solvent is removed under reduced pressure. The product is extracted using dichloromethane and washed with 1 N HCl solution followed by brine solution (3× 30 mL). The organic part is dried over sodium sulfate, and the solvent is evaporated using rotary evaporator. The resultant extract is purified by column chromatogram using hexane:dichloromethane (5:2) as eluent. Compound 2 is obtained as a red solid powder (0.5 g, 43 % yield).

¹H NMR (CDCl₃, 400 MHz): δ 8.09 (d, *J*= 8 Hz, 4H), 8.0 (d, *J*= 16 Hz, 4H), 7.82 (d, *J*= 16 Hz, 4H), 7.72 (d, *J*= 8 Hz, 4H), 7.69 (s, 2H), 3.96 (s, 6H) ppm.

¹³C NMR (CDCl₃, 100 MHz): δ 166.88, 159.54, 141.99, 132.20, 130.75, 130.12, 129.31, 127.53, 127.20, 126.74, 52.94 ppm.

Calculated mass C₂₈H₂₆N₂O₄Se [M+H]⁺ 505.0588, found [M+H]⁺ 505.0608

Synthesis of 4,4'-((1E,1'E)-benzo[2,1,3]selenadiazole-4,7-diylbis(ethene-2,1-diyl))dibenzoic acid (compound 1, ODBA): 0.2 g of compound 2 is dissolved in 10 mL tetrahydrofuran and 2 N NaOH in methanol solution added dropwise up to reaching basic pH. The reaction mixture is monitored by TLC (thin layer chromatography) until no starting material is left. The reaction mixture is concentrated under

benzo[2,1,3]selenadiazole-4,7-diylbis(ethene-2,1-diyl)dibenzoic acid, ODBA) powder in the solution slowly under constant stirring for a period of time until the solution becomes uniform red color. The resulting red-color solution is then transferred into a stainless steel Teflon lined autoclave and heated at 95 °C for 6 h. After the hydrothermal reaction, the precipitate is collected and washed several times with de-ionized water. The washed precipitate is then dried at 70 °C for 10 h in air to obtain orange-like organo-di-benzoic acidified ZnO powder. The resultant powders are named as ZnO nanoparticles (NPs), OZ10, OZ50, and OZ100, respectively. The synthesis process of ODBA-ZnO hybrid material is schematically shown in Figure 4.2.

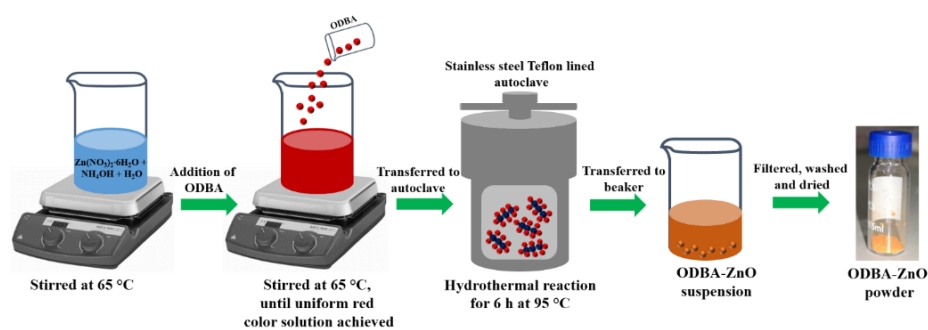


Figure 4.2. Schematic of the synthesis steps of organo-di-benzoic acidified ZnO nanostructures.

4.2.3. Sensor Fabrication

A Corning glass substrate having a dimension of 3 (length) × 3 (width) × 0.5 mm (thick) with two interdigitated Pt electrodes (IDEs) on top is used to fabricate the gas sensor. Each Pt electrode consists of 5 fingers (250 (length) × 25 (width) × 1 μm (thick)), and the distance between the adjacent fingers of two sets of electrodes is 25 μm. A certain amount of ODBA-ZnO powder is dispersed in de-ionized water to form a suspension. The sensor fabrication is carried out by the suspension deposition onto the IDEs realized on the glass substrate, by a simple drop cast technique, and calcination at 120 °C for a night in the air. The device schematic, scanning electron micrograph of IDEs, sensing layer deposited on IDEs and sensing layer micrograph are shown in Figure 4.3. Sensor response is defined as $\text{response (\%)} = |R_g - R_a| / R_a \times 100$, where, R_g is the resistance

of the hybrid sensor at a given time during exposure to target gas and R_a is the resistance value of the hybrid sensor in the air ambient.

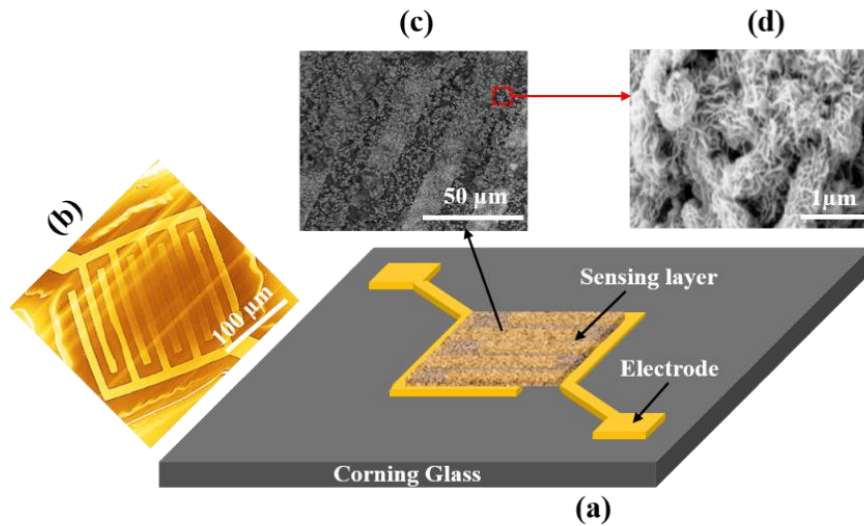


Figure 4.3. (a) Device schematic, (b) FESEM image of the IDEs on the glass substrate, (c) FESEM image of the sensing layer deposited on IDEs patterned glass substrate, (d) magnified FESEM of the sensing layer.

4.3. Results and Discussions

4.3.1. Morphology and Composition

4.3.1.1. Field Emission Scanning Electron Microscopy

The morphology of the obtained hybrid material is characterized by FESEM. Figure 4.4(a)-(b) shows the FESEM images of the the as-grown ODBA-ZnO nanostructures. It can be observed from that the ODBA-ZnO hybrid material is highly porous and comprises of net-like hierarchical structures. The magnified FESEM image of the net-like ODBA-ZnO nanostructures is shown in the inset of Figure 4.4(a).

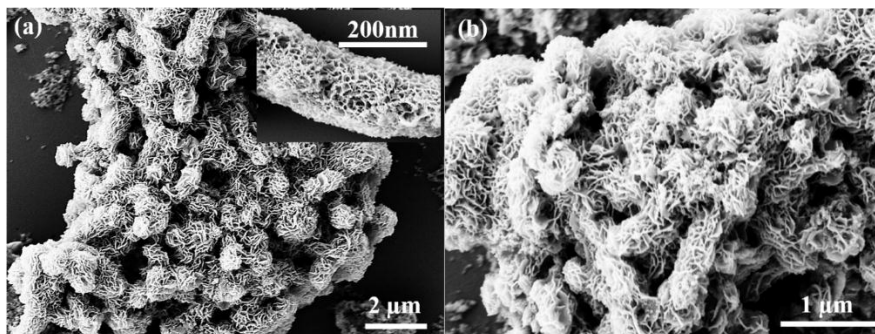


Figure 4.4. FESEM images of ODBA-ZnO hybrid material at (a) lower magnification, (b) higher magnification. Inset of Figure 6.4(a) shows higher magnification of the ODBA-ZnO hierarchal structures.

It is important to note that without the addition of ODBA (0 mg) in the solution during hydrothermal synthesis, the ZnO nanoparticles are grown with dimension of $200 \times 100 \text{ nm}^2$, as can be seen in Figure 4.5.

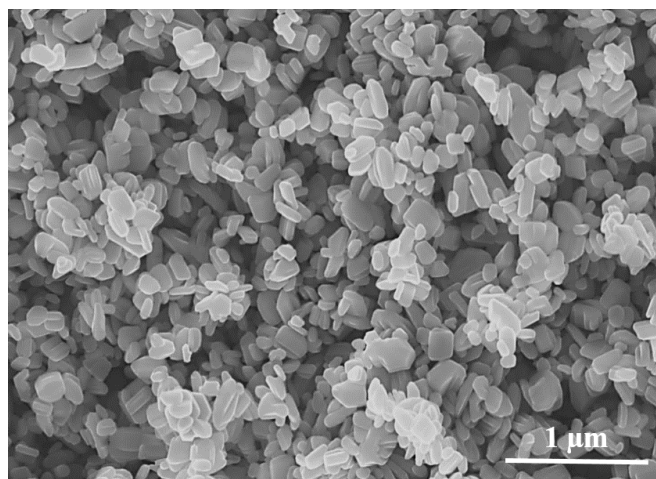


Figure 4.5. FESEM image of ZnO NPs sample.

4.3.1.2. Energy Dispersive X-Ray Spectroscopy

The EDX mapping of the ODBA-ZnO nanohybrids is shown in Figure 4.6. Strong signal of elemental Zn and O are corresponding to ZnO. And signal of elemental C, Se, and O are corresponding to ODBA. Ensuring the presence of these materials in the ODBA-ZnO nanohybrid.

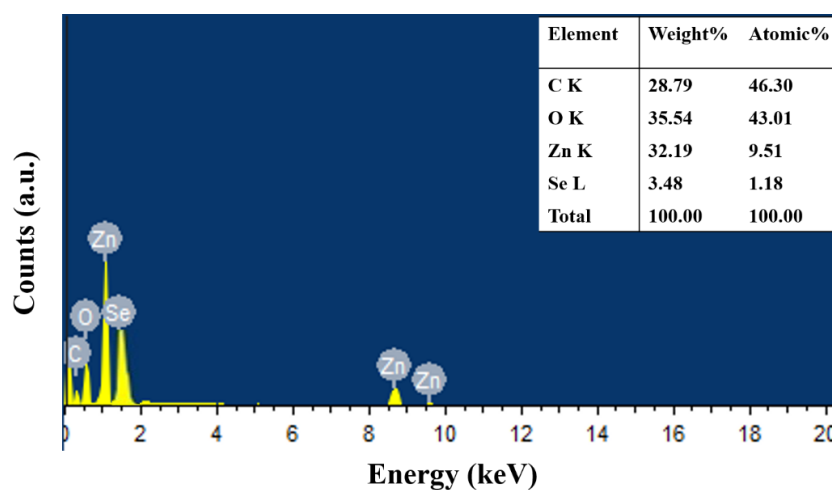


Figure 4.6. EDX pattern of the ODBA-ZnO nanohybrid.

4.3.1.3 X-Ray Diffraction

The XRD profiles of ZnO, ODBA-ZnO, and ODBA film are shown in Figure 4.7. As can be observed, all the diffraction peaks related to ZnO nanoparticles coincided with the standard data file (JCPDS: 79-0208) which confirm the wurtzite structure of the ZnO [56]. The broad peak (15-35°) is observed in the ODBA pattern, indicating that the ODBA is essentially amorphous. A broad diffraction peak (23-25.49°) related to ODBA and some of the diffraction peaks related to ZnO are observed in the XRD spectra of ODBA-ZnO nanohybrid. However, the broadening range of the diffraction peak corresponding to ODBA in ODBA-ZnO has reduced, the calculated full width at half-maximum (FWHM) value reduced nearly 7 times, indicating improved crystallinity of ODBA in ODBA-ZnO hybrid material.

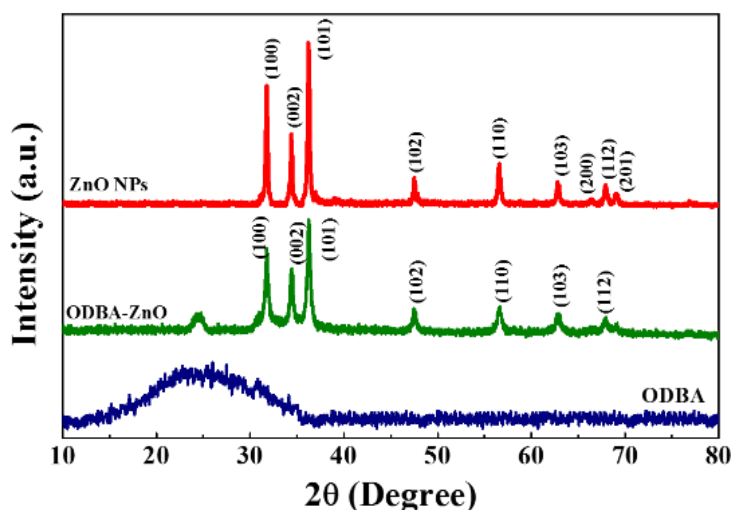


Figure 4.7. XRD pattern of ZnO nanoparticles (red), ODBA-ZnO hybrid (green), and amorphous ODBA (blue).

4.3.1.4 Thermogravimetric Analysis

TGA is carried out to determine the decomposition temperature of the ODBA-ZnO nanohybrids. The TGA curve of ODBA-ZnO powder in the range of room temperature to 800 °C at a heating rate of 10 °C/min is given in Figure 4.8. It can be seen that, over the temperature range of 27-137 °C, there is no weight loss indicating almost no water in the calcined ODBA-ZnO powder. The significant weight loss (nearly 33%)

occurred between 137 and 550 °C, which can be attributed to the decomposition of organic compounds from the ODBA-ZnO hybrid, i.e., conversion of organic groups into CO, CO₂, and H₂O. No further weight loss is observed beyond 550 °C, indicating the complete removal of organic compounds from the hybrid at 550 °C.

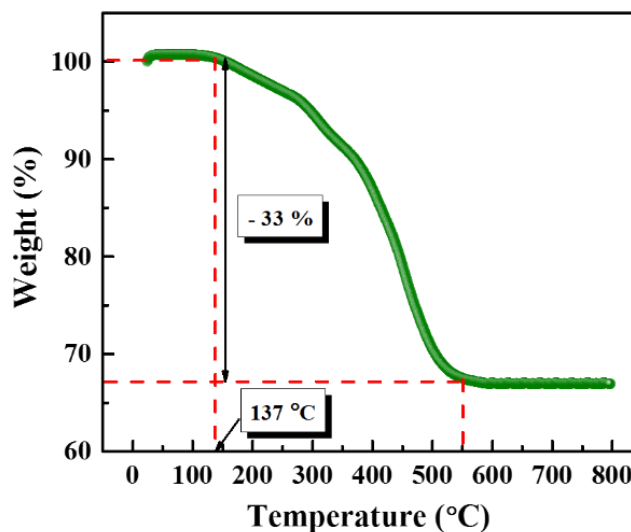


Figure 4.8. TGA analysis of the ODBA-ZnO hybrids.

4.3.1.5. BET Surface Area Analysis

The N₂ adsorption-desorption tests are performed to investigate the inner architecture of the porous ODBA-ZnO hybrid material. The N₂ adsorption-desorption isotherms and pore size distribution (inset) of the ODBA-ZnO powder are shown in Figure 4.9.

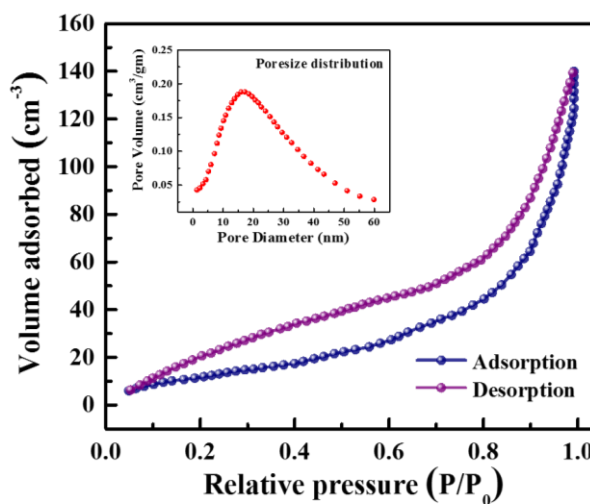


Figure 4.9. BET surface area analysis of ODBA-ZnO hybrid material. Inset shows pore size distribution of the ODBA-ZnO hybrid material.

The isotherm profile exhibits a hysteresis loop in the entire range of relative pressure, which indicates that ODBA-ZnO material has large porosity in its architecture. The BET surface area of the porous ODBA-ZnO nanomaterial is calculated to be 57 m²/g. The pore size distribution of the ODBA-ZnO hybrid material exhibits the presence of a broad peak in pore size region of 5-50 nm. The average pore size calculated using the Barrett-Joyner-Halenda (BJH) method and desorption branch of nitrogen isotherm is around 16.5 nm.

4.3.2. Growth Mechanism

Precursor concentration, growth temperature, and growth mechanism are essential parameters in a hydrothermal synthesis that can tune the unique functional properties of the nanomaterial. For the case of single-pot hydrothermal synthesis of ODBA-ZnO, initially, the reaction between precursor salt (Zn(NO₃)₂·6H₂O) and the base (NH₄OH) in the water solvent medium creates hexagonal zinc hydroxide (Zn(OH)₂) nuclei at 65 °C. Next, the covalent bonds formed between the Zn(OH)₂ nuclei and ODBA at 95 °C, to give structural stability in the hybrid structure [57]–[59]. At the same time, alternating layer-by-layer assembly of organic ODBA and inorganic Zn(OH)₂ creates a chain-like structure as shown in Figure 4.10. During calcination the zinc hydroxide phases of the lamellar hybrid architecture are converted into oxide phases.

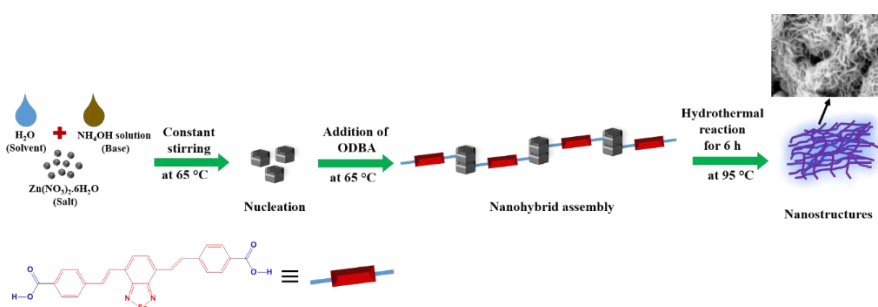


Figure 4.10. Growth mechanism of ODBA-ZnO hybrid architecture.

4.3.3. Gas Sensing Properties

Four types of sensors are fabricated using the prepared samples (i.e., ZnO NPs, OZ10, OZ50, and OZ100) as sensing materials. Then, the CO sensing properties of the sensors are investigated. First, the sensor responses are examined at 100 °C towards 100 ppm of CO, and the results are shown in Figure 4.11. It is observed that the sensors comprising of OZ10, OZ50, and OZ100 as sensing material show resistance increasing response towards CO gas, i.e., electrical resistance of the sensors increases as CO is introduced in the test chamber. The sensor comprising OZ50 as sensing material shows a maximum response of 31% as compared to OZ10 (24%) and OZ100 (14%) sensor.

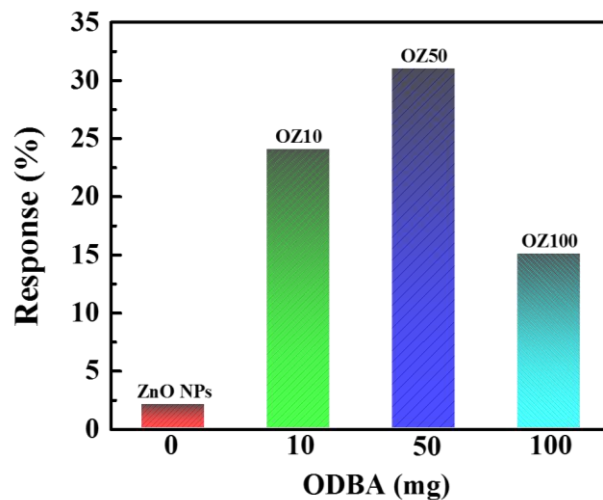


Figure 4.11. Effect of ODBA weight variation on the CO sensing performance by the ODBA-ZnO nanohybrid sensors.

Here, it is important to mention that a similar trend of behavior is observed for 3,4- dihydroxybenzoic acidified tin oxide based sensor [53]. On the other hand, the sensor comprising of ZnO NPs as sensing material shows resistance decreasing response towards CO, i.e., electrical resistance of the sensor decreases as CO is introduced in the test chamber. It should be noted that ZnO is an *n*-type material and CO is a reducing gas, and, thus, the resistance decreases in ZnO NPs based sensor in presence of CO is expected as it is observed by other researchers [60]–[62].

It is a well-known fact that the responses of the metal oxide-based gas sensors are greatly dependent on its operating temperature. Therefore,

to determine the optimal operating temperature, the responses of the four types of sensors to 100 ppm CO at different temperatures ranging from room temperature to 350 °C are tested and the results are shown in Figure 4.12(a). As observed in Figure 4.12(a), the sensors based on OZ10, OZ50, and OZ100 materials show a rapid increase in response as temperature increases from room temperature to 125 °C and attain a maximal response value at 125 °C. The maximum response reached by OZ10, OZ50, and OZ100 based sensors to 100 ppm CO is 28, 35, and 18%, respectively. The temperature rise beyond 125 °C results in a sudden decrease in the response of sensors, and, beyond 250 °C, the responses are negligible. So the optimal operating temperature for ODBA-ZnO nanohybrids sensors is 125 °C. The bare ZnO NPs sensor shows a nearly linear increase in response as temperature increases from 100 to 300°C, and, beyond 300 °C, the sensor response decreases slowly. Therefore, the optimal operating temperature for ZnO NPs based sensor is 300 °C. Here, one should note that the reason for the optimal temperature of 125 °C for ODBA-ZnO nanohybrid sensors can be understood easily from the TGA curve (Figure 4.8). Below 137 °C, the ODBA and ZnO bond interaction is well preserved, as indicated by zero weight loss in TGA curve. That means that, below 137 °C, the charge transportation phenomena between the ODBA and ZnO in the nanohybrid are undisturbed. However, beyond 137 °C, the decomposition of organic components from the ODBA-ZnO nanohybrid is initiated by the thermal energy, as indicated by weight loss in the TGA curve. As a result, the bond interaction between ODBA and ZnO breaks. Consequently, the charge transportation phenomena between the ODBA and ZnO gets hampered, as indicated by the sudden decrease in sensor response beyond 125 °C.

To examine the effect of the variation of CO concentration on sensor response, the OZ50 based sensor is further exposed in different concentrations of CO at the optimal temperature of 125 °C. The dynamic response and recovery characteristics of the OZ50 sensor to a varying concentration (5-500 ppm) of CO at 125 °C is shown in Figure 4.12(b). The results in Figure 4.12(b) reveal that, as concentration of CO

increases, the response also increases. The response observed at 5, 10, 50, 100, 200, and 500 ppm CO is 2.4, 8, 23, 35, 51, and 72%, respectively. In the low concentration range (5-100 ppm), the response is nearly linear. However, at higher CO concentration, the response is nearly saturated. The increase in sensor response with increasing CO concentration can be approximated by exponential function, $y = 73.93(1 - \exp(-0.0064 * x))$, where y is the sensor response and x is the CO concentration, as shown in Figure 4.12(c). In Figure 4.12(d), the single-cycle transient response and recovery characteristics are shown for the OZ50 sensor to 50 ppm CO at 125 °C. The response and recovery time values are 91 and 175 s, respectively.

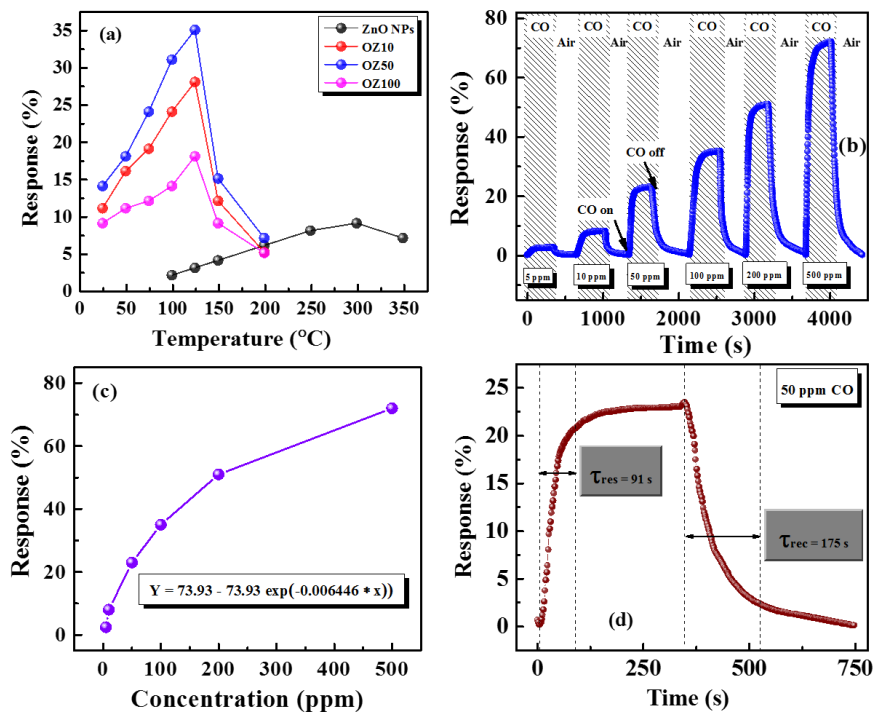


Figure 4.12. (a) Temperature-dependent response of ZnO NPs, OZ10, OZ50, and OZ100 sensor, (b) dynamic response-recovery characteristics to CO concentration varying from 5 to 500 ppm, (c) response vs. concentration of CO, and (d) single transient response of OZ50 sensor.

The dynamic response characteristics of the OZ50 sensor, as the concentration of CO is increased in a step-wise manner from 5 to 100 ppm and final recovery in the air are shown in Figure 4.13(a). It is

observed that the sensor exhibits a stable response in the CO environment and witnessed a quick recovery in the air. In Figure 4.13(b), the response repeatability is shown for the OZ50 sensor at 125 °C. The repeatability is measured by exposing the sensor to 100 ppm CO and air for continuous three response/recovery cycles. The result exhibits that the sensor has good repeatability to CO. The effect of humidity on the gas sensing properties of the sensor is an important factor, especially if the gas sensing is performed at a low temperature [63]. The responses of the OZ50 sensor measured under 23, 42, 66, and 83% relative humidity are given in Figure 4.13(c).

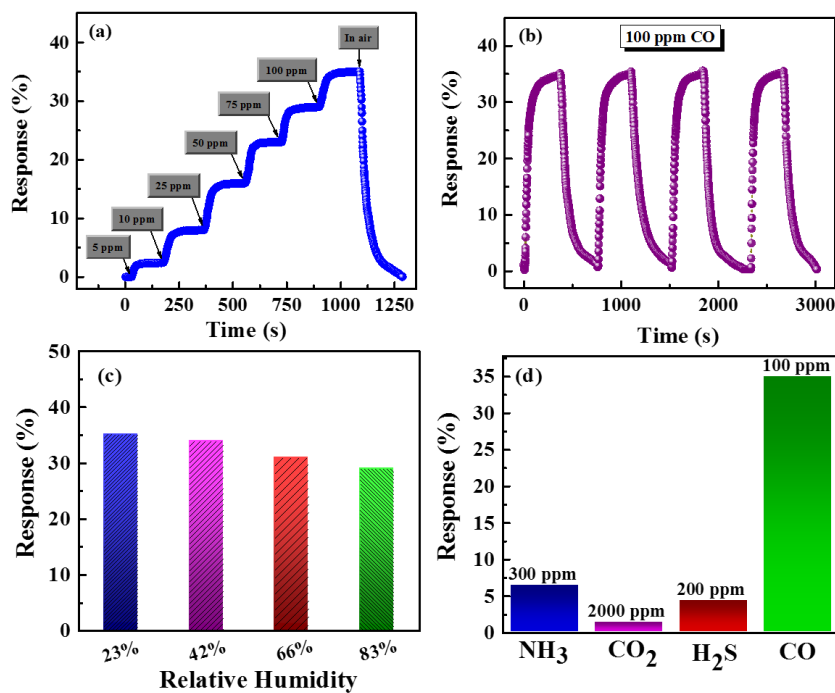


Figure 4.13. (a) Dynamic response properties to step-wise increase in CO concentration, (b) repeatability study to 100 ppm CO, (c) effect of humidity on the response, and (d) selectivity study against different gases of OZ50 sensor.

It is observed that the increase in relative humidity in the test chamber leads to slight decrease in the sensor response, as seen in Figure 4.13(c). The response measured at 23, 42, 66 and 83% relative humidity is 35.2, 34.1, 31.4 and 29.5%, respectively. The response time and recovery times are seen to rise as relative humidity rises in the test chamber, i.e.,

the response gets sluggish as the relative humidity increases. To test the selectivity parameter of the ODBA-ZnO sensor, the sensor is exposed to different other gases such as NH₃, H₂S, and CO₂ at 125 °C and the results are shown in Figure 4.13(d). As observed in Figure 4.13(d), the responses to 300 ppm NH₃, 2000 ppm CO₂, 200 ppm H₂S and 100 ppm CO are 6.3, 1.4, 4.3 and 35.21%, respectively. It is clear that among other test gases, the sensor has demonstrated stronger selectivity for CO. A comparative analysis of CO sensing properties between the ODBA-ZnO nanohybrid sensor and the previously reported CO sensors available in the literature is represented in Table 4.1.

Table 4.1. Comparative performance analysis of various CO sensors.

M	S/D	T (°C)	C (ppm)	R (%)	τ_{Res}/τ_{Rec}	S (%)	Other Test Gases	Ref.
ODBA-ZnO	Single-pot hydrothermal	125	100	35	91/175s	~ 88%	CO ₂ , NH ₃ , H ₂ S	Our work
Mesoporous carbon	Dielectrophoresis	250	30	5.7	115/211 s	NA	NA	[64]
[Rh ₂ (form) ₂ (ox)] ₄	Spin-coating	150	5000	85.7	300/200 s	~ *50	CH ₄ , NO ₂	[65]
Pt/Cr-SnO ₂	Spray Pyrolysis	275	1000	14	NM	~ *57	CH ₄ , Ethanol, NO ₂	[66]
Pd-LaCoO ₃ nanowires	Sol-gel/electrospinning	60	100	1	423/377 s	~*55	CO ₂ , NO, O ₂	[67]
CuO/rGO	LbL self-assembly	RT	100	5.33	70/160 s	~ *70	CO ₂ , NO ₂ , H ₂ , SO ₂ ,	[68]

							CH ₄ , NH ₃	
Al/ZnO nanorod	Microem ulsion method	350	100	60	11/10 min	NA	NA	[69]
M: Material, S/D: Synthesis/deposition method, C: Gas/VOC concentration, T: Operating temperature, R: Response/sensitivity, *: Calculated from given results, NM: Not addressed.								

The CO sensing properties of the sensor are comparable with other existing CO sensors [64]–[69]. However, the selectivity and response achieved by the existing CO sensors are evidently lower than the ODBA-ZnO nanohybrid sensor. The ODBA-ZnO nanohybrid sensor provided the highest selectivity of 88% to 100 ppm CO at lower operating temperature of 125 °C. As seen in Table 4.1, the ODBA-ZnO sensor not only has best selectivity but also has low optimal temperature and comparable response to CO, which is the basic requirement for the development of a low-cost, highly selective, portable CO sensor.

4.3.4. CO Sensing Mechanism

The resistance increasing response to a reducing gas like CO of ODBA-ZnO hybrid sensor cannot be explained by a conventional combustion mechanism. Therefore, an interaction between the functional group of ODBA and ZnO should exist. The probable sensing mechanism for the resistance increasing response of ODBA-ZnO hybrid could be the following: It is well-known that a covalent bond is formed between the carboxylic group of ODBA and Zn(OH)₂ during the hybrid material formation [70], [71]. This covalent bond provides a path for electric charge to transport throughout the alternating ODBA and ZnO layer. When the ODBA-ZnO sensor is exposed to gases having a stronger interaction with the hydroxyl groups of the interfaces, among these, only CO is strongly polar and could actively interact with the hydroxyl groups of the interfaces and could create complex ion at the interface. This probably blocks the charge transport path throughout the alternating

ODBA and ZnO layer. Due to this fact, the resistance of the ODBA-ZnO hybrid material increases rapidly and saturates after some time. As this reaction is bilateral, after removing CO from the surroundings of the ODBA-ZnO sensor, the complex ions vanish and the charge transport path is restored or resistance of the ODBA-ZnO hybrid material decreases.

At higher humidity, the presence of water molecule facilitates an alternating pathway for proton conduction [72]. The protons (H^+ ions) coming from water attached to ODBA augments in the electrical conduction besides the normal conduction *via* covalent bonds in ODBA. This additional conductivity in humid environment contradicts with the resistance increase in ODBA-based sensor under CO environment. Therefore, the overall response reduces in correspondence to the rise in relative humidity.

4.4. Conclusion

In conclusion, ODBA-ZnO nanohybrid material is successfully synthesized *via* the single-pot hydrothermal method. The FESEM images reveal porous and floppy structure of the ODBA-ZnO nanohybrids. The TGA analysis reveals that organic component (ODBA) decays from the ODBA-ZnO nanohybrids as temperature of the nanohybrids increases beyond 137 °C. The ODBA-ZnO nanohybrid sensor demonstrated excellent CO sensing properties at the optimal temperature of 125 °C. The nanohybrid sensor shows 35% response to 100 ppm CO at 125 °C. The optimal temperature of 125 °C for ODBA-ZnO nanohybrid sensor is also supported by the TGA analysis. The short response time of ~ 91 s and average recovery time of ~ 175 s are observed to 100 ppm CO at 125 °C. Further, the remarkable selectivity value of ~ 88% to CO is observed in comparison to other test gas like CO₂, H₂S, and NH₃. The synergetic effect between the ODBA and ZnO is the possible reason for enhancement of CO selectivity and sensitivity of the ODBA-ZnO nanohybrid sensor. This contribution reports on synthesizing ODBA-ZnO nanohybrid material for achieving

unprecedented selectivity to CO working at a low optimal operating temperature of 125 °C.

4.5. References

- [1] D. N. Bateman, “Carbon Monoxide,” *Medicine (Baltimore)*, vol. 31, no. 10, pp. 41–42, Oct. 2003.
- [2] S. H. Heinemann, T. Hoshi, M. Westerhausen, and A. Schiller, “Carbon monoxide – physiology, detection and controlled release,” *Chem. Commun.*, vol. 50, no. 28, pp. 3644–3660, Mar. 2014.
- [3] P. C. and C. Mumford, *Hazardous Chemicals Handbook Second Edition*. Butterworth-Heinemann, 2002.
- [4] S. S. Park, J. Kim, and Y. Lee, “Improved Electrochemical Microsensor for the Real-Time Simultaneous Analysis of Endogenous Nitric Oxide and Carbon Monoxide Generation,” *Anal. Chem.*, vol. 84, no. 3, pp. 1792–1796, Feb. 2012.
- [5] U. Hasegawa, A. J. van der Vlies, E. Simeoni, C. Wandrey, and J. A. Hubbell, “Carbon Monoxide-Releasing Micelles for Immunotherapy,” *J. Am. Chem. Soc.*, vol. 132, no. 51, pp. 18273–18280, Dec. 2010.
- [6] M. E. Moragues *et al.*, “Sensitive and Selective Chromogenic Sensing of Carbon Monoxide via Reversible Axial CO Coordination in Binuclear Rhodium Complexes,” *J. Am. Chem. Soc.*, vol. 133, no. 39, pp. 15762–15772, Oct. 2011.
- [7] D. Benito-Garagorri, M. Puchberger, K. Mereiter, and K. Kirchner, “Stereospecific and Reversible CO Binding at Iron Pincer Complexes,” *Angew. Chemie Int. Ed.*, vol. 47, no. 47, pp. 9142–9145, Nov. 2008.
- [8] C. Lin *et al.*, “High Performance Colorimetric Carbon Monoxide Sensor for Continuous Personal Exposure Monitoring,” *ACS Sensors*, vol. 3, no. 2, pp. 327–333, Feb. 2018.

- [9] G. S. Marks, H. J. Vreman, B. E. McLaughlin, J. F. Brien, and K. Nakatsu, "Measurement of Endogenous Carbon Monoxide Formation in Biological Systems," *Antioxid. Redox Signal.*, vol. 4, no. 2, pp. 271–277, Apr. 2002.
- [10] Y. Morimoto, W. Durante, D. G. Lancaster, J. Klattenhoff, and F. K. Tittel, "Real-time measurements of endogenous CO production from vascular cells using an ultrasensitive laser sensor," *Am. J. Physiol. Circ. Physiol.*, vol. 280, no. 1, pp. H483–H488, Jan. 2001.
- [11] B. Wang *et al.*, "Improved and excellent CO sensing properties of Cu-doped TiO₂ nanofibers," *Chinese Sci. Bull.*, vol. 55, no. 3, pp. 228–232, Jan. 2010.
- [12] T. Li, Y. Wu, J. Huang, and S. Zhang, "Gas sensors based on membrane diffusion for environmental monitoring," *Sensors Actuators B Chem.*, vol. 243, pp. 566–578, May 2017.
- [13] G. Maduraiveeran and W. Jin, "Nanomaterials based electrochemical sensor and biosensor platforms for environmental applications," *Trends Environ. Anal. Chem.*, vol. 13, pp. 10–23, Jan. 2017.
- [14] M. Bao *et al.*, "Plate-like p-n heterogeneous NiO/WO₃ nanocomposites for high performance room temperature NO₂ sensors," *Nanoscale*, vol. 6, no. 8, pp. 4063–4066, Apr. 2014.
- [15] X. Deng, L. Zhang, J. Guo, Q. Chen, and J. Ma, "ZnO enhanced NiO-based gas sensors towards ethanol," *Mater. Res. Bull.*, vol. 90, pp. 170–174, Jun. 2017.
- [16] E. P. Stuckert, C. J. Miller, and E. R. Fisher, "The Effect of Ar/O₂ and H₂O Plasma Treatment of SnO₂ Nanoparticles and Nanowires on Carbon Monoxide and Benzene Detection," *ACS Appl. Mater. Interfaces*, vol. 9, no. 18, pp. 15733–15743, May 2017.

- [17] S. K. Youn, N. Ramgir, C. Wang, K. Subannajui, V. Cimalla, and M. Zacharias, "Catalyst-Free Growth of ZnO Nanowires Based on Topographical Confinement and Preferential Chemisorption and Their Use for Room Temperature CO Detection," *J. Phys. Chem. C*, vol. 114, no. 22, pp. 10092–10100, Jun. 2010.
- [18] J.-Y. Park, S.-J. Song, and E. D. Wachsman, "Highly Sensitive/Selective Miniature Potentiometric Carbon Monoxide Gas Sensors with Titania-Based Sensing Elements," *J. Am. Ceram. Soc.*, vol. 93, no. 4, pp. 1062–1068, Apr. 2010.
- [19] D. Majumder and S. Roy, "Development of Low-ppm CO Sensors Using Pristine CeO₂ Nanospheres with High Surface Area," *ACS Omega*, vol. 3, no. 4, pp. 4433–4440, Apr. 2018.
- [20] K. Giriya, S. Thirumalairajan, V. R. Mastelaro, and D. Mangalaraj, "Catalyst free vapor–solid deposition of morphologically different β -Ga₂O₃ nanostructure thin films for selective CO gas sensors at low temperature," *Anal. Methods*, vol. 8, no. 15, pp. 3224–3235, Apr. 2016.
- [21] Y.-J. Chiang and F.-M. Pan, "PdO Nanoflake Thin Films for CO Gas Sensing at Low Temperatures," *J. Phys. Chem. C*, vol. 117, no. 30, pp. 15593–15601, Aug. 2013.
- [22] Y.-C. Chen, Y.-R. Shen, and C.-L. Hsiao, "A carbon monoxide interdigitated-capacitor gas sensor based upon a n-type Zn₂SnO₄ thin film," *J. Mater. Sci. Mater. Electron.*, vol. 29, no. 2, pp. 1658–1663, Jan. 2018.
- [23] J.-C. Ding, H.-Y. Li, Z.-X. Cai, X.-D. Zhang, and X. Guo, "LaCoO₃-based sensors with high sensitivity to carbon monoxide," *RSC Adv.*, vol. 5, no. 81, pp. 65668–65673, Jul. 2015.
- [24] M. H. Saberi, Y. Mortazavi, and A. A. Khodadadi, "Dual selective Pt/SnO₂ sensor to CO and propane in exhaust gases of gasoline engines using Pt/LaFeO₃ filter," *Sensors Actuators B Chem.*, vol. 206, pp. 617–623, Jan. 2015.

- [25] M. Hjiri, L. El Mir, S. G. Leonardi, A. Pistone, L. Mavilia, and G. Neri, "Al-doped ZnO for highly sensitive CO gas sensors," *Sensors Actuators B Chem.*, vol. 196, pp. 413–420, Jun. 2014.
- [26] M. Ahsan, T. Tesfamichael, M. Ionescu, J. Bell, and N. Motta, "Low temperature CO sensitive nanostructured WO₃ thin films doped with Fe," *Sensors Actuators B Chem.*, vol. 162, no. 1, pp. 14–21, Feb. 2012.
- [27] N. Singh, C. Yan, and P. S. Lee, "Room temperature CO gas sensing using Zn-doped In₂O₃ single nanowire field effect transistors," *Sensors Actuators B Chem.*, vol. 150, no. 1, pp. 19–24, Sep. 2010.
- [28] E. Ogel *et al.*, "Comparison of the Catalytic Performance and Carbon Monoxide Sensing Behavior of Pd-SnO₂ Core@Shell Nanocomposites," *ChemCatChem*, vol. 9, no. 3, pp. 407–413, Feb. 2017.
- [29] D. Majumder, A. Datta, M. K. Mitra, and S. Roy, "Kinetic analysis of low concentration CO detection by Au-loaded cerium oxide sensors," *RSC Adv.*, vol. 6, no. 95, pp. 92989–92995, Sep. 2016.
- [30] V. B. Kamble and A. M. Umarji, "Achieving selectivity from the synergistic effect of Cr and Pt activated SnO₂ thin film gas sensors," *Sensors Actuators B Chem.*, vol. 236, pp. 208–217, Nov. 2016.
- [31] T. Ghodselahi, H. Zahrabi, M. H. Saani, and M. A. Vesaghi, "CO Gas Sensor Properties of Cu@CuO Core-Shell Nanoparticles Based on Localized Surface Plasmon Resonance," *J. Phys. Chem. C*, vol. 115, pp. 22126–22130, 2011.
- [32] C. Wang, P. Zhao, and S. Liu, "PdO/SnO₂ hollow nanospheres for carbon monoxide detection," *Phys. status solidi*, vol. 212, no. 8, pp. 1789–1794, Aug. 2015.

- [33] L. Wang, Z. Lou, R. Wang, T. Fei, and T. Zhang, "Ring-like PdO–NiO with lamellar structure for gas sensor application," *J. Mater. Chem.*, vol. 22, no. 25, p. 12453, Jun. 2012.
- [34] M.-R. Yu, R.-J. Wu, and M. Chavali, "Effect of 'Pt' loading in ZnO–CuO hetero-junction material sensing carbon monoxide at room temperature," *Sensors Actuators B Chem.*, vol. 153, no. 2, pp. 321–328, Apr. 2011.
- [35] A. M. Azad, "Behavior of a New ZrO₂-MoO₃ Sensor for Carbon Monoxide Detection," *J. Electrochem. Soc.*, vol. 139, no. 10, p. 2913, Aug. 1992.
- [36] H. Yamaura, Y. Iwasaki, S. Hirao, and H. Yahiro, "CuO/SnO₂-In₂O₃ sensor for monitoring CO concentration in a reducing atmosphere," 2011.
- [37] L. Wang, A. U. Rehman, H. Wu, B. Wu, L. Li, and K. Shi, "Submicrochains composed of massage ball-like WO₃ @CuWO₄ composites for high-efficiency CO gas sensing applications at room temperature," *RSC Adv.*, vol. 6, no. 74, pp. 69999–70007, Jul. 2016.
- [38] N. Miura, T. Raisen, G. Lu, and N. Yamazoe, "Highly selective CO sensor using stabilized zirconia and a couple of oxide electrodes," *Sensors Actuators B Chem.*, vol. 47, no. 1–3, pp. 84–91, Apr. 1998.
- [39] C. S. Prajapati and N. Bhat, "Highly Sensitive CO Sensor Based on Thickness-Selective ZnO Thin Film: Device Fabrication and Packaging," *Cryst. Res. Technol.*, vol. 54, no. 4, p. 1800241, Apr. 2019.
- [40] A. Kaushik, R. Kumar, S. K. Arya, M. Nair, B. D. Malhotra, and S. Bhansali, "Organic–Inorganic Hybrid Nanocomposite-Based Gas Sensors for Environmental Monitoring," *Chem. Rev.*, vol. 115, no. 11, pp. 4571–4606, Jun. 2015.

- [41] S. Wang, Y. Kang, L. Wang, H. Zhang, Y. Wang, and Y. Wang, "Organic/inorganic hybrid sensors: A review," *Sensors Actuators B Chem.*, vol. 182, pp. 467–481, Jun. 2013.
- [42] M. Faustini, L. Nicole, E. Ruiz-Hitzky, and C. Sanchez, "History of Organic-Inorganic Hybrid Materials: Prehistory, Art, Science, and Advanced Applications," *Adv. Funct. Mater.*, p. 1704158, Apr. 2018.
- [43] Y. A. Shchipunov, T. Y. Karpenko, and A. V. Krekoten, "Hybrid organic–inorganic nanocomposites fabricated with a novel biocompatible precursor using sol-gel processing," *Compos. Interfaces*, vol. 11, no. 8–9, pp. 587–607, Jan. 2005.
- [44] P. Gómez-Romero *et al.*, "Hybrid organic–inorganic nanocomposite materials for application in solid state electrochemical supercapacitors," *Electrochem. commun.*, vol. 5, no. 2, pp. 149–153, Feb. 2003.
- [45] L. Tabrizi and H. Chiniforoshan, "Sonochemical synthesis of Au nanowires in the III–I oxidation state bridged by 4,4'-dicyanamidobiphenyl and their application as selective CO gas sensors," *Dalt. Trans.*, vol. 44, no. 5, pp. 2488–2495, Jan. 2015.
- [46] M. Shojaei, S. Nasresfahani, and M. H. Sheikhi, "Hydrothermally synthesized Pd-loaded SnO₂/partially reduced graphene oxide nanocomposite for effective detection of carbon monoxide at room temperature," *Sensors Actuators B Chem.*, vol. 254, pp. 457–467, Jan. 2018.
- [47] N. H. Ha, D. D. Thinh, N. T. Huong, N. H. Phuong, P. D. Thach, and H. S. Hong, "Fast response of carbon monoxide gas sensors using a highly porous network of ZnO nanoparticles decorated on 3D reduced graphene oxide," *Appl. Surf. Sci.*, vol. 434, pp. 1048–1054, Mar. 2018.
- [48] L. Dang *et al.*, "Heterostructured Co₃O₄/PEI–CNTs composite: fabrication, characterization and CO gas sensors at room

- temperature,” *J. Mater. Chem. A*, vol. 2, no. 13, pp. 4558–4565, Mar. 2014.
- [49] J.-H. Kim, A. Katoch, H. W. Kim, and S. S. Kim, “Realization of ppm-level CO detection with exceptionally high sensitivity using reduced graphene oxide-loaded SnO₂ nanofibers with simultaneous Au functionalization,” *Chem. Commun.*, vol. 52, no. 19, pp. 3832–3835, Feb. 2016.
- [50] S. F. Liu, S. Lin, and T. M. Swager, “An Organocobalt–Carbon Nanotube Chemiresistive Carbon Monoxide Detector,” *ACS Sensors*, vol. 1, no. 4, pp. 354–357, Apr. 2016.
- [51] S. Ogata, H. Tagaya, M. Karasu, and J. ichi Kadokawa, “New preparation method for organic-inorganic layered compounds by organo derivatization reaction of Zn(OH)₂ with carboxylic acids,” *J. Mater. Chem.*, vol. 10, no. 2, pp. 321–327, Jan. 2000.
- [52] T. Zhang, S. Mubeen, B. Yoo, N. V. Myung, and M. A. Deshusses, “A gas nanosensor unaffected by humidity,” *Nanotechnology*, vol. 20, no. 25, p. 255501, Jun. 2009.
- [53] I. Matsubara, K. Hosono, N. Murayama, W. Shin, and N. Izu, “Organically hybridized SnO₂ gas sensors,” *Sensors Actuators B Chem.*, vol. 108, no. 1–2, pp. 143–147, Jul. 2005.
- [54] S. Maiti, R. G. Jadhav, S. M. Mobin, T. K. Mukherjee, and A. K. Das, “Insights into the Aggregation Behaviour of a Benzoselenadiazole-Based Compound and Generation of White Light Emission,” *ChemPhysChem*, vol. 20, no. 17, pp. 2221–2229, Sep. 2019.
- [55] S. Maiti, A. R. Chowdhury, and A. K. Das, “Benzoselenadiazole-based nanoporous Covalent Organic Polymer (COP) as efficient room temperature heterogeneous catalyst for biodiesel production,” *Microporous Mesoporous Mater.*, vol. 283, pp. 39–47, Jul. 2019.

- [56] S. L. Patil, M. A. Chougule, S. Sen, and V. B. Patil, "Measurements on room temperature gas sensing properties of CSA doped polyaniline-ZnO nanocomposites," *Meas. J. Int. Meas. Confed.*, vol. 45, no. 3, pp. 243–249, Apr. 2012.
- [57] S. Verma, M. K. Manna, S. K. Pandey, A. K. Das, and S. Mukherjee, "Benzo[ghi]perylene monoimide based photosensitive lamellar Cd-doped ZnO nanohybrids," *RSC Adv.*, vol. 4, no. 107, pp. 62603–62614, Nov. 2014.
- [58] M. K. Manna, Aaryashree, S. Verma, S. Mukherjee, and A. K. Das, "Lamellar Peptide-Cadmium-Doped Zinc Oxide Nanohybrids That Emit White Light," *Chempluschem*, vol. 81, no. 3, pp. 329–337, Mar. 2016.
- [59] Aaryashree *et al.*, "Synergetic Accrual of Lamellar Nanohybrids for Band-Selective Photodetection," *J. Phys. Chem. C*, vol. 121, no. 26, pp. 14037–14044, Jul. 2017.
- [60] P. Rai and Y. T. Yu, "Synthesis of floral assembly with single crystalline ZnO nanorods and its CO sensing property," *Sensors Actuators, B Chem.*, vol. 161, no. 1, pp. 748–754, Jan. 2012.
- [61] C. Liangyuan *et al.*, "Synthesis of 1-dimensional ZnO and its sensing property for CO," *Sensors Actuators, B Chem.*, vol. 143, no. 2, pp. 620–628, Jan. 2010.
- [62] S. K. Lim, S. H. Hwang, S. Kim, and H. Park, "Preparation of ZnO nanorods by microemulsion synthesis and their application as a CO gas sensor," *Sensors Actuators, B Chem.*, vol. 160, no. 1, pp. 94–98, Dec. 2011.
- [63] D. Acharyya and P. Bhattacharyya, "Alcohol sensing performance of ZnO hexagonal nanotubes at low temperatures: A qualitative understanding," *Sensors Actuators B Chem.*, vol. 228, pp. 373–386, Jun. 2016.
- [64] C.-Y. Liu, C.-F. Chen, J.-P. Leu, C.-C. Lu, and K.-H. Liao,

- “Fabrication and carbon monoxide sensing characteristics of mesostructured carbon gas sensors,” *Sensors Actuators B Chem.*, vol. 143, no. 1, pp. 12–16, Dec. 2009.
- [65] S. Lo Schiavo, P. Piraino, A. Bonavita, G. Micali, G. Rizzo, and G. Neri, “A dirhodium(II,II) molecular species as a candidate material for resistive carbon monoxide gas sensors,” *Sensors Actuators B Chem.*, vol. 129, no. 2, pp. 772–778, Feb. 2008.
- [66] V. B. Kamble and A. M. Umarji, “Achieving selectivity from the synergistic effect of Cr and Pt activated SnO₂ thin film gas sensors,” *Sensors Actuators B Chem.*, vol. 236, pp. 208–217, Nov. 2016.
- [67] J.-C. Ding, H.-Y. Li, Z.-X. Cai, X.-X. Wang, and X. Guo, “Near room temperature CO sensing by mesoporous LaCoO₃ nanowires functionalized with Pd nanodots,” *Sensors Actuators B Chem.*, vol. 222, pp. 517–524, Jan. 2016.
- [68] D. Zhang, C. Jiang, J. Liu, and Y. Cao, “Carbon monoxide gas sensing at room temperature using copper oxide-decorated graphene hybrid nanocomposite prepared by layer-by-layer self-assembly,” *Sensors Actuators B Chem.*, vol. 247, pp. 875–882, Aug. 2017.
- [69] S. K. Lim *et al.*, “Synthesis of Al-doped ZnO Nanorods via Microemulsion Method and Their Application as a CO Gas Sensor,” *J. Mater. Sci. Technol.*, vol. 31, no. 6, pp. 639–644, Jun. 2015.
- [70] B. Mandal *et al.*, “ π -Conjugated Amine–ZnO Nanohybrids for the Selective Detection of CO₂ Gas at Room Temperature,” *ACS Appl. Nano Mater.*, vol. 1, no. 12, pp. 6912–6921, Dec. 2018.
- [71] Aaryashree *et al.*, “Functionalized Oligo(p -Phenylenevinylene) and ZnO-Based Nanohybrid for Selective Ammonia Sensing at Room Temperature,” *IEEE Sens. J.*, vol. 19, no. 8, pp. 2847–2854, Apr. 2019.

- [72] T. C. D. Doan, J. Baggerman, R. Ramaneti, H. D. Tong, A. T. M. Marcelis, and C. J. M. van Rijn, "Carbon dioxide detection with polyethylenimine blended with polyelectrolytes," *Sensors Actuators B Chem.*, vol. 201, pp. 452–459, Oct. 2014.

Chapter 5

Synthesis of ZnO/MoO₃ Composite for Methanol Sensing Application

5.1. Introduction

Methanol (CH₃OH) is a colorless, flammable and volatile organic compound used as a raw material for the production of fuel, solvents, and antifreezes, etc. Excessive concentration of methanol in the surrounding area may cause inhalation and resulting headaches and blindness etc. Unlike ethanol, the consumption of methanol is poisonous and can even lead to death. Therefore, it is very important to detect methanol in the surrounding environments. Recently lots of effort has been made by researchers to improve the sensitivity and selectivity of the methanol sensor, for example, Han *et al.* synthesized Ce-doped In₂O₃ nanosphere-based sensor displaying response of 35 towards 100 ppm methanol [1]. Tang *et al.* prepared SnO₂-ZnO composite nanofiber and the sensor response towards 50 ppm methanol is 18 [2]. Li *et al.* reported the ionic liquid-assisted synthesis of WO₃ nanoparticle for enhanced methanol sensing properties [3]. Although methanol sensors have already been investigated, the selectivity of these sensors is very poor and optimized sensor operating temperature is reasonably high. Therefore, methanol sensors with high response, high selectivity, and comparatively low operating temperature have aroused tremendous interest on account of their highlighted roles in the areas of public safety and environmental monitoring.

This chapter discusses a strategy for enhancing the VOC sensing performance of the novel rose-like ZnO/MoO₃ composite prepared *via*

hydrothermal method followed by solution-based synthesis approach, which exhibited high selectivity to methanol with moderate response.

5.2. Experimental

5.2.1. Synthesis of ZnO Microcubes

In a typical procedure, 1.48 g of zinc nitrate hexahydrate ($\text{Zn}(\text{NO}_3)_2 \cdot 6\text{H}_2\text{O}$, 0.1 M) is added in 50 mL of deionized water (resistivity = $18.0 \text{ M}\Omega\text{cm}^{-1}$) and under vigorous stirring, 2 g of sodium hydroxide pellet (NaOH, 1 M) is added to the solution. Once NaOH pellet completely dissolved in the solution (pH = 11.8), the mixed solution is then transferred into a 100 mL Teflon-lined stainless steel autoclave and kept at 120 °C for 48 h. After hydrothermal reaction, a solid white layer is formed which is collected by centrifugation, then washed several times with deionized water and finally dried at 100 °C for 6 h which yielded the white product of ZnO microcubes.

5.2.2. Synthesis of MoO₃ Micrograss

0.926 g of ammonium molybdate tetrahydrate ($(\text{NH}_4)_6\text{Mo}_7\text{O}_{24} \cdot 4\text{H}_2\text{O}$, 15 mM) is ultrasonically dispersed into 50 mL of deionized water. To this, 10 ml of nitric acid (HNO_3) is added and mixed completely under constant stirring for 15 min. The mixed solution is then transferred into a 100 mL Teflon-lined stainless steel autoclave and heated at 120 °C for 48 h with a heat pulsing is done for 1/6 of T_{HT} (T_{HT} = total heat treatment time, i.e., 48 h) and cooling off is done for 1/6 of T_{HT} , i.e., the frequency of pulsed temperature is $1/16 \text{ h}^{-1}$. After cooling down to room temperature naturally, the white product is collected by centrifugation and washed several times with deionized water. After drying at 100 °C for 6 h, a white product of α -MoO₃ micrograss like structure is obtained.

5.2.3. Synthesis of Rose-Like ZnO/MoO₃ Composite

For 1:1 molar ratio (ZnO/MoO₃(1:1)), 0.216 g of MoO₃ micrograss like powder is first dispersed in 2 ml of deionized water/methanol (1:1, v/v) solution under constant stirring. Secondly, 0.121 g of ZnO microcube powder is dispersed in 2 mL of deionized water/methanol (1:1, v/v) solution under constant stirring. The above two solutions are then mixed

and ultrasonicated for 15 min to form a uniform solution. The solution is further stirred under constant stirring of 2000 rpm at 65 °C for 30 min to form a uniform gel-like solution. Finally this solution is drop casted on top of the glass for further characterization. For 1:2 molar ratio (ZnO/MoO₃(1:2)) and 2:1 molar ratio (ZnO/MoO₃(2:1)), 0.08 g ZnO microcube and 0.287 g MoO₃ micrograss, and 0.162 g ZnO microcube and 0.143 g MoO₃ micrograss are taken respectively and the same procedure is followed as in case of 1:1 molar ratio.

5.2.4. Sensor Fabrication

Planar resistive type device is fabricated using ZnO, MoO₃ and ZnO/MoO₃ composite as sensing layers. The sensing layer is deposited using drop cast technique on top of SiO₂/Si substrate (1.5 cm × 1 cm) and calcined at 400 °C for 2 h for sensing test. Platinum contacts are made on top of sensing layer by magnetron sputtering technique (10⁻⁷ mbar) using a suitably designed metal shadow mask. The contact dimension is 1 mm × 1 mm and the distance between two lateral contacts is 5 mm. Sensor response is defined as response (%) = $|R_a - R_g|/R_a \times 100$, where, R_g is the resistance of the sensor at a given time during exposure to target gas and R_a is the resistance value of the sensor in the air ambient.

5.3. Results and Discussions

5.3.1. Morphology and Crystalline Structure

5.3.1.1. Field Emission Scanning Electron Microscopy

Figure 5.1(a) shows FESEM image of ZnO microcubes with an average side length of 2.5-3 μm. The FESEM image shown in Figure 5.1(b) reveals uniform α-MoO₃ micrograss-like structure with an average width of the grass of 1-1.5 μm. Figure 5.1(c) and (d) shows FESEM images of ZnO/MoO₃ composite before and after calcination, respectively. It can be observed that micrograss-like MoO₃ structures are transformed into petals-like structures centering on pistil-like ZnO microcube, forming a rose-like composite (Figure 5.1(c)). After calcination more dense rose-like structure is observed (Figure 5.1(d)). The average dimension of rose-like ZnO/MoO₃ composite structure is 5 μm in diameter.

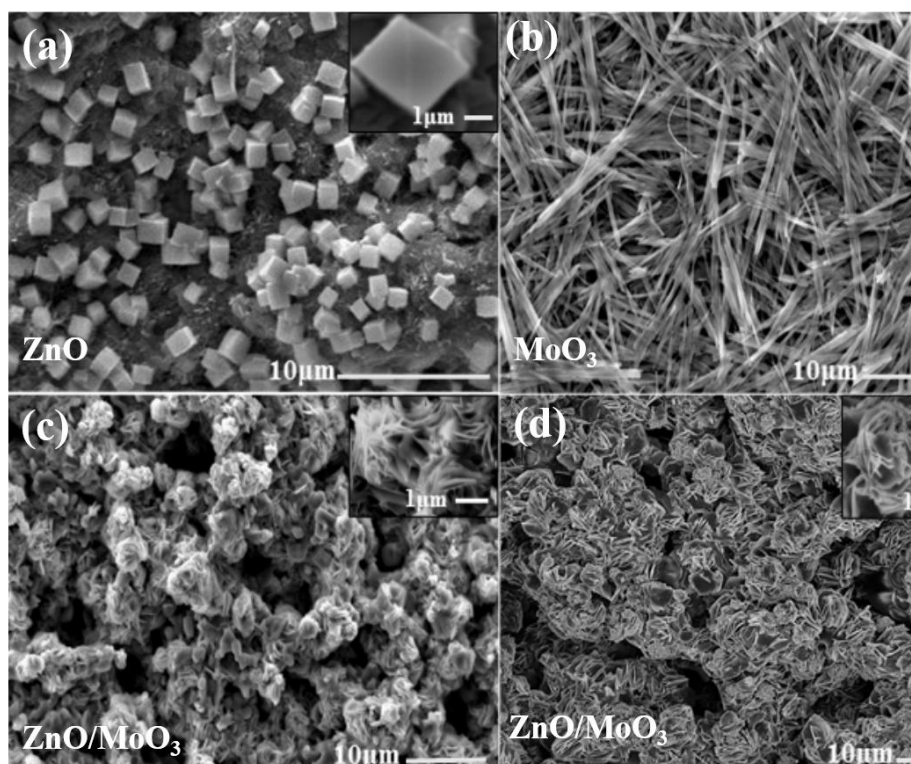


Figure 5.1. FESEM images of (a) ZnO microcubes, (a) MoO₃ micrograsses, (c) ZnO/MoO₃ composite before calcination, (d) ZnO/MoO₃ composite after calcination, respectively. Insets in (a) (c) and (d), represent magnified images of ZnO microcube and rose like composites, respectively.

5.3.1.2. X-Ray Diffraction

Figure 5.2(a) shows XRD patterns of α -MoO₃ micrograss-like structure. No diffraction peaks corresponding to impurity are observed, suggesting a high crystallinity and purity of α -MoO₃. All diffraction peaks of ZnO microcubes, as shown in Figure 5.2(b), are in good agreement with hexagonal wurtzite ZnO structure. Figure 5.2(c) shows XRD pattern of ZnO/MoO₃(1:1) composite, where all diffraction peaks corresponding to hexagonal ZnO can be observed easily. Diffraction peaks corresponding to MoO₃(020), MoO₃(040) and MoO₃(060) for orthorhombic α -MoO₃ are also observed, this implies that both ZnO and

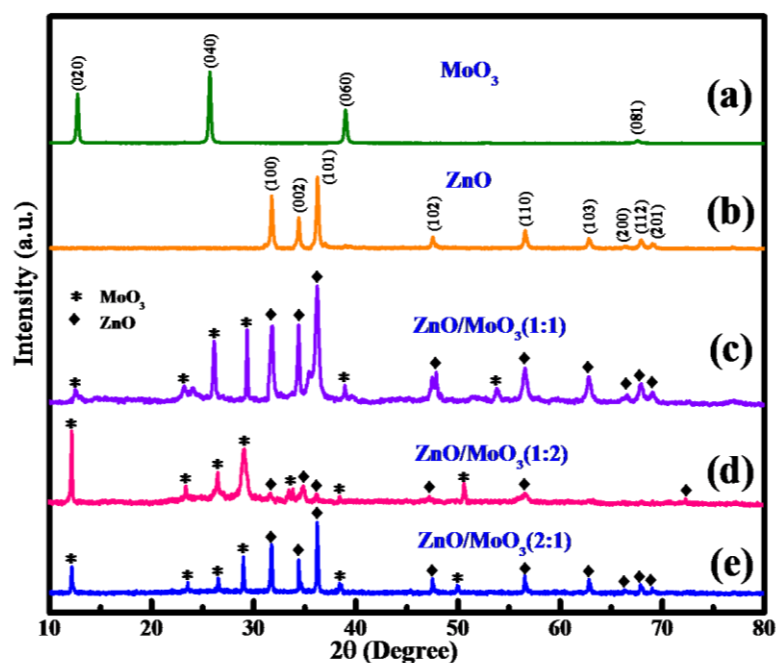


Figure 5.2. XRD pattern of (a) MoO₃ micrograss, (b) ZnO microcubes, (c) ZnO/MoO₃(1:1), (d) ZnO/MoO₃(1:2), and (e) ZnO/MoO₃(2:1) composites.

α -MoO₃ are present in the composite. However, some of the new peaks corresponding to α -MoO₃ (e.g., MoO₃(021), MoO₃(110)) are also observed in the composite, suggesting that crystal structure are deviated for α -MoO₃ in the composite. This is because MoO₃ micrograss are transformed into petal-like structure in the composite as seen in FESEM images (Figure 5.1(c)-(d)). Increasing the content of MoO₃ in the composite (ZnO/MoO₃(1:2)) results in decreasing intensity of the ZnO peaks as seen in Figure 5.2(d), suggesting the dominance of MoO₃ in the composite. Vice versa has been observed in case of increasing the content of ZnO in the composite (ZnO/MoO₃(2:1)) as seen by Figure 5.2(e).

5.3.1.3. X-Ray Photoluminescence Spectroscopy

The ZnO/MoO₃(1:1) composite is further characterized by XPS measurements. The shift of the binding energy has been observed due to the presence of adventitious carbon contamination. Figure 5.3(a), (b) and (c) represents the XPS analysis of O 1s, Zn 2p and Mo 3d core level region of the ZnO/MoO₃(1:1) composite, respectively. The peak located

at 531.6 eV corresponding to the electronic states of the O 1s. The peak located at 1026.06 eV and 1049.13 eV corresponding to Zn 2p_{3/2} and Zn 2p_{1/2}, respectively. Peak located at 229.06 eV and 235.26 eV are corresponding to doublet pattern of Mo 3d_{5/2} and Mo 3d_{3/2}. These XPS results further prove the presence of ZnO and MoO₃ in the ZnO/MoO₃ composite.

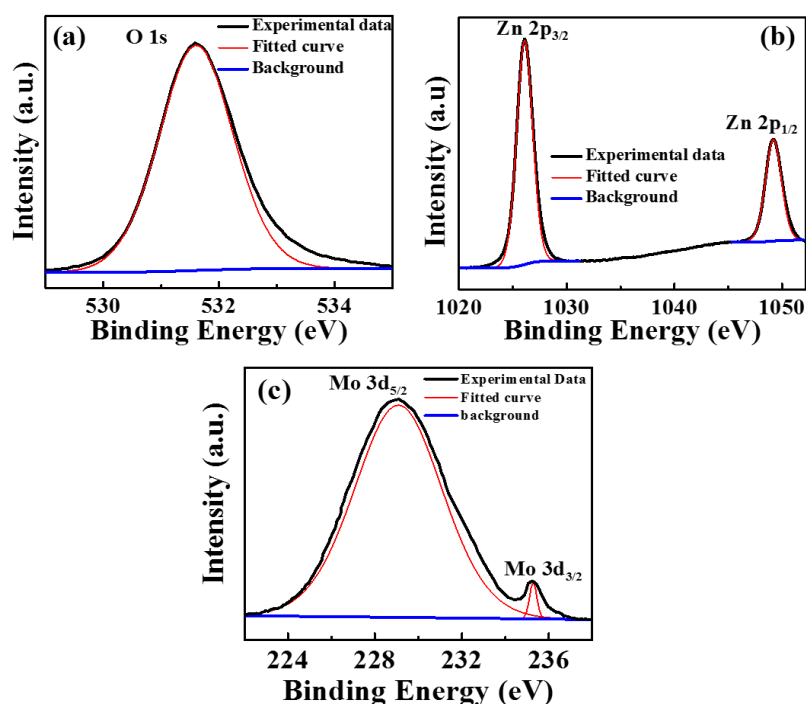


Figure 5.3. XPS spectra of ZnO/MoO₃(1:1) composite (a) O 1s core level region, (b) Zn 2p core level region, and (c) Mo 3d core level region.

5.3.1.4. Brunauer–Emmett–Teller Surface Area Analysis

The BET surface area of the grown material is evaluated by using nitrogen adsorption and desorption isotherm as shown in Figure 5.4(a), (b) and (c). The isotherm profile can be categorized as type IV with a small hysteresis loop, which indicates that mesoporous structure exists in all the MoO₃ micrograss, ZnO microcube, and ZnO/MoO₃ composite materials. The N₂-BET surface area in the low-pressure range of the ZnO microcube, MoO₃ micrograss and ZnO/MoO₃(1:1) composite is 3.84, 2.49 and 17.89 m²/g respectively. Transformation of MoO₃ micrograss-like structure into petals-like structure (evidently seen in

FESEM images of composite (Figure 5.1(c)-(d)) in the composite, led to increase the surface area of the composite dramatically.

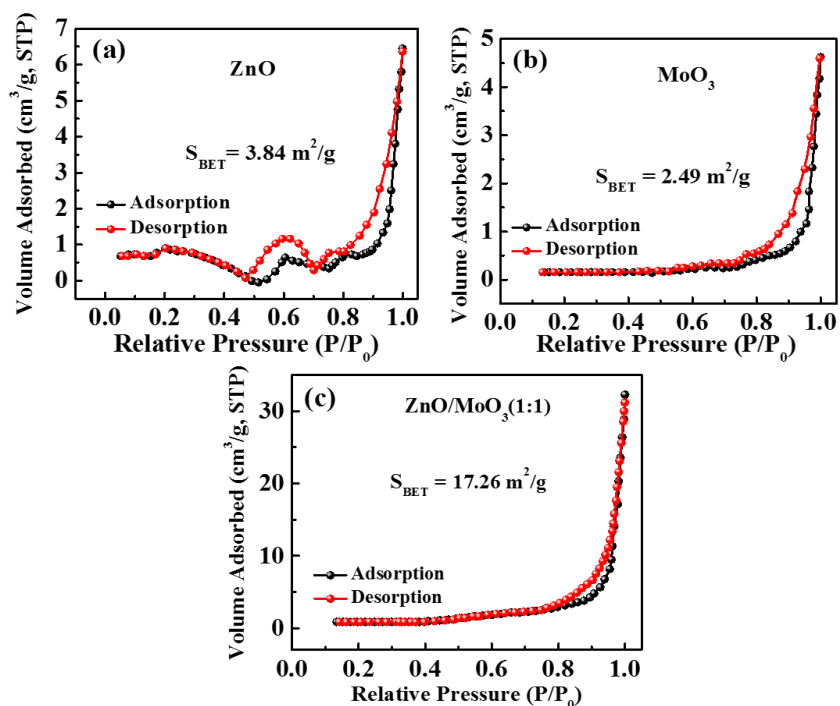


Figure 5.4. Nitrogen adsorption-desorption isotherm of (a) ZnO microcubes, (b) MoO₃ micrograss and (c) rose-like ZnO/MoO₃(1:1) composite.

5.3.1.5. Formation Mechanism

The possible formation mechanism can be described as illustrated in Figure 5.5. At the initial stage of sonication and stirring, α -MoO₃ micrograsses are attached to the wall of ZnO microcubes with the help of temperature treatment at 65 °C. While drying at 100 °C for 6 h, those surrounded micro grasses are reoriented to form petals of rose-like composite in which ZnO microcubes act as pistils. Finally, after calcination at 400 °C for 2 h, denser rose-like composite is obtained. Here one should note that, transformation of micrograss like α -MoO₃ into petal like structure has been achieved only by applying pulsed temperature during growth of α -MoO₃, in case of step temperature (constant temperature at 120 °C for 48 h) straight α -MoO₃ microbelts are obtained, which are unable to make rose-like composite.

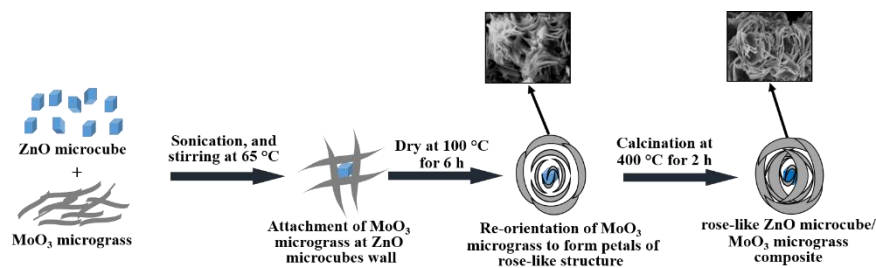


Figure 5.5. Formation mechanism of rose-like ZnO/MoO₃ composite.

5.3.2. VOCs Sensing Performance of Composite Material

It is well known that the operating temperature is an important factor for semiconductor oxide sensors for its great influence on the gas and vapor sensing process. To determine the optimum operating temperature, response (%) of all the five types of devices towards 100 ppm methanol in the air are tested as a function of operating temperature as demonstrated in Figure 5.6.

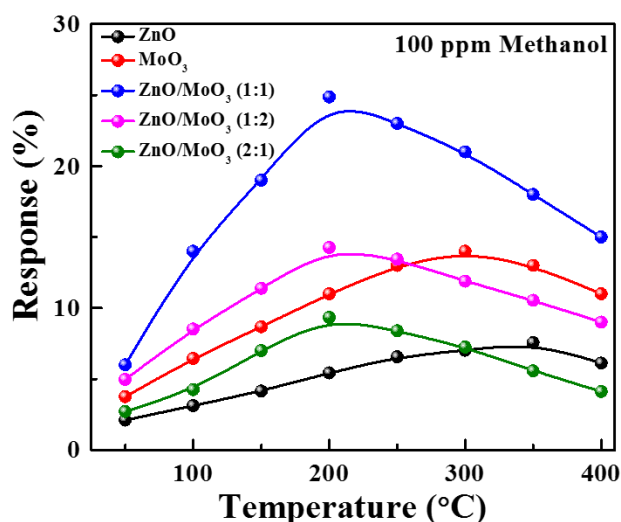


Figure 5.6. Response of 5 different devices for different temperatures at 100 ppm methanol.

As observed, the response varied with operating temperature for all the devices ranging from 50 °C to 400 °C. The response is seen to rise with increasing operating temperature up to a certain temperature and then decrease, rapidly in case of composite based sensor and slowly in case of bare metal oxide based sensors. In this case, highest response (%) exhibited by ZnO/MoO₃(1:1), ZnO/MoO₃(1:2), and ZnO/MoO₃(2:1) composite sensors are 24.87, 14.26 and 9.35, respectively, at 200 °C, after which the response decreases. Therefore, the optimum operating

temperature for composite type sensors are 200 °C. In case of MoO₃ micrograss based sensor, sensor shows maximum response of 14.11 at 300 °C, further, rise in temperature beyond 300 °C resulted in decrease in sensor response. Therefore the optimum operating temperature for MoO₃ micrograss based sensor is determined to be 300 °C. While in case of ZnO microcube based sensor, sensor exhibited maximum response of 7.56 at 350 °C, after which the response decreases slowly. Therefore, the optimum operating temperature for ZnO microcube based sensor is determined to be 350 °C. These phenomena can be understood from the mechanics and kinetics of gas adsorption-desorption on the surface of bare and composite sensors [4], [5]. At lower temperatures, slow chemical activation of composite would have led to a lower response. The initial rise in temperature would facilitate the chemical reaction and then promote the vapor response. If the operating temperature is too high, some of the adsorbed molecules could escape from the surface before those taking part in the reaction process because of their higher activation, thereby causing a reduction in the sensor response.

To investigate response-recovery characteristics for methanol sensing by the as-fabricated composite and bare sensors, methanol concentration variation sensing study has been performed in the range of 5-500 ppm at their optimized operating temperature, as shown in Figure 5.7(a)-(e). Evidently, ZnO/MoO₃(1:1) composite sensor has the highest response (%) of 56 at 500 ppm methanol. The response of ZnO/MoO₃(1:2) and ZnO/MoO₃(2:1) composite sensors are 47 and 22.63, respectively. While MoO₃ micrograss based sensor exhibited response of 42.52 at 500 ppm methanol. Response from sensor based on ZnO microcubes is observed to be the lowest of 20.18 at 500 ppm methanol. Figure 5.7(f) illustrates the response of five different types of sensors versus different concentration of methanol at their optimized operating temperature, for particular ppm response is measured 5 times repeatedly and results represented here with error bar (mean, upper and lower value). Inset of Figure 5.7(f) shows the response (%) vs. concentration in the low concentration range (5-50ppm) of methanol for all the devices.

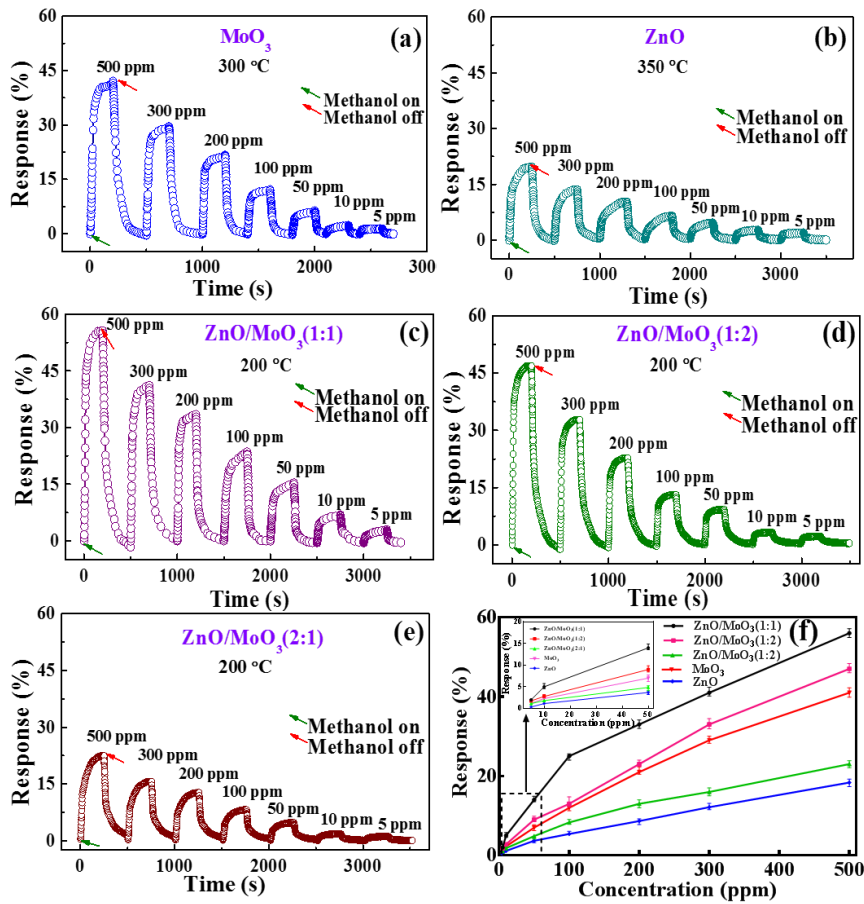


Figure 5.7. Real-time dynamic response and recovery characteristics for sensors based on (a) α - MoO_3 micrograss, (b) ZnO microcubes, (c) $\text{ZnO}/\text{MoO}_3(1:1)$, (d) $\text{ZnO}/\text{MoO}_3(1:2)$, and (e) $\text{ZnO}/\text{MoO}_3(2:1)$ composites, respectively, towards varied methanol concentrations (5-500 ppm) at their optimum operating temperature. (f) Response of 5 different type sensors as a function of methanol vapor concentration at their optimum operating temperature. Inset of Figure 5.7(f) shows response (%) vs. concentration at low concentration range of 5-50 ppm methanol.

In the range of 5-100 ppm of methanol, the response is seen to rise almost linearly with the increase of methanol concentration, in this range, $\text{ZnO}/\text{MoO}_3(1:1)$ composite sensor showed highest slope which implies that it can detect methanol very well even at low concentration (5-10 ppm).

Figure 5.8(a) shows a single cycle response and recovery characteristics of the composite sensor (1:1 molar ratio) towards 500 ppm of methanol

at 200 °C. The response and recovery time are calculated to be about 54 s and 118 s, respectively. Response time is almost half of the recovery time due to the fact that the adsorption process is faster than the desorption process on the surface of composite sensor.

The selectivity of the composite sensor is repeatedly tested by exposing it to 500 ppm of different VOC, including methanol, ethanol, 2-propanol, acetone, benzene, toluene and xylene, at 200 °C as shown in Figure 5.8(b). As observed in Figure 5.8(b), the response of composite sensor towards methanol is 56%, which is almost 2.5 times larger than ethanol (22%) and almost 5 times larger than xylene (11%). The results signify that the as-prepared rose-like ZnO/MoO₃(1:1) composite sensor displays superior selectivity (60%) towards methanol against other interference VOC.

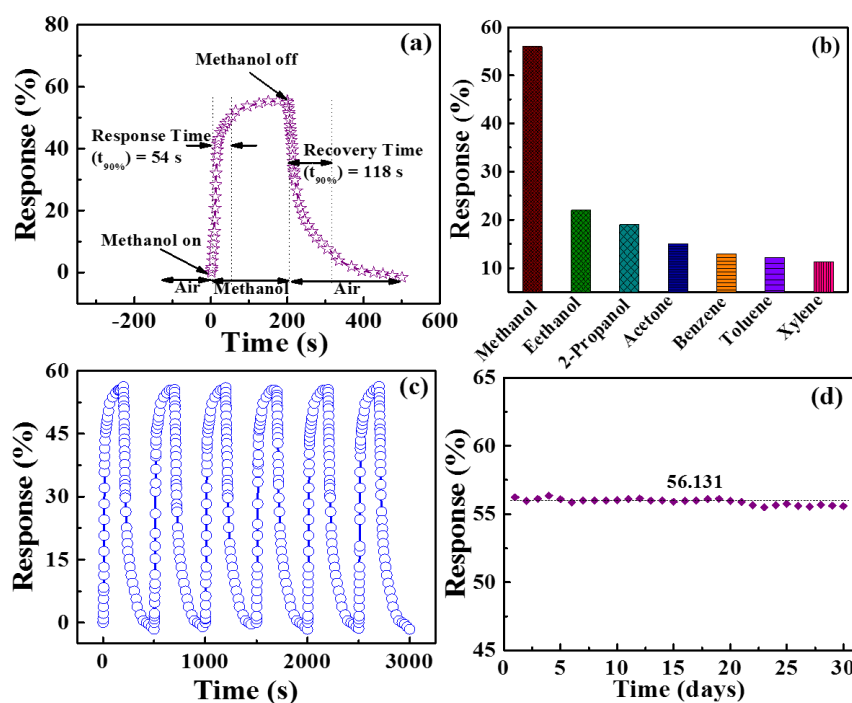


Figure 5.8. (a) Single transient response, (b) selectivity against other interference, (c) repeatability, (d) long-term stability, of the ZnO/MoO₃(1:1) composite sensor at 500 ppm methanol at the optimized operating temperature 200 °C.

In practical implementations, repeatability and the long-term stability of the VOC sensor are the two important factors for real-time monitoring of sensor signal. Figure 5.8(c) shows repeatability of the ZnO/MoO₃(1:1) composite sensor in exposure to 500 ppm methanol for continuous 6th cycles at the optimum operating temperature 200 °C, and

device shows almost constant response during sensing test. The stability of composite sensor is measured at 500 ppm methanol at the optimum operating temperature 200 °C for 30 days, and average response is measured to be 56.13, as depicted in Figure 5.8(d). It can be noted that the sensors exhibited nearly constant sensor signals during the test, indicating good stability, which is required for real-time sensor application for continuous monitoring of methanol. A comparative analysis between performance of composite sensor and other previously reported sensor is summarized in Table 5.1.

Table 5.1. Comparison of methanol sensing performance of MOX based sensors.

M	S/D	T (°C)	C (ppm)	R	S (%)	Selective against	Ref.
ZnO/MoO ₃ composite	Hydro thermal	200	500	56 [#]	60	Ethanol, 2-propanol, acetone, benzene, toluene, xylene	Our work
Al-doped ZnO thin film	Spray pyrolysis technique	275	500	44 [#]	NA	NA	[16]
Zn-doped SnO ₂ nanorod cluster	Hydro thermal	320	100	50 [*]	NA	NA	[8]
CdS doped SnO ₂	Screen-printing technology	200	5000	70 [#]	20	Acetone, LPG	[17]
ZnO nanoparticle	Spray pyrolysis technique	300	150	75.8 [*]	30	Ethanol, 2-propanol	[18]
WO ₃ nanoparticle	Hydro thermal	260	100	24.49 [*]	33	2-propanol, ethyl acetate, toluene	[3]
CuO thinfilm	DC magnetron sputtering	350	2500	29 [#]	48	Ethanol	[9]

*Response = R_a/R_g , #Response = $((R_a - R_g)/R_a) \times 100$, NM - Not Addressed, M: Material, S/D: Synthesis/deposition method, C: Methanol concentration, T: Operating temperature, R: Response/sensitivity.

It is noteworthy that composite sensor fabricated in our work exhibited the best selectivity towards methanol as compared to others reported in the literature [6], [7], as could be observed in Table 5.1. As is observed, there are various material to sense methanol such as WO₃ nanoparticle [3], Zn-doped SnO₂ nanorod cluster [8], CuO thin films [9] and so on.

However, selectivity of these sensors towards methanol is comparatively lower and optimized operating temperature is higher. On the other hand, our fabricated ZnO/MoO₃(1:1) composite sensor showed a high value of selectivity of 60% towards 500 ppm methanol at lower operating temperature of 200 °C.

5.3.3. VOCs Sensing Mechanism

ZnO and MoO₃ are typically *n*-type metal oxide semiconductors. Their response mechanism involves the interaction between the detected vapors and chemisorbed oxygen ions on the surface of the materials, leading to the resistance change of the sensor. In order to clarify the methanol sensing performance of the rose-like ZnO/MoO₃ composite sensor, a possible reaction mechanism is proposed, as presented in Figure 5.9(a). Considering the values of energy band gap and electron affinity of ZnO (3.37 and 4.35 eV) [10] and MoO₃ (3.1 and 6.7 eV) [11] at room temperature, energy band diagram of the heterojunction is plotted in Figure 5.9(b).

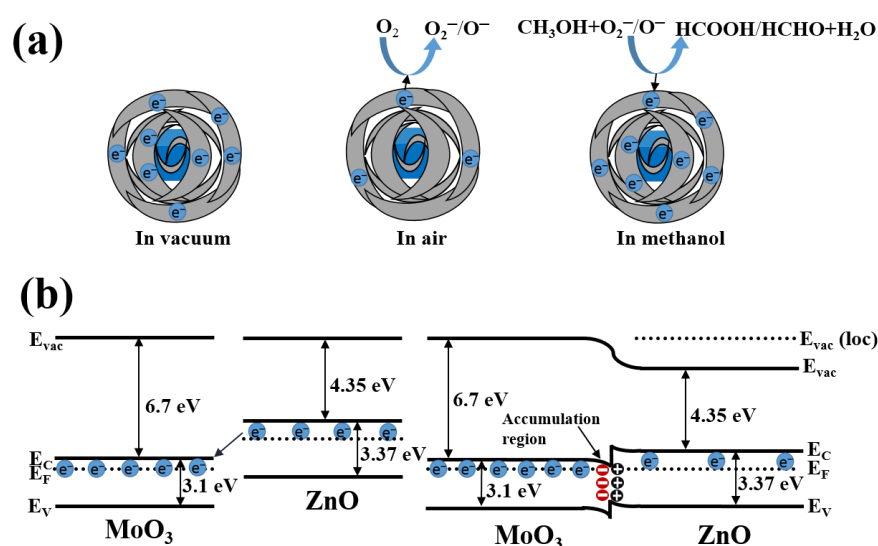
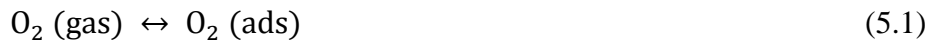
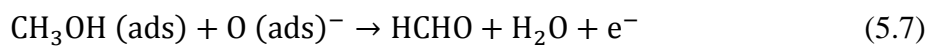


Figure 5.9. (a) Schematic diagram of the proposed reaction mechanism of the as-prepared composite in vacuum, air and methanol, respectively. (b) schematic illustration of the sensing mechanism of ZnO/MoO₃ heterostructure composite.

Under vacuum condition, due to the existence of *n*-type metal oxide and *n-n* hetero-interface of ZnO and MoO₃, the concentration of electrons in the conduction band of petal-like MoO₃ inside the rose-like composite structure is higher, as observed in Figure 5.9(a). In air, the oxygen molecules can be adsorbed onto the outer surface of these petal-like MoO₃ and can capture free electrons at the conduction band and eventually can create adsorbed O_x⁻ ions (O₂(ads)⁻, O(ads)⁻, and O(ads)²⁻) at the surface, and a thick space charge region would be formed. As a result, a surface potential barrier would be created for an electron to cross from one petal-like structure to another, which would lead to higher electrical resistance. This mechanism can be shown as follows [12]:



When the composite sensor is exposed to methanol, methanol diffuses and reacts with those adsorbed oxygen and frees the trapped electrons back into the conduction band, which leads to thinner space charge region and reduced potential barrier for an electron crossing from one petal-like MoO₃ to another, which leads to low electrical resistance. The possible reaction mechanisms with methanol are as follows [2]:



The remarkable methanol sensing and selectivity performance observed in ZnO microcube/MoO₃ micrograss based composite sensors may have two-fold reasons. First, from the FESEM images, it can be observed that MoO₃ micrograss-like structure has been transformed to petal-like structure within the rose-like composite, which indeed increases the surface area for more vapor adsorption. Second, the composite (ZnO and MoO₃) in this study causes the formation of three potential barriers such

as ZnO-ZnO, MoO₃-MoO₃ and ZnO-MoO₃. The band formation of ZnO-MoO₃ *n-n* heterojunction may play an important role in the enhancement of the sensor selectivity and sensitivity [13]–[15]. MoO₃ has lower Fermi energy level than that of ZnO, so automatically electrons at conduction band will be transferred from ZnO to MoO₃ for equalization of Fermi energy level under thermodynamic equilibrium condition, leading to the formation of an accumulation layer at MoO₃ side of the heterojunction, as presented in Figure 5.9(b). The increase of electrons on the surface of MoO₃ is able to facilitate more adsorption sites for oxygen molecules. Interestingly, in the rose-like composite, MoO₃ acts as petals for easy adsorption of oxygen molecules and more absorbed oxygen ions provides more sensing sites and shows high response. Here it should be emphasized that the probable reason for obtaining higher response for ZnO/MoO₃(1:1) composite sensor may be the availability of most number of *n-n* heterojunctions between ZnO microcube and MoO₃ petals like structure compared to other composites such as ZnO/MoO₃(1:2) and ZnO/MoO₃(2:1).

5.4. Conclusion

In summary, rose-like ZnO/MoO₃ based composites are prepared by hydrothermal followed by solution based synthesis method. The obtained samples are applied as a sensor material for detecting volatile organic compounds including ethanol, methanol, 2-propanol, acetone, benzene, etc. and their gas sensing properties are examined. It is found that the rose-like ZnO/MoO₃(1:1) composite sensor shows the best performance towards methanol compared to other sensors based on either ZnO microcube or MoO₃ micrograss. The response (%) of the ZnO/MoO₃(1:1) composite sensor to 500 ppm methanol is 56 at a low optimum operating temperature of 200 °C, which is almost 3 times than that of only ZnO microcube based sensor. Apart from the high selectivity, sensor exhibited very stable response-recovery properties and long-term stability. These favorable results suggest that as prepared rose-like ZnO/MoO₃(1:1) composite is a promising material for methanol detection.

5.5. References

- [1] D. Han, P. Song, S. Zhang, H. Zhang, Q. Xu, and Q. Wang, "Enhanced methanol gas-sensing performance of Ce-doped In_2O_3 porous nanospheres prepared by hydrothermal method," *Sensors Actuators B Chem.*, vol. 216, pp. 488–496, Sep. 2015.
- [2] W. Tang, J. Wang, P. Yao, and X. Li, "Hollow hierarchical SnO_2 -ZnO composite nanofibers with heterostructure based on electrospinning method for detecting methanol," *Sensors Actuators B Chem.*, vol. 192, pp. 543–549, Mar. 2014.
- [3] Z. Li, J. Li, L. Song, H. Gong, and Q. Niu, "Ionic liquid-assisted synthesis of WO_3 particles with enhanced gas sensing properties," *J. Mater. Chem. A*, vol. 1, no. 48, p. 15377, 2013.
- [4] L. Liu *et al.*, "Improved selective acetone sensing properties of Co-doped ZnO nanofibers by electrospinning," *Sensors Actuators B Chem.*, vol. 155, no. 2, pp. 782–788, Jul. 2011.
- [5] X. Xu *et al.*, "Effects of Al doping on SnO_2 nanofibers in hydrogen sensor," *Sensors Actuators B Chem.*, vol. 160, no. 1, pp. 858–863, Dec. 2011.
- [6] N. Yamazoe, "New approaches for improving semiconductor gas sensors," *Sensors Actuators B Chem.*, vol. 5, no. 1–4, pp. 7–19, Aug. 1991.
- [7] B. Bhowmik, V. Manjuladevi, R. K. Gupta, and P. Bhattacharyya, "Highly Selective Low-Temperature Acetone Sensor Based on Hierarchical 3-D TiO_2 Nanoflowers," *IEEE Sens. J.*, vol. 16, no. 10, pp. 3488–3495, May 2016.
- [8] X. Ding, D. Zeng, and C. Xie, "Controlled growth of SnO_2 nanorods clusters via Zn doping and its influence on gas-sensing properties," *Sensors Actuators B Chem.*, vol. 149, no. 2, pp. 336–344, Aug. 2010.
- [9] M. Parmar and K. Rajanna, "Copper (II) oxide thin film for methanol and ethanol sensing," *Int. J. SMART Sens. Intell. Syst.*, vol. 4, no. 4, pp. 710–725, 2011.
- [10] P. Sharma, R. Singh, V. Awasthi, S. K. Pandey, V. Garg, and S.

- Mukherjee, "Detection of a high photoresponse at zero bias from a highly conducting ZnO:Ga based UV photodetector," *RSC Adv.*, vol. 5, no. 104, pp. 85523–85529, Oct. 2015.
- [11] J. Meyer, A. Shu, M. Kröger, and A. Kahn, "Effect of contamination on the electronic structure and hole-injection properties of MoO₃/organic semiconductor interfaces," *Appl. Phys. Lett.*, vol. 96, no. 13, p. 133308, Mar. 2010.
- [12] S. H. Yan *et al.*, "Synthesis of SnO₂-ZnO heterostructured nanofibers for enhanced ethanol gas-sensing performance," *Sensors Actuators, B Chem.*, vol. 221, pp. 88–95, Dec. 2015.
- [13] W.-H. Zhang and W.-D. Zhang, "Fabrication of SnO₂-ZnO nanocomposite sensor for selective sensing of trimethylamine and the freshness of fishes," *Sensors Actuators B Chem.*, vol. 134, no. 2, pp. 403–408, Sep. 2008.
- [14] W. Zeng, T. Liu, and Z. Wang, "Enhanced gas sensing properties by SnO₂ nanosphere functionalized TiO₂ nanobelts," *J. Mater. Chem.*, vol. 22, no. 8, p. 3544, 2012.
- [15] Y. Liu *et al.*, "Highly sensitive and humidity-independent ethanol sensors based on In₂O₃ nanoflower/SnO₂ nanoparticle composites," *RSC Adv.*, vol. 5, no. 64, pp. 52252–52258, 2015.
- [16] P. P. Sahay and R. K. Nath, "Al-doped ZnO thin films as methanol sensors," *Sensors Actuators B Chem.*, vol. 134, no. 2, pp. 654–659, Sep. 2008.
- [17] L. Yadava, R. Verma, and R. Dwivedi, "Sensing properties of CdS-doped tin oxide thick film gas sensor," *Sensors Actuators B Chem.*, vol. 144, no. 1, pp. 37–42, Jan. 2010.
- [18] C. S. Prajapati and P. P. Sahay, "Alcohol-sensing characteristics of spray deposited ZnO nano-particle thin films," *Sensors Actuators B Chem.*, vol. 160, no. 1, pp. 1043–1049, Dec. 2011.

Chapter 6

Synthesis of MoO₃ Nanostructures for Ethanol Sensing Application

6.1. Introduction

Ethanol (CH₃CH₂OH) is an important raw material used in the manufacture of organic chemicals, gasohol, preservatives, medicine and alcoholic beverages. Ethanol sensors are used for biomedical processing, food quality control, breathing analysis, and chemical reaction monitoring. Thus, the detection of ethanol with high sensitivity and accuracy is the current market demand. MoO₃ is known to be a good candidate for ethanol sensing due to its high ethanol sensitivity. In the last decade, a significant efforts have been invested by researchers to improve MoO₃ nano-morphology based ethanol sensor. For example, Fangxu *et al.* [1] have synthesized grinding and sonication based 2D-MoO₃ nanosheets and their fabricated sensor shows good response as compared to that of bulk-MoO₃. Chen *et al.* [2] have prepared single crystalline MoO₃ nanoplates via an acid-base reaction, which has shown an enhanced sensing performance to ethanol vapor. Yunusi *et al.* [3] have reported the fabrication of MoO₃ sub-micron belt sensor, which has exhibited good sensing response for ethanol. In addition, Yan *et al.* [4] have synthesized hierarchical MoO₃ nanostructures and their fabricated sensor has excellent ethanol sensing properties. However, all these sensors have exhibited either low selectivity or high operating temperature, and, therefore, there is still a need for improvement of MoO₃ nanostructure-based ethanol sensor. To improve the ethanol sensing properties of MoO₃ nanostructures further, tailoring of MoO₃

nanostructures is the key concept to achieve defect-controlled and well-defined MoO₃ nanostructures with nanoscale dimensions and high surface to volume ratio [5].

This chapter discusses a novel path to tailor the MoO₃ nanostructures from nanobelts to ultra-long nanofibers, which exhibited excellent selectivity as well as high sensitivity to ethanol.

6.2. Experimental Section

6.2.1. Synthesis of MoO₃ Nanocrystals

In a typical synthesis, ammonium heptamolybdate tetrahydrate ((NH₄)₆Mo₇O₂₄·4H₂O (1 g)) is dissolved in 50 mL of distilled water under constant stirring at room temperature. After 15 min of stirring, 10 mL nitric acid (HNO₃) is added slowly into the solution. After next 15 min of stirring, the obtained transparent solution is transferred to a 100 mL stainless steel Teflon-lined autoclave. Then, the autoclave is heated to 120 °C. One set of the experiment is done under constant temperature (120 °C) for different reaction times of 6 h (sample M₁), 12 h (sample M₂), 24 h (sample M₃), and 48 h (sample M₄), as shown in Figure 6.1.

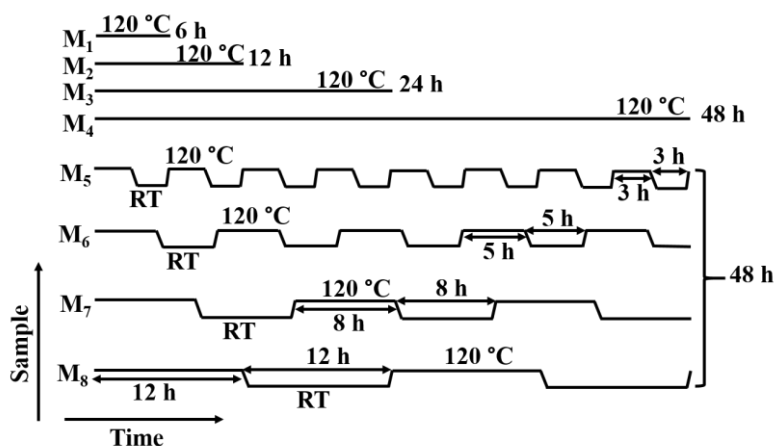


Figure 6.1. Schematic of growth plan for all the samples (M₁-M₈).

In another case, we considered the total time for heat treatment (T_{HT}) constant for 48 h, however, we repeated the process of heating (at 120 °C, heater ON) and cooling off (room temperature, RT, heater is OFF) for samples in autoclave periodically in order to observe the

morphological modifications. For sample M₅, heat pulsing (heater is ON) is done for 1/16 of T_{HT} and cooling off (heater is OFF) is done for 1/16 of T_{HT}, i.e., the frequency of pulsed temperature is 1/6 h⁻¹; for sample M₆, heat pulsing is done for 5/48 of T_{HT} and cooling off is done for 5/48 of T_{HT}, i.e., the frequency of pulsed temperature is 1/10 h⁻¹; for sample M₇, heat pulsing is done for 1/6 of T_{HT} and cooling off is done for 1/6 of T_{HT}, i.e., the frequency of pulsed temperature is 1/16 h⁻¹; and for sample M₈, heat pulsing is done for 1/4 of T_{HT} and cooling off is done for 1/4 of T_{HT}, i.e., the frequency of pulsed temperature is 1/24 h⁻¹. The complete synthesis process flows are shown in Figure 6.1. After the hydrothermal reaction, the white precipitate is collected through centrifugation and washed many times with absolute ethanol and distilled water in succession and finally dried at 70 °C for 3 h for further characterization.

6.2.2. Sensor Fabrication

As obtained MoO₃ nanostructured powder is mixed in 2 mL DI water and stirred for 15 min to get a uniform solution. After this process, the solution is drop casted on top of the interdigitated electrode (Pt) coated SiO₂/Si substrate (1.5 cm × 1 cm) and calcined at 300 °C for 2 h for sensing test. The interdigitated electrode is made on the top of SiO₂/Si substrate by magnetron sputtering technique (background pressure = 10⁻⁷ mbar) with the help of a suitably designed shadow mask. Sensor response is defined as, response = (R_a/R_g), where R_a is the sensor resistance in air and R_g is the sensor resistance in VOC vapor.

6.3. Results and Discussions

6.3.1. Structural and Morphological Characteristics

6.3.1.1. X-Ray Diffraction

The X-ray diffraction (XRD) patterns of the MoO₃ nanostructures grown at constant temperature for different reaction time and for constant reaction time with different temperature pulsing are shown in Figure 6.2. All the MoO₃ nanostructures grown in these process exhibit three significant peaks (020), (040) and (060), which can be indexed to orthorhombic α -MoO₃ (JCPDS: 35-0609) [6]. No foreign peaks are

observed and this indicates that a high purity α -MoO₃ nanobelts and nanofibers are obtained. In Figure 6.2, it can be easily observed that, under different reaction times, the diffraction peak intensities increase with the reaction time increase and achieve the maximum at 48 h reaction time (M₄ sample). In the case of pulsed temperatures of various

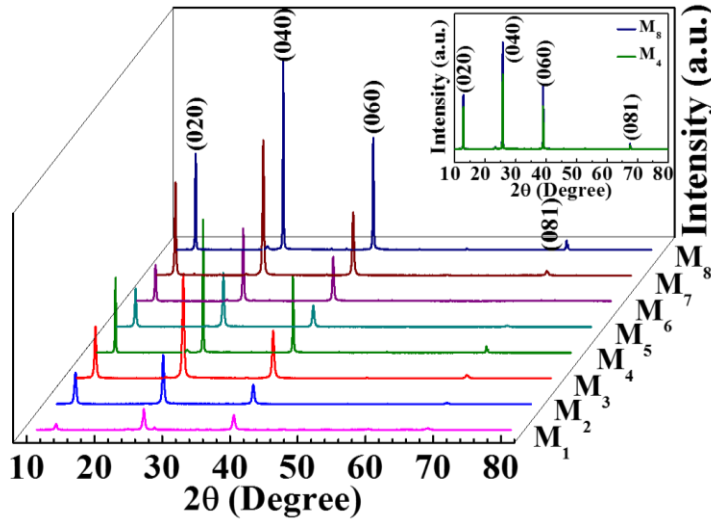


Figure 6.2. XRD pattern of M₁-M₈ samples. Inset shows comparison of diffraction peak intensity of M₈ and M₄ samples.

frequencies at constant reaction time, the diffraction peak intensities increase with the frequency decrease and reached a maximum at 1/24 h⁻¹ frequency (M₈ sample). However, it should be noted that intensities of M₈ sample are higher than that of sample M₄ as shown in the inset of Figure 6.2, indicating that the adoption of frequency dependent pulsed temperature improves the crystalline quality of MoO₃. The crystallite size is calculated by using Debye-Scherer equation,

$$D_{hkl} = \frac{k\lambda}{\beta \cos\theta} \quad (6.1)$$

where D_{hkl} refer to the mean linear dimension of the crystal perpendicular to the (hkl) plane, λ is the X-rays wavelength (1.54 Å for Cu-K α), β (radians) is the FWHM, θ is the diffraction angle and constant k value is 0.89. For each sample, the crystallite size is calculated using most intense peak (040) around $2\theta = 25.69^\circ$. The crystallite sizes calculated using above equation are 21.8, 23.4, 24.1 and 54.5 nm for the

M₁, M₂, M₃ and M₄ samples, respectively, and 28, 31.7, 36.3 and 54.3 nm for M₅, M₆, M₇ and M₈ samples, respectively. It can be noted that, crystallite size increases with increase of reaction time in the samples grown at a constant temperature for different reaction time. On the other hand, the crystallite size increases with decreasing frequency of pulsed temperature in the samples prepared under various temperature pulses at a constant time.

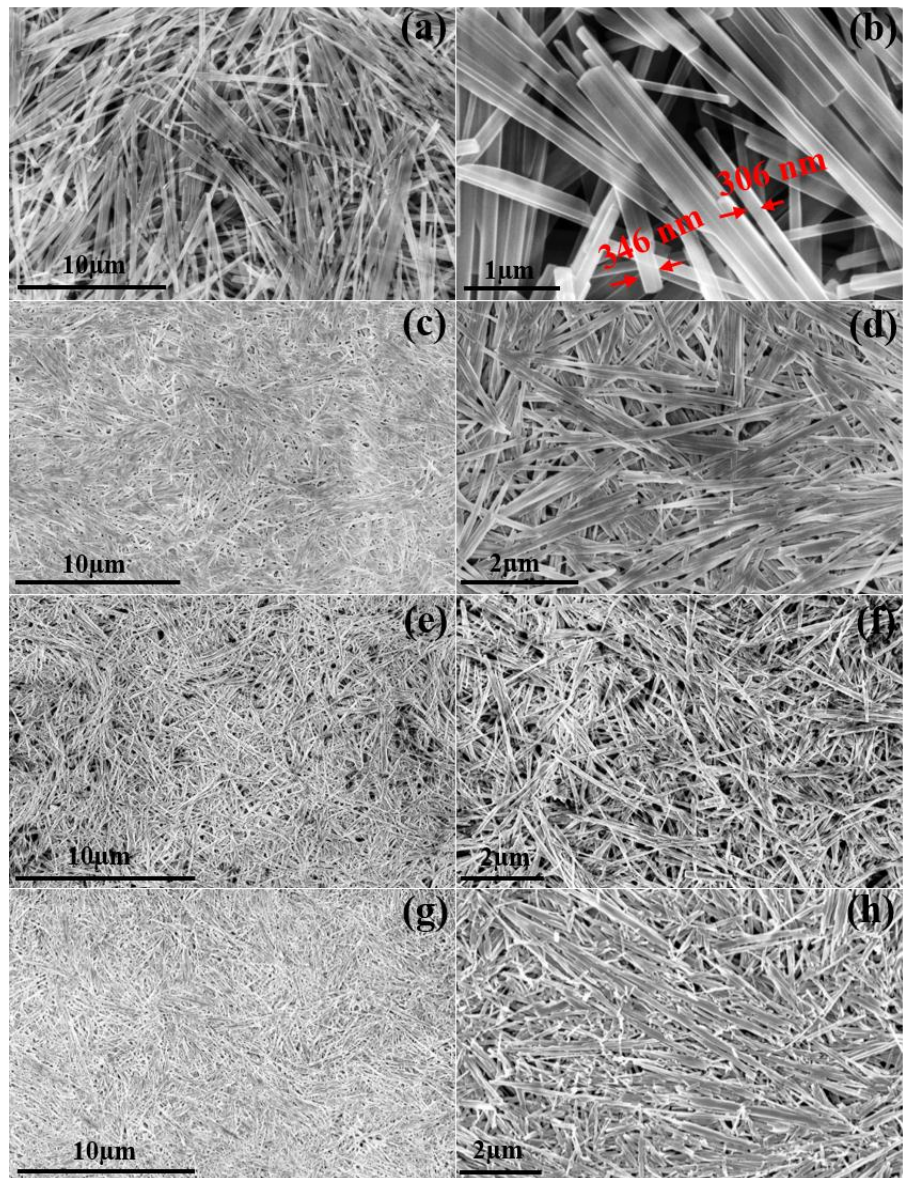


Figure 6.3. FESEM images of samples M₄ (a-b), M₃ (c-d), M₂ (e-f), and M₁ (g-h) which are grown at constant temperature for different reaction time.

6.3.1.2. Field Emission Scanning Electron Microscopy

Figure 6.3(a)-(h) shows the FESEM images of nanostructured MoO₃ obtained at constant temperature of 120 °C for 6, 12, 24 and 48 h of reaction time. The M₁ sample synthesized for 6 h of reaction time (Figure 6.3(g)-(h)), shows particles different in size and most of the belts have a distorted shape.

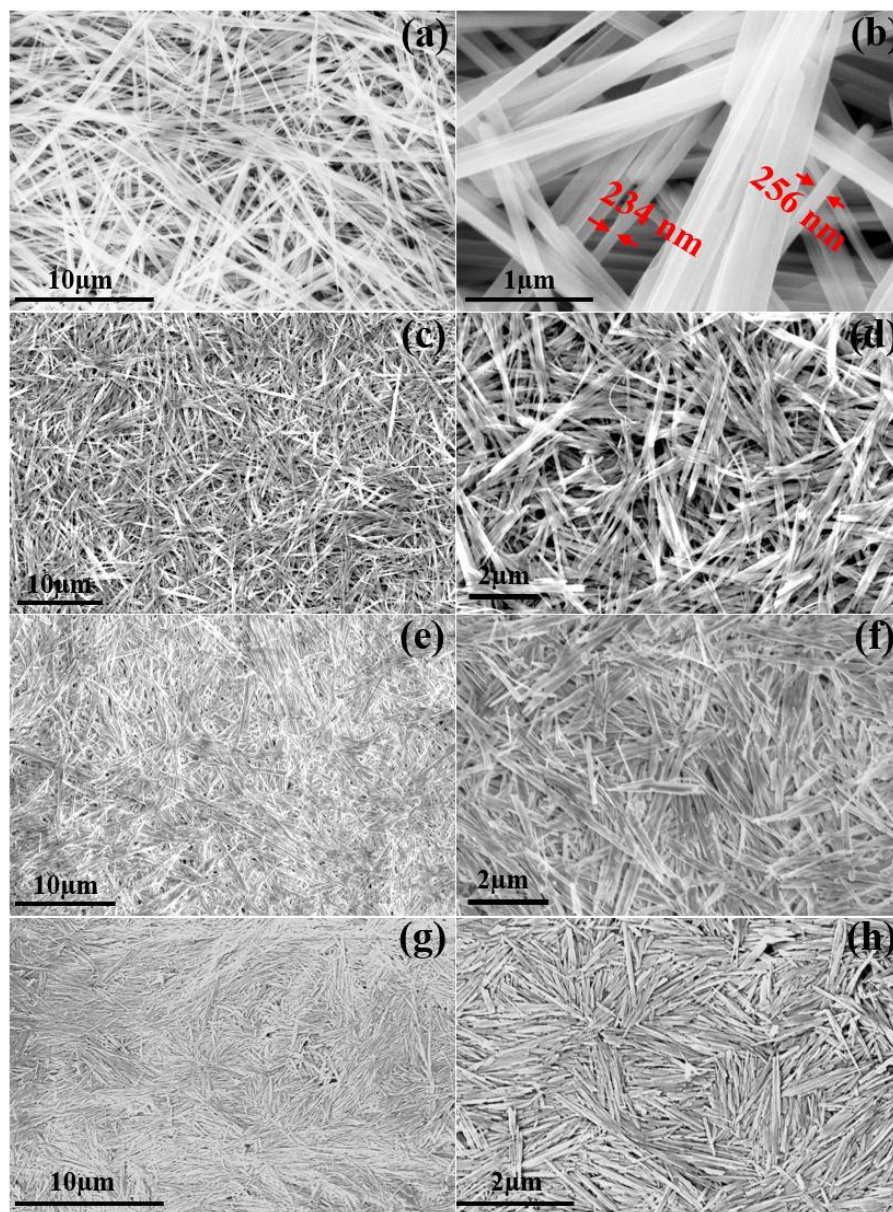


Figure 6.4. FESEM images of samples M₈ (a-b), M₇ (c-d), M₆ (e-f), and M₅ (g-h) which are grown at constant time (48 h) with different frequency of pulsed temperature.

However, increasing reaction time to 12 h (sample M₂ (Figure 6.3(e)-(f))) and 24 h (sample M₃ (Figure 6.3(c)-(d))), non-uniform belts are gradually grown in uniform size and shape to a symmetrical morphology. Finally, at longer reaction time, i.e., at 48 h (sample M₄ (Figure 6.3(a)-(b))) monodispersed distribution of nanobelts are formed with typical lengths of about 10-20 μm and the width is in the range of 300-400 nm.

Figure 6.4(a)-(h) shows FESEM images of nanostructured MoO₃ obtained at 120 °C for 48 h with different frequency of pulsed temperature process. The sample synthesized at a higher frequency of 1/6 h⁻¹ (sample M₅ (Figure 6.4(g)-(h))) and 1/10 h⁻¹ (sample M₆ (Figure 6.4(e)-(f))), shows a uniform distribution of shorter length nanobelts with tip at the end. As frequency decreases to 1/16 h⁻¹ (sample M₇ (Figure 6.4(c)-(d))), the belts have a tendency to transform to nanofiber-like forms, and, at this frequency, a mixture of nanobelts and nanofibers is observed. Also, the nanobelts length increases in the [0k0] direction, and crystal quality improves significantly as it is indicated by intensities of the XRD peaks. A complete change in morphology is observed at a lower frequency of 1/24 h⁻¹ (sample M₈ (Figure 6.4(a)-(b))), where all the nanobelts are completely transformed into highly crystalline ultra-long nanofibers. The length of the nanofibers is several tens of micrometer and the width is in the range of 200-300 nm.

6.3.1.3. Transmission Electron Microscopy

Figure 6.5(a) and (b) show STEM and TEM images of MoO₃ nanofibers, respectively. These figures reveal that high crystalline and uniform nanofibers with 200-300 nm width and lengths of several tens of micrometers are obtained. Figure 6.5(c) shows HR-TEM image of a single nanofiber, the interplanar spacing along (100) and (001) planes are determined to be 0.39 and 0.36 nm, respectively. Near the surface, the whitish shell region is probably a defective region which is created by the application of pulsed temperature during hydrothermal growth. Figure 6.5(d) shows the SAED pattern of a MoO₃ nanofiber, which is

recorded perpendicular to the growth axis of the nanofiber and can be indexed to the [010] zone of orthorhombic α - MoO_3 . The [001] direction of the electron diffraction pattern is parallel to the fiber axis, indicating that the growth occurs along the [001] direction. Also, the spot pattern of SAED further confirms nanofibers are single crystalline in nature.

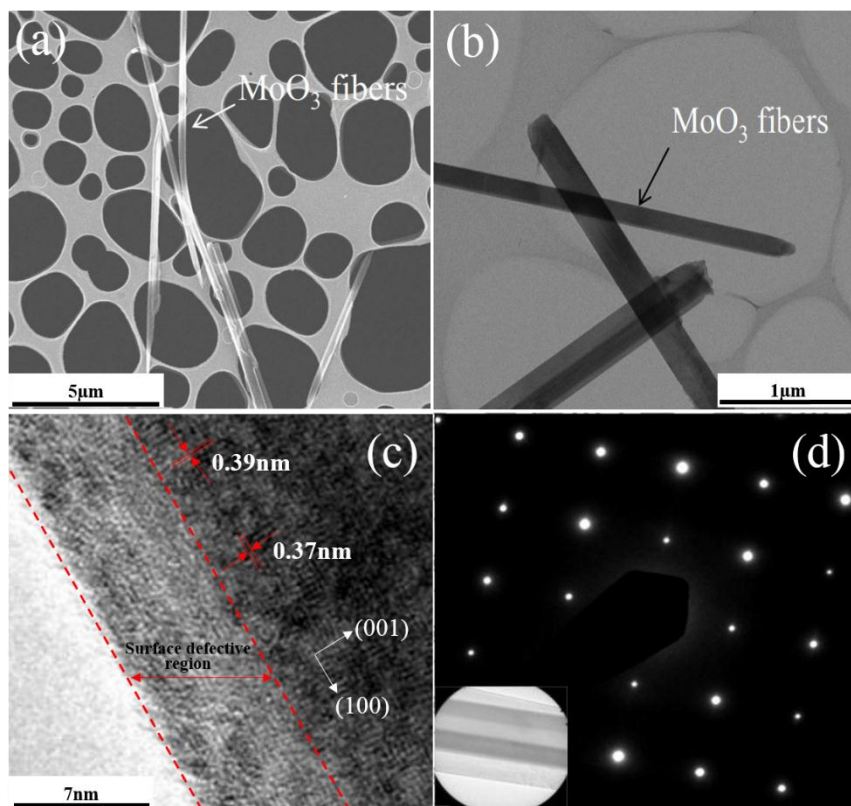


Figure 6.5. (a) STEM image of MoO_3 nanofibers on the TEM grid, (b) TEM image of MoO_3 nanofibers, showing width in 200-300 nm range (c) and (d) are HRTEM and SAED pattern of the nanofibers, respectively.

6.3.1.4. Brunauer–Emmett–Teller Surface Area Analysis

The BET surface area and pore volume of the MoO_3 nanofibers and nanobelts are evaluated by using nitrogen adsorption and desorption isotherm, as shown in Figure 6.6(a) and (b). The isotherm profile can be considered as type IV with a small hysteresis loop, which specifies that MoO_3 nanofibers and nanobelts comprise of mesoporous structure. The N_2 -BET surface area in the low-pressure range of MoO_3 nanofibers (M_8 sample) is calculated to be $4.48 \text{ m}^2/\text{g}$ and the total pore volume is 0.0019

cc/g, and for MoO₃ nanobelts (sample M₄) it is observed to be 2.37 m²/g and 0.0013 cc/g.

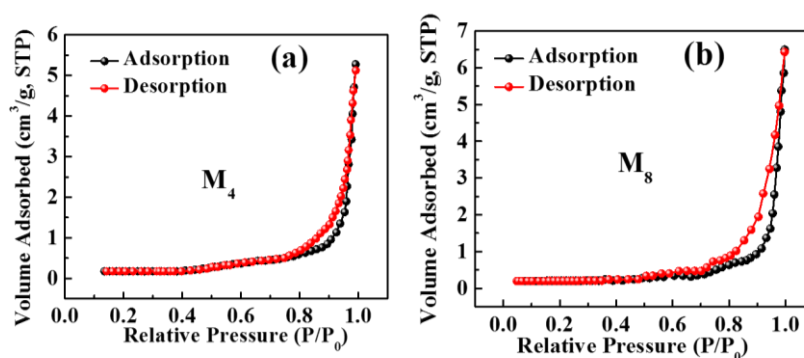
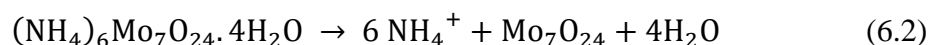


Figure 6.6. BET surface analysis of (a) MoO₃ nanobelts (M₄) and (b) MoO₃ nanofibers (M₈) samples.

6.3.1.5. Growth Mechanism

The functional properties of the nanostructures are predominantly determined by their growth mechanism. From the above experimental results, it is confirmed that, due to higher Mo:H⁺ ratio (1:25), temperature above the boiling point of water and longer reaction time lead to domination of α -MoO₃ nucleation process from the beginning without the appearance of h-MoO₃ metastable crystal phase. The formation mechanism of α -MoO₃ nanobelts can be divided into three successive phases: (1) formation of α -MoO₃ nuclei (2) formation of α -MoO₃ crystal nucleus arrays via self-assembly process (3) formation of α -MoO₃ nanobelts through Ostwald ripening. At the initial phase, the reaction between reactant reagents i.e. ammonium heptamolybdate tetrahydrate, nitric acid, and water lead to the formation of Mo₇O₂₄⁶⁻, NH₄⁺, H⁺, OH⁻, and NO₃⁻ ions in the solution as below:



The reaction between these ionized species leads to the formation of α -MoO₃ nuclei *via* equation (5). After this, MoO₃ crystal nuclei aggregate

together to minimize the surface energy and then self-assemble into arrays to form distorted and non-uniform nanobelts. Finally, the non-uniform distorted nanobelts are transformed into monodispersed nanobelts through Ostwald ripening process over time as shown in Figure 6.7(a). The formation of nanofiber like MoO_3 has been achieved by simply applying two cycles of temperature, i.e., at $1/24 \text{ h}^{-1}$ frequency (time period of 24 h). In the first cycle (12 h), the formation of $\alpha\text{-MoO}_3$ nuclei, self-assembly and incomplete ripening occur to form irregular shape and size of nanobelts. In the second cycle, for certain period of time, the rapid growth of the nanobelts in the $[0k0]$ direction occurs due to already formed $\alpha\text{-MoO}_3$ nuclei and $\alpha\text{-MoO}_3$ crystal nucleuses arrays in the first cycle, thereby changing shape from nanobelt to nanofiber like structure as shown in Figure 6.7(b).

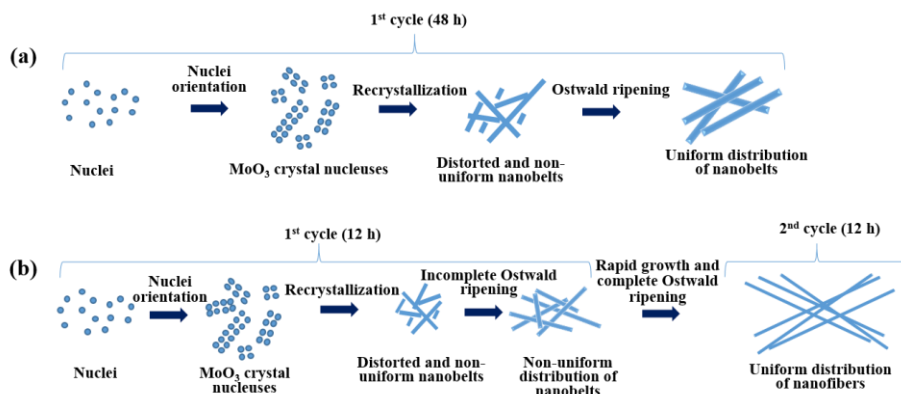


Figure 6.7. Schematic of growth mechanism of (a) MoO_3 nanobelts and (b) nanofibers.

After a certain time, the growth process stops due to the unavailability of $\alpha\text{-MoO}_3$ nuclei. At this time, the removal of lattice oxygen process starts due to the hydrogen reduction process, in the presence of excess H^+ ions in the solution. Reduction initially involved the removal of weaker oxygen anions; the stronger ones require more severe reduction conditions [7]. This reduction process creates more surface area and defect sites in MoO_3 nanofibers which is beneficial for enhanced gas/VOCs sensing application [8]. As frequency increases to $1/16 \text{ h}^{-1}$, first and second cycle growth is similar to the case of nanofibers growth, however, after the second cycle, growth rate slows dramatically and

reduction process continues. Here, it should be noted that effective growth time is 8 h in the first cycle and another 8 h in the second cycle thereby decreasing the length of the belts and fibers. Increasing frequency to $1/10 \text{ h}^{-1}$ and $1/6 \text{ h}^{-1}$, here, the growth process is for few cycles in the beginning and in the rest of the cycles reduction process dominates. As a result, due to a decrease in effective growth time, only the nanobelts are observed with shorter length and tip at the ends. At this point, it is worth to mention that, how the vacancies are created by the application of frequency dependent pulsed temperature. In case of pulsed temperature, during 2nd, 3rd, or 4th cycle of growth, hydrogen reduction process dominates over continual growth process. Here, the reduction process causes loss of oxygen atoms from the molybdenum oxide lattice. As a result of this, valance state of Mo reduces, and depend upon the reduction condition, Mo valance state may vary from Mo^{6+} to Mo^{4+} or even lower valance states ($\text{Mo}^{\delta+}$, $0 < \delta < 3$) [9]. However, the mechanism of reduction and specific nature of these valance state is not well understood yet. Nevertheless, the probable formation mechanism of different Mo valance state is shown in Figure 6.8 [7].

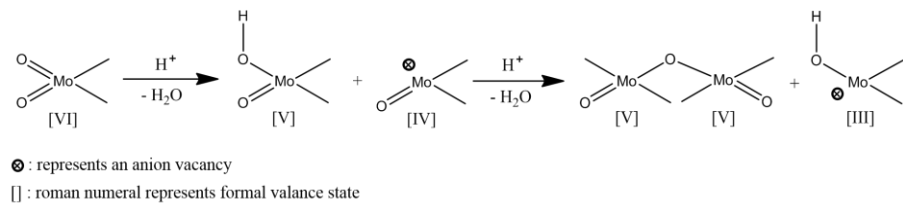


Figure 6.8. Reduction mechanism of different Mo valance state.

At first, proton is chemisorbed by the nonbridge oxygen anions of Molybdenum, as a result, Mo^{5+} formed with a hydroxyl group in it [10]. At the same time, Mo^{4+} is also produced by removing water from the Mo oxide with an oxygen vacancy in it. Further, in the presence of proton, dehydroxylation of Mo^{5+} occur by the removal of water to produce a pair of Mo^{5+} , and further hydrogenation of the Mo^{4+} lead to formation of Mo^{3+} with a vacancy and OH in it. Such active sites are very effective for exchanging hydrogen between gases and solid [11], [12], in other words these active sites are very useful for gas sensing application.

It is observed that, as frequency of the pulsed temperature increases, the crystal quality of the MoO₃ nanostructures degrade, i.e., at low frequency the crystal quality is highest (as seen in Figure 6.2). There is also a relationship between the vacancy generation and the frequency of the pulsed temperature. At low frequency, a greater number of vacancies are created on the complete and stable MoO₃ nanostructures, and vacancies are uniform throughout the surface. However, at higher frequency, lower density and non-uniform vacancies are formed at the surface of incomplete and unstable MoO₃ nanostructures. This fact can be understood by the sample response to ethanol in the proceeding section. It can be observed that, M₈ sample displays maximum and M₅ minimum response to a particular concentration of ethanol. Also, vacancies in a high crystalline MoO₃ nanostructure provides a superior carrier transport path, which may be the reason for faster response and recovery time in M₈ sample as compared to other samples. These facts reveals that, low frequency pulsed temperature during hydrothermal growth is optimal frequency for gas sensing application.

6.3.2 Ethanol Sensing Properties

The as-synthesized MoO₃ nanostructures are used as a sensing material for fabricating chemical sensor. Here, M₁-M₈ samples used to make the devices are named as M₁-M₈ devices. The gas sensing properties of which are evaluated using various VOCs, including ethanol, methanol, isopropanol, benzene, toluene, xylene, and acetone. The response of a MOX semiconductor gas sensor is extremely influenced by its operating temperature, which is a well-known fact.

In the beginning, 100 ppm ethanol vapor is used to perform gas sensing tests for all the devices at a varying operating temperature to define the optimum operating temperature for all the devices (M₈-M₁). The test results are shown in Figure 6.9. Initially, it is observed that, as the temperature increases, the response increases and attains a peak value at a certain temperature. However, from that temperature, the response decreases as temperature increases further for all the devices (M₈-M₁).

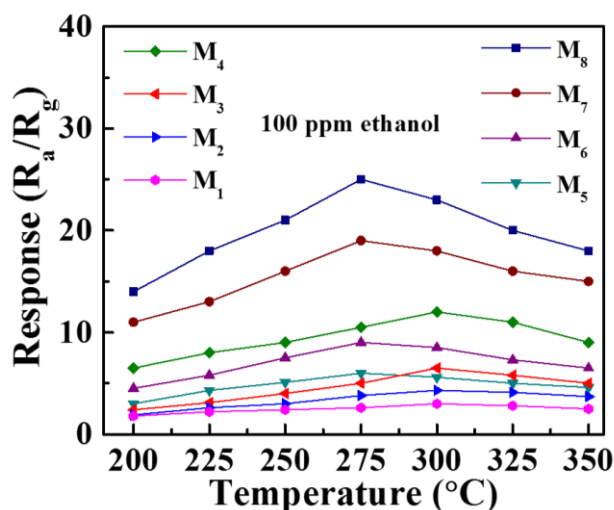


Figure 6.9. Response of M₁-M₈ devices in exposure to 100 ppm ethanol at different measurement temperatures.

The sensors made of MoO₃ nanobelts (which are grown at constant temperature for different reaction time, i.e., M₄-M₁ devices) show relatively higher optimum operating temperature of 300 °C compared to the sensors made of nanofibers and nanobelts (which are grown at pulsed temperature process, i.e., M₈-M₅ devices) which show optimum operating temperature of 275 °C. The response of M₄-M₁ devices measured under 100 ppm ethanol at the optimum operating temperature (300 °C) are 12, 6.5, 4.3 and 3 respectively, whereas for M₈-M₅ devices it is 25, 19, 9 and 6 at 275 °C optimum operating temperature. Evidently, sensor based on MoO₃ nanofibers, which are grown by frequency dependent pulsed temperature, shows higher sensitivity for ethanol compared to sensors based on MoO₃ nanobelts, which are grown at constant temperature.

All the other sensing response tests are further carried out at their optimized operating temperature for comparison. Figure 6.10(a) and (c) show real-time response-recovery characteristics of the sensors based on MoO₃ nanobelts (which are grown at constant temperature for different reaction time, i.e., M₄-M₁ devices) and MoO₃ nanofibers and nanobelts (which are grown at pulsed temperature method, i.e., M₈-M₅ devices) measured under various concentrations (10-200 ppm) of ethanol at their optimum operating temperature, respectively. Obviously, at all ethanol

concentrations, the sensor based on MoO₃ nanofibers (M₈ device) exhibited higher response than other sensors based on MoO₃ nanobelts. The maximum response observed for MoO₃ nanofibers based sensor (M₈ device) is 53 at 200 ppm ethanol, whereas sensor based on mixture of MoO₃ nanobelts and nanofibers, i.e., M₇ device shows second highest response of 38 at 200 ppm ethanol and sensor based on uniform MoO₃ nanobelts, i.e., M₄ device shows third highest response of 21 at 200 ppm ethanol.

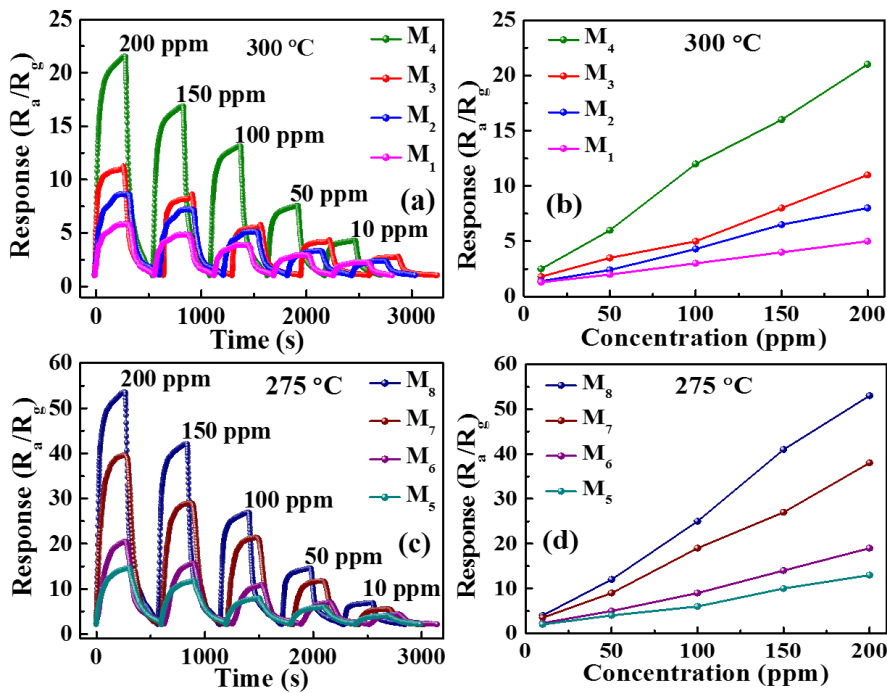


Figure 6.10. Real-time dynamic response and recovery characteristics of (a) M₁-M₄, (c) M₅-M₈ devices and corresponding response vs. concentration plot of (b) M₁-M₄, (d) M₅-M₈ devices.

The significantly improved response of MoO₃ nanofibers demonstrates advantages of frequency dependent pulsed temperature growth over constant temperature growth. Figure 6.10(b) and (d) show response vs. concentration curves of M₄-M₁ and M₈-M₅ devices, respectively, which shows that the response increases to a different extent with increasing gas concentration for all the devices. The MoO₃ nanofibers (M₈) and a mix of nanofibers and nanobelts (M₇) show responses of approximately 4-53 and 3.5-38, respectively, at 10-200 ppm ethanol. In contrast, the

uniform nanobelts (M_4) shows a relatively lower response of about 2.5-21 at 10-200 ppm ethanol. The results suggest that, for detecting ethanol, the response of M_8 - M_5 devices, i.e., those grown at a frequency dependent pulsed temperature are obviously better than that of M_4 - M_1 devices, i.e., those grown at constant temperature for different reaction time.

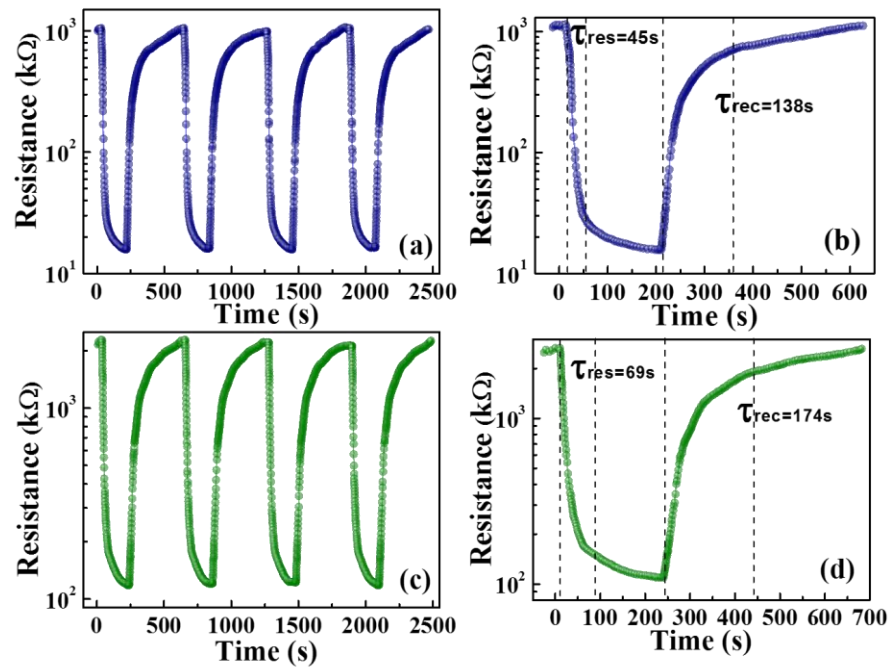


Figure 6.11. (a) and (c) shows repeatability study of M_8 and M_4 device, (b) and (d) shows single-cycle response and recovery characteristics of M_8 and M_4 device.

Figure 6.11(a) and (c) show the response-recovery characteristics of M_8 and M_4 devices for continuous four cycles corresponding to 200 ppm ethanol at their optimal operating temperature. Clearly, it can be seen that the sensor response is consistent throughout the cycles without any hysteresis to repeated exposure of 200 ppm ethanol; showing an outstanding reproducibility and stability of the sensors. Figs. 6.11(b) and (d) show single-cycle response and recovery characteristics of M_8 and M_4 devices, respectively. It is clear that, for both types of sensors, the sensor response changes quickly upon exposure to ethanol. However, more time is required to remove adsorbed ethanol from the surface of these MoO_3 nanostructures upon exposure to air. The response and

recovery times of the M_8 and M_4 devices are (45, 138) and (69, 174) s, respectively. Expectedly, the sensor based on MoO_3 nanofibers (M_8 device) shows faster response and recovery times compared to sensor based on MoO_3 nanobelts (M_4 device). For practical applications, gas sensors are required not only to have high sensitivity, quick response and recovery times, but also a very good selectivity towards specific molecules. Therefore, the responses of the two sensors (i.e., M_8 and M_4 device) for various VOCs including methanol, propanol, benzene, toluene, xylene, acetone, and ethanol are tested to measure the selectivity of the sensors.

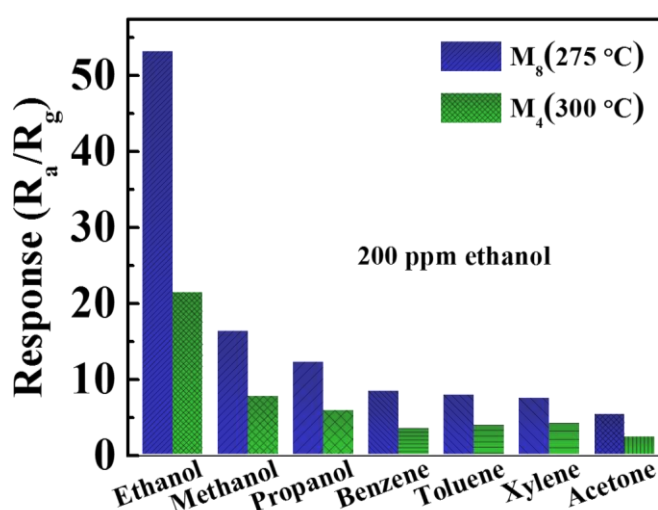


Figure 6.12. Selectivity study of M_8 and M_4 sample at their optimum operating temperature in exposure to 200 ppm of different VOCs.

As shown in Figure 6.12, the responses of the MoO_3 nanofibers based sensor (M_8 device) for the six VOCs are all higher in comparison to those of the MoO_3 nanobelts based sensor (device M_4). In addition, the sensor based on MoO_3 nanofibers (M_8 device) shows a superior response to ethanol as compared to the other VOCs. The response is 3.5-10.6 times higher than those for other tested VOCs, which indicates an excellent selectivity to ethanol. The enhanced response of MoO_3 nanofibers (M_8 device) based sensor compared to the MoO_3 nanobelts

(device M₄) based sensor is attributed to the almost double surface area and more surface defects present in MoO₃ nanofibers [8].

In addition, a comparison of ethanol sensing performance between our MoO₃ nanofibers and nanobelts based sensor and literature reported MoO₃ nanostructured based sensors is presented in Table 6.1.

Table 6.1. Comparison of ethanol sensing properties of various MoO₃ nanostructures.

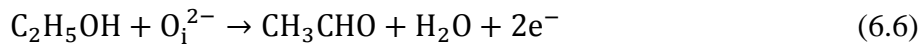
M	T (°C)	C (ppm)	R	Ref.
MoO ₃ nanofibers	275	200	53	Our Work
MoO ₃ nanobelts	300	200	21	Our Work
MoO ₃ nanoplates	300	200	40	[2]
MoO ₃ submicron belts	370	200	15	[3]
MoO ₃ nanorods	300	1000	112	[13]
Net-like porous MoO ₃	350	200	17	[14]
MoO ₃ hollow microtubules	240	200	36	[15]
MoO ₃ microrod	300	600	14	[16]
MoO ₃ nanorod	200	200-600	<20	[17]
M: Material, S/D: Synthesis/deposition method, C: Gas/VOC concentration, T: Operating temperature, R: Response/sensitivity				

It can be noted from the Table 6.1 that, all the MoO₃ nanostructures based ethanol sensor reported so far, mostly focuses on increasing surface area of the nanostructures by following a particular synthesis method, which result in poor sensitivity and selectivity. However, up to now, there is still no report on controlling the defects (which are beneficial for sensing application) as well as the surface area in MoO₃ nanostructures, showing superior ethanol sensing performance as discussed in our work. It also can be noted that, the MoO₃ nanofibers sensor in our work exhibits the better ethanol sensing characteristics

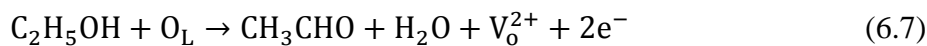
compared to other nanostructured MoO₃ sensors reported previously. These results strongly prove that the frequency dependent pulsed temperature is a new way to tailor metal oxide nanostructures for getting high sensitivity and selectivity in the field of VOC/gas sensing applications.

6.3.3. Ethanol Sensing Mechanism

Though MoO₃ is an *n*-type metal oxide semiconductor, its gas sensing mechanism is mainly driven by lattice oxygen (i.e., interstitial oxygen (O_i²⁻) and oxygen vacancies (V_o²⁺)) rather than chemisorbed oxygen [18]. MoO₃ is known to be a very good catalyst for oxidation reaction, which is useful for sensing various organic compounds [13], [19], [20]. At a defective MoO₃ crystal surface, interstitial oxygen (O_i²⁻) and oxygen vacancies (V_o²⁺) coexist under defect equilibrium, and it can be written as follows:



or



As a result of these reactions, the concentration of interstitial oxygen decreases and concentration of oxygen vacancy increases. However, in both the reactions, the generation of free electrons occurs, i.e., conductivity of the MoO₃ increases or resistance decreases in reducing gas. Also, since vacancy is a donor and interstitial oxygen is an acceptor, the increase of donors and decrease of acceptors result in a gas response increase. At this point it is worth to mention that application of frequency dependent pulsed temperature during hydrothermal growth creates more defect in MoO₃ nanofibers, which facilitate superior ethanol sensing performance compared to MoO₃ nanobelts which are grown at constant temperature or even better sensing performance than those previously reported MoO₃ nanostructures based ethanol sensors [2], [3], [13]. Also, it is important to explain the reason for high response to ethanol as compared to other volatile organic compounds. The

formation of dehydrogenated ionic fragments of the organic molecules, by the surface oxygen vacancies of the MoO₃ nanofibers, is primarily depend by their dissociative ionization energy [21]. In case of alcohol, during the dehydrogenation reaction, surface oxygen vacancies of the MoO₃ nanofibers activate the C-O and O-H bonds of alcohol and consequently dissociate into [CH₃O]⁻, [CH₃CH₂O]⁻, and [CH₃CH₂CH₂O]⁻ fragments. Such dissociation probability is determined by electron donating ability of the organic molecules (e.g., ethanol), which is also determined by the Feshbach resonances energy of the organic molecules [21]. Lower the Feshbach resonances energy implies better electron donation ability or easy dissociation of organic molecules. It has reported earlier that Feshbach resonances energy for ethanol dissociation is lower (8.2 eV) than the methanol (10.2 eV) and propanol (12.1 eV) [22], [23]. As a result, the dissociation of ethanol on the surface of the MoO₃ nanofibers is higher than that of methanol and propanol. This could be the primary reason for the high response towards ethanol among the other alcohol. In case of aromatic hydrocarbon (e.g., benzene, toluene, and xylene) and acetone, these are adsorbed on the surface of the metal oxide surface only at the presence of surface adsorbed oxygen, as aforementioned, MoO₃ does not have adsorb oxygen or rare adsorbed oxygen, therefore the response to these VOCs are very low as compared to ethanol. Also, absence of dehydrogenation reaction for these compounds results in a very low response.

6.4. Conclusion

In conclusion, the influence of frequency dependent pulsed temperature on the morphological, structural and VOCs sensing properties of hydrothermally grown MoO₃ nanostructures is systematically investigated. At first, the reaction time was optimized, while keeping the concentration of reaction reagents and temperature constant for uniform growth of MoO₃ nanobelts. Further, at the optimal reaction time, the frequency-dependent pulsed temperatures are applied for a structural modification. In this process, dimensions, morphology,

and crystallinity of the nanostructures are significantly transformed by the applied frequency dependent pulsed temperature. The applied constant temperature for a longer period of time revealed the uniform nanobelt growth, whereas applied low-frequency pulsed temperature showed uniform nanofiber growth. The XRD pattern analysis reveals that all the nanostructures formed in these processes are highly crystalline orthorhombic α -MoO₃. Compared to other MoO₃ nanostructures, VOCs sensing properties of the MoO₃ nanofibers based sensor exhibited the best response for ethanol. The improvement of sensing performance could be due to the enhancement of surface area and surface defects present in the MoO₃ nanofibers. These results suggest that the as-synthesized MoO₃ nanofibers material is a promising candidate for ethanol sensor.

6.5. References

- [1] F. Ji *et al.*, “2D-MoO₃ nanosheets for superior gas sensors,” *Nanoscale*, vol. 8, no. 16, pp. 8696–8703, Apr. 2016.
- [2] D. Chen *et al.*, “Single-crystalline MoO₃ nanoplates: topochemical synthesis and enhanced ethanol-sensing performance,” *J. Mater. Chem.*, vol. 21, no. 25, p. 9332, Jun. 2011.
- [3] T. Yunusi, C. Yang, W. Cai, F. Xiao, J. Wang, and X. Su, “Synthesis of MoO₃ submicron belts and MoO₂ submicron spheres via polyethylene glycol-assisted hydrothermal method and their gas sensing properties,” *Ceram. Int.*, vol. 39, no. 3, pp. 3435–3439, Apr. 2013.
- [4] H. Yan, P. Song, S. Zhang, Z. Yang, and Q. Wang, “Facile fabrication and enhanced gas sensing properties of hierarchical MoO₃ nanostructures,” *RSC Adv.*, vol. 5, no. 89, pp. 72728–72735, Aug. 2015.
- [5] S. Wang *et al.*, “Enhanced HCHO gas sensing properties by Ag-loaded sunflower-like In₂O₃ hierarchical nanostructures,” *J.*

- Mater. Chem. A*, vol. 2, no. 18, pp. 6598–6604, Apr. 2014.
- [6] V. V. Atuchin *et al.*, “Sublimation growth and vibrational microspectrometry of α -MoO₃ single crystals,” *J. Cryst. Growth*, vol. 318, no. 1, pp. 987–990, Mar. 2011.
- [7] J.-G. Choi and L. T. Thompson, “XPS study of as-prepared and reduced molybdenum oxides,” *Appl. Surf. Sci.*, vol. 93, no. 2, pp. 143–149, Feb. 1996.
- [8] S. Bai *et al.*, “Ultrasonic synthesis of MoO₃ nanorods and their gas sensing properties,” *Sensors Actuators B Chem.*, vol. 174, pp. 51–58, Nov. 2012.
- [9] W. C. Moshier, “Surface Chemistry of Sputter-Deposited Al-Mo and Al-Cr Alloys Polarized in 0.1N KCl,” *J. Electrochem. Soc.*, vol. 136, no. 2, p. 356, Feb. 1989.
- [10] J. G. Choi, R. L. Curl, and L. T. Thompson, “Molybdenum nitride catalysts. I. Influence of the synthesis factors on structural properties,” *J. Catal.*, vol. 146, no. 1, pp. 218–227, Mar. 1994.
- [11] J.-G. Choi, J. R. Brenner, C. W. Colling, B. G. Demczyk, J. L. Dunning, and L. T. Thompson, “Synthesis and characterization of molybdenum nitride hydrodenitrogenation catalysts,” *Catal. Today*, vol. 15, no. 2, pp. 201–222, Jun. 1992.
- [12] J. M. J. G. Lipsch and G. C. A. Schuit, “The CoOMoO₃Al₂O₃ catalyst. III. Catalytic properties,” *J. Catal.*, vol. 15, no. 2, pp. 179–189, Oct. 1969.
- [13] N. Illyaskutty *et al.*, “Alteration of architecture of MoO₃ nanostructures on arbitrary substrates: Growth kinetics, spectroscopic and gas sensing properties,” *Nanoscale*, vol. 6, no. 22, pp. 13882–13894, Oct. 2014.
- [14] W. Zeng, H. Zhang, Y. Li, and W. Chen, “Net-like MoO₃ porous architectures: synthesis and their sensing properties,” *J. Mater. Sci. Mater. Electron.*, vol. 25, no. 1, pp. 338–342, Jan. 2014.

- [15] P. Song, Q. Wang, J. Li, and Z. Yang, "Morphology-controllable synthesis, characterization and sensing properties of single-crystal molybdenum trioxide," *Sensors Actuators B Chem.*, vol. 181, pp. 620–628, May 2013.
- [16] K. Galatsis *et al.*, "Comparison of single and binary oxide MoO₃, TiO₂ and WO₃ sol–gel gas sensors," *Sensors Actuators B Chem.*, vol. 83, no. 1–3, pp. 276–280, Mar. 2002.
- [17] E. Comini, L. Yubao, Y. Brando, and G. Sberveglieri, "Gas sensing properties of MoO₃ nanorods to CO and CH₃OH," *Chem. Phys. Lett.*, vol. 407, no. 4–6, pp. 368–371, May 2005.
- [18] A. Bielański and J. Haber, "Oxygen in Catalysis on Transition Metal Oxides," *Catal. Rev.*, vol. 19, no. 1, pp. 1–41, Jan. 1979.
- [19] S. S. Sunu, E. Prabhu, V. Jayaraman, K. I. Gnanasekar, T. K. Seshagiri, and T. Gnanasekaran, "Electrical conductivity and gas sensing properties of MoO₃," *Sensors and Actuators B-Chemical*, vol. 101, no. 1–2, pp. 161–174, Jun. 2004.
- [20] Z. Li, Y. Li, E. Zhan, N. Ta, and W. Shen, "Morphology-controlled synthesis of α -MoO₃ nanomaterials for ethanol oxidation," *J. Mater. Chem. A*, vol. 1, no. 48, p. 15370, 2013.
- [21] D. Acharyya and P. Bhattacharyya, "Alcohol sensing performance of ZnO hexagonal nanotubes at low temperatures: A qualitative understanding," *Sensors Actuators B Chem.*, vol. 228, pp. 373–386, Jun. 2016.
- [22] A. J. Fletcher, E. J. Cussen, D. Bradshaw, M. J. Rosseinsky, and K. M. Thomas, "Adsorption of Gases and Vapors on Nanoporous Ni₂(4,4'-Bipyridine)₃(NO₃)₄ Metal–Organic Framework Materials Templated with Methanol and Ethanol: Structural Effects in Adsorption Kinetics," *J. Am. Chem. Soc.*, vol. 126, no. 31, pp. 9750–9759, Aug. 2004.
- [23] A. Hazra, K. Dutta, B. Bhowmik, and P. Bhattacharyya, "Highly

Repeatable Low-ppm Ethanol Sensing Characteristics of p -TiO₂-Based Resistive Devices,” *IEEE Sens. J.*, vol. 15, no. 1, pp. 408–416, Jan. 2015.

Chapter 7

Simulation and Realization of Readout Circuits towards the Development of Lab-Based Portable Gas/VOC Sensors

7.1. Introduction

Increasing human activity led to life on the planet under the threat of ambient pollution and exposed to various toxic gases. In order to avoid these issues the demand of low cost and high accuracy portable gas/VOC sensing system is increasing every year. The MOX based chemiresistive sensors are ideal candidate to fulfil this criteria due to their low fabrication cost and high sensitivity to target gas/VOC at an elevated temperature. The lab developed MOX based resistive sensors must be integrated with the electronic circuitry in order to use them as a handheld/portable device for practical detection of gases/VOCs. The base resistance of the MOX based sensors could vary from some $k\Omega$ to as high as few $G\Omega$, and this resistance is a combination of three main aspects (a) baseline resistance which depends on the type of sensitive layer and its fabrication technique, (b) drift in the baseline resistance due to temperature and mechanical aging, and (c) Variation in resistance in presence of target gas/VOC and the amount of variation is depends on the concentration of the target gas/VOC. Generally, the art of sensor resistance monitoring is mainly divided into two categories (1) classical interface/indirect interface and (2) direct interface, as shown in Figure 7.1 [1].

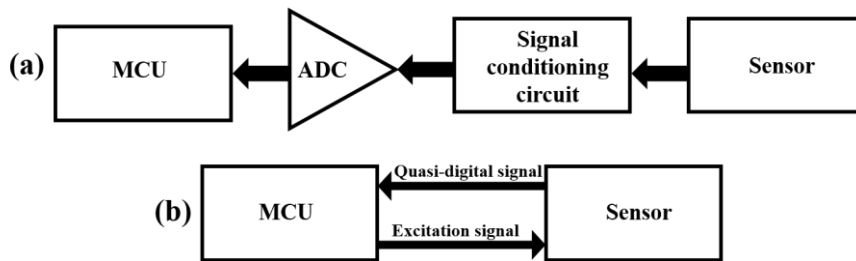


Figure 7.1. (a) classical/indirect interface (b) direct interface.

In classical interface, sensor is connected to signal conditioning circuit, where sensor resistance to voltage conversion, filtering, amplification, and linearization are performed. Next, the resulting analogue signal is send to an analogue to digital converter for its digital conversion. Finally, the microcontroller unit process the digital data with other devices to display the information of measured sensor data (Figure 7.1. (a)). Usually, in the classical interface, a high-stability voltage generator (dc voltage of 1 V) is used to power the sensor and a high resolution pico-ammeter is used to measure the current [2]. The resistance value is measured by voltage to current ratio and subsequently response can be measured by relative changes ($\Delta R/R_{air}$) of the resistance. In this process a high resolution analog to digital converter is required to measure a very small current corresponding to a large resistance. If the sensor resistance varies over many decades for example six decades (from $k\Omega$ to $G\Omega$), then the required resolution of ADC is 27 bit ($\log_2 10^8 = 26.6$), which is practically very big. It is possible to realize 27 bit resolution ADC by using multiplexed architecture but it is not a solution in terms of low cost. Also the required resolution can be reduced to 14 by dividing the total range into three parts (from 10Ω to $1000 k\Omega$, $1000 k\Omega$ to $100 M\Omega$, and $100 M\Omega$ to $10 G\Omega$) with the help of auto scaling circuits. However, this type of circuit leads to increase complexity and required calibration of the circuits, which increases cost of the system as well. Thereby, the indirect interface technique is not suitable for the development of low cost portable gas sensors.

On the other hand, in direct interface, the sensor is directly connected to MCU without using any signal conditioning circuit or ADC. In direct

interface circuit topology, microcontroller excites the sensor with an AC signal (generally, pulse wave) to get a time-modulated acknowledge signal. The analogue information (frequency, time period etc.) of the acknowledge signal can be measured directly by the inbuilt timer in microcontroller. Subsequently, the resistance of the sensor can be calculated using the analogue information of the acknowledge signal. The direct interface topology is very simple in comparison to the classical or indirect interface topology in terms of component use, physical space, and power consumption. It uses few components and an 8-bit microcontroller. Direct interface topology is very useful for the development of battery powered low cost portable gas sensors.

As most of the MOX based chemiresistive gas/VOC sensors require a certain temperature (100-400 °C) for their operation. Therefore, the electronic circuit interface also requires a temperature controlling circuits for monitoring the temperature of the microheater of the sensor.

This chapter discusses the simulation and implementation of a low cost and direct interface based resistance readout circuit and a temperature controller circuit, towards the development of lab based portable gas/VOC sensor system.

7.2. Sensor Circuits

Although there are many direct interface based resistance readout circuits reported in the literature. For example, Flammini *et al* [3] reported a direct interface circuit for monitoring high value of resistance, Lombardi *et al* [4] reported a CMOS based interface circuit, Depari *et al* [5] reported a low cost interface circuit for monitoring high resistance. However, among these, a direct interface based resistance readout circuit and a temperature control circuit provided by Sharma *et al* [6] is suitable for developing low cost portable sensors.

7.2.1. Resistance Readout Circuit

The proposed direct interface circuit is based on a RC circuit (Figure 7.2.(a)), where, the microcontroller measure the time (τ) required to charge a capacitor (C) to a threshold voltage through an unknown

resistance (R), then the resistance value (R) is calculated using the relation of these three i.e. R, C, and τ .

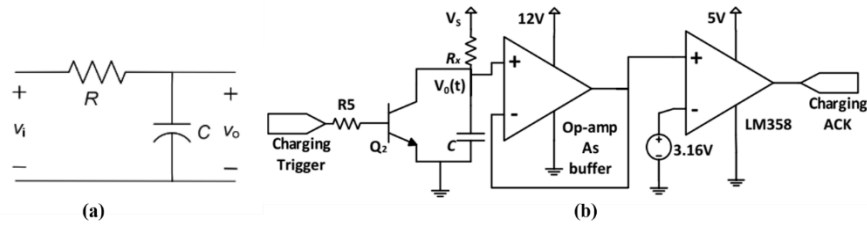


Figure 7.2. (a) RC circuit (b) resistance readout circuit [6].

Figure 7.2.(b) shows resistance readout circuit topology, primary component includes one AC pulse source (trigger charging), one BJT as switch, one unknown resistance R_x , one known capacitor C, one op-amp as buffer, and one op-amp as comparator.

The operation of the above circuit can be explained as below:

Trigger charging on: During the trigger charging high time, transistor Q_2 is on i.e. switch is close, during this period capacitor discharges instantly i.e. $V_o(t) = 0$ V, at the positive input terminal of comparator voltage is 0, so the output of the comparator is negative 0 V.

Trigger charging off: During the trigger charging low time, transistor Q_2 is off i.e. switch is open, during this period capacitor C charges through resistor R_x , voltage across capacitor $V_o(t)$ increases exponentially and reaches to 5 V, output of the comparator remain low as long as $V_o(t)$ is below a certain threshold voltage (3.16 V), output of the comparator switches its value from low to high when $V_o(t)$ reaches threshold value and remain high as long as $V_o(t)$ above threshold voltage.

During this process, initially capacitor C is discharged, when a voltage V_i is applied at the input through a resistance R, the output voltage $V_o(t)$ can be expressed as below

$$V_o(t) = V_i(1 - e^{-\frac{t}{RC}}) \quad 7.1$$

Time required to charge capacitor C from 0 V to certain threshold voltage V_{TH} is

$$T = RC \ln\left(\frac{V_i}{V_i - V_{TH}}\right) \quad 7.2$$

If V_{TH} is 63% of the input voltage V_i i.e. $V_{TH} = 0.63V_i$ (if $V_i = 5$ V then $V_{TH} = 3.16$ V), here time required to charge the capacitor to a voltage $0.63V_i$ known as time constant of the RC circuit, here $T = \tau$, the above equation become simplified one as below

$$T = \tau = RC \quad 7.3$$

So, for a fixed capacitance C, R can be calculated if one can measure the time constant of the circuit with the following equation.

$$R = \frac{\tau}{C} \quad 7.4$$

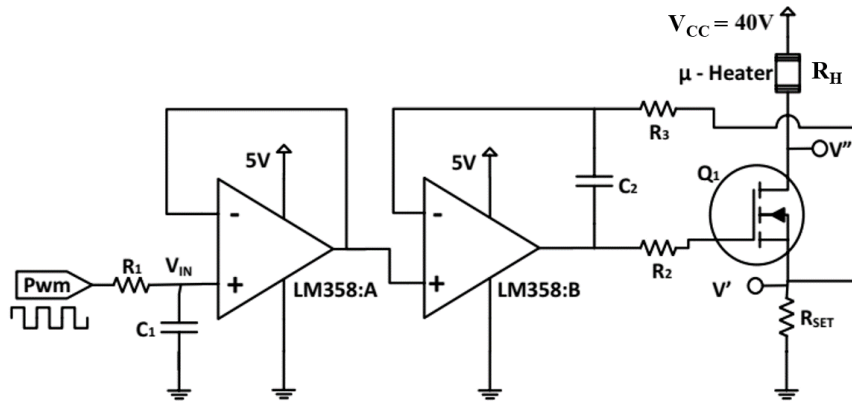
τ is the time between trigger charging low and charging acknowledge high or output comparator high, which can be measured by microcontroller timer counter.

7.2.2. Temperature Control Circuit

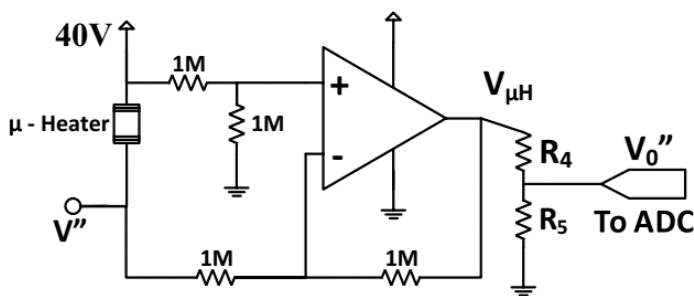
The proposed temperature control circuit is based on load independent voltage controlled current source (VCCS) circuit, where VCCS circuit is realized through current sink topology [7]. In current sink topology, gate of a FET is connected to the output of a unity gain op-amp and voltage across the source resistance R_{SET} is fed to the negative input of the op-amp. Voltage (V_{IN}) at the positive input of the op-amp forces to drop across the source resistance R_{SET} , which generates following sink current

$$I_{SINK} = \frac{V_{IN}}{R_{SET}} \quad 7.5$$

This sink current is independent of the drain resistance or heater resistance (R_H) as long as the voltage V_{CC} is not capable of holding current through R_H and R_{SET}



(a)



(b)

Figure 7.3. Temperature control circuit: (a) load independent VCCS and (b) differential amplifier[6].

Figure 7.3(a) shows the temperature controller circuit employing load independent VCCS topology. It uses a PWM source generated from microcontroller, a RC low pass filter which passes only DC part of the PWM. Op-amp LM358: A as buffer and current sink topology unit as mentioned before.

The voltage V_{IN} (which is input voltage of the VCCS topology) can be varied from 0 V to 5 V by varying the duty cycle of the PWM. As per Equation 7.5 the sink current is depends on this voltage V_{IN} . So sink current can vary from 0 to I_{MAX} , where, $I_{MAX} = 5/R_{SET}$.

Heater Current:

As there is no current through the gate of the FET, therefore, the sink current is same as the current through the heater. Although $V_{IN} \approx V'$, yet V' must be measured to get the precise current. V' can be measured by connecting it to any pin of the analog port A of the microcontroller through a buffer.

$$I_{\mu H} = I_{SINK} = \frac{V'}{R_{SET}} \quad 7.6$$

Heater Resistance:

Microheater resistance is the ratio of voltage across heater to the current through the heater ($I_{\mu H}$). Voltage across heater can be measured using a difference amplifier followed by an appropriate divider to limit (0-5 V) the input voltage at the analog input of the microcontroller, as shown in Figure 7.3(b). The heater voltage can be expressed as below

$$V_{\mu H} = (V_{CC} - V'') = \left(1 + \frac{R_4}{R_5}\right) V_0'' \quad 7.7$$

From Equation 7.6 and 7.7, the resistance of the microheater can be expressed as below

$$R_{\mu H} = \frac{V_{\mu H}}{I_{\mu H}} = R_{SET} \left(1 + \frac{R_4}{R_5}\right) \frac{V_0''}{V'} \quad 7.8$$

Heater Temperature:

The temperature of the heater is controlled by the current flowing through it. The temperature of the microheater can be estimated from the resistance of the microheater using the well known following relation

$$R_{T\mu H} = R_{0\mu H}(1 + \alpha_{\mu H}(T - T_0)) \quad 7.9$$

Where, $R_{T\mu H}$ is the resistance of the microheater at temperature T, $R_{0\mu H}$ is the resistance of the microheater at room temperature T_0 (29 °C), and $\alpha_{\mu H}$ is the temperature coefficient of the microheater material.

Form Equation 7.9 temperature of the heater can be expressed as follow

$$T = T_0 + \frac{1}{\alpha_{\mu H}} \left(\frac{R_T}{R_0} - 1\right) \quad 7.10$$

7.3. Simulation of the Circuits

The simulation of the above resistance readout and temperature control circuit are done in Proteus 8 software and corresponding programming is done in Ateml Studio 7 software.

The simulation of the circuits can be divided in two phases as described below

Phase 1: Initializing process, during this time temperature of the microheater is achieved to the require point by the microcontroller. Figure 7.4 shows the real-time screen capture image during the initialization process in simulation.

Phase 2: Resistance readout, after the initializing process i.e. when temperature of the microheater is achieved to the require temperature resistance monitoring process starts. According to the resistance value LCD display the situation of the concentration of the analyte gas/VOC. Figure 7.5 shows the real-time screen capture image during the monitoring of the sensor resistance in simulation. Figure 7.6 shows the timing diagram in digital oscilloscope, when oscilloscope inputs are connected to input of the resistance readout circuit, at node of the charging capacitance, and at the output of the resistance readout circuit, respectively.

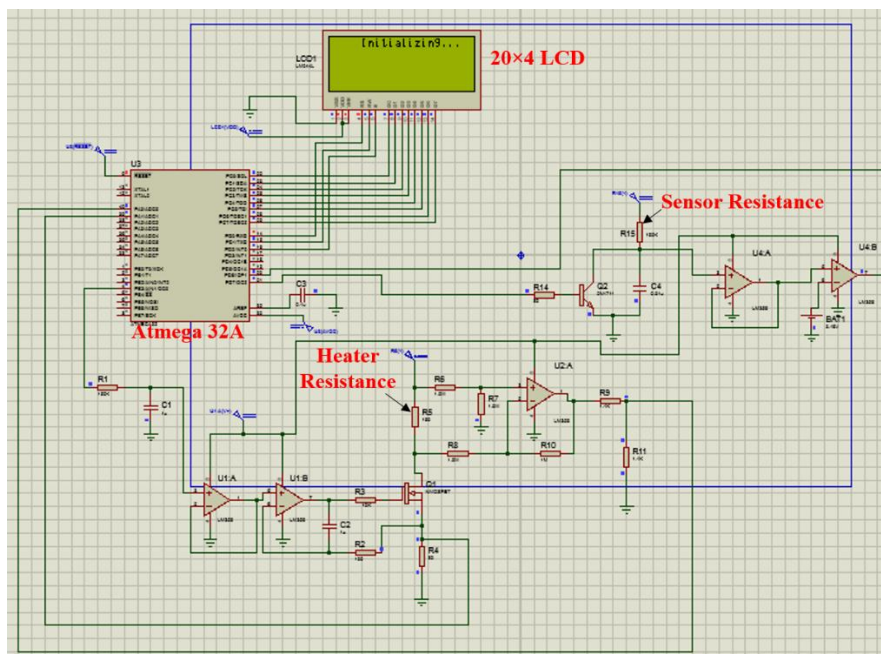


Figure 7.4. Simulation of the circuits under phase 1.

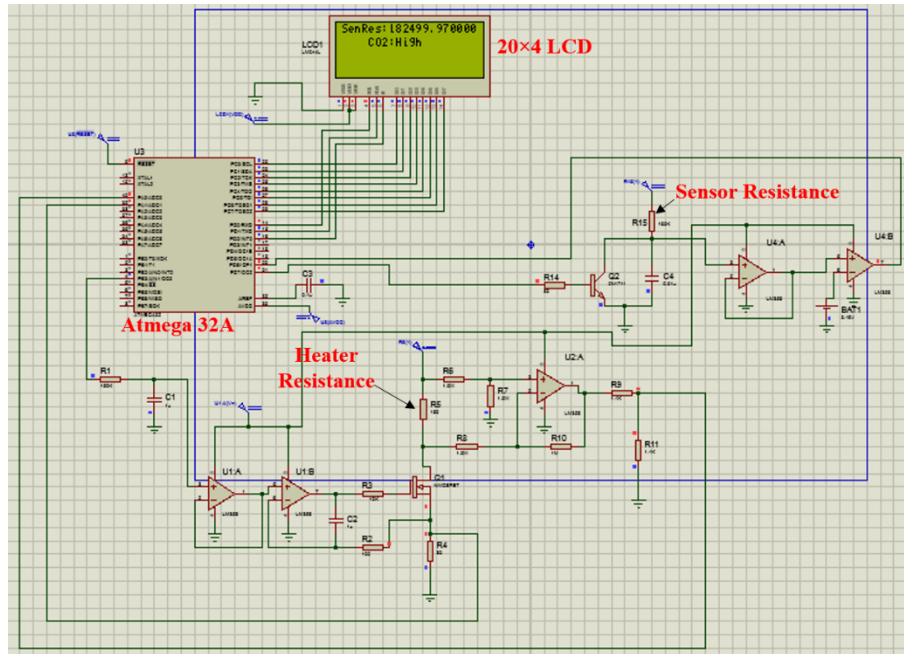


Figure 7.5. Simulation of the circuits under phase 2.

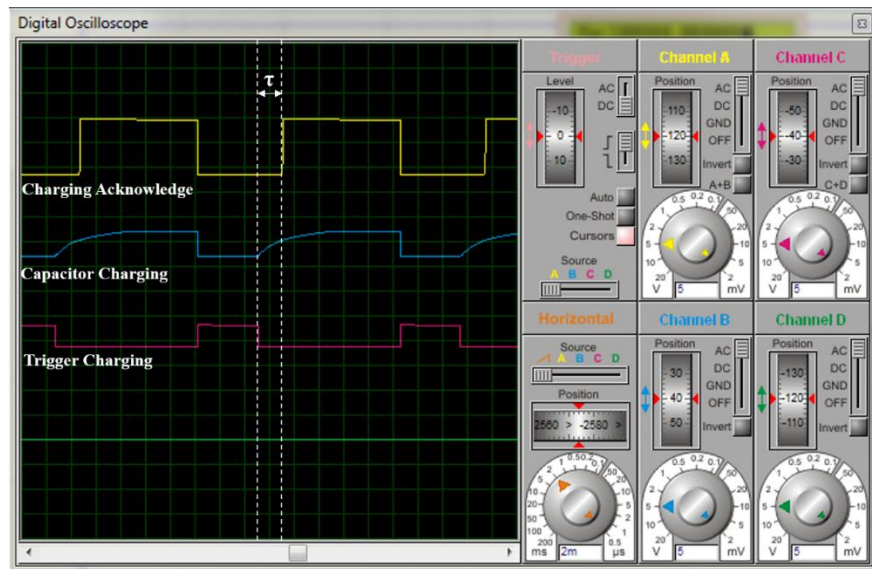


Figure 7.6. Resistance readout circuit: captured response in oscilloscope.

Main program includes two header files one for LCD operation and another for PWM generation. All these programs are described in the following section.

LCD Header File:

```
#ifndef LCD
#define LCD

#include <avr/io.h>
#include <util/delay.h>
#include <stdlib.h>
#include <math.h>
```

```

char FirstColumnPositionofLCD[4] = {0, 64, 20, 84};

void InitializeLCD (void);
void Check_If_LCD_Is_Busy (void);
void Peek_A_Delay (void);
void Send_A_Command (unsigned char command);
void Send_A_Character (unsigned char character);
void Send_A_String (char *stringofcharacters);
void GotoLCDLocation (uint8_t x, uint8_t y);
void Send_A_StringtoLCDLocation (uint8_t x, uint8_t y, char
*stringofcharacters);
void Send_An_IntegertoLCDLocation (uint8_t x, uint8_t y, int
IntegertoDisplay, char NumberofDigits);
void Send_A_DoubletoLCDLocation (uint8_t x, uint8_t y, double
DoubletoDisplay, char Width);

void InitializeLCD ()
{
    DDRD |= (1<<PIND0)|(1<<PIND1)|(1<<PIND2);
    _delay_ms(15);

    Send_A_Command(0x01);
    _delay_ms(2);
    Send_A_Command(0x38);
    _delay_us(50);
    Send_A_Command(0b00001100);
    _delay_us(50);
}

void Check_If_LCD_Is_Busy()
{
    DDRC = 0x00;
    PORTD |= 1<<PIND1;
    PORTD &=~ (1<<PIND0);
    while (PORTC >= 0x80)
    {
        Peek_A_Delay ();
    }
    DDRC = 0xFF;
}

void Peek_A_Delay()
{
    PORTD |= 1<<PIND2;
    asm volatile ("nop");
    asm volatile ("nop");
    PORTD &=~(1<<PIND2);
}

void Send_A_Command(unsigned char command)
{
    Check_If_LCD_Is_Busy();
    PORTC = command;
    PORTD &=~(1<<PIND0);
    PORTD &=~(1<<PIND1);
    Peek_A_Delay();
    PORTC=0;
}

void Send_A_Character(unsigned char character)
{
    Check_If_LCD_Is_Busy();
    PORTC= character;
}

```

```

        PORTD |= 1<<PIND0;
        PORTD &=~ (1<<PIND1);
        Peek_A_Delay();
        PORTC=0;
    }
    void Send_A_String (char *stringofcharacters)
    {
        while (*stringofcharacters>0)
        {
            Send_A_Character(*stringofcharacters++);
        }
    }
    void GotoLCDLocation (uint8_t x, uint8_t y)
    {
        Send_A_Command(0x80 + FirstColumnPositionofLCD[y-1] + (x-1));
    }

    void Send_A_StringtoLCDLocation (uint8_t x, uint8_t y, char
    *stringofcharacters)
    {
        GotoLCDLocation(x, y);
        Send_A_String(stringofcharacters);
    }
    void Send_An_IntegertoLCDLocation (uint8_t x, uint8_t y, int
    IntegertoDisplay, char NumberOfDigits)
    {
        char stringtoDisplay[NumberOfDigits];
        itoa(IntegertoDisplay, stringtoDisplay, 10);
        for(int i=1; i<NumberOfDigits; i++)
        {
            Send_A_String(" ");
        }
        Send_A_StringtoLCDLocation(x, y, stringtoDisplay);
    }

    void Send_A_DoubletoLCDLocation (uint8_t x, uint8_t y, double
    DoubletoDisplay, char Width)
    {
        char StringtoDisplay[Width];
        dtostrf(DoubletoDisplay, Width, 6, StringtoDisplay);
        for(int i=1; i<Width;i++)
        {
            Send_A_String(" ");
        }
        Send_A_StringtoLCDLocation(x, y, StringtoDisplay);
    }
}
#endif

```

PWM Header File:

```

#ifndef PWM
#define PWM

#include <avr/io.h>

void InitializePWM16D4 (void);
void InitializePWM16D5 (void);
void InitializePWM8B3 (void);
void InitializePWM8D7 (void);
void SetPWM16D4Duty (int Duty1B);
void SetPWM16D5Duty (int Duty1A);

```

```

void SetPWM8B3Duty (int Duty0);
void SetPWM8D7Duty (int Duty2);
void SetMaxCountforPWM16 (int MaxCount);

void InitializePWM16D4 (void)
{
    DDRD |= 1<<PIND4;
    TCCR1A |= 1<<COM1B1 | 1<<WGM11;
    TCCR1B |= 1<< WGM12 | 1<<WGM13 | 1<<CS10;
}

void InitializePWM16D5 (void)
{
    DDRD |= 1<<PIND5;
    TCCR1A |= 1<<COM1A1 | 1<<WGM11;
    TCCR1B |= 1<< WGM12 | 1<<WGM13 | 1<<CS10;
}

void InitializePWM8B3 (void)
{
    DDRB |= 1<<PINB3;
    TCCR0 |= 1<<COM01 | 1<<WGM01 | 1<<WGM00 | 1<<CS02;
}

void InitializePWM8D7 (void)
{
    DDRD |= 1<<PIND7;
    TCCR2 |= 1<<COM21 | 1<<WGM21 | 1<<WGM20 | 1<<CS22;
}

void SetPWM16D4Duty (int Duty1B)
{
    OCR1B = Duty1B;
}

void SetPWM16D5Duty (int Duty1A)
{
    OCR1A = Duty1A;
}

void SetPWM8B3Duty (int Duty0)
{
    OCR0 = Duty0;
}

void SetPWM8D7Duty (int Duty2)
{
    OCR2 = Duty2;
}

void SetMaxCountforPWM16 (int MaxCount)
{
    ICR1 = MaxCount;
}

#endif

```

Main Program:

```

#define F_CPU 1000000UL
#include <avr/io.h>

```

```

#include <avr/interrupt.h>
#include <util/delay.h>
#include <stdlib.h>
#include "LCD.h"
#include "PWM.h"

uint16_t ADCRES0, ADCRES1 = 0;

void InitializeADC(void);

int main(void)
{
    unsigned int a, b, c, low;
    int i=10;
    double static volatile Heatercurrent, Heatervoltage,
    Heaterresistance;

    InitializeLCD();

    InitializePWM8D7();
    SetPWM8D7Duty(75);

    InitializePWM8B3();
    SetPWM8B3Duty(i);

    InitializeADC();

    ADCSRA|=1<<ADSC;

    while (1)
    {
        Heatervoltage=((2*ADCRES0/1024.00)*5);
        Heatercurrent=((ADCRES1/1024.00)*5)/80;
        Heaterresistance=(Heatervoltage/Heatercurrent);
        if(i<150)
        {
            i++;
            SetPWM8B3Duty(i);
            Send_A_StringtoLCDLocation(5,1,"Initializing...");
            _delay_ms(10);
        }
        else
        {
            TCCR1A = 0;
            TCNT1=0;
            TIFR |= (1<<ICF1);
            TCCR1B = 0x41;
            while ((TIFR&(1<<ICF1)) == 0);
            uint8_t Lowbita=ICR1L;
            a = ICR1H<<8|Lowbita;
            TIFR |= (1<<ICF1);

            TCCR1B = 0x01;
            while ((TIFR&(1<<ICF1)) == 0);
            uint8_t Lowbitb=ICR1L;
            b = ICR1H<<8|Lowbitb;
            TIFR |= (1<<ICF1);

            TCCR1B = 0x41;
            while ((TIFR&(1<<ICF1)) == 0);
            uint8_t Lowbitc=ICR1L;
            c = ICR1H<<8|Lowbitc;
        }
    }
}

```

```

        TIFR |= (1<<ICF1);

        TCCR1B = 0;
low=c-b;
double Low_in_Time = (low*0.000001);
double SensorResistance = ((Low_in_Time-0.0048210)*100000000);

if(SensorResistance<100000.000000)
    {
        Send_A_StringtoLCDLocation(1,1,"SenRes:");
        Send_A_DoubletoLCDLocation(8,1,SensorResistance,10);
        Send_A_StringtoLCDLocation(5,2,"CO2:Low");
    }
else if(SensorResistance>100000.000000 &&
SensorResistance<150000.000000)
    {
        Send_A_StringtoLCDLocation(1,1,"SenRes:");
        Send_A_DoubletoLCDLocation(8,1,SensorResistance,10);
        Send_A_StringtoLCDLocation(5,2,"CO2:Midum");
    }
else if(SensorResistance>150000.000000 &&
        SensorResistance<200000.000000)
    {
        Send_A_StringtoLCDLocation(1,1,"SenRes:");
        Send_A_DoubletoLCDLocation(8,1,SensorResistance,10);
        Send_A_StringtoLCDLocation(5,2,"CO2:High");
    }
else if(SensorResistance>200000.000000)
    {
        Send_A_StringtoLCDLocation(1,1,"SenRes:");
        Send_A_DoubletoLCDLocation(8,1,SensorResistance,10);
        Send_A_StringtoLCDLocation(5,2,"CO2:Dangerous");
    }
    }
}

ISR(ADC_vect)
{
    uint8_t Lowbit = ADCL;
    uint16_t Totalbit = ADCH<<2 | Lowbit>>6;
    switch (ADMUX)
    {
        case 0x60:
            ADCRES0 = Totalbit;
            ADMUX = 0x61;
            break;

        case 0x61:
            ADCRES1 = Totalbit;
            ADMUX = 0x60;
            break;

        default:
            break;
    }
    ADCSRA|=1<<ADSC;
}

void InitializeADC ()

```

```

{
    ADCSRA |= 1<<ADEN;
    ADCSRA |= (1<<ADPS1) | (1<<ADPS0);
    ADMUX |= 1<<ADLAR;
    ADMUX |= 1<<REFS0;
    ADCSRA |= 1<<ADIE;
    sei();
}

```

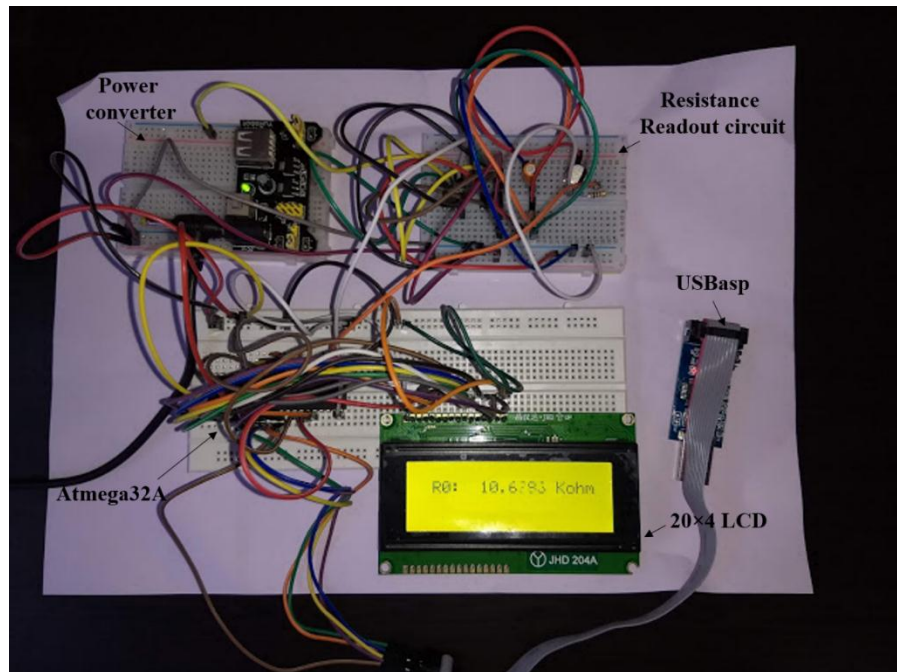


Figure 7.7. Practical realized resistance readout circuit in breadboard platform.

7.4. Practical Realization

After the successful simulation of the resistance readout and temperature control circuits, we moved towards the realization of these circuits practically in breadboard platform. In this regard, we procured all the required discrete component from local market. Figure 7.7 shows the image of the realized resistance readout circuit.

Finally, the resistance variation of the MoO₃ nanofibers sensor is monitored with the realized resistance readout circuit when exposed to 50 ppm ethanol at 275 °C in the sensing chamber. The result is shown in Figure 7.8.

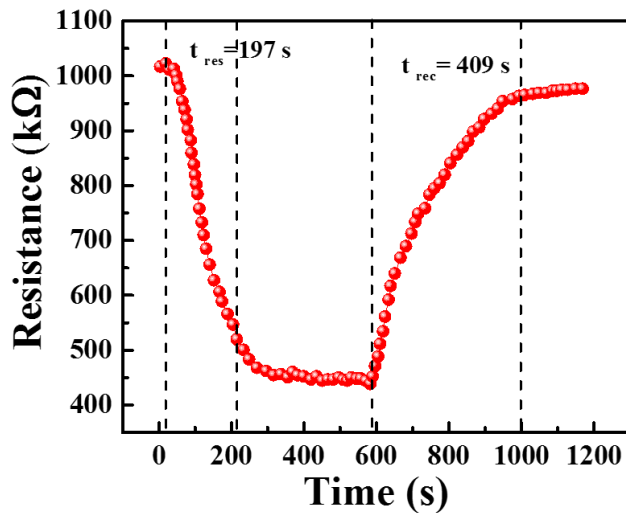


Figure 7.8. Monitoring the resistance of the MoO₃ nanofibers sensor with the resistance readout circuit at 50 ppm ethanol exposure at 275 °C.

7.5. Drawbacks

Although the simulated/realized circuits in this work has certain advantages (including low cost and simple operation) over other circuits, however, it has some critical drawbacks as described below.

- In the resistance readout circuit, the resistance read out range is fixed for a fixed charging capacitance C , for example if $C = 0.01 \mu\text{F}$, the measurable resistance range is from $10 \text{ k}\Omega$ to $1 \text{ M}\Omega$. At low charging capacitance (e.g. $0.001 \mu\text{F}$) the resistance measurement range shifts upward but at the same time measurement error increases.
- Since the excitation voltage is AC square wave, the effect of the presence of parasitic capacitance in parallel sensor resistance is unavoidable. However, this circuit does not include the measurement of parasitic capacitance which can lead to error in resistance measurement.

7.6. PCB Layout Design

After the successful realization of the resistance readout circuit, it is essential to realize the circuit in printed circuit board (PCB) platform

for stable measurements. In PCB platform, circuits are integrated in a less area and provides a stable system. Figure 7.9 shows the design schematic and Figure 7.10 shows the 3-D layout of the of the resistance readout and temperature control circuits for further development towards portable gas sensor.

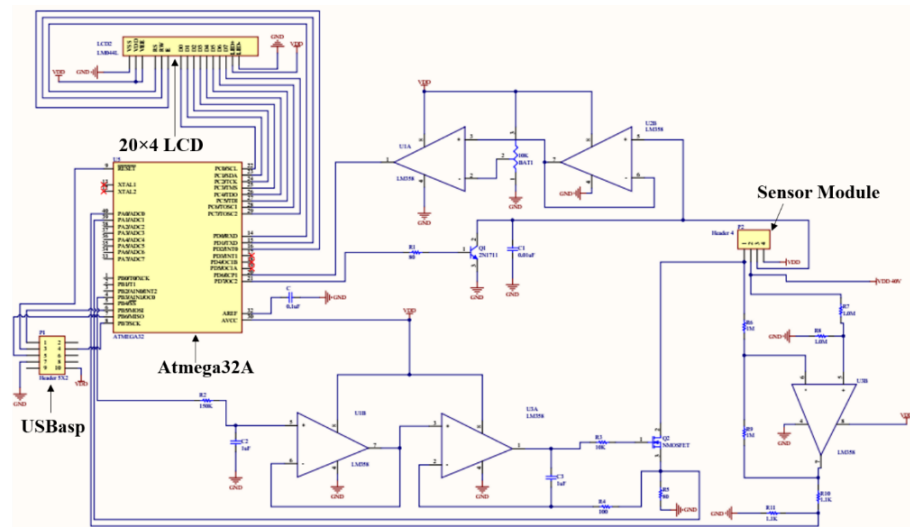


Figure 7.9. Rearrangement of the components for PCB layout design.

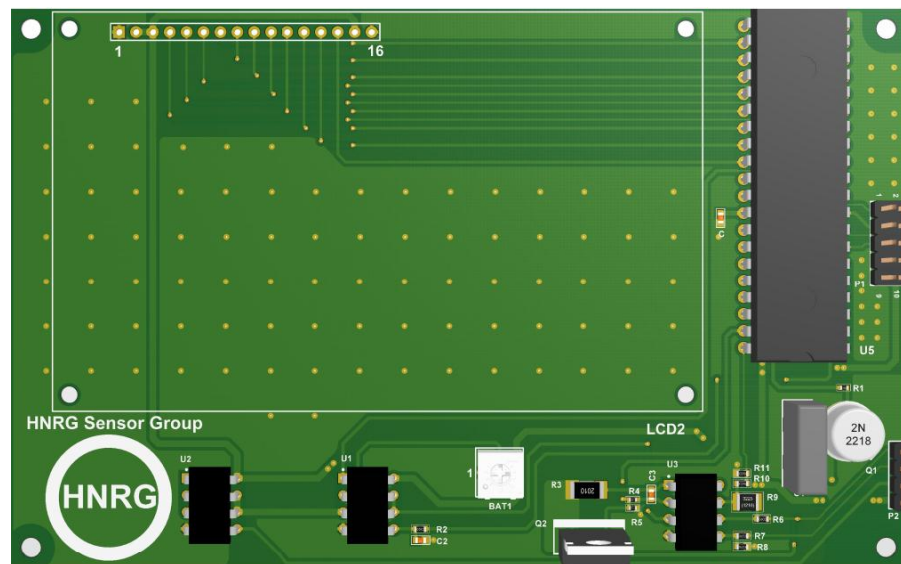


Figure 7.10. 3-D view of the PCB layout design.

7.7. Conclusion

In summary, a low cost gas sensing circuit is simulated and practically realized towards the development of a lab based portable gas

sensor. The realized circuit exhibits good measurement accuracy for the resistance range 10 k Ω to 1M Ω . Basically, this circuit is good for monitoring thin film MOX resistance. PCB design of the simulated circuits is made to realize a compact and stable measurement system.

7.8. References

- [1] R. P. Areny and J. G. Webster, *Sensors and Signal Conditioning*, Second. New York: John Wiley & Sons, 2012.
- [2] M. Grassi, P. Malcovati, and A. Baschirotto, "A high-precision wide-range front-end for resistive gas sensors arrays," *Sensors Actuators B Chem.*, vol. 111–112, pp. 281–285, Nov. 2005.
- [3] A. Flammini, D. Marioli, and A. Taroni, "A Low-Cost Interface to High-Value Resistive Sensors Varying Over a Wide Range," *IEEE Trans. Instrum. Meas.*, vol. 53, no. 4, pp. 1052–1056, Aug. 2004.
- [4] A. Lombardi *et al.*, "A CMOS integrated interface circuit for metal-oxide gas sensors," *Sensors Actuators B Chem.*, vol. 142, no. 1, pp. 82–89, Oct. 2009.
- [5] A. Depari, A. Flammini, D. Marioli, S. Rosa, and A. Taroni, "A low-cost circuit for high-value resistive sensors varying over a wide range," *Meas. Sci. Technol.*, vol. 17, no. 2, pp. 353–358, Feb. 2006.
- [6] D. K. Sharma, R. S. V. Dwara, B. A. Botre, and S. A. Akbar, "Temperature control and readout circuit interface for Mox based NH₃ gas sensor," *Microsyst. Technol.*, vol. 23, no. 5, pp. 1575–1583, May 2017.
- [7] Z. Richards, "How to generate current sources and sinks of arbitrary magnitude," 2015.

Chapter 8

Conclusion and Future Scope

8.1. Conclusions

The first/initial part of this thesis work was on the development of a gas/VOC sensing system for evaluating sensing performances of the sensors. One custom made stainless steel chamber was designed for flow-through measurement having a heater assembly, gas inlet and outlet. Two glass bubbler and one glass mixer chamber were fabricated in the institute workshop. Teflon pipes were used to establish the gas flow channels from the cylinder to the sensing chamber *via* MFC, bubbler, and mixer. A GPIB was used to interface Keithely 2612A with the system to monitor the resistance of the sensors.

The second/main part of this thesis work was on the development of ZnO and MoO₃ based tailored, composite, and hybrid materials for efficient gas/VOC sensing applications. The main findings in this part of work are described below.

Finding room temperature CO₂ sensing properties of π -conjugated amine-ZnO nanohybrids

A naphthalene based π -conjugated amine and ZnO based nanohybrids was synthesized *via in-situ* hydrothermal process on an IDEs coated PDMS substrate. Materials characterization techniques confirms the hybrid formation with layer-by-layer assembly structure. Room temperature CO₂ sensing properties of the nanohybrids were investigated systematically. Nanohybrids sensor exhibited good response (30% to 5000 ppm) to CO₂ with negligible response to other gases (e.g., CO, NH₃, H₂S) showing excellent selectivity (~ 91%) to CO₂. Admirable mechanical stability under different bending conditions

and less humidity effect on CO₂ sensing performance makes the NBA-ZnO nanohybrids a good candidate for developing wearable CO₂ sensor.

Highly selective CO sensing properties of organo-di-benzoic acidified ZnO nanohybrids at low temperature

An organo-di-benzoic acidified zinc oxide (ODBA-ZnO) nanohybrids was synthesized *via* single-pot hydrothermal method, which could detect CO gas with minimum cross sensitivity to other toxic gases like H₂S, NH₃, and CO₂. Material characterization revealed that ODBA-ZnO nanohybrids were highly porous and comprises of net-like hierarchical structures. TGA study revealed that beyond 137 °C organic component start dissociated from the hybrid material making the nanohybrids unstable beyond this temperature. The maximum response achieved by organo-di-benzoic acidified ZnO nanohybrids was ~ 35% at 100 ppm CO, which was comparable with the earlier reports, however, selectivity attained at this point was 88% which was much better than the previous reports. The operating temperature of the nanohybrid sensor was 125 °C, which was supported by TGA data. High selectivity, low humidity effect, and comparable response to CO, these characteristics indicates that ODBA-ZnO nanohybrid material has great potential for developing highly selective CO sensor.

Rose-like ZnO/MoO₃ composites as a highly selective methanol sensing material

ZnO microcubes and MoO₃ micrograss were synthesized separately through hydrothermal method, next, certain amount of each powder were mixed in water/methanol (1:1) medium under constant stirring and heating. During this process, MoO₃ micrograss transformed into petals like structure centering around ZnO microcube (pistil) to form rose-like composites. Material characterization revealed that surface area of the composites dramatically increased due to the presence of MoO₃ petals like structure. VOCs sensing performance of the composite sensor displayed good selectivity (60%) characteristics to methanol with excellent repeatability and comparable sensitivity. The presence of *n-n*

(ZnO-MoO₃) heterojunction combined with unique structural morphology led to exhibit enhance methanol sensing properties of the composite. Favorable sensing results suggest that developed rose-like composite is a promising material for methanol detection.

Obtaining surface defective MoO₃ nanofibers and their utilization as superior ethanol sensing material

A novel pulsed temperature route was adopted for alteration of MoO₃ nanostructures, from nanobelts to surface defective nanofibers. During hydrothermal process, applied constant temperature for 48 h leads to growth of uniform MoO₃ nanobelts, while applied low frequency pulsed temperature leads to growth of surface defective uniform MoO₃ nanofibers. A through material characterizations and VOCs sensing investigation revealed that MoO₃ nanofibers were superior for ethanol sensing due to their higher surface area and higher defects at the surface. The sensitivity achieved by MoO₃ nanofibers sensor to 200 ppm ethanol was 53 which is much better than the sensitivity exhibited by MoO₃ nanobelts sensor and other results reported previously. Excellent ethanol sensing properties of MoO₃ nanofibers suggest that it has great potential for developing high performance ethanol sensor.

The third/final part of this thesis work was on the development of a low cost electronic circuit interface for monitoring real-time resistance of the sensors and controlling temperature of the microheater. In this regard, the comparative literature survey presents a simple and low cost circuit reported by Sharma *et al.* Subsequently, the simulation of these circuits was performed in the Proteus 8 software, where programming was performed in the Atmel Studio 7 software. During the simulation, it was observed that resistance readout circuit can measure resistance with good accuracy when the resistance is in the range of 10 k Ω -1M Ω . After successful simulation of these circuits, resistance readout circuit was practically realized in breadboard platform with the help of discrete components. Using this realized resistance readout circuit, the resistance of the MoO₃ nanofiber sensor was monitored with good accuracy when exposed to 50 ppm ethanol. Finally, PCB layout design of the resistance

readout circuit was made towards the development of lab-based hand held portable gas sensors.

8.2. Future Scopes

The research work carried out in this thesis work yielded significant amount of knowledge regarding the use of ZnO and MoO₃ based nanomaterials for gas and VOC sensing applications. Yet, there are few research aspects that can be explored as a future work, they are mentioned below.

- Work on improving the long term stability of the nanohybrids sensor can be examined by incorporating different organic moiety.
- A suitable microheater design can be made for low power consumption as well as uniform heat distribution by exploring different heater patterns and their optimization.
- Other resistance readout circuit can be explored for increasing the measurement resistance range.
- PCB design can be further developed for practical gas/VOCs sensing applications.